THICK TARGET PIXE ANALYSIS

Carlos A. Pineda-Vargas

A thesis submitted in partial fulfilment of the requirements for the degree of Doctor of Philosophy

in the Department of Chemistry
University of Cape Town

September 1992

Acknowledgements

I wish to express my most sinsere appreciation to all those who have assisted me in bringing this thesis to completion and in particular to:

- my supervisor, Dr M. Peisach of the National Accelerator Centre (NAC), for his guidance, active participation, continuous support and enthusiasm during the execution of this project;
- my university supervisor, Professor D.A. Thornton of the University of Cape Town, for his encouragement and support throughout the years of my association with his department;
- Mr L. Jacobson, of the McGregor museum, Kimberley, for the close cooperation in the archaeological projects and stimulating discussions on archaeometry;
- Dr D.D. Cohen of the Australian Nuclear Science and Technology Organization, for supplying me with the necessary cross section data for the evaluation of the matrix correction factors;
- The Groote Schuur Hospital, for giving me the oportunity to be a member of their staff and allowing me to execute all the experinemts at NAC.
- The technical staff of the Van der Graaff group at the National Accelerator Centre, G. Ackermann, H. Schmitt, T. Swart, K. Springhorn and C. Wikner for their friendly assistence and efficient operation of the accelerator;
- Dr J.V. Pilcher for his asistant in the electronic for high energy PIXE and the system management of the different computer programs used for data manipulation;
- my father in law Dr O. Molnar for his constant encouragement and moral support during the execution of this work;
- Professor A. Rodgers of the University of Cape Town for the estimulating discussions on kidney stone formation and the proof readindg of the manuscript for chapter 6;
- Dr. A.H. Botha, Head of the Cyclotron at NAC and his accelerator staff, for the high quality beams, delivered for the experiments of high energy PIXE;
- Mr P. Groenewald for his patient and expert execution of the drawings;
- Mr S. Hendricks for the photography of the drawings;
- Mr T.K. Marais for his help in my straggle with the word processing;
- my parents for thier prayers and continuous moral support;
- most importantly to my wife Eva and my daughters Michelle and Nicole, for bearing with patience and understanding the long hours spent away in conducting this thesis.

THICK TARGET PIXE ANALYSIS

Carlos Alfredo PINEDA-VARGAS

National Accelerator Centre, P.O.Box, Faure, 7131, South Africa

September 1992

Abstract

The evaluation of the physical parameters governing the X-ray yield production in thick targets by charged particles was investigated and matrix correction factors (MCF) were calculated for a wide variety of materials including values for all pure non-gaseous elements or their compounds for the K_α and L_α X-ray lines. These factors were calculated for 1, 2, 3 and 4 MeV proton bombarding energies.

A new methodology named - Common Matrix Type - (CMT) was developed for the determination of trace element concentrations in carbon-rich materials, such as most biological materials, with unkown matrix composition. A universal set of MCF values for these materials was established for trace elements with $Z \geq 19$ and irradiations with proton energies in the range of 1 to 4 MeV.

A similar methodology was developed for silicon- and calcium-rich materials where the main components, Al, Si and Ca do not vary appreciably in their concentrations. Due to secondary X-ray fluorescence effects inside the target material, CMT methodologies were found unsuitable for iron- and gold-rich materials.

CMT methodologies were applied successfully for the determination of trace elemental concentrations in a wide variety of thick target materials, which included archaeological cultural materials, biological tissues and geological ores. The technique of correspondence analysis was used for the statistical analysis of the extended data matrix generated in most of the applications. This technique of interpretation of multielemental data proved to be a valuable tool in this work.

Two modes of PIXE application i.e. macro- and micro-modes were evaluated at different ion bombarding energies ranging from 1 to 85 MeV. Experimental X-ray production cross sections at 66 and 85 MeV were evaluated and found to correlate well with theory based on the plane wave Born approximation (PWBA) for the K_α and K_β lines. It was found that the irradiation of intermediate thickness samples of geological ores by energetic protons (66 MeV) is a suitable technique for the determination of small traces of rare earth metals with detection limits for analysis expected to be below the $\mu g.g^{-1}$ range. The fact that energetic protons can be used means that no need for matrix correction is necessary.

Micro-PIXE with low energy protons was found suitable for the determination of small traces of metals in human kidney stones and for the study of interrelationships between trace element concentrations with time of stone formation, in stones excreted from a single patient.

SUMMARY

The physical parameters governing the X-ray yield production in thick targets under bombardment with protons from 1 to 4 MeV were evaluated for analytical application. Included in the study were the compilation of matrix correction factors (MCF) for most solid elements or pure single compounds as well as compilations of the depth of analysis, ranges, total X-ray absorption and proton energies inside the target, using the most intense K and L X-ray lines. This information is presented in appendices C and D. A Fortran computer program RD1 was written for the evaluation of the MCF values. The importance of the data lies in the fact that, because the MCF is independent of the experimental conditions, this data may be used for the rapid evaluation of X-ray yields in thick targets of pure metals for PIXE calibration under any specific conditions.

This work attempts to group most existing methodologies for analysis of thick targets in a framework relevant to the thick target PIXE analyst. Methodologies for materials with known and unknown matrix composition were considered. In addition to previous methodologies a new approach, named - Common Matrix Type - (CMT) was developed for the determination of elemental concentrations in carbon-rich materials with unknown matrix composition.

Since the organic matrix composition of biological materials is often unknown, an empirical composition, that of cellulose, was assumed. This assumption was tested and found to be valid for trace elements with $Z \geq 19$, for which the maximum relative standard deviation for a set of 14 different biological standard reference materials was less than 10%. Hence a universal set of MCF values for biological materials was established for proton energies of 1, 2, 3 and 4 MeV. These values may be interpolated for intermediate proton energies. Verification of the validity of the derived universal set of MCF values, obtained from the determination of the trace elements in the known standard materials, led to predicted values which in general agreed with the known concentrations.

A similar approach was applied to silicon- and calcium-rich materials, where the main components, Al, Si and Ca do not vary appreciably in their concentrations. As before, the MCF values for elements with $Z \geq 19$ were found to be relatively constant, over a wide range of different reference materials. A case study with the standard reference material NIST-D837 steel alloy was used to evaluate the variability of the physical parameters involved in thick target PIXE yield in iron-rich materials. It was found that CMT methodology was unsuitable for these types of materials, due to secondary X-ray fluorescence effects. A similar situation applied to gold-rich materials. Since the MCF are the more critical parameters in the cal-

Contents

Chapter 1

Introduction

For a wide variety of sample materials ranging from valuable cultural history specimens to geological ores, the determination of minor and trace metals often has to be accomplished without destroying their original form. Futhermore the search for correlations between the elemental concentrations and other properties related to the nature and physical location of the same materials requires that samples be handled with care, and minimal sample preparation manipulations applied, in order to ensure their preservation. Some analytical techniques based on X-ray emission such as Electron Probe Microanalysis (EPMA) and X-ray fluorescence (XRF) have been used in the past for such purposes but the sensitivity of their analysis and high background levels of the former limit application for the determination of trace elements in bulk analysis, while the latter usually requires the sample to be in a particular geometric form, thus destroying the physical shape of the specimen. Although other techniques suited for this kind of investigation are available, long and tedious sample manipulation protocols have to be followed to prepare the specimens for analysis, thus also disturbing the original form of the samples materials.

Characteristic X-rays are produced by the creation of vacancies in the inner electron shells, followed by the subsequent filling of those vacancies by the less tightly bound electrons from others shells. Since the energy of the X-rays is equal to the energy difference between binding energies of the electron in the two shells, each element has a set of characteristic X-rays which are energetically unique. Electron vacancies in atoms can be generated by irradiation with photons (XRF) or with charged particles (PIXE).

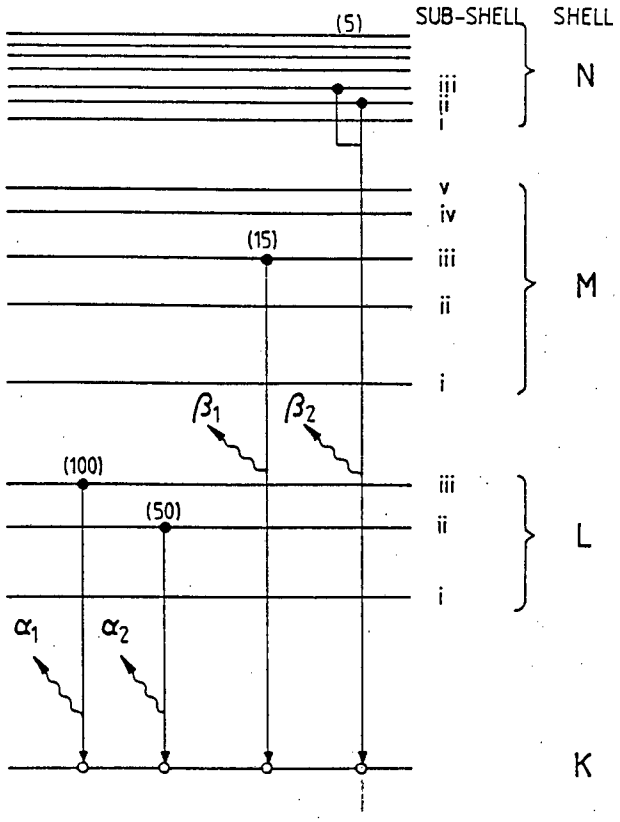

Figure 1.1: *Most intense prompt K X-rays. The values in parentheses indicate relative intensities.*

When the innermost electron shell, the K-shell, is ionised an X-ray resulting from an electron falling to fill such a vacancy is termed a K X-ray. The electron transitions are governed by well known selection rules: $\Delta n \geq 1$, $\Delta l = \pm 1$, $\Delta j = 0, \pm 1$ (where n, l and j are the principal, orbital angular and total angular quantum numbers respectively). The allowed K transitions most used for analysis are schematically illustrated in Figure 1.1. The energy difference between the K_{α_1} and the K_{α_2} is so small for elements up to about Z = 42 that they are usually not resolved by solid state detectors. The same applies for the K_{β_1} and the K_{β_2}. In the case when an electron vacancy occurs in the second and third shells, the emitted X-rays are termed L and M X-rays respectively. There are three different L sub-shells which can be ionised. Therefore, the energy of an L X-ray depends not only on the origin of the electron but also on the L sub-shell to which its falls. The more intense of these are ilustrated in Figure 1.2. The situation for the M-shell is similar, but much more complex.

Since its first use [Jo 70] in the early seventies, Proton-Induced X-ray Emission

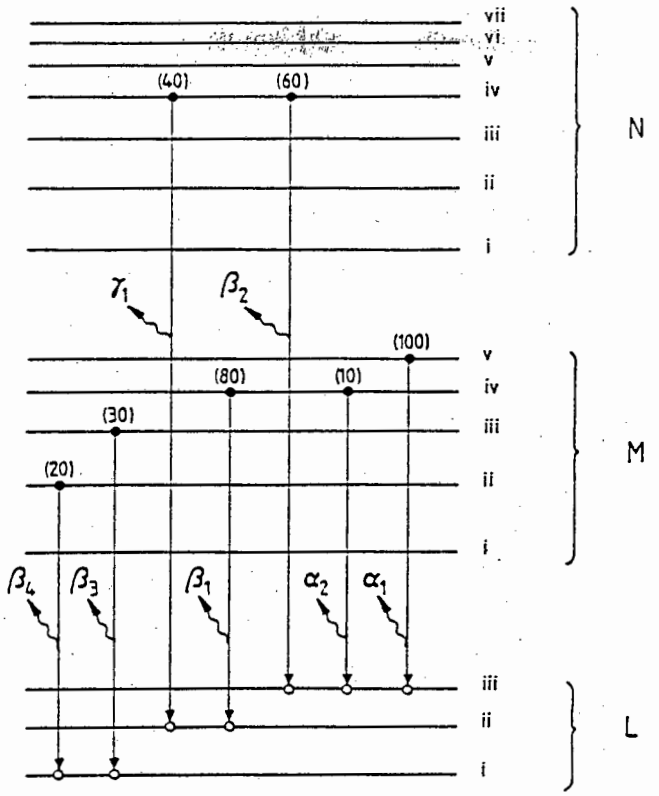

Figure 1.2: *Most intense prompt L X-rays. The values in parentheses indicate relative intensities.*

spectrometry (PIXE) has become a popular analytical technique because it is non-destructive, fast, multielemental and suited for the determination of trace elements in the surface and near-surface layers of materials, particularly in those cases where the available amount of sample material is very small.

The application of PIXE for the determination of elemental compositions in thick target materials, often referred to as TTPIXE, has been the object of much research in the recent past [Ah 77],[Ca 81],[Ca 83],[Pi 88]. In such targets the bombarding ion is stopped completely within the bulk of the target material. It is clear from the above that such a definition of a thick target in the framework of Ion Beam Analysis is dependent on the type of bombarding particle and its initial energy.

Generally speaking most of the sample materials being analysed in the laboratories have thickness varying from a few microns to a millimeter. The rapid slowing down of the projectile in the target material when penetrating the sample, changes the cross-section for X-ray production and the X-ray yield as well. These effects occur in parallel with the absorption of X-rays on the way out the sample and is greater when analyzing low Z elements such as Na, Mg, Al, Si, P and S. These effects create

difficulties for the analysis of thick targets. On the other hand the accuracy of the TTPIXE technique depends to a large extent on fully interpreting X-ray spectra arising from thick targets.

Vis-a-vis these problems there is a need for more precise data on X-ray production cross sections at all energies of interest and a detailed description of the slowing down of the beam particles in the targets considering its overall composition and structure [Am 86]. Accuracies in the 5 to 10 % range have been achieved in spite of the above mentioned problems. It is clear that the relative precision and results for thin targets may be markedly better.

The total X-ray yield from any analysis therefore depends strongly on the matrix composition of the sample under investigation. In the proton energy range between 1 and 4 MeV the typical depth of analysis is in the range of few mg/cm^2, which is comparatively much smaller than the total range of the projectile. Thus PIXE is essentially a *near surface* analytical technique.

As a result most of the PIXE work done initially was directed to the study of thin films which does not require elaborate calculations in converting from count yield to elemental concentration. The determination of trace metal concentrations is relatively simple with detection limits approaching the ng/g level but sample preparation requires special attention. This has led to the growing interest in thick target PIXE analyses where minimal sample preparation is required.

The discussions in this work will be devoted mainly to the analytical applications of protons in the usual energy range between 1 to 5 MeV where typical proton ranges vary from 5 to 80 mg/cm^2, and the use of energy-dispersive X-ray spectrometry with lithium-drifted silicon or intrinsic germanium detectors.

1.1 Thin targets

The analysis of thick specimens by PIXE is related to thin film analysis. The major difference between the two cases being that in thick samples the bombarding ion loses a substantial amount of its energy (intermediate thickness target) or is completely stopped (infinitely thick target) (see Figure 1.3). In the case of a thin film the count

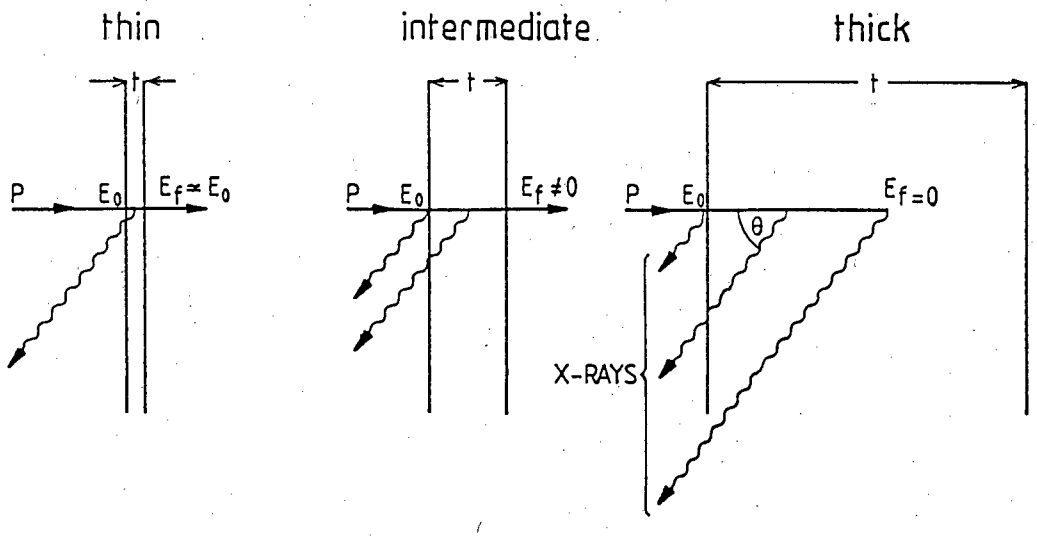

Figure 1.3: *Diagrammatic representation of X-rays from thin, intermediate and thick targets.*

yield does not contain a term for matrix absorption, because the film is considered thin enough not to absorb the X-rays (even the low energy X-rays) and the X-ray ionisation cross section within the whole thickness of the thin film can be considered constant. It is therefore appropriate to start the discussion on thick target yields by examining the thin target case.

The X-ray yield, $Y_o(Z)$ (in counts per second), for an element Z and atomic mass A_z, in a thin film of areal density $M_a(Z)$ (in μg.cm^{-2}), bombarded with proton beams of energy E_o (in MeV) is given by

$$Y_o(Z) = N_p M_a(Z) \sigma_I(Z_1 E) \omega_z b_z \epsilon_z N_A \Omega / A_z \tag{1.1}$$

Where N_p is the bombarding current (in protons per second)

$\sigma_I(Z, E)$ is the ionisation cross section of element Z, at energy E

ω_z is the fluorescence yield

b_z is the branching ratio

ϵ_z is the detection efficiency for the measured X-ray

N_A is Avogadro's number

Ω is the solid angle subtended by the detector

We can now define a constant $k(Z)$ which includes geometrical factors and yield constants, as

$$k(Z) = \omega_z b_z \varepsilon_z N_A \Omega / A_z \tag{1.2}$$

then

$$Y_o(Z) = N_p M_a(Z) k(Z) \sigma_I(Z, E) T \tag{1.3}$$

The transmission factor, T, has a value of unity when there is no absorption of the measured X-ray within the target material. A thin target has been defined as one in which the energy loss of a bombarding proton beam is negligible. However, even when the energy loss of the beam is small, the value of the transmission factor, T, can still be appreciably different from unity, especially for low energy X-rays. The variation of T as a function of proton energy loss for X-rays from elements in the atomic number range $12 \leq A \leq 39$ (Mg to Y) generated under bombardment with 4000 keV protons are listed in Table 1.1. For the low energy X-rays from the lighter elements, Mg to P, the transmission, even for a loss of as little as 100 keV, is less than 0.5, and steadily decreases with increasing loss of beam energy, i.e. corresponding to thicker targets. These data emphasize the importance of applying a correction for mass absorption of X-rays, especially for intermediate thick targets.

1.2 Transition to thick targets

1.2.1 X-ray yield

For a finite thin target, in which the bombarding beam loses a small amount of energy, and the X-ray production cross section undergoes a variation of only a few percent, the final energy, E_f, is approximately the same as E_o, the bombarding energy. The areal density can then be re-defined as $\rho(Z)dx$ where $\rho(Z)$ is the density of the element Z in the sample and dx can be considered as the thickness of an infinitesimal layer of the target material, i.e. $E_f \simeq E_o$ and $M_a(Z) = \rho(Z)dx$.

In the portion of its path from depth x_i to depth $x_i + dx$ the proton energy falls from

Table 1.1: *Transmission of characteristic K_α X-rays from a relatively thin film of the standard reference material NIES CRM-3 chlorella, under bombardment with protons of 4000 keV.*

Element	Proton Energy Loss (keV)					
	100	200	300	400	500	600
Mg	0.05					
Al	0.16	0.03				
Si	0.30	0.09	0.03	0.01		
P	0.45	0.20	0.10	0.04	0.02	0.01
S	0.57	0.33	0.20	0.12	0.07	0.04
Cl	0.68	0.46	0.32	0.22	0.15	0.11
K	0.81	0.67	0.55	0.45	0.37	0.31
Ca	0.86	0.74	0.64	0.55	0.48	0.42
Ti	0.92	0.84	0.77	0.71	0.65	0.60
Cr	0.95	0.90	0.85	0.81	0.77	0.74
Mn	0.96	0.92	0.88	0.85	0.82	0.79
Fe	0.97	0.94	0.91	0.88	0.85	0.82
Ni	0.98	0.96	0.94	0.92	0.90	0.88
Cu	0.98	0.96	0.95	0.93	0.92	0.90
Zn	0.99	0.97	0.96	0.94	0.93	0.92
As	0.99	0.97	0.96	0.97	0.96	0.95
Br	0.99	0.99	0.98	0.98	0.97	0.97
Rb	1.00	0.99	0.99	0.98	0.98	0.97
Sr	1.00	0.99	0.99	0.99	0.98	0.98
Y	1.00	0.99	0.99	0.99	0.98	0.98

Voids in the table refer to transmission factors < 0.01

E_i to $E_i - dE$ and the relationship between x_i and E_i is,

$$x_i = \int_{E_0}^{E_i} \frac{dE}{\rho S(E)} \tag{1.4}$$

where $S(E)$ is the matrix stopping power in eV per unit thickness and ρ is the total target density.

By definition $\frac{\rho(Z)}{\rho}$ is the trace element concentration C_z. Then the mass of the trace element per unit area in the slice $(x_i, x_i + dx)$ is,

$$\rho(Z)dx = C_z \frac{dE}{S(E)}. \tag{1.5}$$

Now equation 1.3 can be rewritten as:

$$Y_o(Z) = N_p k(Z)\sigma_I(E_0, Z)C_z \frac{dE}{S(E)}T. \tag{1.6}$$

For any layer, i, of thickness ΔE_i, in a thick target, the yield of X-rays from element Z is given by

$$Y_i(Z) = N_p k(Z)\sigma_I(E_i, Z)T(E_i)C_z \frac{\Delta E}{S(E)} \tag{1.7}$$

where $T(E_i)$ is the absorption from a depth x_i of the matrix.

The thick target material may be considered as consisting of n layers, in each of which the bombarding beam loses an equal amount of energy, ΔE, and in which the mean energy, E_i is considered to be constant over the entire layer. Then the total X-ray yield for element Z resulting from the generation of X-rays from all the n layers is equal to:

$$Y(Z) = N_p k(Z)C_z \frac{E_0}{n} \sum_{i=1}^{n} \sigma_I(E_i, Z)\frac{T(E_i)}{S(E)} \tag{1.8}$$

this summation can be converted to:

$$Y(Z) = N_p k(Z)C_z \int_{E_0}^{0} \sigma_I(E, Z)\frac{T(E)}{S(E)}dE \tag{1.9}$$

Multiplying and dividing by the ionisation cross section at the surface $\sigma(E_0, Z)$ which is approximately constant then the X-ray yield can be expressed in terms of a unitless relative ionisation cross section $\sigma_R(E, Z)$,

$$Y(Z) = N_p K(Z)C_z \int_{E_0}^{0} \frac{\sigma_R(E, Z)T(E)}{S(E)}dE \tag{1.10}$$

where $K(Z) = k(Z)\sigma(E_0, Z)$ is known as the geometrical factor or sensitivity factor. Equation 1.10 can be written as,

$$Y(Z) = N_p K(Z)C_z I(Z) \tag{1.11}$$

$I(Z)$ is the integral dependent on the matrix type and denotes a matrix correction factor (MCF) for the yield Y_o in *thick targets*. For computational purposes, the integral, I, may now be rewritten as a summation:

$$I = \sum_{i=o}^{m} \frac{\sigma_R(E_i)}{\mu_z} exp(-\mu_z x_i)\left[1 - exp(-\mu_z \cdot \int_{E_{i+1}}^{E_i} \frac{dE}{S(E_i)})\right] \tag{1.12}$$

The value of μ_z is given by

$$\mu_z = \sum_{j=1}^{m} W_j \mu_{zj} \tag{1.13}$$

where the matrix consists of m elements and μ_{zj} is the mass absorption coefficient for the K X-ray of element z by element j in the matrix, whose mass concentration in the matrix is W_j.

The range x_i is given by

$$x_i = \sum_{k=o}^{i-1} \Delta E / S(E_k) \tag{1.14}$$

It is convenient to define the MCF as the inverse of the integral, I, thus

$$F(Z) = I^{-1}. \tag{1.15}$$

The method of numerically integrating $F(Z)$ is described in Appendix A. An algorithm was developed for the computation of $F(Z)$, and a Fortran computer program was written for the routine evaluation of these factors. They are described in Appendix B. In order to obtain a working compromise between accuracy and the duration of the computation, the value of ΔE has to be selected with care. Experience has shown [Pi 88] that ΔE values of 1 keV, 5 keV, 5 keV and 10 keV are suitable for bombardments with 1, 2, 3 or 4 MeV protons respectively.

The variation of $F(Z)$ as a function of the energy of the K X-rays in the standard reference material Animal Bone IAEA-H5 bombarded with protons of 1, 2, 3 and 4 MeV is shown [Pi 88a] in Figure 1.4. For elements above about Ni (Z=28), i.e. for K X-ray energies > 7 KeV, the rate of change of the $F(Z)$-values is small, so that the knowledge of the compositions of the matrix is not critical. However, for analysis involving lighter elements, the rapid change of $F(Z)$ with K X-ray energy implies that the concentration of matrix components should be well known. Since the effective depth of analysis increases with increasing bombarding energy, the value of the MCF increases in importance when analysing light elements with more energetic protons. The penetration depth in organic material is shown as function of the proton energy in Figure 1.5, from which it may be noted that low energy protons should be preferred for the analysis of such elements in organic material, because the

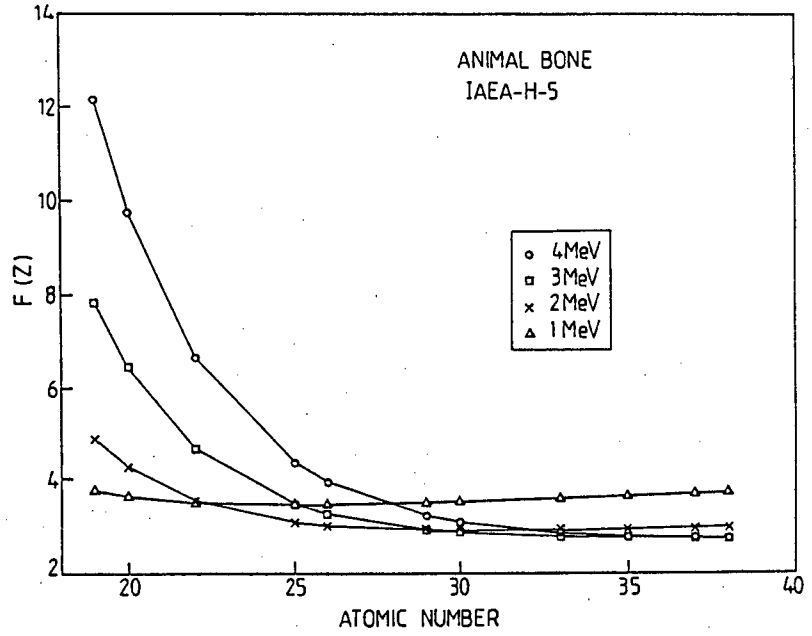

Figure 1.4: *The variation of the $F(Z)$ values with the K_α X-ray energy for the bombardment of Animal bone with protons between 1 and 4 MeV.*

total penetration depth is so small. It is implied that the sample material must be highly homogeneous.

The total thick target yield Y^T due to element Z, generated in a material of specific matrix composition has basically three components;

$$Y^T = Y^p + Y^s + Y^t \tag{1.16}$$

where Y^p is the primary excitation, Y^s is the contribution from secondary excitation by several processes among which X-ray fluorescence excitation plays the major role and Y^t is due to tertiary fluorescence effects. Depending on the type of matrix composition the value of Y^s can be substantial while Y^t has been found [Ca 89] to be small in most cases and hence it will not be considered here. The effect of the secondary fluorescence term Y^s will be treated in chapter 4. The rest of this work will concentrate on the primary contribution of Y^p only, which will be referred to as $Y(Z)$, as before.

Because of the complexity of the calculation process, some laboratories have opted for approximate methods to evaluate MCF values, by by-passing the calculation of the integral I in equation 1.11, and replacing it with separate semi-empirical functions of

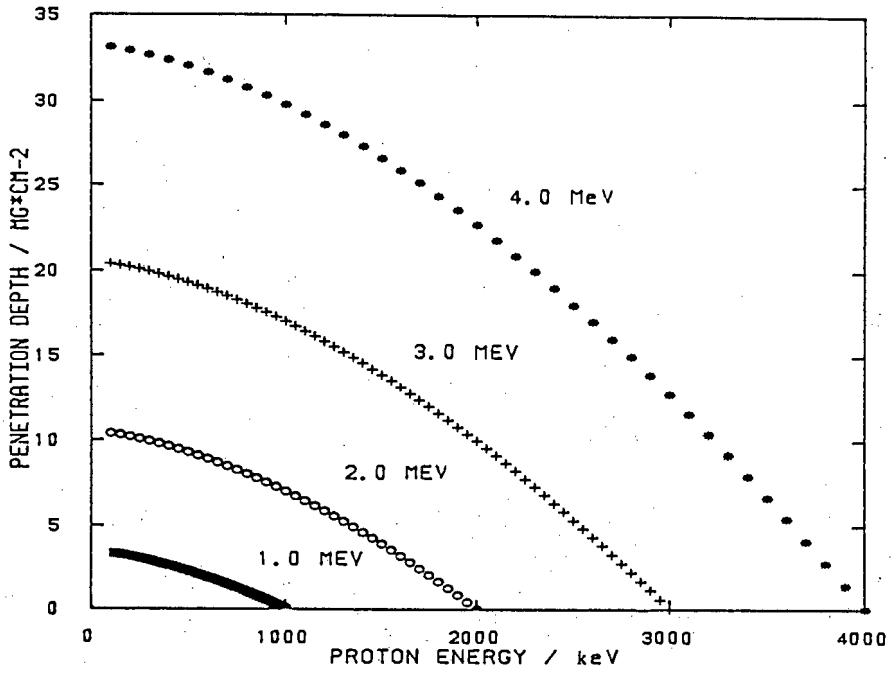

Figure 1.5: *Penetration depths of protons in organic materials.*

cross-sections, stopping power and absorption coefficients [Al 86],[Al 89],[Ga 81],[Sm 86].

1.2.2 Evaluation of the geometrical factor

The constant factor $K(Z)$ may be obtained in the following manners:

(1) By calculation from tabulated values of the parameters concerned,

(2) Experimentally from measurements on thin targets, and,

(3) Experimentally from measurements of thick targets of pure elements.

By calculation

Several tabulations exist for the values of ω, the fluorescent yield, [Ba 72],[Kr 79] and b the branching ratio [Ne 70],[Sl 72],[Sc 74]. The parameters of counting efficiency, ε, and the solid angle subtended by the detector, Ω, have to be measured. The K-shell fluorescence yield is known with good accuracy [Ba 72] and can be used with confidence. The estimated uncertainties in the value of ω_K are 3-5% for $10 \leq Z \leq 20$, 1-3% for $20 \leq Z \leq 30$ and $< 1\%$ for higher Z values. A critical assessment [Ca 88] of the L-shell fluorescent yields, showed that self-consistent values within

Table 1.2: *Recommended fluorescence yields [Ba 72]*

K-shell			L-shell				
Z	Element	ω_K	Z	Element	ω_1	ω_2	ω_3
13	Al	0.038	56	Ba	0.06		0.05
14	Si	0.043	65	Tb	0.18	0.165	0.188
15	P	0.060	67	Ho		0.170	0.19
16	S	0.082	68	Er		0.185	0.19
17	Cl	0.0955	70	Yb		0.188	0.19
19	K	0.155*	71	Lu			0.24
20	Ca	0.138*	72	Hf			0.22
22	Ti	0.221	73	Ta		0.25	0.24
23	V	0.253	74	W			0.24
24	Cr	0.283	75	Re			0.28
25	Mn	0.313	76	Os			0.29
26	Fe	0.342	77	Ir			0.25
27	Co	0.366	78	Pt		0.33	0.30
28	Ni	0.414*	79	Au			0.30
29	Cu	0.443	80	Hg		0.35	0.35
30	Zn	0.479*	81	Tl	0.07	0.35	0.35
31	Ga	0.528	82	Pb	0.08	0.36	0.42
33	As	0.588	83	Bi	0.11	0.35	0.37
34	Se	0.596*	90	Th			0.47
35	Br	0.622*	92	U			0.47
37	Rb	0.669					
38	Sr	0.702					
39	Y	0.711*					

* Interpolated values

an accuracy of 1% could be obtained from the interpolation of tabulated values [Ch 81], for the elements $36 \leq Z \leq 96$, except that the fitted value for Tc (Z=43) has an estimated uncertainty of about 1.7%. A list of useful values of the fluorescent yield is given in Table 1.2. Transition probabilities, or relative emission rates of the K components have been calculated, using several theoretical approximations, the most useful of which are those of Scofield [Sc 74a],[Sc 74b] and Cohen [Co 87]. In general, measured data show good agreement with theory, but some discrepancies still remain [Sa 74] in the atomic number region $21 \leq Z \leq 32$. The tabulations of

Cohen [Co 87] are restricted to protons of between 2 and 3 MeV. Since accurate K_β/K_α ratios are essential in sorting out the spectral overlaps that occur in typical TTPIXE spectra, it is important to take into account the discrepancies with theory in the database of transition probabilities. The data, referred to above, enable the analyst to compile a library of emission rates of the K- and L-shell X-ray lines for each element. In this approach it is important to make an exact correction for the absorption of the X-ray signal through the absorber interposed between detector and target. If the thickness of this absorber is not well known, it must be calibrated.

Early theoretical calculations of the ionisation cross section, $\sigma_I(Z,E)$, made use of either the Binary Encounter Approximation or the Plane Wave Born Approximation (PWBA), but more accurate values were obtained [Br 81] by improving the PWBA approach by the inclusion of a number of effects in what has become known as the ECPSSR model. This acronym is derived from the inclusion of various effects such as energy loss (E), coulomb repulsion between projectile and target (C), polarisation and binding energy changes of inner electrons through perturbed stationary states (PSS) and relativistic effects (R). The ECPSSR model is accurate within 10% for $10 \leq Z \leq 92$ and for $0.02 \leq E \leq 160$ MeV. Ionisation cross sections for both K and L X-rays excited by both protons and helium ions with energies between 100 keV and 10 MeV have been tabulated [Co 88],[Pa 89] for most elements. Cross sections for selected elements bombarded with protons from 1.0 to 4.5 MeV are given in Table 1.3 for K and in Table 1.4 for Lα X-rays.

Experimentally, from thin targets

Although the above approach is the standard procedure in several laboratories [Ba 78],[Ca 75],[Cl 81], it may be more convenient to express the parameters in equation 1.11 in terms of practical units. Instead of needing to determine the absolute efficiency of the detector, which requires the use of well-calibrated sources, the sensitivity factor, $K(Z)$, can be evaluated easily by irradiating a set of thin film standards of known thickness of pure elements. Figure 1.6 shows plots of the variation of $K(Z)$ (in units of counts $\mu g^{-1}.cm^2\ \mu C^{-1}$) with the energy of K_α X-rays (in keV), for different proton bombarding energies. It may be noted that for the heavier elements,

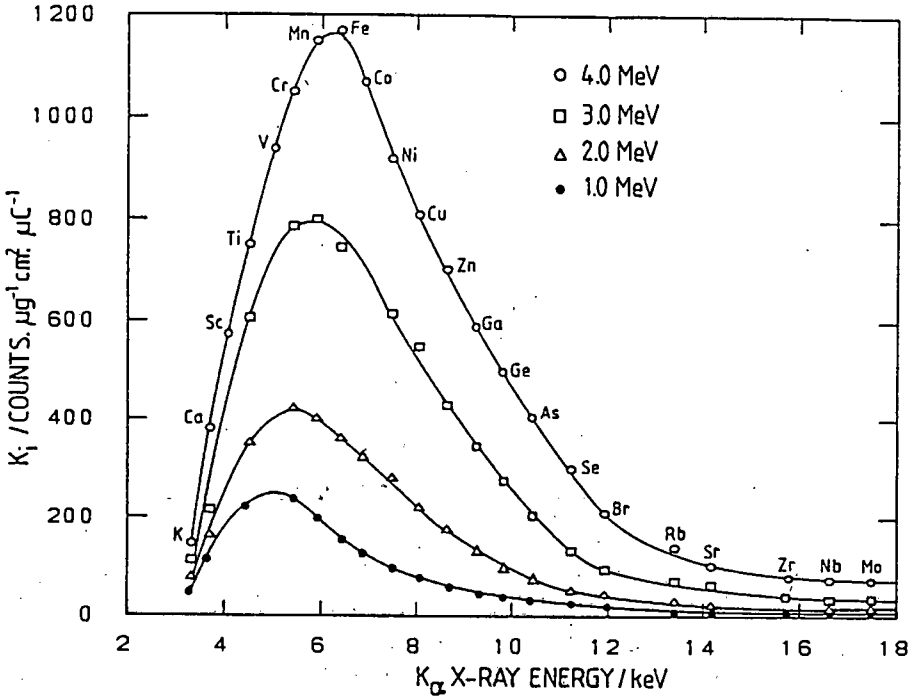

Figure 1.6: *The variation with the energy of K_α X-rays of the sensitivity factor, $K(Z)$ for proton bombarding energies of 1,2,3 and 4 MeV.*

there is relatively little change in the value of $K(Z)$. The effect on $K(Z)$ of absorbers interposed between the target and the detector is shown in Figure 1.7.

Experimentally, from thick targets

Since the bombardment of thin films often causes deterioration, either as a result of sample evaporation or decomposition, the reliability of thin sample standards is often limited. By contrast, thick targets of pure elements or compounds, or of standard materials, can readily be made and used repeatedly with confidence. From such thick targets, $K(Z)$ values can be obtained for each element as required. Obviously, the use of well-characterised reference materials would be advantageous, since a single analysis would provide information on the $K(Z)$ values of a wide range of elements, provided the composition of the matrix itself, is known.

For thick targets equation 1.11 applies, but can conveniently be rewritten as

$$Y(Z) = QC_z K(Z) I(Z) \tag{1.17}$$

where Q is the integrated bombarding charge in coulombs, C_z is the concentration of element Z in $\mu g.g^{-1}$ derived from $\rho(Z)/\rho_{tot}$. To convert basic units, N_p number

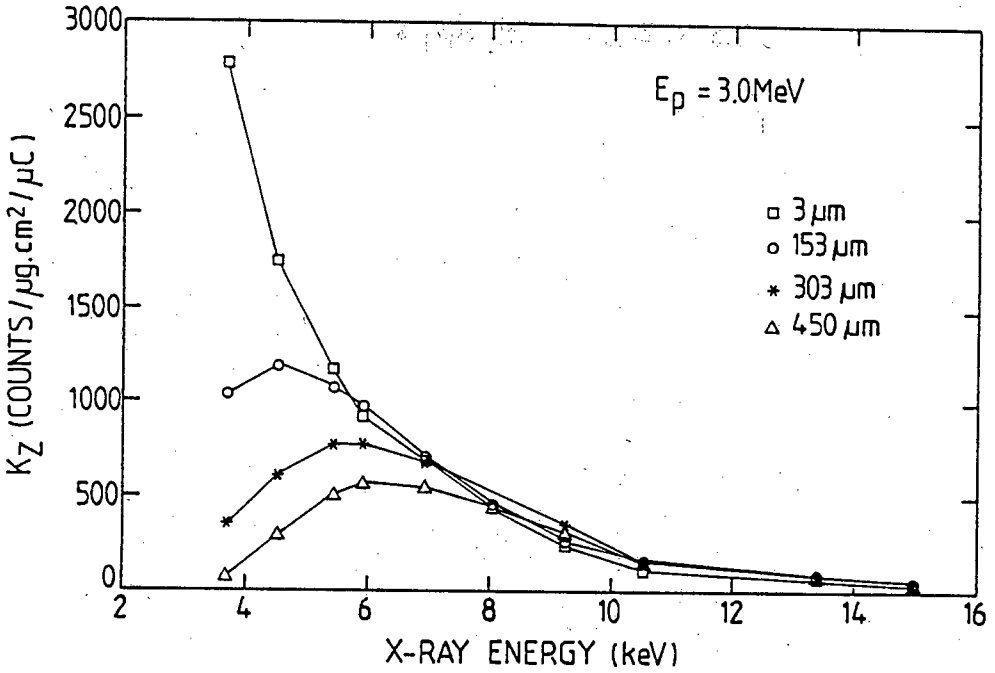

Figure 1.7: *The effect on $K(Z)$ of methyl methacrylate absorbers interposed between the bombardment target and the detector, for K_α X-rays of the lighter elements excited by protons of 3 MeV.*

of protons per second, to practical units, Q coulombs, a numerical factor is used, which has been included in the constant factor $K(Z)$. From equation 1.17 the value of $K(Z)$ becomes

$$K(Z) = \frac{Y(Z).F(Z)}{QC_z} \tag{1.18}$$

In this form only $F(Z)$ has to be calculated, as in the previous sections, while the other parameters have to be measured experimentally. Values of $F(Z)$ for the Kα X-rays from useful thick targets are given in Table 1.5 for proton energies of 1, 2, 3 and 4 MeV. Included in the table are the corresponding depths, p, at which the contribution to the X-ray count becomes negligible. Similar data for selected heavy elements and their Lα X-rays are given in Table 1.6 Appendices C and D give a complete list of practical $F(Z)$-values for most of all non-gaseous elements from K to U at different proton bombarding energies and for the K_α and the L_α lines, which can be used easily for the calculation of elemental X-ray yields in any geometry.

Table 1.5: *F(Z)-values for selected pure elements and compounds for Kα X-rays excited by protons.*

Target Material	Z	E_p=1 MeV p*	$F(Z)$	E_p=2 MeV p*	$F(Z)$	E_p=3 MeV p*	$F(Z)$	E_p=4 MeV p*	$F(Z)$
$BaCl_2$	17	1.06	19.06	1.85	50.24	1.89	94.78	2.29	158.95
KBr	19	1.81	6.67	4.20	14.05	4.70	25.62	5.84	40.15
Mn	25	2.16	4.82	6.90	6.41	9.06	10.07	12.27	17.03
Fe	26	2.17	4.90	6.81	6.50	8.91	10.14	12.05	14.72
Co	27	2.30	4.91	7.31	6.19	9.83	9.36	13.45	13.42
Ni	28	2.26	5.00	7.23	6.18	9.69	9.06	13.31	13.19
GaN	31	2.26	4.30	4.66	5.45	6.51	7.46	7.89	10.12
Ge	32	2.57	4.67	5.16	6.00	7.03	8.36	8.38	11.43
As_2O_3	33	2.26	4.22	4.85	5.16	6.94	6.86	8.53	9.12
SE	34	2.56	4.64	5.21	5.78	7.19	7.84	8.66	10.53
KBr	35	2.35	4.03	8.64	4.19	13.54	5.28	21.18	6.63
$RbNO_3$	37	1.97	4.00	4.60	4.37	7.05	5.24	9.18	6.41
$SrCO_3$	38	1.98	4.00	7.92	3.50	13.72	3.79	23.49	4.13
Y_2O_3	39	2.30	4.14	8.94	3.76	17.64	4.09	24.98	4.79
Zr	40	2.78	4.30	10.47	4.05	20.06	4.57	27.36	5.52
Nb_2O_3	41	2.45	3.56	9.73	3.14	19.62	3.27	28.52	3.65
Mo	42	2.89	4.25	11.22	3.83	21.84	4.11	30.76	4.73
Ag	47	3.05	4.79	11.89	4.07	19.52	4.48	32.13	4.94
Cd	48	3.25	4.63	12.41	3.87	20.92	4.05	35.40	4.23
In	49	3.29	4.66	12.33	3.99	20.48	4.30	34.11	4.65
Sn	50	3.27	4.64	12.65	3.92	21.22	4.16	35.71	4.42
Sb	51	3.21	4.63	12.93	3.81	21.87	3.99	37.16	4.16
Te	52	3.36	4.43	13.30	3.70	32.60	3.85	38.43	4.00
C_5NO_3	55	2.20	4.44	9.27	3.48	16.75	3.39	29.81	3.27
$BaCl_2$	56	2.49	4.50	10.31	3.54	18.46	3.47	32.66	3.37

*Depth in mg/cm^2 at which the contribution to the X-ray yield is negligible.

Table 1.6: *F(Z)-values for selected heavy elements and compounds for Lα X-rays excited by protons.*

Target		E_p=1 MeV		E_p=2 MeV		E_p=3 MeV		E_p=4 MeV	
Material	Z	p*	$F(Z)$	p*	$F(Z)$	p*	$F(Z)$	p*	$F(Z)$
Ta	73	3.39	8.34	7.97	13.98	9.10	23.05	11.37	33.99
W	74	3.51	8.19	8.25	13.78	9.33	22.71	11.79	33.54
Au	79	3.94	6.87	10.54	10.17	12.44	16.23	16.08	23.50
HgS	80	3.48	5.77	9.83	8.14	12.09	13.06	15.68	10.09
Pb	82	4.28	5.72	13.32	7.10	16.93	10.62	22.74	14.85
Bi	83	4.16	5.60	13.21	6.98	16.91	10.46	22.73	14.61
ThF_4	90	2.90	5.06	10.30	5.66	14.35	8.15	20.28	11.31
UO_2	92	3.36	5.28	11.42	6.21	15.49	9.12	21.14	12.72

*Depth in mg/cm^2 at which the contribution to the X-ray yield is negligible.

1.3 Discussion on physical parameters

Because of the importance of all physical parameters involved in the evaluation of the MCF, it is relevant to give here a discussion on the interrelationship between them.

As stipulated on the tables of Appendices C and D, the list of the parameters for each proton energy and X-ray line is as follows:

1. Target material.
2. Element of interest.
3. Depth of analysis p.
4. The integral $I(Z)$ and its reciprocal $F(Z)$.
5. The total absorption factor ABS through all the layers of integration
6. The exit energy E-EXIT, i.e. the energy after which the contribution to the yield is negligeable.
7. The total range of the protons inside the thick target.

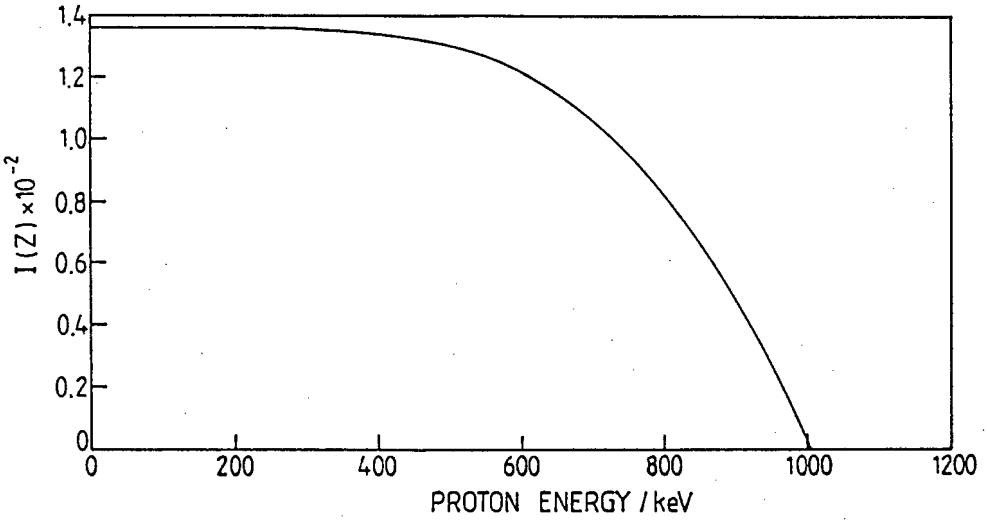

Figure 1.8: *Plot of the integral $I(Z)$ against the proton bombarding energy on irradiations of cement-based materials with 1 MeV protons.*

As shown in Figure 1.8 for irradiations with 1 MeV protons on a cement based material the $I(Z)$ integral increases as the proton energy decreases. At about 400 keV proton energy, the value for $I(Z)$ seems to stabilize. This energy is the energy at the depth of analysis after which there is no more contribution to the value of $I(Z)$. In other words $I(Z)$ converge to a constant value as from 400 keV.

As shown in Figure 1.9, where $F(Z)$-values in the same cement material are plotted against the atomic number, these $F(Z)$-values tend to increase after a particular Z value. This increase depends on the ion bombarding energy and the type of material under consideration. A possible explanation for this increase in the $F(Z)$-values as Z increase to heavy metals could be due to the increase of the electron density for heavy elements.

The increase of $F(Z)$-values with Z number is of much relevance in TTPIXE as this could explain the interrelationship between other pairs of parameters listed above. This can be shown clearly when $F(Z)$-values are plotted against the depth of analysis p. As can be seen from Figure 1.10a for a certain Z the $F(Z)$-value increases as discussed above but in addition the depth of analysis decreases. These two effects combined explain the *horseshoe* effect for heavy elements in this type of analysis.

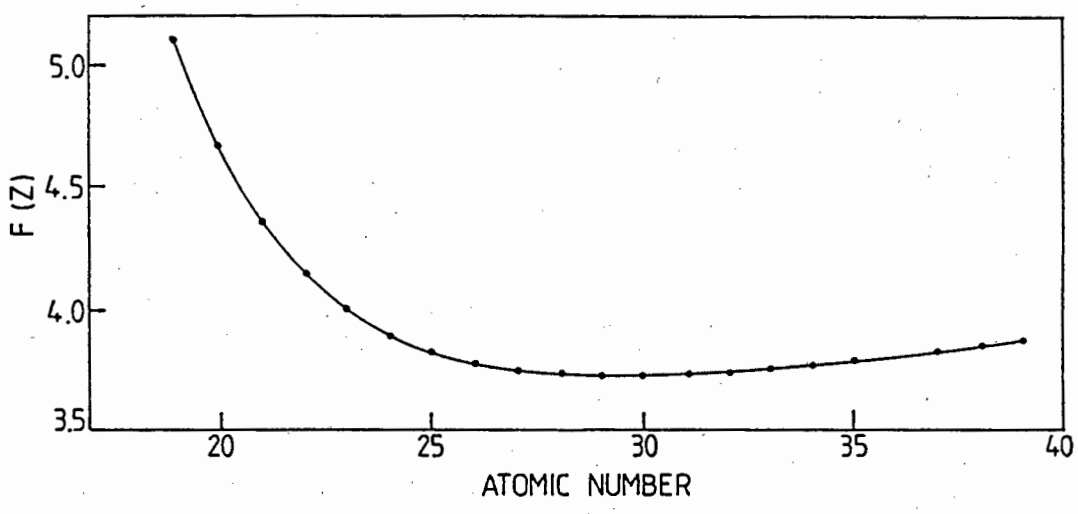

Figure 1.9: *Plot of the $F(Z)$-values in cement-based materials against the atomic number for 1 MeV protons.*

A similar type of situation exist if we look at the relationship between $I(Z)$ and p (see Figure 1.10b) and between absorption and p (see Figure 1.10c). The exit proton energy at which there is no more contribution to the value of the MCF, has a linear relationship with the depth of analysis as seen in Figure 1.10d. On the other hand the relation between the depth of analysis and the calculated proton range in any material depends critically on the bombarding energy. Table 1.7 shows this fact for the case of $CuInSe_2$ and $AgInSe_2$ compounds and pure carbon irradiated at 1.5 and 4.0 MeV protons. We can see from this table that the relative depth of analysis is smaller when samples are irradiated with 1.0 MeV protons. This points again to the fact, that $F(Z)$-values being smaller at smaller bombarding energies, the accuracy of the analysis increases. The same rationale applies to carbon with a further increase of the depth of analysis to about 68% for 4.0 MeV protons. The variation of the depth of analysis for carbon-rich materials against the atomic number is shown in Figure 1.11. The range equal to 26.1 mg/cm^2 is marked as a straight line constant for all elements. For low Z elements, like potassium, this depth of analysis is about 46% of the total range but increase to a maximum of 70% in the region of $26 \leq Z \leq 30$. This means that for this set of elements the depth of analysis does not impose a

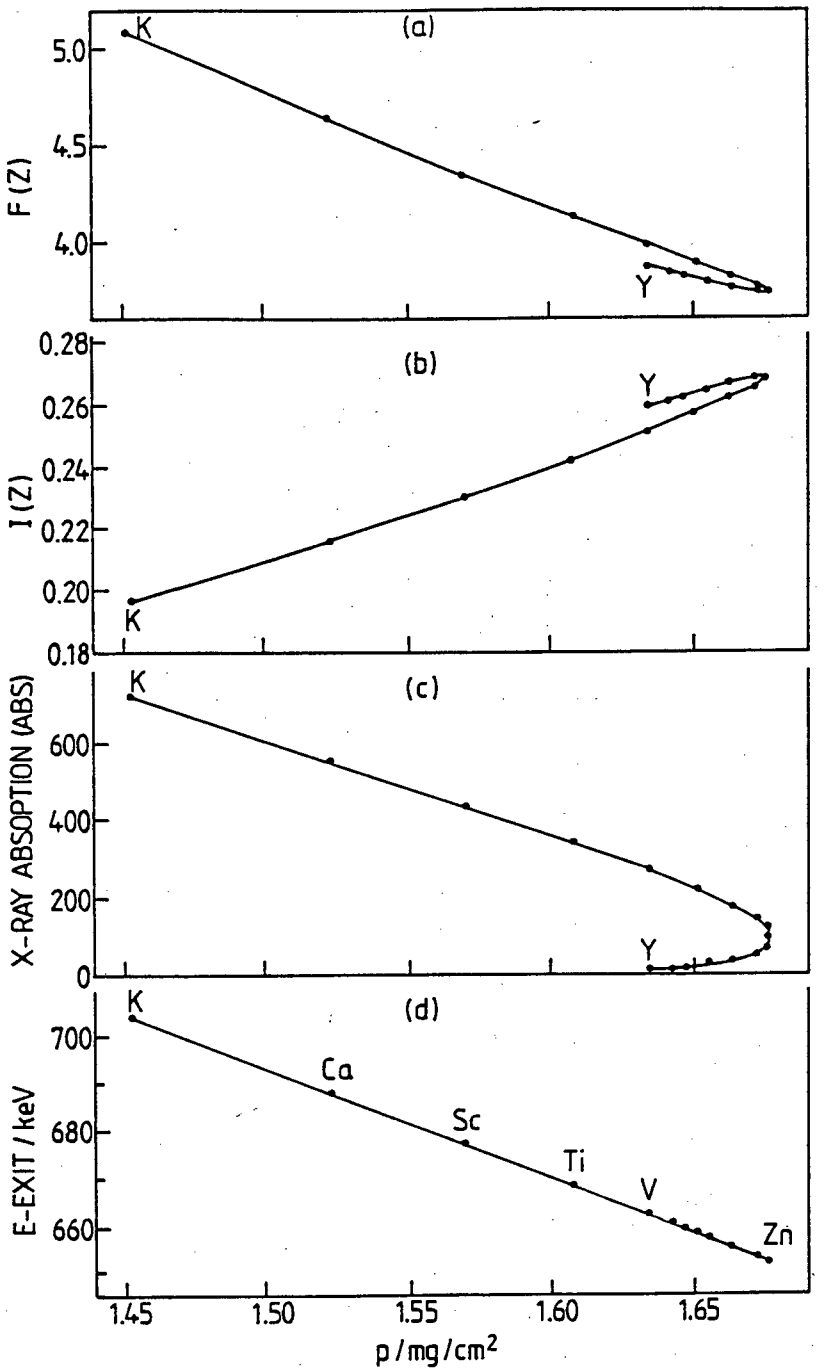

Figure 1.10: *Plots of (a) $F(Z)$ (b) $I(Z)$ (c) the absorption ABS and (d) E-EXIT against the depth of analysis p for irradiations with 1 MeV protons in cement-based materials.*

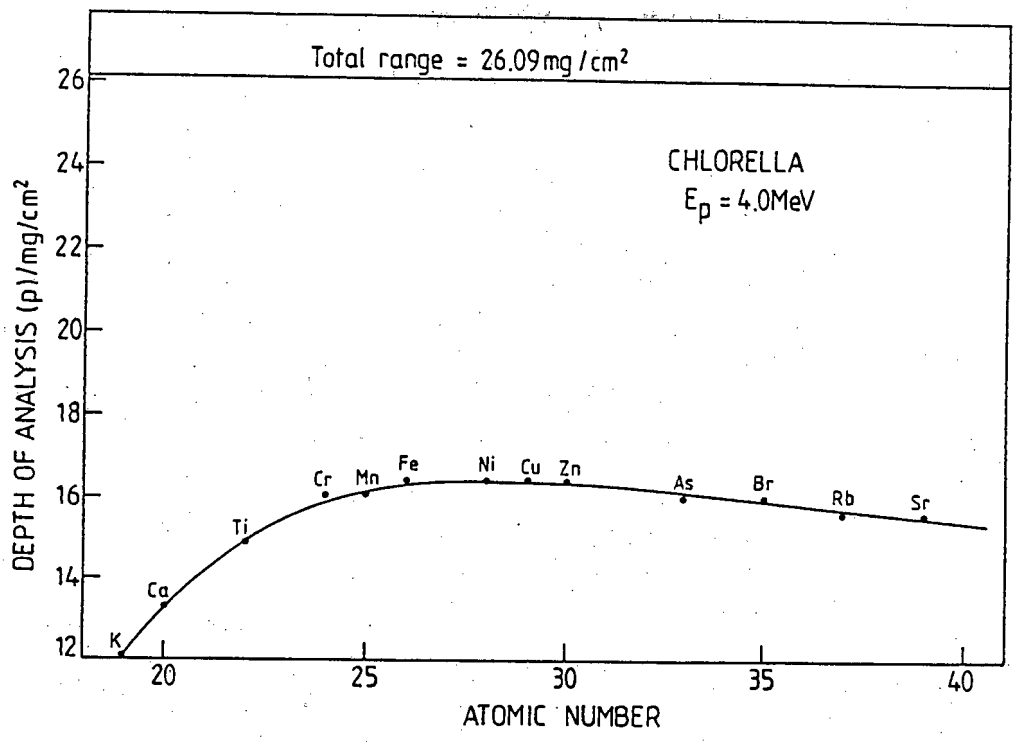

Figure 1.11: *Variation of the depth of analysis p, with atomic number, for carbon-rich materials.*

Table 1.7: *Relation between depth of analysis p and range in carbon and $AInSe_2$ compounds ($A = Cu, Ag$) at 1.5 and 4.0 MeV protons.*

$E_p = 1.5MeV$

	Cu	Se	Ag	In	Range
C	2.39	2.34	2.23	2.22	5.33
$CuInSe_2$	2.80	3.00	3.05	3.05	12.20
$AgInSe_2$	2.97	3.17	3.29	3.29	12.80

$E_p = 4.0MeV$

	Cu	Se	Ag	In	Range
C	20.60	20.10	19.10	19.00	27.60
$CuInSe_2$	12.90	17.10	22.60	23.00	48.60
$AgInSe_2$	13.00	17.60	24.00	24.30	57.30

critical correction for analytical purposes.

1.4 Scope of this work

The determination of trace element concentrations in thick targets by PIXE spectrometry is in a stage of refinement. Physical processes occurring under irradiation of such targets are not yet fully understood and need for fundamental research spurred the developments of methodologies for analysis in TTPIXE.

The main concern of this work was directed firstly, to the treatment, development and organization of the basic theoretical background for thick target PIXE in a general framework (as has already been shown in this chapter), which can be of relevance to the analyst, secondly, to the evaluation of the magnitude of the constraints in the calculation of elemental concentrations in thick target materials and thirdly to the application of different kind of methodologies of analysis in the usual Macro-mode, in Micro-PIXE and in High-energy Macro-PIXE.

These constraints generally cited as *matrix correction factors* were evaluated in different sample materials such as pure metals or their compounds, biological and environmental reference materials.

Chapter 1 describes the theoretical considerations for the evaluation of matrix correction factors, as well as an analysis of the interrelationship between all physical parameters involved in the calculation of such factors.

Chapter 2 describes the experimental techniques used in this work as related to sample preparation, description of the X-ray spectrometry detection system and data handling primarily for the Macro-mode. Since PIXE is a multielemental technique the information generated on the concentrations of major, minor and trace elements can be considerable. If required, all this data can be potentially useful for the interpretation of results. The common procedure in many laboratories involves the calculations of elemental ratios between only few elements. In this manner a large amount of information is lost or forgotten in the archives of the analyst. Mathematical statistical methods of multivariate and cluster analysis have come to the rescue of these archival data. More specifically, Correspondence Analysis, a tech-

nique developed in the early seventies [Be 69] to treat multielemental data has been used by relatively few authors [Gi 84],[Ja 91],[Pe 92]. This powerful technique of interpretation of multielemental data has proved to be a valuable tool in this work. The fundamentals of this technique are also given in Chapter 2 together with simple examples to demonstrate how it works.

The accurate measurement of the beam current as well as the effect on the background on the analysis of thick insulating target materials is also treated in Chapter 2. A brief review on different methods used to solve the above-mentioned problem is given there. Of particular interest are the results of experimental data on secondary X-ray effects in binary metals oxides and fluorides.

Chapter 3 deals with methodologies of analysis for thick samples with a known matrix composition, in particular with the use of internal and external standards applied to medicine, biology and archaeology.

Chapter 4 deals with methodologies for the analysis of thick samples with unknown matrix composition and the development of strategies to simplify the determination of trace metals in carbon, silicon, calcium, iron and gold-rich materials.

Chapter 5 presents a study on the implementation and development of high-energy PIXE at the 200 MeV Cyclotron of the National Accelerator Centre (NAC)at Faure, and demonstrates the uses of energetic protons for the determination of traces of rare earth and heavy metals in "intermediate" thick targets of geological standard materials.

Chapter 6 presents some results of analysis of kidney stones undertaken at the newly developed Proton Microprobe of the Van der Graaff accelerator, NAC. Some methodologies described in previous chapters were applied to Micro-PIXE for the determination of trace elements. Simultaneous techniques such as RBS and PIPPS were implemented for the determination of major and minor components. These results establish Micro-TTPIXE as a useful technique for the microanalysis of small kidney stones excreted in a time sequence and the study of the possible role of trace elements in their formation and growth.

Chapter 2

Experimental procedures

2.1 Sample preparation

2.1.1 Thin films

For the quantitative evaluation of the sensitivity factors $K(Z)$, thin targets of pure metals or their compounds were used. Several batches of thin deposits, evaporated on 3 μm thick mylar and mounted on aluminium frames were obtained from Messrs. Micromatter Co., Deer Harbor, U.S.A., and kept under vacuum until required. Table 2.1 shows the chemical composition of the thin films together with the areal densities of the deposits. The reported accuracy of the thicknesses of the deposits was $\pm$ 5% in the range between 30 and 75 $\mu g/cm^2$. Table 2.2 shows a comparison of reported and measured values for a batch of thin film standards checked by backscatter analysis using 2 MeV $^4He^+$ ions. In all cases (except Gd and Hg-Ag amalgam) the values were well within the stated accuracy of the suppliers.

2.1.2 Intermediate thickness specimens

Biomedical

For the determination of concentrations of trace elements in blood serum of infants and mothers, the samples were collected at birth and at regular intervals up to one year after birth. Appropriate measures were taken to prevent contamination of the samples [Ve 85]. Samples were immediately frozen and kept at - 70°C until analyzed. 100μl of sera were spiked with 5 μl of yttrium standard solution for analysis. 10 μl

Table 2.1: *Thin film standards by evaporation.*

Element	Chemical form	thickness/ (μg/cm^2)	Element	Chemical form	thickness/ (μg/cm^2)
Mg	Mg	53	Ag	Ag	44
Al	Al	42	Cd	Cd	59
Si	SiO	52	In	In	42
P	GaP*	59	Sn	Sn	38
S	CuS*	56	Sb	Sb	53
Cl	NaCl*	45	Te	Te	54
K	KI*	(48.3;53)	Ba	BaF_2	(48;56.9)
Ca	CaF_2	38	La	LaF_3	(31;56;63)
Sc	ScF_3	45	Ce	CeF_3	(42;50.1;55.3)
Ti	Ti	41	Pr	PrF_3	(48.9;50.5;51)
V	V	46	Nd	NdF_3	(44.5;52.9;57)
Cr	Cr	38	Sm	SmF_3	(53.9;54.3)
Mn	Mn	50	Eu	EuF_3	(45.4;53.5;61)
Fe	Fe	53	Gd	GdF_3	(51.4;55.1;59)
Co	Co	32	Tb	TbF_3	(47;51.3)
Ni	Ni	47	Dy	DyF_3	(43.9;51.6;52)
Cu	Cu	41	Ho	HoF_3	(56.8;65)
Zn	Zn	53	Er	ErF_3	(46.5;50.4)
Ge	Ge	52	Tm	TmF_3	(49.7;51.2)
As	As	63	Yb	YbF_3	(51.2;53.2;60)
Se	Se	51	Lu	LuF_3	(45.6;46.7)
Br	CsBr*	(41.9;48;58)	W	WO_3	(41.8;71)
Rb	$RbNO_3$	42	Pt	Pt	(44;46.6)
Sr	SrF_2	43	Au	Au	(44;50.3)
Y	YF_3	42	Hg	Hg-Ag Amalg.	(38;69)
Nb	Nb_2O_3	64	Tl	TlCl	(48.2;53)
Mo	MoO_3	47	Pb	Pb	(39.4;54)
Rh	Rh	49	Bi	Bi	46.1
Pd	Pd	53	Th	ThF_4	36.4
			U	UF_4	56

(*) Used for both elements
Values in brackets represent more than one film purchased.

Table 2.2: *Backscatter analysis of the thin standards.*

Element	Reported thickness /$\mu g.cm^{-2}$	Measured thickness /$\mu g.cm^{-2}$	Difference /%
Mg	55.46	53.00	-4.6
Al	43.27	42.00	-3.0
SiO	49.93	52.00	4.0
NaCl	47.45	46.00	-3.2
CaF_2	37.81	38.00	0.5
Ti	39.83	41.00	2.9
V	48.40	46.00	-5.2
Cr	39.03	38.00	-2.7
Mn	51.25	50.00	-2.5
Fe	53.14	53.00	-0.3
Co	31.00	32.00	3.1
Ni	46.09	47.00	1.9
CuS	55.50	56.00	0.9
Cu	41.58	41.00	-1.4
Zn	53.41	53.00	-0.8
GaF	58.35	59.00	1.1
Ge	52.68	52.00	-1.3
As	63.99	63.00	-1.6
Se	51.48	51.00	-0.9
$RbNO_3$	41.40	42.00	1.4
YF_3	40.63	42.00	3.3
Nb_2O_3	64.97	64.00	-1.5
MoO_3	46.58	47.00	0.9
Rh	48.75	49.00	0.5
Pd	52.97	53.00	0.1
Ag	43.17	44.00	1.9
Cd	60.40	59.00	-2.4
In	42.53	42.00	-1.3
Sn	37.79	38.00	0.5
Sb	52.21	53.00	1.5
Te	52.74	54.00	2.3
KI	53.59	53.00	-1.1
CsBr	49.48	48.00	-3.1
La	57.81	56.00	+3.1
Ce	54.99	55.30	-0.6
Pr	52.06	50.50	+3.0
Nd	53.71	52.90	+1.5
Sm	51.84	54.30	-4.7
Eu	43.52	45.50	-4.3
Gd	51.10	55.10	-7.8
Tb	51.83	51.30	+1.0
Dy	51.29	51.60	-0.6
Ho	58.04	56.80	+2.1
Er	45.32	46.50	-2.6
Tm	48.95	51.20	-4.6
Yb	51.88	51.20	+1.3
Lu	46.26	46.70	-1.0
WO_3	72.18	71.00	-1.7
Au	43.00	44.00	2.3
Hg-Ag	41.04	38.00	-8.0
Pb	56.38	54.00	-4.4

of this solution was deposited onto a support of Makrofol (Siemens, Germany) 2 μm thick, stretched over an aluminium holder and spread over an area of approximately 50 mm^2. These deposits were freeze-dried during a period of 24 hours to yield targets of sera suitable for in-vacuum PIXE analysis.

Geological

Geological standards were obtained from the South African Bureau of Standards and the US National Institute of Technology and Standards. After homogenisation of the powder material and reduction of the grain size, a small amount, about 4-5 mg, of geological sample was transferred to a specially designed aluminium centrifuge tube of 10mm diameter (see Figure 2.1) the base of which was an aluminium frame covered with a Mylar film of about 10 μm thickness. Before adding any liquid, the centrifuge tube was mounted in a mixer which had both a vortex and a shaking action, and shaken for about 30 seconds in order to ensure that particles adhering to the walls of the aluminium centrifuge tube were transferred to the Mylar film. To the powder was added about 10μl of chloroform containing 0.05% of Tensol Cement, a dichloromethane mixture supplied by Messrs African Explosive and Chemical Industry, Wadeville, South Africa, to act as a binder to fix the powder to the Mylar. The centrifuge tube was then again mounted in the mixer for about 2 minutes to produce a homogeneous suspension, which was centrifuged at 3000 rpm, while the centrifuge was surrounded with a hot-air bath. After 2 hours the chloroform had distilled and the glue dried. In this way a uniform, thin, circular target of about 5.7 mg/cm^2 was produced, which could readily be mounted and kept unchanged during bombardment under vacuum.

The uniformity of the deposit was visually checked by light transmission when viewed against a strong light source. If it was found that the quality of the targets depended critically on the particle type of the geological ore, with the best targets produced from the fines. The target area was sufficiently large to allow for the irradiation of several spots for replicate analysis.

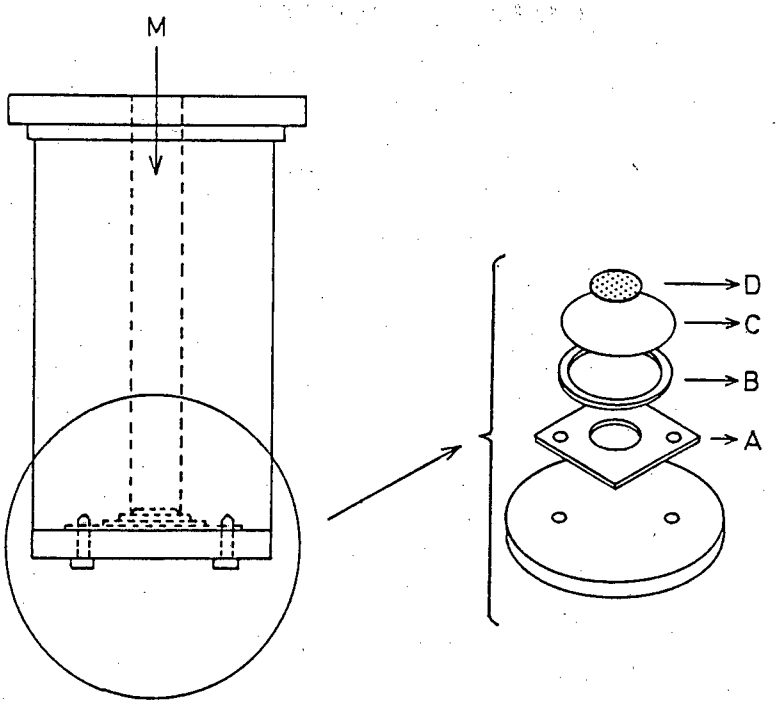

Figure 2.1: *Diagrammatic representation of the approach used for the preparation of intermediate thickness targets of geological ores: A - Aluminium holder; B - PTFE sealing ring; C - Mylar substrate; D - Sample deposit.*

2.1.3 Thick targets

Biological

Dried biological materials were powdered by the brittle fraction technique [Iy 76], [Iy 77] using liquid nitrogen cooling and teflon-covered steel balls in teflon containers shaken on the Microdismembrator supplied by Messrs Braun of Mebungen, West Germany. About 1g of powdered material was compressed in a Beckmann 10-ton hydraulic press into tablets of 13mm diameter and about 2mm thick. Figure 2.2 shows a diagrammatic representation of the type of die used to press the pellets. The paper rings and discs shown in the figure gave extra mechanical strength to allow for safer handling of the final pellet, while the paper discs also served to protect the die from any damage by small crystals of harder materials, and to decrease the possibility of cross-contamination between samples. Compression of material was carried out under vacuum to remove trapped air. It was assumed that all sample specimens were homogeneous. Prior to irradiation, all the targets were stored in a

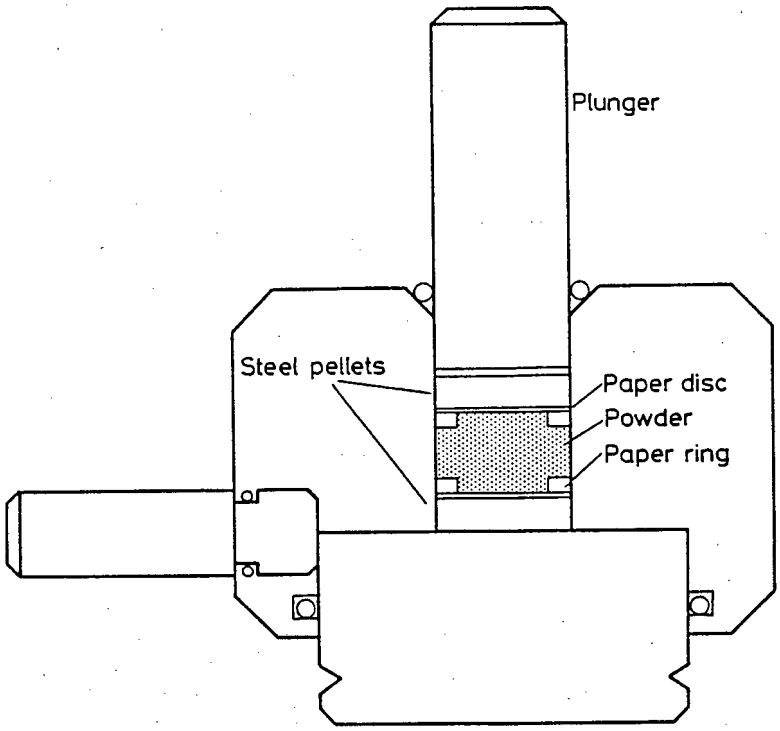

Figure 2.2: *Schematic representation of the die used for making target pellets.*

vacuum dessicator. All sample preparation was undertaken in a clean environment on a laminar flow bench where particles of more than 0.5 μm in diameter were filtered out. Standard reference materials (SRMs) of biological origin were obtained from:

1. National Institute of Standards and Technology (NIST), Gaithersburg, Maryland, U.S.A.,

2. Analytical Quality Control Services of the International Atomic Energy Agency, IAEA, Vienna, Austria, and

3. National Institute for Environmental Studies, NIES, Environmental Agency, Tsukuba Ibaraki, Japan.

Geological and Archaeological

SRM of geological ores were obtained from:

1. NIST, Gaithersburg, Maryland, U.S.A.,

2. South African Bureau of Standards, SABS, Pretoria, South Africa and

3. United States Geological Survey.

Thick pellets of these materials were prepared in the same way as previously described.

Archaeological materials, including source materials such as clay samples and archaeological artefacts were obtained from several areas of southern Africa. The clay specimens were compressed into pellets as previously described. Unlike source materials, archaeological specimens of artefacts, potsherds and others such as glass and porcelains were analysed without pre-treatment, but care was taken to remove superficial adhering particulates which were not part of the artefact. The specimens were mounted in such a way that the geometry of the target for irradiation was kept constant and presented an analytical surface that was relatively flat.

Pure metals and compounds

For the quantification of TTPIXE measurements using the methodologies of analysis described here, targets of pure elements were preferred. Where metals were available, they were used. In some cases elements were available only in a powdered form as compounds. These were used as compressed tablets, provided the material was sufficiently refractive to withstand the temperatures generated during bombardment. The chemical form of the targets used here is shown in Table 2.3.

2.2 Facilities for irradiation

A large proportion of this work was carried out on the 6 MeV Faure Van de Graaff accelerator (VDG). Beams of protons in the energy region of between 1 and 5 MeV were used. The precision of selected beam energies was of the order of 2 keV and its stability of the order of keV. In addition $^4He^+$ beams were used for backscatter analysis.

2.2.1 The beam line

The accelerator beam was focussed onto the target as a spot between 0.5 and 3.5 mm, the dimensions of which were determined by a series of tantalum collimators.

Table 2.3: *Elemental thick target standards.*

Element	Chemical form(s)	Element	Chemical form(s)
Na	NaCl;NaOH;Na_2CO_3	In	In
Mg	Mg;$Mg(OH)_2$;MgO	Sn	Sn
Al	Al	Sb	Sb(sponge)
Si	Si	Te	Te
P	$NaPO_3$	I	KI
S	S	Cs	CsCl;$CsNO_3$
Cl	NaCl	Ba	$BaCl_2$
K	KBr;KI;KCO_3	La	La_2O_3
Ca	CaF_2	Ce	CeO_2
Sc	Sc_2O_3;ScF_3	Pr	Pr_2O_3
Ti	Ti	Nd	Nd_2O_3;$Nd(NO_3)_3.6H_2O$
V	V	Sm	Sm_2O_3;SmF_3
Cr	Cr	Eu	Eu_2O_3
Mn	Mn	Gd	Gd_2O_3
Fe	Fe	Tb	Tb_2O_3
Co	Co	Dy	Dy_2O_3
Ni	Ni	Ho	Ho_2O_3
Cu	Cu	Tm	Tm_2O_3
Zn	Zn	Yb	Yb_2O_3
Ga	GaN	Lu	Lu_2O_3
Ge	Ge	Hf	HfF_4
As	As_2O_3	Ta	Ta
Se	Se(sponge)	W	W
Br	KBr	Re	Re
Rb	$RbNO_3$;RbCl;Rb_2SO_4	Os	Os(sponge)
Sr	$SrCO_3$;$Sr(NO_3)_2$	Ir	Ir
Y	Y_2O_3	Pt	Pt
Zr	Zr	Au	Au
Nb	NbO;Nb_2O_5	Hg	$HgPO_4$
Mo	Mo	Tl	Tl_2SO_4;Tl_2O_3
Ru	Ru(sponge)	Pb	Pb
Rh	Rh	Bi	Bi
Pd	Pd	Th	ThF_4
Ag	Ag	U	UO_2
Cd	Cd		

Three different collimators were used to define the beam spot. The first of these was situated at a distance of approximately 5 meters from the detector assembly. The beam-defining variable collimator was situated at approximately one meter from the detector. An anti-scattering collimator was positioned just outside the scattering chamber to prevent scattered protons from hitting the target frame or other metal components inside the chamber.

2.2.2 The scattering chamber

The aluminium scattering chamber [Gi 76] was situated immediately behind the anti-scattering collimator and was electrically insulated from the beam line by means of a PTFE junction. It could therefore serve as its own Faraday cup to integrate the bombarding current directly. A schematic diagram of the chamber is presented in Figure 2.3. The chamber was designed for optimum efficiency and for the simultaneous use of three detectors. The scattered charged particles were detected by a Si surface barrier detector mounted at 135° to the incident direction of the beam, in a plane above the horizontal. The X-rays excited by the ion beam were measured by an X-ray detector detector mounted in a port at 90° to the beam direction. The geometry of the apparatus allowed for positioning the detector window close to the target surface thus increasing the solid angle especially for detection of small amounts of metals. Gamma-rays from nuclear interactions were measured externally by a gamma-ray detector, positioned at 45° to the beam in a recess of the chamber where the wall had been thinned to reduce the attenuation of low energy radiation. The chamber was easily isolated from the remainder of the accelerator vacuum system with a single-stroke hand-operated vacuum lock. The size and position of the beam could be viewed on a quartz window at the rear of the chamber.

Automatic sample changer

Samples were mounted at 45° to the direction of the beam on a vertical ladder which had space for ten holders with an additional vacant position for beam alignment and covered with a lining of Perspex to prevent excitation of the metal by scattered protons. The ladder was fitted into the shaft of a motor drive and kept accurately at

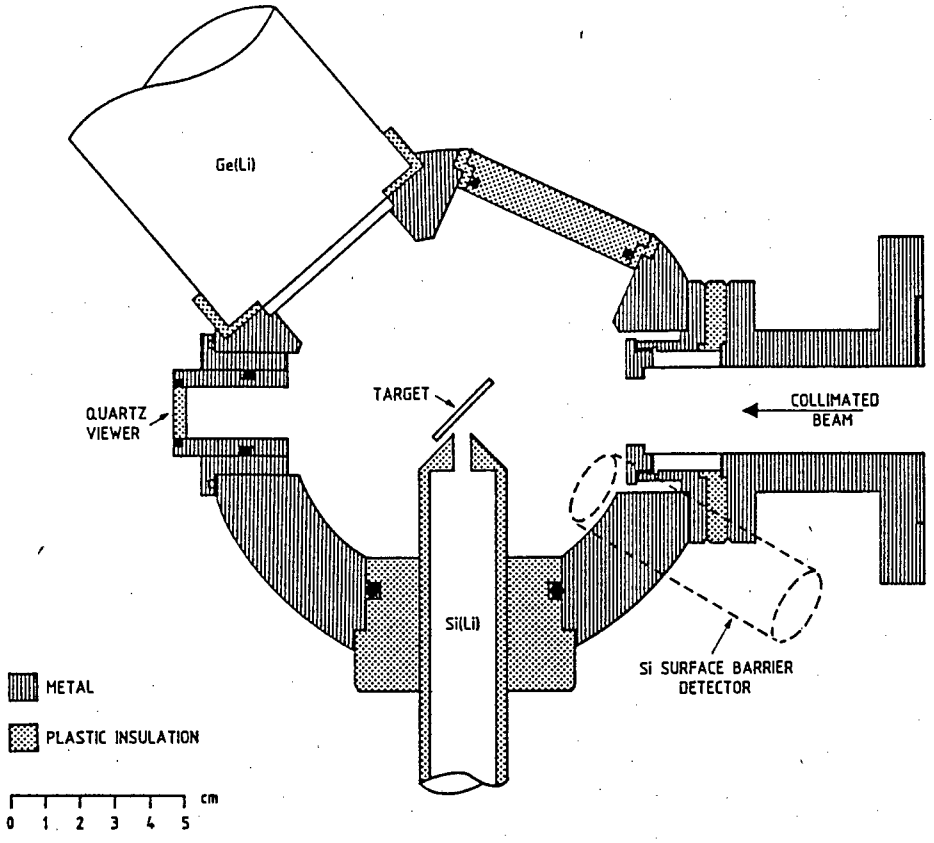

Figure 2.3: *Design of the multi-purpose scattering chamber at the Van de Graaff Group, National Accelerator Centre, in which samples were irradiated and prompt radiation analysed using three different detectors [Gi 76].*

the centre of the scattering chamber by two sets of grooved nylon wheels on either side (see Figure 2.4). The position of the ladder was controlled by a stepping motor operating at six pulses per mm, through a 25:1 gear, thereby enabling the target to be positioned accurately within about 6 μm, at pre-selected speeds from 1 to 400 steps per second. By moving the ladder in the chamber under remote control, it was possible to bombard ten targets without disruption of the vacuum system.

X-ray Detectors housing

The dipstick detectors were housed in a horizontal pipe made of Perspex, (see Figure 2.5). The total length of the tube was 20 cm, allowing for the position of the detector window to be adjusted from 2 to 22 cm from the point of incidence on the target surface to cope with varying X-ray fluxes from thick targets. The distance of the detector and the bombarding current were optimised so that the dead time of the

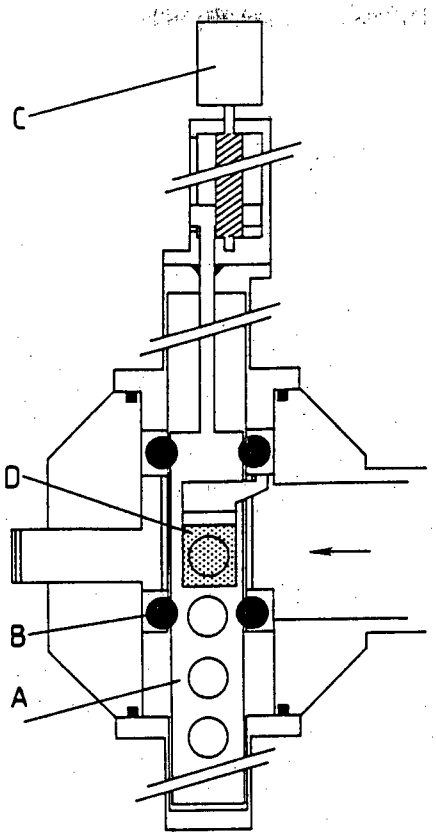

Figure 2.4: *Automatic sample changer: A - Sample ladder; B - Nylon positioning wheels; C - Stepping motor; D - Aluminium foil diffuser.*

counting equipment did not exceed about 10%. The front of the detector was shielded from stray radiation by a lead collimator with a 6mm aperture, which fitted over the dipstick pipe for a length of about 4cm. The detector was further screened from gamma radiation by standard lead bricks.

Rotating absorber holder

A multipurpose rotating absorber holder with manual external control which could locate 8 different types of absorbers was placed immediately parallel to the tube pipe housing of the detector (see Figure 2.5). This allowed the rapid and accurate optimisation of low energy X-ray absorption without the need for opening the scattering chamber. This system was found to be particularly useful in cases where the intensity of the X-rays from the major components in the target matrix was too high, degrading the quality of the spectra.

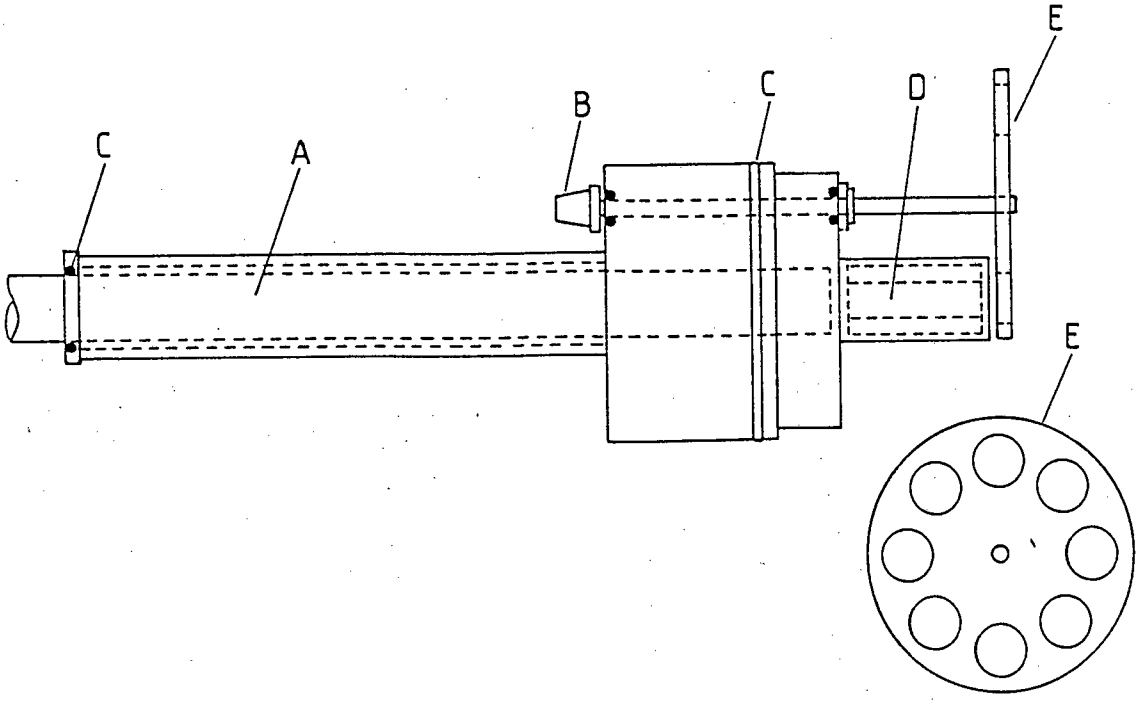

Figure 2.5: *Plastic housing for the Si(Li) detector which allows the positioning of the detector at different distances from the target surface to be able to cope with different X-ray count rates; A - Si(Li) detector; B - Absorber wheel knob; C - O-rings; D - Perspex collimators; E - Absorbers wheel.*

Anti-sparking thin foil support

An aluminium support, shown in Figure 2.4, was designed to hold a thin foil used to generate an electron flux to prevent charge build-up and sparking from insulators such as carbon based materials. It was found that the 2 μm aluminised Hostaphan was suitable for 1 and 2 MeV proton irradiation, while 5 μm aluminium foils were suitable for 3 and 4 MeV beams.

2.2.3 External mode

Most archaeological samples, could be analysed in vacuum, but due to limitations in size by the geometry of the vacuum chamber, large specimens were analysed in the external mode (see Figure 2.6) [Bo 79]. The quartz viewer at the rear of the chamber was then removed and replaced by an aluminium pipe fitted with a 10 μm

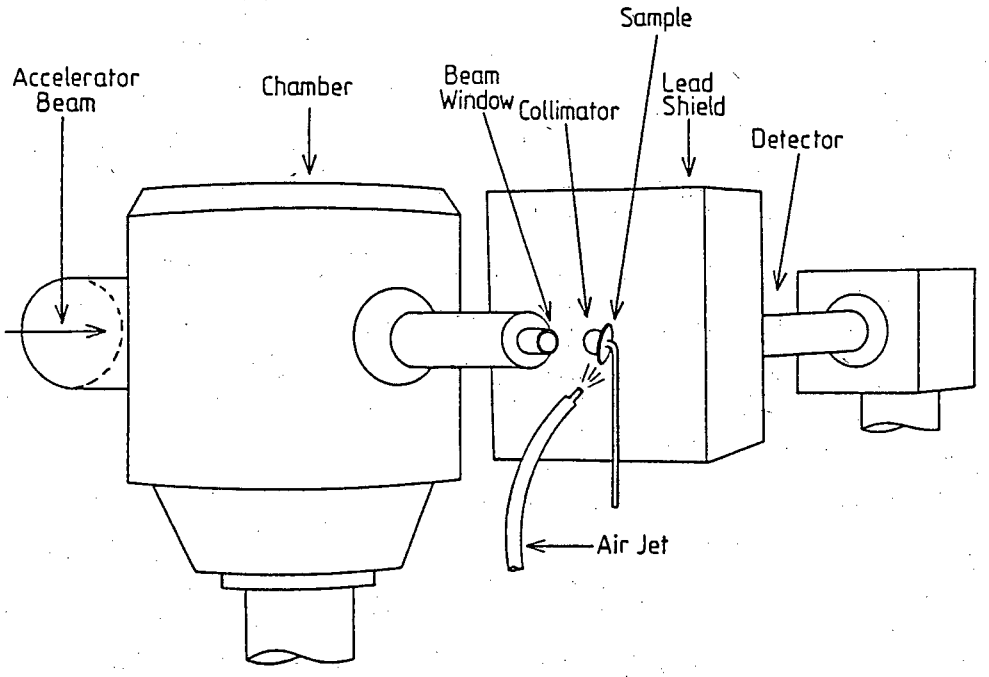

Figure 2.6: *The external beam facility at the Faure Van de Graaff accelerator.*

thick beryllium exit foil. Depending on the nature of the investigations, windows of Havar, Mylar and nickel were also used. After emerging through this window the focussed beam was allowed to fall on the target placed approximately 1cm from the window and mounted at 45° to the direction of the incident beam. The X-ray detector was shielded from the chamber and exit window by a lead shield and it viewed the irradiated spot on the target through a Perspex-lined collimated hole. The entire shield assembly was connected to the upper surface of the chamber (not shown in Figure 2.6) in order to preserve a constant geometrical arrangement. The sample position was adjusted externally so as to place the face of the sample at the intersection between the center of the beam and the detector axis. The detector viewed the sample at 90° to the incident beam. The distance between the exit window and the sample surface was 22 mm while the distance to the detector could be adjusted by shifting the detector in the direction of its axis as required, to suit the different count rates.

For very fragile samples such as intact old glass objects low currents were used. To

reduce the danger of thermal damage to the sample a jet of filtered compressed air was directed onto the region of incidence of the beam. Samples of large size or awkward shape such as pottery and glassware were mounted individually. Small tablets were mounted on a remote controlled ladder as in vacuum-PIXE. In most investigations involving the analysis of archaeological artefacts, there was little interest in determining light elements. For this reason, and to reduce the X-ray count rate, suitable absorbers of methyl methacrylate were mounted in front of the active area of the detector face. This effectively restricted the analysis to X-rays having energies above 3 keV.

The measurement of the current was difficult. In some cases, indirect ways to measure the current were considered, but most of the measurements in this mode merely required current monitoring, rather than a knowledge of the absolute value. Depending on the type of target under investigation, beam currents ranged from about 0.5 to 3 nA, and the duration depended on the content of the element(s) of interest.

2.2.4 PIXE-induced X-ray emission

For the analysis of trace elements with absorption edges below that of minor or major components of the matrix, such as steels, where iron makes up to about 80% of the whole matrix, the above scattering chamber was modified by a steel assembly inside the chamber. X-rays generated in a primary target were used to excite X-rays in the target material under investigation. To prevent X-ray excitation of the major component in the target the primary target was chosen in such a way that its absorption edge was below the absorption edge of the major component in the target.

A beam of H_2^+ ions was directed on to the primary target, which consisted of a water-cooled disc 18mm in diameter and about 3mm thick. In order to generate sufficiently intense X-ray fluxes, a current of 3 to 8 μA was used to bombard the primary target. The aperture, which collimated the primary X-rays onto the surface of the sample, was a 3mm hole in the steel assembly. Subsequently, when it was found that the Fe X-rays from the steel were scattered into the X-ray detector, the collimator was replaced by graphite with the same dimensions.

2.2.5 The detectors

The Si(Li) detector

Kα X-rays from elements with $12 \leq Z \leq 56$ and Lα X-rays of heavy metals were detected with a dipstick planar type lithium-drifted silicon detector supplied by Detector System GMBH, Germany. The detector was assembled inside a cryostat which had to be cooled to liquid nitrogen temperature six hours prior to operation. It had an active area of 30mm^2 and a thickness of 3mm. The beryllium window in front of the detector was 1 mil thick and its distance to the inside silicon crystal was 3mm $\pm$ 1mm. The reported peak-to-compton ratio was 1800:1, with an energy resolution of 163 eV at 5.898 keV.

Intrinsic germanium detector

Low energy gamma-rays and Kα X-ray lines of rare earths and heavy metals were detected by a high resolution Canberra dipstick planar germanium detector (Int-Ge), having a P-I-N structure. The active diameter was 5.64mm with an active area of 25 mm^2. The thickness of the crystal was 5mm and it was placed at 5mm from the 0.05mm berylium window.

Other detectors used in this work

A silicon surface barrier detector for the measurements of prompt alpha particles in Rutherford backscattering spectrometry (RBS) was used particularly for the measurements of thin films thicknesses and to find the more likely matrix compositions in biological and geological materials.

A lithium-drifted germanium detector (Ge(Li)), was used simultaneously with the Si(Li) detector for the detection of prompt gamma rays to obtain information on low Z major and minor components. The Ge(Li) detector had a resolution of 2.3 keV measured at 1332 keV ^{60}Co gamma-ray energy.

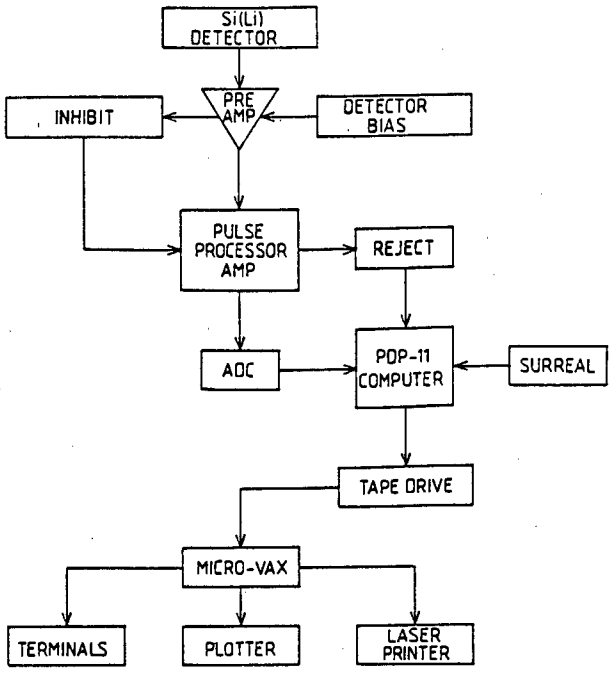

Figure 2.7: *Diagramatic representation of the electronic system used for Si(Li) spectrometry.*

2.2.6 Electronic counting system

The diagram of the electronic system used for Si(Li) spectrometry is shown in Figure 2.7. The output pulses from the Si(Li) detector were transmitted through a charge-sensitive preamplifier with pulsed optical feedback which ensured a low electronic noise, to a high resolution pulse processor unit model 1500A supplied by the Nucleus Inc., USA., containing a linear amplifier with suitable pulse-shaping networks, an active baseline restorer circuit, a pulse pile-up rejection (PUR) circuit, a fast discriminator for timing and pulse pile-up inspection, a signal stretcher, linear gate and a biased amplifier. In addition a 0 to -1000 Volts high voltage supply was included to bias the Si(Li) detector. Both preamplifier and pulse processor were able to handle high count rates without appreciable loss of energy resolution. The pulses were then transmitted to a 4096-channel analog to digital converter (ADC). A current integrator, set to count for either a pre-determined time or to accumulate pre-selected total charge, automatically switched off the measuring system. The total dead time of the system was obtained by integrating the contribution of all dead time components and represented by a total live operational time of the whole system. This value of

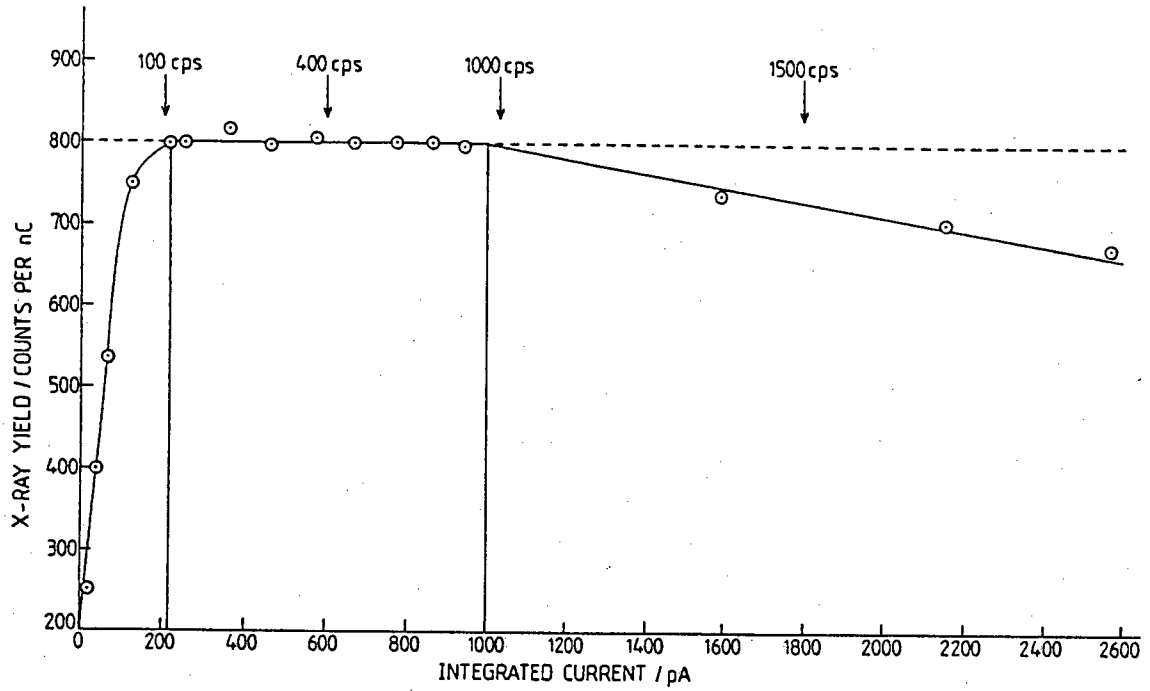

Figure 2.8: *Variation of the Kα X-ray yield (excited on a pure thick target of Copper) with the integrated proton beam current.*

the live time was stored in the first channel of the X-ray spectrum. The dead time was evaluated experimentally in a standard geometry which was kept constant for the whole duration of this investigation by checking the linearity of the normalised X-ray count yield with ion beam current. For this purpose a thick target of Cu was irradiated with 2.0 MeV protons with currents ranging from 58 pA to 7 nA. The K_α X-ray yield count was recorded and plotted against the corresponding current (see Figure 2.8). Between count rates of 100 cps and about 1000 cps the dead time was negligible, but increased steadily with the increase in count rate. An identical arrangement was used for the Int-Ge detector.

2.3 Data handling

The availability of the PDP-11 on-line computer assisted materially in the smooth running of the experiments by instantaneously supplying information such as peak position, peak areas and energy calibration on demand. At the end of each run,

the spectrum was recorded on magnetic tape to be processed off-line. A micro-VAX computer was used for all spectrum fitting and for data manipulation

2.3.1 Spectrum evaluation

Shape of the peak

When a well-defined X-ray of constant energy is measured in an ideal detecting system, for which there are no coincidences or escapes, the shape of the spectrum peak is a symmetrical Gaussian. However, no detection system is ideal and deviations from the gaussian shape are always experienced. With thick targets, the lower energy X-rays have to be measured over a background of relatively intense bremsstrahlung, resulting in asymmetric peaks. To overcome this problem, accurate subtraction of background is essential. General approaches for dealing with the fitting of backgrounds in TTPIXE have been suggested as follows:

(a) A background baseline may be fitted to a set of minima in the experimental spectrum chosen as far away as possible from peaks. When there exists a large number of peaks in a limited energy region, this approach cannot be applied [Ge 89].

(b) An analytical expression may be fitted, which describes the background with the smallest number of parameters, as, for example, the program AXIL [Va 81].

(c) An iterative stripping process may be used to remove peaks using an asymmetric weighting function at each iteration. Peak structure information is obtained by using a digital filter to suppress the background [Ma 89].

In addition the variation of background shape with the type of matrix composition is a typical feature in TTPIXE analysis. This point will be discussed further in chapter 4. With higher energy X-rays, such as the K X-rays from elements $Z \geq 35$ having energies between about 15 to 30 keV, the spectrum peak shows appreciable low-energy tailing. This effect is due to Compton scattering of the X-rays before reaching the detector. The magnitude of the effect is about 1-5% of that of the main

elemental spectrum peak and extends for about 3 keV below the energy of the main peak. The effect depends on the geometry and characteristics of the detector and has to be ascertained at the measuring facility. Analytical expressions can then be applied to cope with the low-energy tail.

Validity of the peak integral

Ideally the integral of the peak area should be a direct measure of the elemental concentration. However, several effects either add or subtract a contribution to the counts measured at the peak energy, and have to be taken into account when concentrations are calculated.

Escape peaks

The formation of escape peaks is due to the generation of an X-ray in the detector matrix by the incoming elemental X-ray. When this secondary X-ray is not integrated in coincidence with the incoming X-ray, it represents an energy loss and appears in the spectrum as an additional peak, with energy difference equivalent to that of the secondary X-ray (whether Si or Ge). The magnitude of the effect is less than or about the order of 1% and is important for Si(Li) detectors measuring the K X-rays from the elements $17 \leq Z \leq 35$. The intensity of the escape peak decreases with increasing X-ray energy. The effect is much smaller for Ge-detectors. An example of escape peaks for Int-Ge detectors is shown in Figures 2.9. The occurrence of escape peaks represent a loss of counts from the main elemental spectrum peak. Since the intensity of the escape peak is a fixed proportion of that of the elemental peak, allowance for its formation may be made either during calibration, when the escape peak may be ignored, or by adding the integral counts from the escape peak to that of the main elemental peak.

Pile-up effects

When two (or more) pulses from X-rays at the detector, arrive within the peak processing interval, the energies of the pulses are summed and result in additional spectrum peaks. The use of long integration times in the electronic circuitry, though

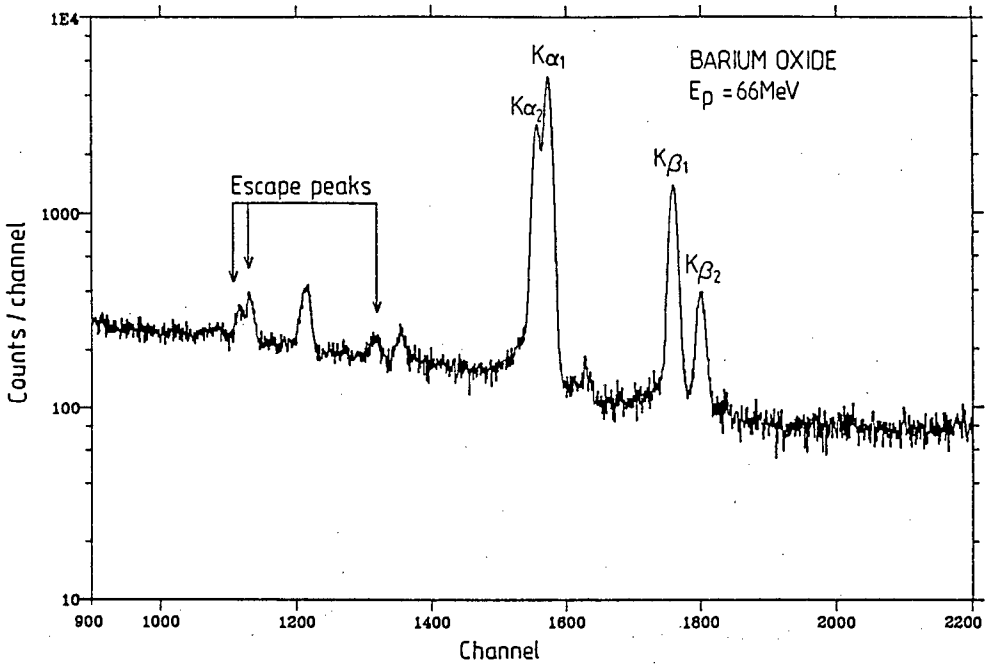

Figure 2.9: *Spectrum of a barium oxide sample obtained with a high purity Int-Ge detector, showing the germanium escape peaks from the different K-shell lines of barium. The peaks that are not identified in the spectrum are due to the surroundings in the accelerator line..*

advantageous for resolution, increases the possibility of coincidences and hence sum peaks. When two X-rays are truly coincident, there is no possibility of eliminating the sum peak effect, but when there is a short time interval between them, fast electronic processing will greatly reduce the effect (see Figure 2.10). For accurate analysis the duration that the pile-up rejection system was in operation has to be known, since the elimination of an X-ray pulse implies the loss of count rate and hence results in inaccurate analyses. Such inaccuracies can be corrected for by calibration of sum peak intensities as a function of count rate.

When the pulse from an elemental X-ray is summed with a background pulse, the effect is to increase the apparent background of the system. By removing the bombarding beam from the target during the pulse processing time, background pulses cannot be generated to add to the pulse from the elemental X-ray. Demand pulsing of the bombarding beam can be carried out by parallel electrostatic deflectors placed along the beam tube some few meters from the target, and triggered by the detection of an X-ray pulse [Al 87]. Since the duration of the deflection period can

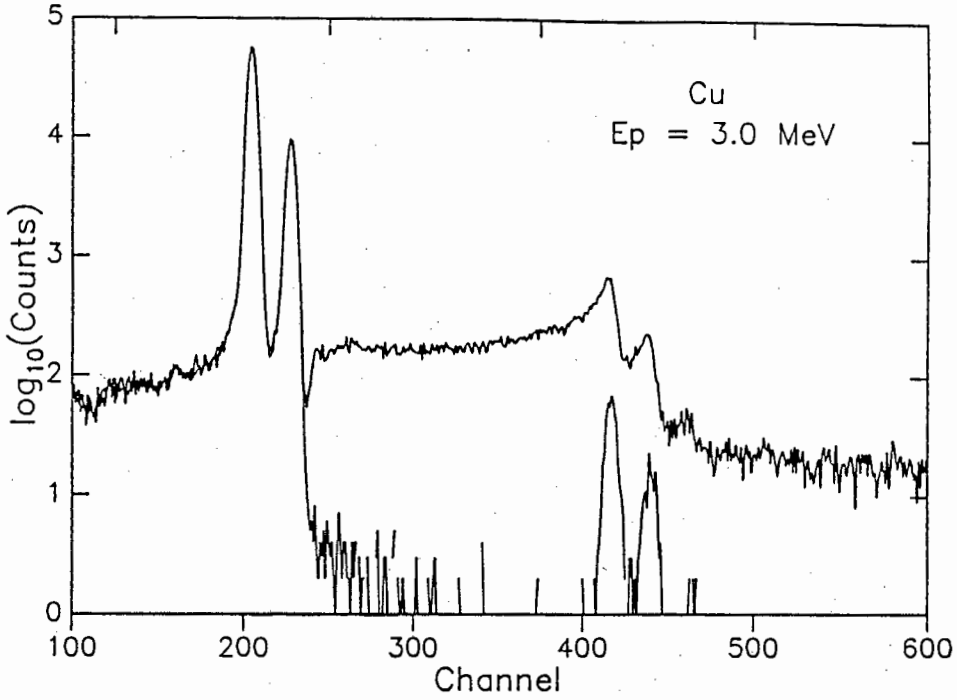

Figure 2.10: *Comparison of spectra from a thick Cu target, obtained with and without (lower spectrum) electronic pile-up rejection system at rates of 2000 and 4000 counts per second.*

be accurately determined, dead time corrections may be more accurate.

Because pile-up effects are a function of the count rate, the intensity of the effect can be reduced by decreasing the intensity of the bombarding beam, and hence decreasing the count rate, or the same result can be obtained by shifting the detection system further from the point of irradiation.

Secondary fluorescence

When an energetic X-ray from a sample component generates a secondary X-ray within the sample, the secondary X-ray will be counted as if generated by the bombarding beam, and hence constitutes a source of error leading to high results. It may be noted that secondary X-rays may be either K X-rays of lighter elements or L X-rays of lower energy. The intensity of secondary X-ray generation will depend on the sample composition [Ah 77],[Ca 89]. Tertiary fluorescence, caused by the same process but by the secondary X-ray, is of negligible intensity and can be ignored in TTPIXE. Table 2.4 lists some intensities for secondary fluorescence. The matrix element is assumed to make up at least 99% of the material and the intensity of

Table 2.4: *Secondary Fluorescence Intensities Ep = 2.0 MeV, θ = 45°.*

Matrix Element	Primary X-ray	Minor Element	Secondary X-ray	Relative Intensity /%
Ni	K	Fe	Kα	54
Zn	K	Fe	Kα	21
Ge	K	Fe	Kα	8.0
Au	L	Zn	Kα	17
Au	L	Cu	Kα	10
Au	L	Co	Kα	4.0
Au	L	Mn	Kα	1.4
Se	K	Au	Lα	28
Rb	K	Au	Lα	19
Zr	K	Au	Lα	10
Mo	K	Au	Lα	4.6
P	K	Si	Kα	21
S	K	Si	Kα	13
Ca	K	Si	Kα	1.4

the secondary fluorescence is given for the minor component as a calculated ratio relative to the calculated value of the primary X-ray [Re 75]. The expected decrease in cross section for secondary fluorescence with increasing energy difference between the exciting primary X-ray and the secondary fluorescence is clearly indicated in the table. Three cases are listed where the same secondary X-ray is excited by different primaries and one case where the same primary X-ray (Au L) excites different secondaries.

Description of program AXIL [Va 81]

The program is based on an algorithm [Ma 63] which ensures convergency of the minimisation process, finds the minimun of chi-squared and combines a gradient search with an analytical solution by linearisation of the fitting function. The program is very dependent on parametrisation of many variables in particular the relative intensities and the mass absorption coefficients which are stored in a library file as

part of the program. Libraries for low energy tail correction are also included. A least-squares fitting algorithm locates the peaks in the spectrum corresponding to energies stored in a library according to a supplied energy and resolution calibration and then fits the peak shapes using Gaussian distributions to which the appropriate background contribution is added. This background is expressed as a polynomial, the coefficients of which are very dependent on the absorption of X-rays in the matrix and interposed absorbers. Fortunately, the values of these coefficients can be optimised interactively by the operator to fit a suitable background profile. Also contained in the software package is a program called AXLIBR which enables the user to change the library in accordance with his own needs. The program provides the user with an analysis report of the nett peak intensities (corrected for background and peak overlap) of the different elements analysed.

2.3.2 Multielemental data evaluation

Being a multielemental technique the output of information from TTPIXE is such that data output could be high. If we suppose that m samples analysed are represented by the rows of the matrix, and n element concentrations by the columns the n x m dimension of the matrix will be difficult to interpret by standard statistical techniques such as cluster analysis [An 73], which plots only one dimension of the data matrix.

Correspondence analysis is a technique which simultaneously displays the rows and columns of a data matrix in a low dimensional space. In other words, from an n x m dimensional space correspondence analysis reduces the data to be displayed to a two dimensional space. In the context of multielemental trace analysis, the display in two dimensions may be interpreted as a map. Samples which are plotted together are similar, and elements plotted close to each other are correlated. The simultaneous display of the rows (samples) and columns (elements) is justified by the "transition formulae" , enabling one to see not only which samples cluster , but also to understand why they are clustered [Gr 84].

Correspondence analysis belongs to the family of statistical techniques that have as their common feature the calculation of the singular value decomposition of a data

was developed [Gr 90]. A typical output of results from such a program applied to a small data matrix obtained from the analysis by PIXE of 6 kidney stones (rows) and 6 elements Fe, Cu, Zn, Br, Sr and Pb (columns) is shown in Table 2.5.

2.4 Analysis of non-conducting samples

One of the more difficult problems to deal with in TTPIXE measurements including the stripping of the PIXE energy spectrum by AXIL, is that of the generation of high bremsstrahlung under irradiation of non-conducting samples such as all biological materials, some geological compounds and calcium-rich materials. Because the optimisation of the background polynomial coefficients is one of the more demanding tasks in the execution of the program AXIL, care must be taken to ensure that such backgrounds are normal and free from bremsstrahlung component arising from the knock-out of secondary electrons inside the matrix of the target as well as other phenomena [Jo 88]. When non-conducting samples are bombarded with protons, the localised charge build-up is accompanied by a build-up of voltage, which continues until the breakdown voltage is reached. When this happens, there is a visible spark discharge after which the process starts over again. The secondary electrons, knocked off from the target materials and from the residual gas in the vacuum chamber, are accelerated by the built-up voltage, causing an appreciable increase in the bremsstrahlung background, sufficient to affect the sensitivity of analysis in an appreciable manner. Accordingly it is essential to ensure that charge build-up does not occur. Techniques that have been developed for this purpose are;

The electron gun method

Since the charge that builds up on the target is positive, it may be neutralised by an electron flux generated from a hot filament placed near the target. The original suggestion [Sh 72] advocated the use of a filament of tungsten heated by the passage of about 0.3A at 6.3V, but this method resulted in the deposition onto the surface, of tungsten, the presence of which was indicated by the observance of W L X-ray peaks in the PIXE spectrum [Go 83]. The contamination can be obviated if a carbon

Table 2.5: *Typical results output table for the correspondence analysis on the kidney stone data.*

DATA MATRIX

		1	2	3	4	5	6	sum
		FE	CU	ZN	BR	SR	PB	
1	1	55	59	94	3	115	2	328
2	2	9	90	76	8	112	21	316
3	3	24	181	55	29	65	23	376
4	4	31	187	62	5	100	17	401
5	5	17	35	65	10	106	14	246
6	6	4	13	50	15	82	11	175
	sum	140	565	402	70	579	86	1842

ROW PROFILES

		1	2	3	4	5	6	sum
		FE	CU	ZN	BR	SR	PB	
1	1	16.8	17.9	28.8	0.9	35.0	0.5	100.0
2	2	2.8	28.6	24.1	2.6	35.5	6.5	100.0
3	3	6.3	48.0	14.7	7.7	17.3	6.0	100.0
4	4	7.7	46.6	15.4	1.3	24.8	4.2	100.0
5	5	6.9	14.2	26.3	3.9	43.0	5.7	100.0
6	6	2.3	7.6	28.6	8.6	46.9	6.0	100.0
	average	7.6	30.7	21.8	3.8	31.4	4.7	100.0

COLUMN PROFILES

		1	2	3	4	5	6	average
		FE	CU	ZN	BR	SR	PB	
1	1	39.6	10.4	23.5	4.3	19.8	1.9	17.8
2	2	6.3	16.0	18.9	11.7	19.3	23.8	17.1
3	3	16.9	32.0	13.8	41.4	11.2	26.2	20.4
4	4	22.1	33.1	15.4	7.4	17.2	19.7	21.8
5	5	12.2	6.2	16.1	13.7	18.2	16.2	13.3
6	6	2.9	2.4	12.5	21.4	14.2	12.3	9.5
	sum	100.0	100.0	100.0	100.0	100.0	100.0	100.0

INERTIAS AND PERCENTAGES OF INERTIA

1	0.121095	65.87%	**********
2	0.047655	25.92%	********
3	0.013831	7.52%	**
4	0.000843	0.46%	
5	0.000425	0.23%	

INERTIA CONTRIBUTIONS OF EACH CELL

		1	2	3	4	5	6
		FE	CU	ZN	BR	SR	PB
1	1	110	51	21	21	4	36
2	2	28	1	2	4	5	7
3	3	2	110	26	45	71	4
4	4	0	98	22	20	17	1
5	5	0	64	7	0	31	2
6	6	19	90	11	31	39	2

Chi-square statistic (if applicable) = 338.59 (d.f.= 25)

ROW CONTRIBUTIONS

I	NAME	QLT	MAS	INR	k=1	COR	CTR	k=2	COR	CTR	k=3	COR	CTR
1	1	999	178	244	321	408	151	-378	567	533	-79	25	79
2	2	955	171	47	62	77	5	143	407	73	153	471	291
3	3	999	204	256	-444	852	333	101	44	44	-155	103	354
4	4	991	218	157	-324	791	188	-115	100	61	115	100	208
5	5	982	133	104	362	916	144	95	63	25	24	4	6
6	6	994	95	192	476	612	178	364	358	265	-94	24	61

COLUMN CONTRIBUTIONS

J	NAME	QLT	MAS	INR	k=1	COR	CTR	k=2	COR	CTR	k=3	COR	CTR
1	FE	997	76	160	121	38	9	-580	869	535	-187	90	192
2	CU	1000	307	414	-496	990	622	-37	5	9	35	5	27
3	ZN	968	218	89	269	960	130	-23	7	2	-8	1	1
4	BR	999	38	120	-102	18	3	571	563	260	-492	418	664
5	SR	991	314	166	298	911	230	61	38	24	64	43	94
6	PB	964	47	51	-121	73	6	415	858	169	81	32	22

filament is used instead [Ah 75]. A current of 2.5 mA at 7 V gave a glow which was sufficient to neutralise the charge from a beam of 50 nA of 2 MeV protons. Deposition of sputtered carbon was prevented by a perforated aluminium cap at a potential of +100 V over the filament.

Poor vacuum method

When the residual gas [Sz 81] or helium [Wi 81] in a scattering chamber is allowed to remain at a pressure of some millimeters the bombarding beam will ionise the gas, thereby providing a path for the charge to leak away from the insulating sample. The presence of some gas has the advantage that it may help to reduce the heating effect of the beam, especially on thermally-sensitive samples. However, the poor vacuum method has several disadvantages. The presence of air generated an unwanted K X-ray line for Ar in the PIXE spectrum, and the pressure of the gas has to be rigidly controlled to prevent variable energy loss by the bombarding protons. This method of prevention of charge build-up is automatically applied when an external beam is used for PIXE analysis [Pe 85],[Kh 81].

Addition of conducting material

An obvious method to convert an insulating sample into a conducting one is to cover the surface of the sample with a conducting film. A suitable film is carbon, which, though conducting, does not generate X-rays which can be measured with the common Si(Li) or Ge detectors. A film of 20nm sputtered from an arc between two carbon electrodes, is sufficient to produce conductivity, yet is thin enough to cause negligible energy loss in the bombarding proton beam, and, in the case of biological samples, does not materially alter the sample matrix [Pa 78].

When the sample material can be obtained as a powder, which is compressed to produce a tablet, the tablet can be made conducting by the inclusion of a known amount of conducting powder. In the first reported use of this method [Jo 62] finely powdered aluminium dust was used, but, since the X-rays from aluminium will be detected in the spectrum, it is more common to use graphite. Care should, however, be taken to ensure that the resulting mixture is homogeneous. The disadvantages

are that the addition of the conducting powder may alter the matrix composition and may introduce contamination.

Thin foil technique

In this work it was decided that the easiest and most effective way to overcome the problem of charge build-up was to use a suitable metal foil placed near to the surface of the sample. Electrons generated by the passage of the bombarding beam serve to neutralise charge build-up on insulating targets. The common foils used for this purpose are nickel, carbon or aluminium [Ch 81a]. (When carbon foils plated with a thin layer of gold are used, backscatter measurements from the gold surfaces provide a means to measure the beam current). Since the foils are not excessively heated, the metal does not deposit on the sample surface and hence sample contamination does not occur. No deterioration of the metal foil by the proton bombarding beam can be observed, even after many hours of use. The X-rays generated from the foil are shielded from the detector and usually are not observed in the PIXE spectrum. The choice of foil thickness depends on the energy of the proton beam [Pi 88]. It was found that 2μm aluminised Hostaphan was suitable for 1 and 2 MeV beams, while for higher energies of 3 and 4 MeV, aluminium foils of 5μm were needed.

Figure 2.12 shows the effect of the thin foil technique to prevent high bremsstrahlung background on a pellet of spinach leaves irradiated with 3 MeV protons. The lower spectrum in the figure was obtained by interposing an aluminium foil of 5μm thickness in front of the target material, and perpendicular to the beam direction. To limit the spread of the beam dimension, the foil should be placed as close to the sample as possible. If, in a suite of samples containing both insulating and conducting specimens in which the latter is analysed without the beam foil technique, the beam energy has to be adjusted to compensate for the energy loss in the thin foil. The PIXE background from a thick target varies with varying proton bombarding energy. Figure 2.13 shows this variation for the standard reference material IAEA-Mussel tissue. The ratio of backgrounds in the region of 3 to 8 keV is approximately 1:1000 for 2 and 4 Mev respectively. Although, the background at 2 MeV is 1000 times smaller than this at 4 MeV the efficiency of detection is smaller at 2 MeV.

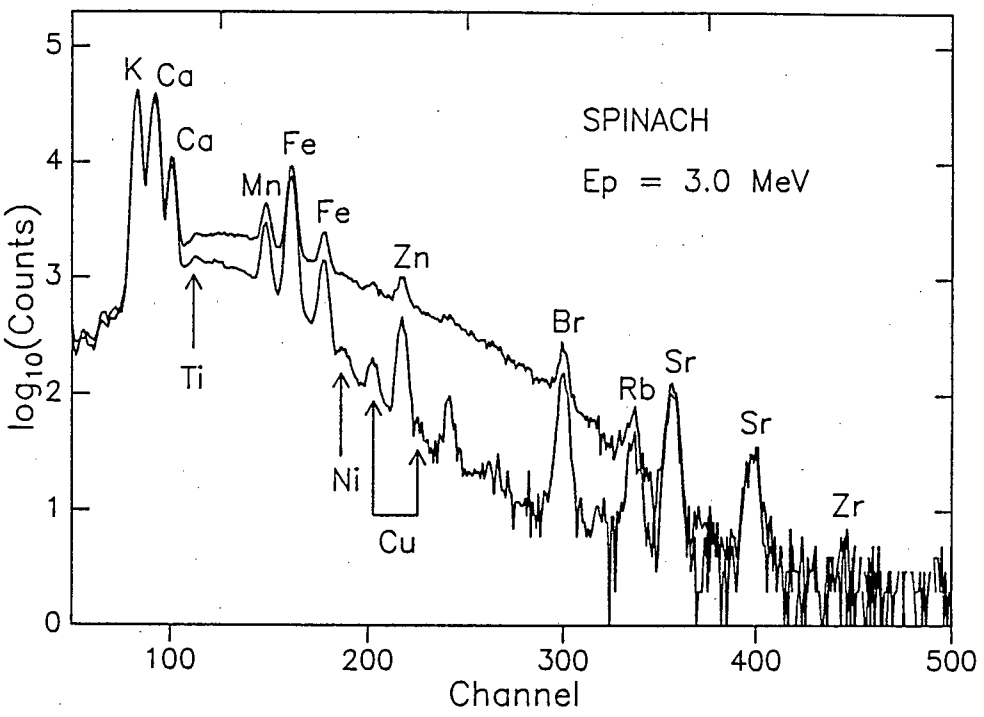

Figure 2.12: *The effect of the charge build-up in an organic target during proton bombardment. The lower spectrum was obtained by interposing a 5-μm aluminiun foil in front of the target.*

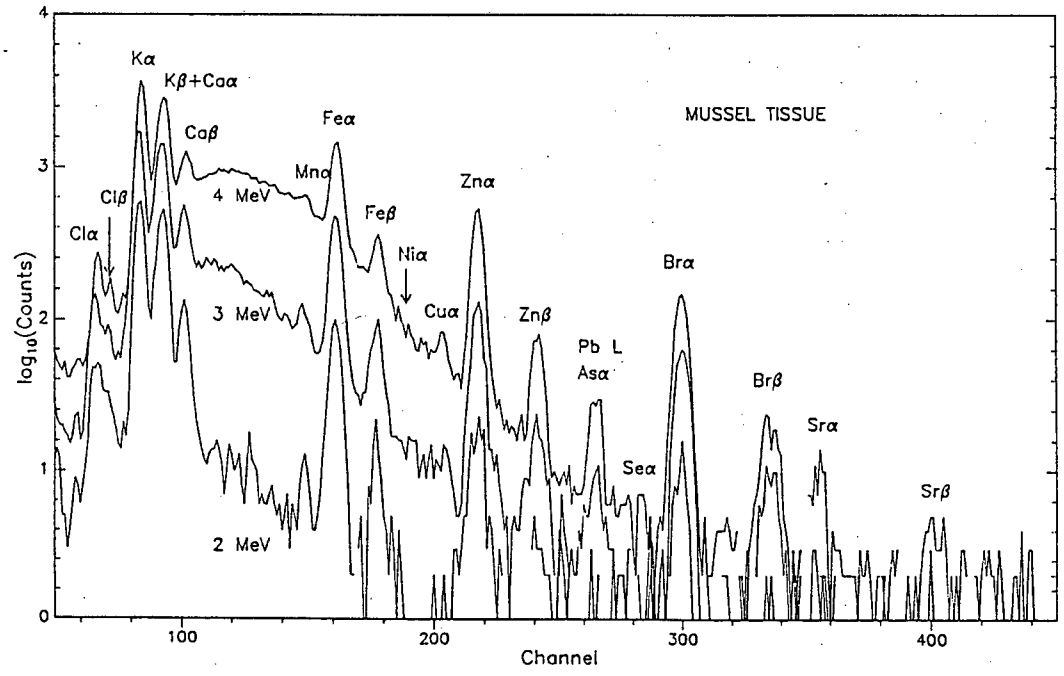

Figure 2.13: *PIXE background variation of a thick target of the standard reference material IAEA-Mussel tissue bombarded at different proton energies.*

From this figure it can be concluded that the best compromise will be somewhere between 2 and 3 MeV.

X-ray yield enhancement by Compton gamma-rays

It is important to mention here that the Compton background component in the PIXE spectrum will increase especially if the target material contains major components of low Z elements such as C, O, N or F. Compton gamma rays resulting from nuclear reactions are responsible for the high background in the high energy region of the spectrum above 8 keV [Jo 92]. This effect is particularly high when analysing non-conducting biological materials for which the $^{19}F(p,\alpha\gamma)^{16}O$ reaction has a strong resonance.

During PIXE irradiations with protons, deuterons and $^3He^+$ ions on homogeneous thick targets of binary metal fluorides an enhanced X-ray yield from the metal components of these compounds was observed [Pe 92].

The experimental data obtained from the bombardment of fluorides of some elements of the first transition series with protons and deuterons of 1333 keV and $^3He^+$-ions of 2000 keV, are given in Table 2.6. The experimental X-ray yields were calculated per unit bombarding charge for the equivalent target containing 100% of the metal under consideration. No range corrections for the matrix effects were taken into account, because in most cases the correction is of the same order of magnitude for the pure metal and the fluoride, and hence would not materially alter the size of the enhancement factor. As the increased yields were observed only in the fluorine-containing compounds the prospect of secondary excitation of the metal X-rays by the 110 and 197 keV gamma-rays of fluoride produced, via coulomb excitation, was considered as a strong possibility, because of the consistent occurrence of the improved yields with all three ion-beams.

Table 2.6: *X-ray yield enhancement in metal fluorides.*

Sample	% Metal	X-ray yield[a]	Enhancement Factor
E_p = 1333 keV			
Cr	100	30 153	6.5
CrF_3	47.71	196 700	
Fe	100	24 416	12.8
FeF_3	49.49	311 881	
E_d = 1333 keV			
Cr	100	369 250	2.0
CrF_3	47.71	722 341	
Fe	100	315 933	2.9
FeF_3	49.49	910 951	
Cu	100	195 347	3.8
$CuF_2{\cdot}2H_2O$	46.19	740 313	
Zn	100	152 507	5.8
ZnF_2	63.24	880 093	
E_τ = 2000 keV			
Cr	100	315 084	1.6
CrF_3	47.71	488 769	
Fe	100	256 944	3.6
FeF_3	49.49	932 361	
Cu	100	153 291	7.0
$CuF_2{\cdot}2H_2O$	46.19	1 073 881	
Zn	100	116 263	2.7
ZnF_2	63.24	312 670	

[a] K_α-counts per μC for a metal content of 100%, uncorrected for range effects.

Chapter 3

Known matrices

In spite of TTPIXE being less time-consuming, the evaluation of elemental concentrations in thick specimens demands a far more thorough control due to the introduction of uncertainties imposed by the quality of the database. The ideal would be to have a standard with the same matrix composition as the sample material to be analysed, but in most cases this is not possible. Often the best that can be done is to use a standard with a matrix more or less similar to that of the sample. Hence the use of such a standard could introduce errors in the elemental concentration due to uncertainties in the databases of stopping power, cross section and attenuation coefficient.

Because the major drawback in TTPIXE is the evaluation of $K(Z)$ and $F(Z)$ factors, the selection of analysis methodologies should be directed to procedures that cancel out the contribution of one or both of these parameters. In the following sections a series of methods of TTPIXE analysis on materials with known composition is presented with examples of applications which make use of these methods. It is evident that, for the calculation of $F(Z)$-values the most important condition is the knowledge of the matrix composition of the material under investigation. So, initially the criterion for selecting a particular method would be based on the accuracy of the information about the matrix composition. However, if such accurate information is not available, a further simplification of the calculation of elemental concentrations in TTPIXE may be achieved if the selection of a standardisation technique is determined by the assumed or empirical matrix composition in each analysis.

3.1 Use of internal standard

Internal standards can take the form of either the addition of a known amount of a selected element not present in the sample, or by selecting one element in the sample as a reference element. While the former procedure can yield absolute concentrations, only relative values can be deduced from the latter procedure unless further inter-calibrations with other standards are subsequently carried out.

When an internal standard is added to the sample, the yield of X-rays from the standard element, can be combined with the yields of the other elements, in the sample to obtain elemental concentrations. From equations 1.15 and 1.17, the concentrations are given by

$$C_z = \frac{Y(Z)}{Y(Z')} \frac{K(Z')}{K(Z)} \frac{F(Z)}{F(Z')} C_{z'} \tag{3.1}$$

where the primed parameters refer to the internal standard element.

With this approach the current need not be measured, nor need corrections be made for the dead time of the measurement. However, the calculation is aggravated by the fact that $K(Z)$ and $F(Z)$ factors have to be calculated for both the element under consideration and for the internal standard element. The method has an additional disadvantage in that the preparation of the thick sample should ensure that the internal standard element is homogeneously distributed.

3.1.1 Previously reported work

An internal standard which is commonly used is yttrium [Cl 81], [Rã 86],[Cl 87], but other elements such as copper [Ts 79] and cesium [Pa 72] have also been used. When precision is essential, it may be advisable to use internal standards of more than one element, chosen so that their emitted X-rays have energies near to those of critical elements to be determined, as for example, the use of zinc and yttrium together [Ca 85] for the analysis of fluid residues.

3.1.2 Application with added internal standard

Rationale of the problem in human biology

The study of the effects of nutrients on health, growth, and development presents certain difficulties. In plant and animal life, a continuous interrelationship exists between nutrients, and no single nutrient acts in isolation. *The spectrum of clinical manifestations and pathophysiologic and biochemical deviations from the normal in both over- and undernutrition is probably determined by patterns rather than deficiencies or excesses of single nutrients.* It is difficult to determine what constitutes *marginal* deficiency of one or more nutrients. Disturbed biochemical and physiologic indices are present in a pediatric age group before deficiencies cause deviations of normal growth and development and clinical manifestations. Nature presumably makes provision for mechanisms that allow for adaptation to mild to moderate deficiencies or excesses of nutrients, including trace elements.

The importance of zinc, copper, selenium, magnesium, and molybdenum in the function of metallo-enzymes, normal growth and development, and disease processes associated with deficiencies or excesses is well recognized [Wo 73],[Hu 81]. Clinical and laboratory findings that can detect large abnormalities in some of these trace elements are easily identified because of a recognizable pattern of clinical and biochemical manifestations and their correction after removal or addition of the appropriate trace element. Examples are lead excess with its hematologic and neurologic disturbances [Ne 79]; zinc deficiency leading to lack of appetite and taste, gastrointestinal disturbances and skin lesions, or to acrodermatitis enteropathica [Wa 80],[Ha 72],[Mo 74]; and selenium deficiency resulting in cardiomyopathy (Keshan disease) [Go 82].

The above deficiency states are easy to recognize but are probably just the tip of the iceberg. Minor excesses or deficiencies of one or more of the trace elements probably give rise to more common but more subtle complex biologic manifestations. *These manifestations may be hard to recognize with standard forms of trace element measurement and standard methods of statistical analysis.* Absolute concentrations are usually carried out on hair, nail clippings, and, commonly, on serum samples in newborns, infants, and children. A relatively large serum sample is required to

measure individually one or more trace elements.

In the investigation of possible trace element deficiency or excesses, single individual measurements are generally not helpful except where very high or very low levels are found. When plotted serially against time and where correlations are sought between levels obtained and biologic states, the patient may occasionally benefit from such investigations. In the study of trace element deficiencies or excesses in the pediatric age group and particularly in the newborn, two major constraints have to be overcome. They are, firstly, the ability to measure simultaneously a number of elements in a small sample of serum or tissue; and secondly, to identify individuals, e.g., mothers and infants at birth, with similar or dissimilar patterns of elemental levels and to find an explanation for such groupings.

The application of PIXE combined with Correspondence Analysis have shown promise in overcoming the above mentioned constraints, and, more specifically, to ascertain their value in identifying trace elements profiles in and between apparently healthy mother/infant pairs before and after birth.

Trace elements in blood sera of mother-baby pairs

Thirty apparently healthy mother/full-term infant pairs were studied at the time of delivery. The mother had to be well nourished and belong to either the middle or upper socioeconomic groups, had to have no history of diseases, infections, blood transfusion, or toxemia during pregnancy or past history of liver disease, had to show no abnormalities on clinical examination, and labour and delivery had to be uncomplicated. The infant had to be delivered by vertex and be appropriate for a gestational age of 37 to 42 weeks. Infants with a history or evidence of asphyxia neonatorum, respiratory distress or disease, central nervous system abnormality, serious illness or failure to thrive during the early neonatal period, exchange transfusion, congenital abnormalities, congenital infections, or any other abnormality on clinical examination were excluded. It was necessary to examine and investigate a large number of mother/infant pairs to obtain the number required for this study.

Maternal venous blood was collected immediately prior to delivery and cord blood at the time of birth. Appropriate measures were taken to prevent contamination of

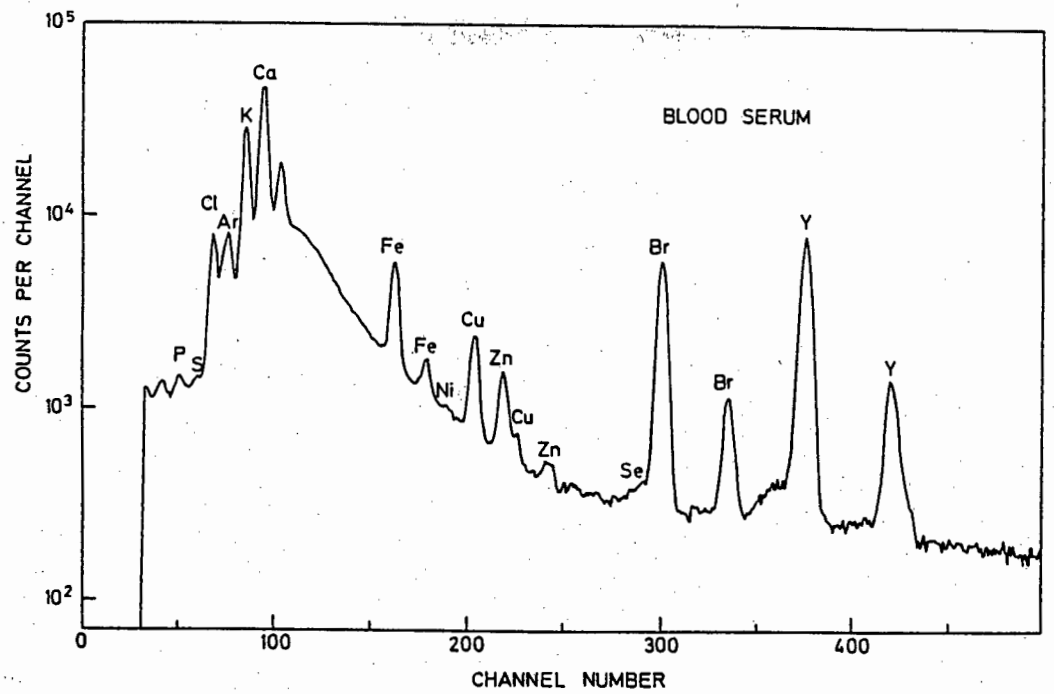

Figure 3.1: *Typical PIXE spectrum of blood serum obtained with a proton beam of 3 MeV and measured in air with an absorber to decrease the intensity of low energy x-rays. The Ar is present in the air and the yttrium was added to the sample as an internal standard.*

the samples with trace elements at all stages (See Chapter 2). A known amount of yttrium was added to serum samples to serve as internal standard for the sample under analysis. Figure 3.1 shows a typical X-ray spectrum of a blood serum sample. Principal elements observed in blood specimens are phosphorus, chlorine, potassium, calcium, iron, copper, zinc, and bromine. Silicon, titanium, chromium, manganese, nickel, gallium, selenium, and lead was also present, but not in all samples. The correspondence analysis plot of the PIXE data for iron, copper, zinc and bromine is shown in Figure 3.2. Points representing the sera of mothers and babies separated into two well-defined groups which showed that the elemental composition of the relevant sera was different. Futhermore, the mapping of the samples showed that the sera of apparently healthy mothers separated into several sub-groups as far as the concentrations of the elements were concerned, and that the sera from their healthy infants were also related to one another in the same way as that of their mothers. This opened the way for the development of new concepts of maternal/fetal interrelationships.

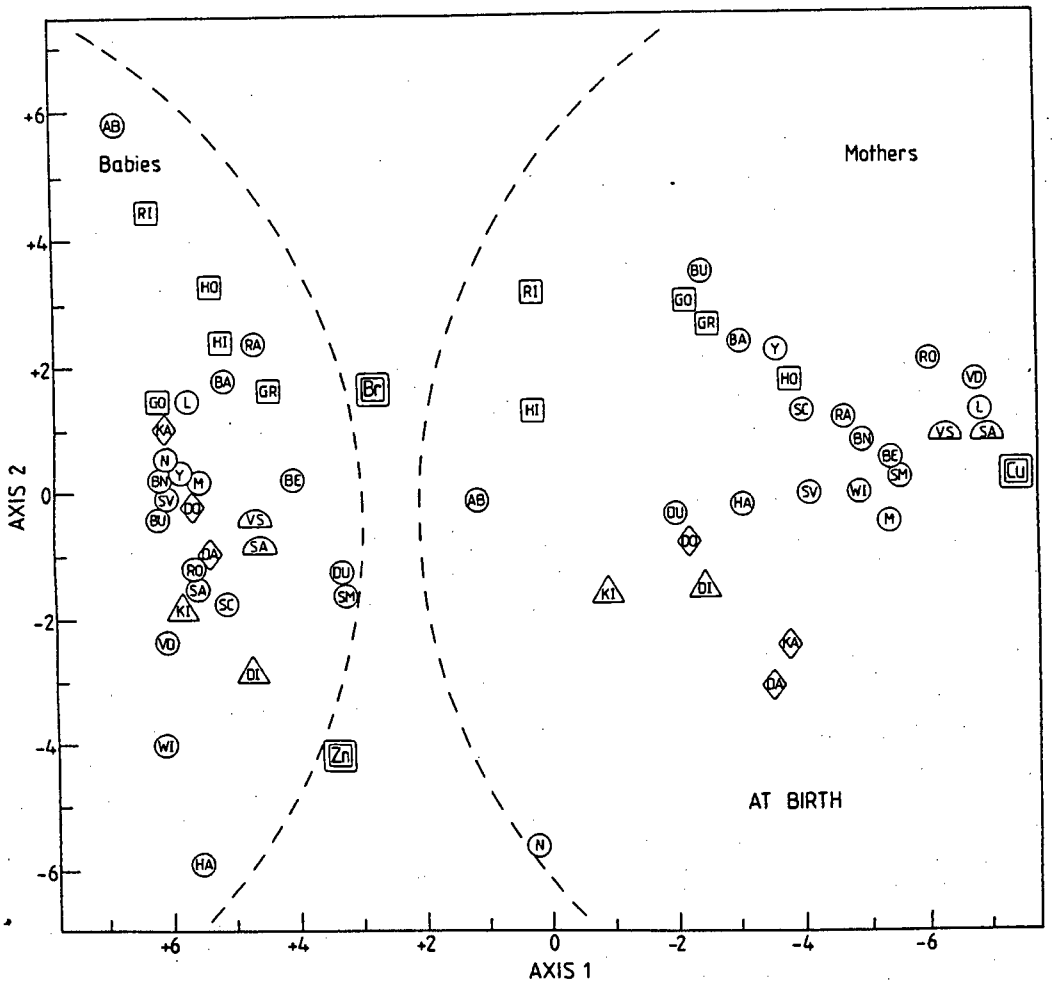

Figure 3.2: *Correspondence analysis plot of 61 sera samples (one mother had twins) showing complete separation between sera of mothers and those of babies. Similar letter combinations identify mother-baby pairs, whereas similar symbols identify groups of mother sera. Baby sera have been marked with corresponding symbols. Apparently overlapping groups are resolved in the vertical direction. Note: Usually, whereas mothers' sera form groups, their corresponding babies have their points as near-neighbors to each other.*

It would appear that for zinc, copper, and bromine a connection exists between the elemental pattern of the mother and that of her fetus. Biological mechanisms must therefore exist for the control of these elemental concentrations and other interrelationships during an uncomplicated pregnancy, labor and birth of the infant.

Extension to time variation

The same set of mothers and infants was followed for twelve months postnatally. Analysis of serum samples collected at fixed intervals during this period provided further information on trace element pattern variations during infancy. It is a medical fact that the blood composition of a mother at the time of giving birth is disturbed from its normal state. Accordingly in further analyses maternal serum concentrations at 3 months were employed as the maternal reference set of data. Using this reference cluster, a pattern emerged in the clustering of the points representing infant sera concentrations at birth and at 3, 6, 9 and 12 months. (See Figure 3.3).

At birth (Figure 3.3a) the infant cluster is separated from the maternal reference set. This separation is more emphasized when the infant cluster is compared with that of mothers at birth as shown in Figure 3.2, confirming the fact that the sera from mothers 3 months after birth, is not the same as at the time of giving birth.

At 3 months (Figure 3.3b) the infant cluster is closer to the maternal reference set but is more diffuse.

At 6 months, when most babies are weaned, (Figure 3.3c) the infant cluster moves further away from the maternal reference set but shows less scatter. The increase in copper concentration coupled to the decrease in the zinc concentration accounts for the separation.

At 9 months (Figure 3.3d) the infant cluster becomes tighter and moves closer to the maternal reference set. The movement is probably explained by the change in the diet of the child, tending to become more similar to that of the mother.

At 12 months (Figure 3.3e) the infant cluster becames effectively indistinguishable from that of the maternal reference set. This is probably due to the fact that the baby's diet is now very similar to that of the mother. As an interesting fact it was

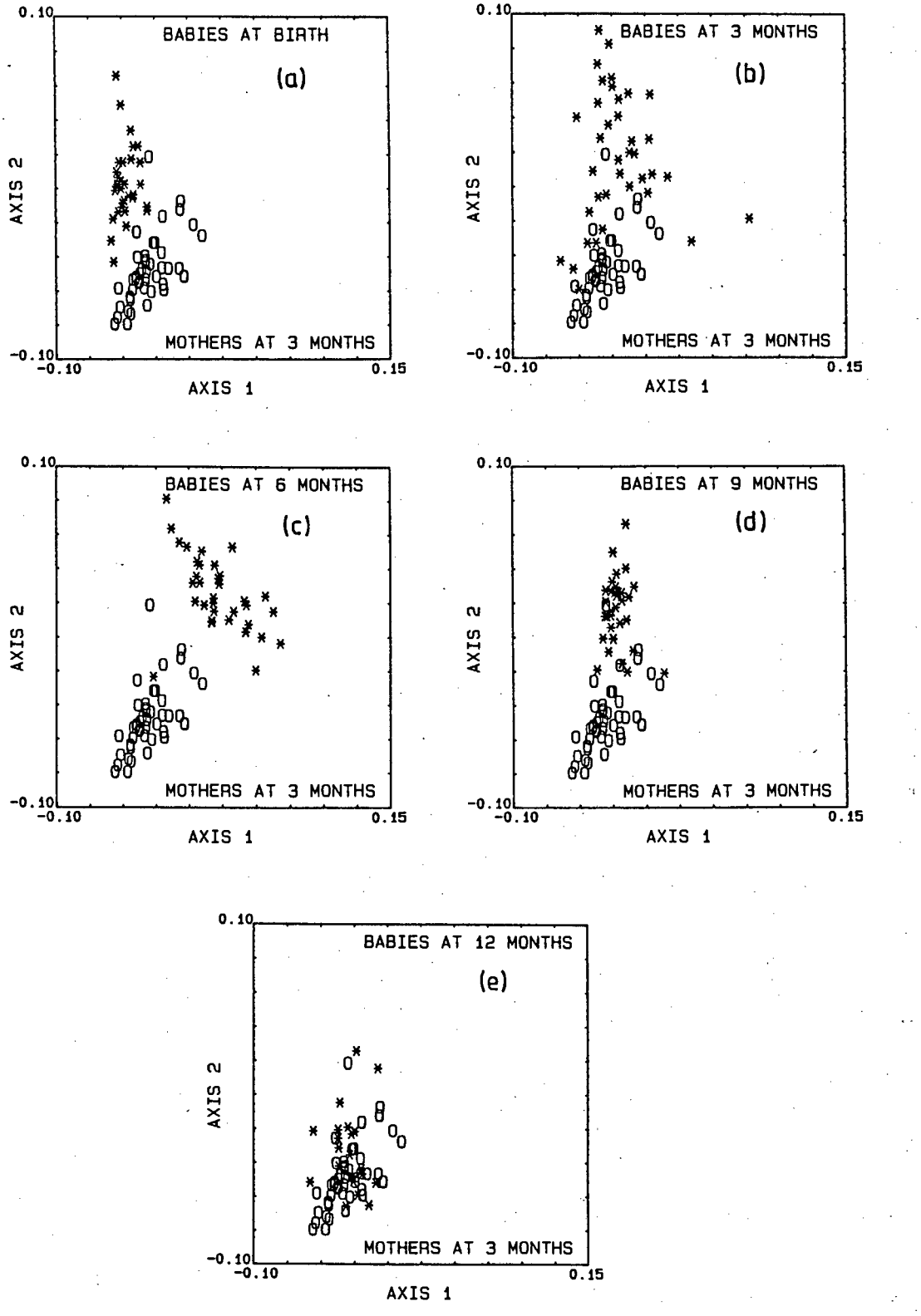

Figure 3.3: *Correspondence analysis plots for trace element composition in blood sera of babies at different time intervals during the first year of life. The sera of mothers at 3 months was taken as the reference set.*

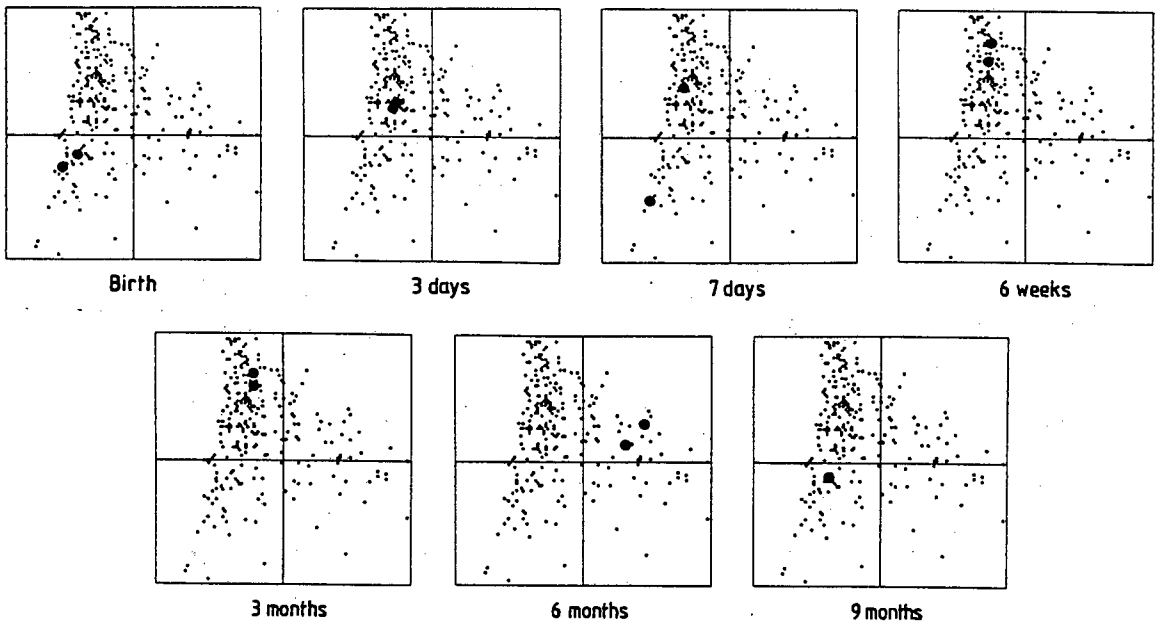

Figure 3.4: *Correspondence analysis plots for trace elements in blood sera of babies, showing the inter-relationship with time of the composition of the sera for a pair of similar twins (marked here as bigger dots).*

noted during the course of this study that a pair of similar twins grouped closely together at birth and maintained this interrelationship with time as shown in Figure 3.4.

3.1.3 Applications by the relative method

When thick targets such as archaeologically important specimens, have to be analysed non-destructively, the addition of foreign elements as internal standards is not possible. Under such conditions, a component element may be considered as an internal standard, relative to which all other elements can be determined. Often, such relative data are sufficient for characterisation of the material or for verifying similarities in trace element composition by multivariate statistical analytical methods. Thus, for example, in the analysis of pottery and clays, the iron concentration varies over a limited range and serves as a useful internal standard [Gi 84], [Gi 85].

Rationale of the problem in archaeology

It has been left to the archaeologist to reconstruct the history of the south-western portion of the African continent prior to the mid-18th century, because the inhabitants of that time left no written records. Archaeological excavations in southern Africa have unearthed a large variety of cultural history material from this period such as potsherds, fragments of Cape and early glasses and rock tool artefacts. The common feature to all these materials is the absence of any authenticated reference material which could assist in establishing their provenance or age. As a start, the external appearance and points of similarity or difference were carefully noted and recorded, but these details were not sufficient to answer the more penetrating questions of the archaeologists.

Many archaeological artefacts are of such importance in cultural history that the need to preserve them intact is accepted without question. At the same time, detailed chemical analysis is required to extend the knowledge of such artefacts beyond what can be deduced from even painstaking external examination. Analysis of the material is thus limited to the *use of nondestructive methods.*. Although the chemical composition of the major components may often be deduced from the type of material itself, the information from such analysis is unlikely to be of significance in establishing provenance or age. Minor components and trace elements, by contrast, can vary over such a wide range of concentrations that their presence may be used to establish groupings of artefacts. Indeed the trace element composition may even be characteristic of a particular site. Accordingly the analytical methods suitable for the study of cultural history need to be sensitive in addition to being nondestructive. Since the trace elements can range over a wide variety of elements, the analytical method of choice should be multielemental.

Once the analytical information is available, the place of origin of the object may be identified by comparing its elemental composition with that of objects of known provenance. In the absence of such reference artefacts, the process of identification becomes a statistical one for which as many objects as possible have to be analysed to construct the necessary data reference set. It was hoped that the data thus

accumulated would lead to objective classification of the materials in place of the very personal and subjective classification that resulted from using design and external examination. Once a firm method of classification had been established, the question that could be tackled was whether trade already existed in the indigenous society and, if it did, to establish the possible trade routes. In this work TTPIXE has been used for nondestructive and multielemental analysis of archaeological artefacts and materials sometimes in combination with other nuclear analytical techniques.

Identification of early Cape glass

The earliest record of glass production in South Africa was by a company formed in 1878 in Woodstock near Cape Town, and continued operations until 1882. During this four-year period household glass objects were manufactured for local sale in competition with similar objects imported from Europe. This early Cape glass, or 'Woodstock' glass named after the area where it was manufactured, has become important in material culture studies and is eagerly sought by museums and private collectors. However, despite the fact that the activities of the early glasshouses have been well documented [Ho 71], the close similarity between the local and imported glassware makes it difficult to distinguish between them. Indeed, in examining the problem of identification of early Cape glass, it has been stated [Sn 81] that " *it is doubtful whether scientific analysis would ever be able to solve the problem* " because the main ingredients were similar to those used elsewhere and some components, like lead, were imported from England.

It is known that fine, pure white sands, well suited for glass making was and is available in large deposits within and near the area of Cape Town. It is unlikely that the nature of the elemental impurities and their concentrations in these sands would resemble those in sands used overseas. Unfortunately the exact locality of the sources of sand used at that time can no longer be identified so that direct comparison of the glass with the source material is no longer possible but some of the impurities could have been carried over into the final products and could thus prove to be useful indicators of origin. Elemental analysis of these glasses, particularly for those components that could have been present as impurities may thus provide

the data which may reveal correlation between the elemental concentrations of the contaminants in the glass and the place of origin as reported by the owners of the objects.

The material submitted for analysis consisted either of fragments of glass from archaeological sites or intact objects from museums or private collections.

During the course of archaeological excavations, cultural materials of a durable nature were recovered, together with fragments of glass. Although the domestic glass objects were broken, they had some advantage over intact glassware, firstly, because they could be designated to a specific place or structure inhabited by people who used the objects, and secondly, because they were found in a sealed context, thus adding weight to their authenticity as a primary source of information.

Six groups of fragments were analysed, as listed in Table 3.1. The fragments from the Drostdy site (marked 1) were from the Dutch period dating to the third quarter of the eighteenth century. The single sample from Welgevallen (marked 2) can similarly be assumed to be a Dutch origin of about the same period. The German group (marked 3) consisted possibly of samples of 18th century roemer glass of unknown provenance. Fragments from the Cape-Dutch homestead site (marked 4) were accompanied by marked ceramics and could confidently be dated to the late 19th century and were possibly imported from England, while those from the La Concordia site (marked 5) were assumed to be of Woodstock manufacture. The English group (marked 6) was of unknown provenance but was reported to be of late 19th century English origin.

The intact objects were mostly wineglasses of different sizes bearing a variety of decorations, punch cups or bowls, tumblers, jars and decanters, from museums and private collections. Most of the objects were stated to be of Woodstock glass, except a medicine bottle from one collection which was thought to be of early Cape glass but from a different place of manufacture, made some years after the Woodstock firms stopped production.

The purpose of the analyses was to obtain data for classification of the glass samples, rather than to obtain information on the absolute concentration of trace elements. Accordingly the integrated counts under the relevant peaks in the spectra were ex-

Table 3.1: *Archaeological Glass Fragments.*

No	Description	Site	Origin	Plot Symbol
1	Octagonal tumbler	Drostdy site, Stellenbosch (Magistrate's court and dwelling)	Dutch late 18th century	1
2	Wine glass rim			
3	Wine glass bowl			
4	Wine glass rim			
5	Tumbler side wall			
6	Unidentififed			
7	Tumbler facetted	Welgevallen Farm, Stellenbosch	Dutch mid 18th century	2
8	Unidentified	Not reported	German	3
9	Unidentified			
10	Wine glass upper bowl	Cape-Dutch Homestead in Cape Town	English 19th century	4
11	Cylindrical bowl			
12	Wineglass conical foot			
13	Tumbler foot fragment			
14	Decanter stopper			
15	Solid handle of water jug	The Farm La Concordia near Paarl	Woodstock 19th century	5
16	Tumbler fluted sides			
17	Wine glass bowl			
18	Container/Jug			
19	Dessert bowl			
20	Wine glass bowl			
21	Wine glass rim			
22	Chimney of oil lamp			
23	Decorated fragment	Not reported	English 19th century	6
24	Decorated fragment			
25	Cup handle			
26	Bowl fragment			
27	Bowl fragment			

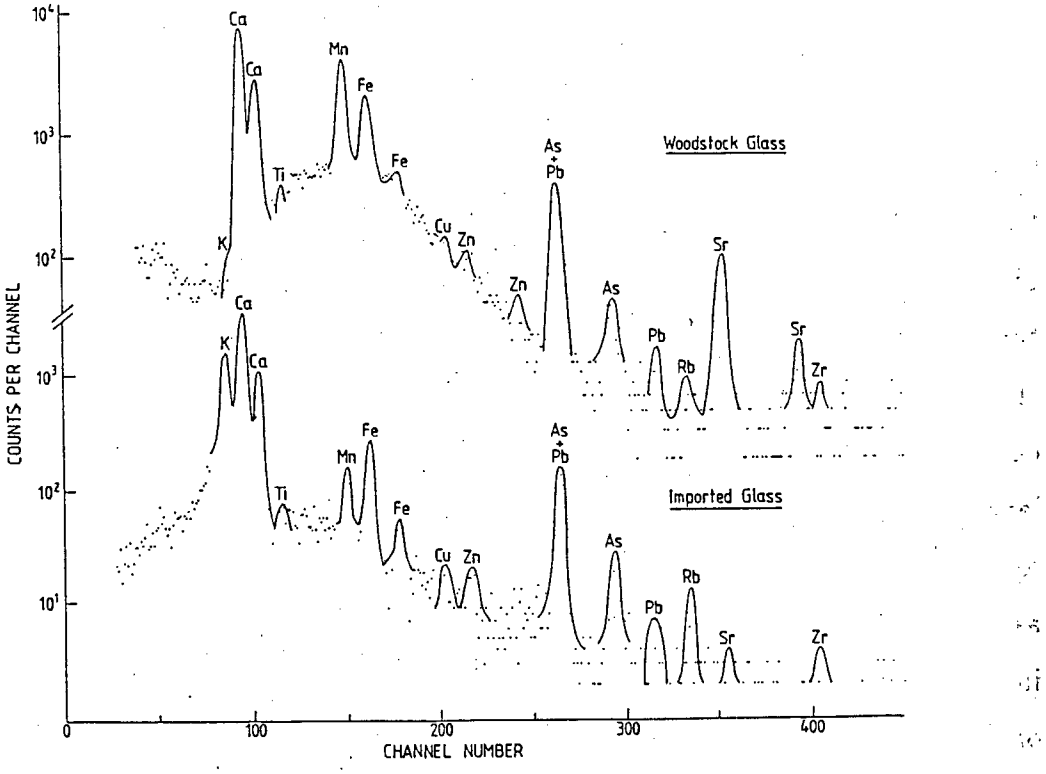

Figure 3.5: *Comparison of X-ray spectra from a specimen of Woodstock glass (upper curve) and from an imported glass. Note the differences in the peak heights of K, Mn and Rb.*

pressed in terms of the yield from Fe, which was taken as an internal standard. In this way errors involved in absolute calibration were eliminated, but the patterns of elemental concentrations were retained. The elements that were measured by PIXE were K, Ca, Ti, Mn, Fe, Cu, Zn, As, Rb, Sr, Zr, Pb,

A typical pair of X-ray spectra obtained with 3 MeV protons is shown in Figure 3.5. The upper spectrum was obtained from a short stemmed wine glass with a typical somewhat stilted and crude fern-leaf design of the early period, while the lower spectrum was measured from a cylindrical bowl with a wheel-engraved geometrical pattern which could confidently be ascribed to imported glassware of European origin. The most important quantitative differences in the relative photopeak intensities in the two spectra are related to the elements K, Mn and Rb. In the upper spectrum the photopeak from Mn is very intense while those from K and Rb are relatively poorly defined. In the lower spectrum the situation is reversed with a prominent peak from K, a relatively well-defined peak from Rb and a considerably reduced photopeak from Mn.

In the absence of accurately identified and analysed specimens of Woodstock glassware, it was decided to apply a correspondence analysis to the analytical data. The data from PIXE analysis yielded a 60 x 11 data matrix from 27 excavated fragments and 33 intact objects.

Since it was known that Pb was usually added to glass to improve the lustre and was thus not a normal impurity in the glass raw materials, this element was an obvious choice for exclusion. As a result of the presence of Pb, the element As had to be determined through its lower intensity K X-ray photopeak, and was thus open to larger relative errors, hence As data should also be excluded. Furthermore, the values for Zn resulted in a poor index of quality. Accordingly Pb, As and Zn were considered as supplementary elements. Also, in view of the fact that the fragments were found in a closer context, it was desired to obtain a plot of the point representing intact objects on the same scale of axes as calculated for the fragments. This was achieved by considering all the data from intact objects as supplementary as well.

Computed data are plotted in Figure 3.6, the upper portion of which is a plot of axis 1 against axis 2, and the lower, of axis 1 against axis 3. Examination of the upper plot of Figure 3.6 shows two major clusters in close proximity, on the left of the Figure, marked 'Woodstock' and 'English'. Minor groups on the left and right are marked 'Dutch', 'European?' and 'German'. A diffuse cluster near the origin is again labelled 'English'. These labels refer to the assumed origins of the fragments as listed in Table 3.1. The two English groups are probably glasses imported from England that were made by different manufacturers. The 'European?' group probably originated in Europe, but its provenance was unknown.

Since most of the intact objects were thought to be of Woodstock origin, it is satisfying to find a fair representation of objects from collections A, C, D, E and G associated with group 5. Also, two objects from collection B are included in the same cluster, although the other three objects from the same collection are associated with the English group 4. Collection F, labelled 'European?' was reported as being of non-Woodstock origin.

Two points in each portion of Figure 3.6 are marked with asterisks. The point from group 5 so marked, was distinctly different in composition from the remaining

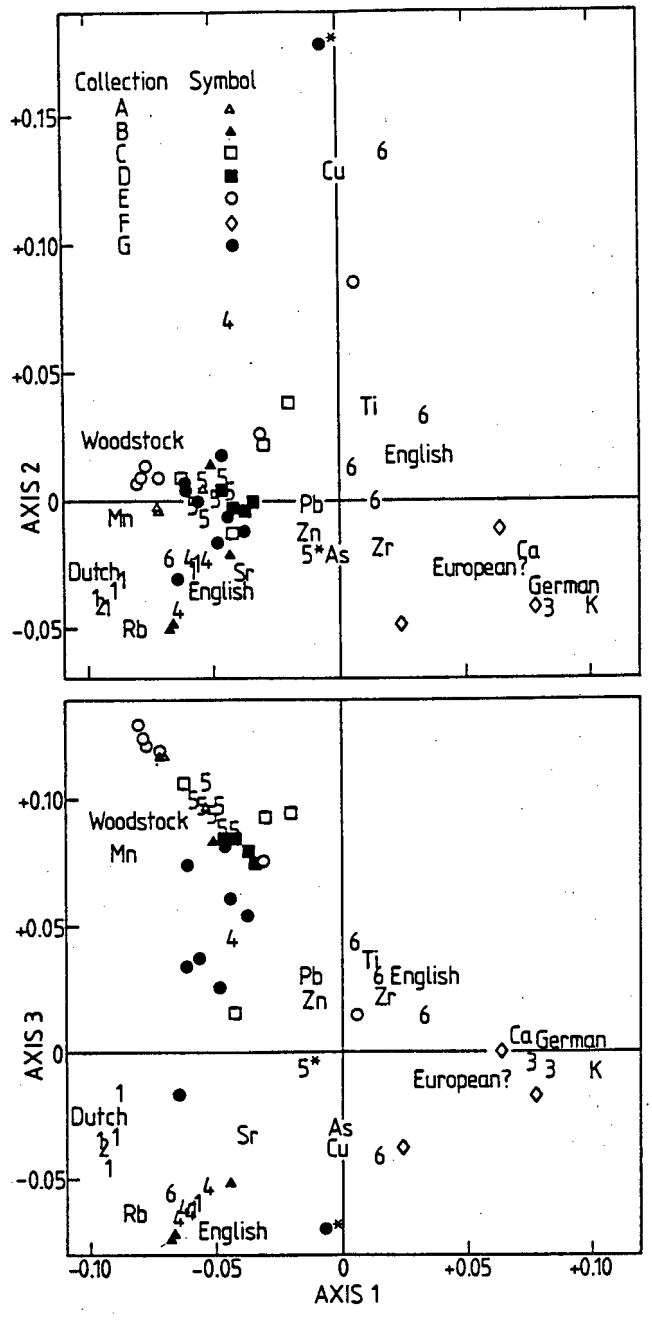

Figure 3.6: *Correspondence analysis plots of Axis 2 (upper plot) and Axis 3 against Axis 1 for 60 samples analysed for 11 elements. Fragments are plotted with numerals and intact objects by symbols for the collections to which they belong. The two points marked with asterisks are described in the text.*

fragments of the same group. This point represents a glass chimney from an oil lamp, numbered 22 in Table 3.1. Subsequent excavation at the La Concordia site produced enough fragments to reconstruct a lamp chimney. Near the upper rim appeared a manufacturer's mark and the words 'Central Vulcan', proving conclusively that this chimney was from a non-Woodstock source and possibly of Czechoslovak origin [Wr 64]. The marked point from collection G was reported as of early Cape origin, but suspected of being from a somewhat later period and manufactured at a site near Glen Cairn, some 25 km from the Woodstock site. The trace element analysis confirmed that the composition was different from that of Woodstock glass, with a considerably higher content of Cu.

The lower portion of Figure 3.6 shows that the proximity of the Woodstock and English groups was more apparent than real. While the groupings obtained from the upper plot retained their cluster make-up, the Woodstock group was now distinguished from the large English group by the fact that the axis 3 coordinates of the former were all positive, whereas those of the latter were strongly negative.

Criteria for classification of Woodstock glass

The importance of the Mn concentration in the classification is borne out by the correspondence analysis plots in Figure 3.6, which show the Woodstock group strongly correlated with the position of the element Mn. The same figures also show that the Woodstock group is remote from the element K. Accordingly the ratio of Mn to K would appear to be a possible diagnostic parameter. The concentration ratio of Mn to K, as given by the count ratio of the corresponding photopeaks in the PIXE spectra, is shown as a frequency histogram in Figure 3.7. The group identities are the same as in Figure 3.6. Most of the samples that formed part of the Woodstock group have count ratios clearly distinct from, and much higher than, those of other groups. Furthermore, it appears that this group can be divided into three subgroups which have Mn/K count ratios between 60 and 100, between 130 and 300 and between 400 and 800. Such a subdivision possibly suggests three periods of manufacture, corresponding to the three developmental stages in the history of the company [Ho 71].

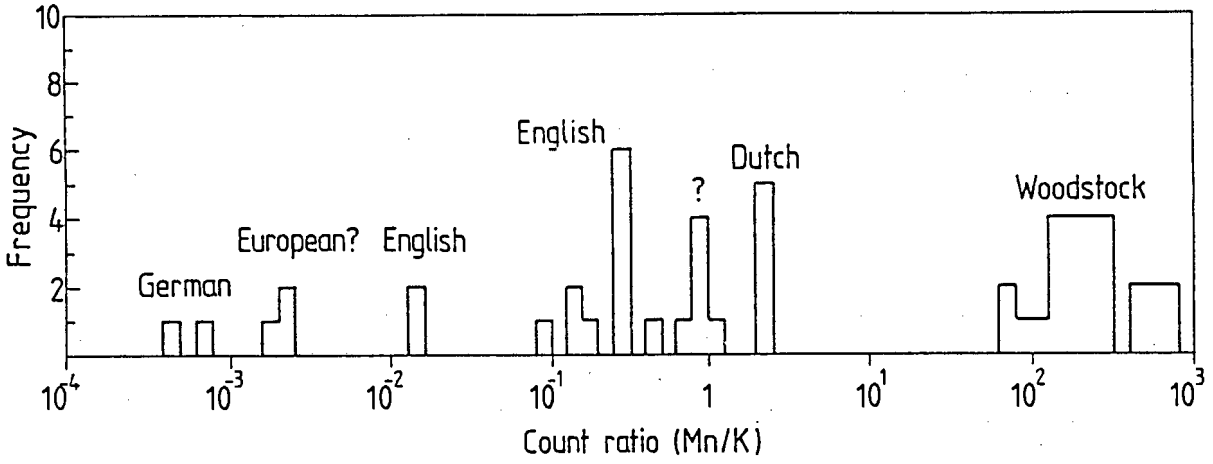

Figure 3.7: *Frequency histogram of objects according to their count ratio of Mn to K. Groups are labelled as in Fig. 3.6. The group marked with an interrogation mark is of Woodstock origin (see text).*

The only specimens which were included in the Woodstock group by correspondence analysis but which have a Mn/K count ratio of about unity is a batch of 6 objects from two different collections, which from the group labelled with an interrogation mark in Figure 3.7. These all contain relatively high concentrations of Mn, but also contain appreciable levels of K. They were clustered with the Woodstock group, because the entire composition of a sample is considered in correspondence analysis when the plot coordinates for the representative point are calculated. In the search for additional element-pair diagnostic parameters, attention may be paid to the mean of some of the elemental concentrations of the various groups, as given by the count ratios relative to Fe in Table 3.2. Here the subgroup 'Woodstock?' is shown to be similar to the main Woodstock group by virtue of its high content of Mn and low content of Rb. Hence a second diagnostic parameter that may be considered is the ratio of Mn to Rb. From the values of the count ratios given in Table 3.2 it is evident that most Woodstock glass specimens have high values of the Mn/Rb count ratio. Count ratios of Mn to K above 60 are good indicators of early Cape glass, however these diagnostic parameters should be used with caution, particularly for specimens

Table 3.2: *Mean values of some elemental concentrations in glasses from different groups.*

Group	Count ratio relative to Fe				
	K	Ca	Mn	Rb	Sr
Woodstock*	213	310000	43400	97	131
Woodstock '?'	14400	93300	13100	29	197
Dutch	1920	28200	4600	471	86
English 1	6000	86200	1460	800	226
English 2	253000	1055000	6960	311	498
German	1008000	4450000	644	666	445

* The group Woodstock '?' was not included in the mean values

which contain appreciable concentrations of both Mn and K.

Soutpansberg pottery study

The kind of interaction between different communities in the northern Transvaal over the last thousand years still remains an open question. Their language is made up of elements from both Shona, which is spoken in the more northerly areas, and Sotho which is characteristic of the south, the two areas being separated by the Soutpansberg mountain range.

Seven different pottery styles have been identified from the Soutpansberg region [Lo 88]. Of these, three are from north of the mountain range two from the south and two are regional, being common to both sides of the mountain (see Table 3.3). Occasionally a southern pottery style may be found on a northern site or vice versa. It is possible that trade, in the modern sense, could have accounted for the transfer, but more complex social explanations are also possible. For example, the formation of marriage alliances between communities in opposite sides of the mountains could have been responsible for the transfer either as a dowry or bride wealth, or the new bride may have used her accustomed style in her new surroundings. The implication is that the physical transfer of pottery would be reflected by its trace element composition being similar to those from its place of origin, whereas a transfer of ideas would

Table 3.3: *Styles and distribution of the analyzed samples.*

Style	Location	No. of samples	
		From north	From south
Letaba	Regional	2	5
Tavhatshena	Regional	1	2
Khami	North	9	5
Mutamba	North	-	1
Mapungubwe	North	11	1
Eiland	South	3	7
Moloko	South	-	6
	Totals:	26	27

result in the pottery containing the trace element pattern of the area in which it was found. Accordingly, a classification of pottery based on stylistic criteria could be different from one based on elemental composition. Excavations covered both sides of the Soutpansberg range. The geological deposits on the southern side consisted of granite and amphibolite, while that in the northern valley was sandstone. Pottery excavated from both sides of the mountains were submitted for trace metal analysis. By appearance, the pottery from the two regions was indistinguishable. A total of 26 sherds taken from seven sites in the northern area and 27 sherds from four sites in the south were used for analysis (see Table 3.3). In addition, reference specimens of daga (a mixture of local clay and organic material such as dung) were taken from two locations on the southern side, one on the northern and one to the north-east. Potsherds were irradiated with 4 MeV protons in the external mode. The elements that were measured were Ar, K, Ca, Ti, V, Cr, Mn, Fe, Ni, Cu, Zn, Ga, Rb, Sr and Zr and a typical X-ray spectrum is shown in Figure 3.8. Because of possible

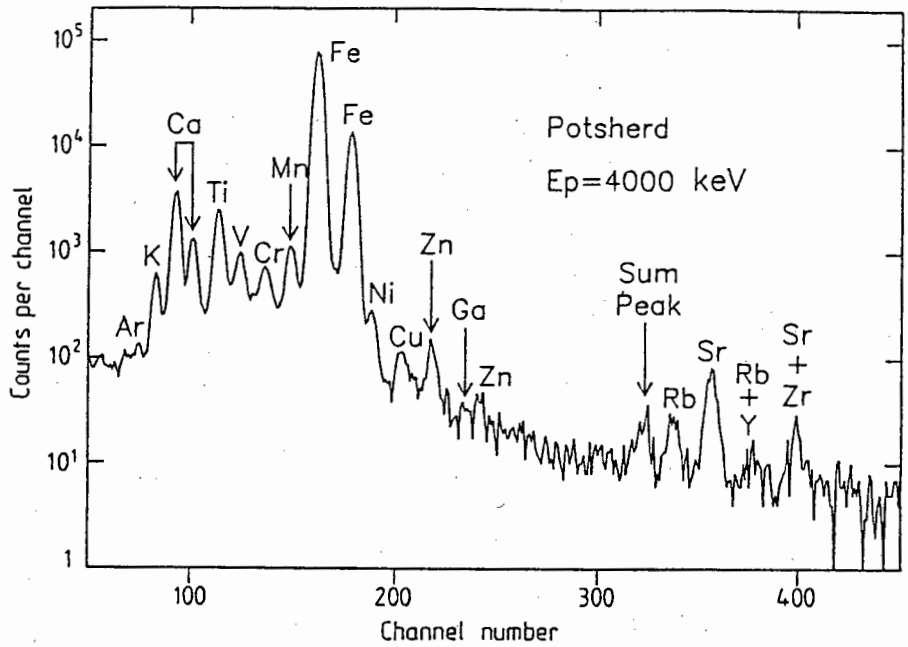

Figure 3.8: *X-ray energy spectrum obtained from the bombardment of a potsherd with 4 MeV protons in the external mode.*

dilution of the elemental concentrations by carbon, and the difficulty of accurately measuring the total beam charge falling on the target material, the data were expressed as count ratios relative to that of Fe in the same sample. The presence of Ar is due to interaction of the proton beam with air in the gap between the window and the sample. The count representing the argon yield was not included as a parameter in subsequent calculations. The data for the measured elements that were common to all the samples were submitted to correspondence analysis. The plots of the first two axes and of the first and third axes are shown in Figure 3.9. The representative points of the pottery samples separated into two major groups with the southern samples lying above the drawn line of separation. The reference clay samples follow the sets according to their provenance, while replicate analyses were satisfactorily close together, indicating over-all agreement between elemental content and precision. When the plot of axis 3 is taken into account, a three-dimensional representation results, in which the points of the southern group are seen to lie partly on, and partly under the plane of the plotted figure, while those from the north are positioned above the plane. The clay samples from the north-east follow those from the north. Since all the samples were selected from specific areas it was assumed

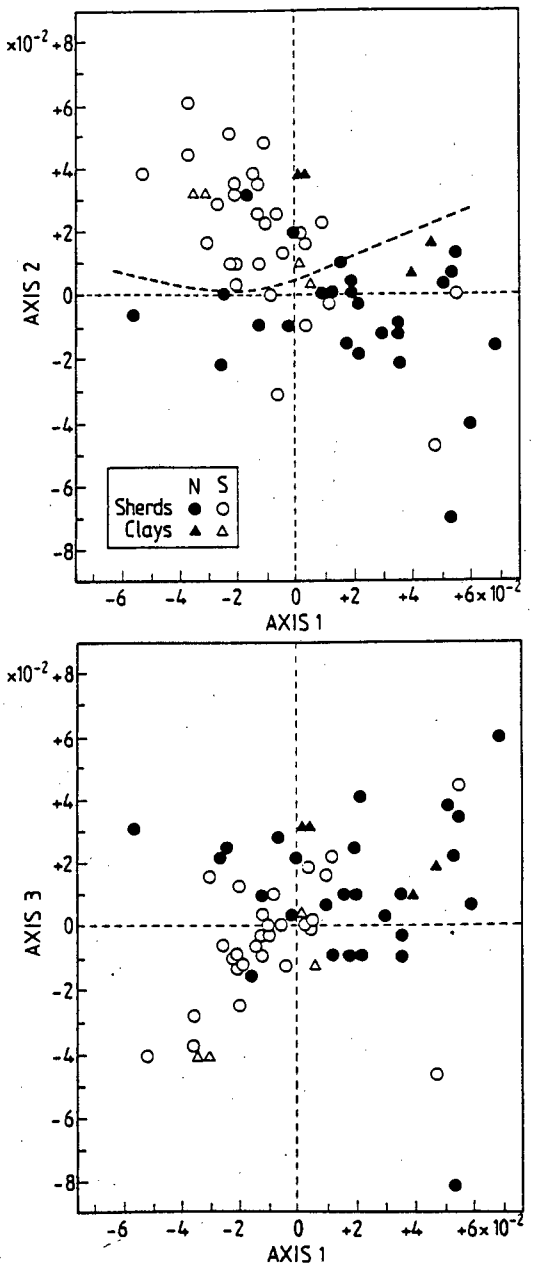

Figure 3.9: *Correspondence analysis plots of the data for potsherd and clay samples analyzed by PIXE for the elements K, Ca, Ti, V, Cr, Mn, Fe, Ni, Cu, Rb, Sr and Zr. The upper part is a plot of the first two axes, which includes 52% of the information content. The lower is a plot of axis 1 against axis 3 which shows the separation of the points in a third dimension, and reflects an additional 18% of the information content.*

that any apparent misclassification was significant.

The distribution of the representative points of the potsherds from the more important northern and southern styles, in the plot of the first two axes are shown separately in Figure 3.10. Since these are subsets of the upper plot of Figure 3.9, the same line of separation is shown on all. Khami-style pottery (see Figure 3.10a), though more characteristic of the northern areas, is also found, in lesser numbers, in the south. This is clearly borne out in Figure 3.10a where the line of demarcation separates the samples into their two groups, with one exception. In this case the sample, though found in the south, has a trace element composition more akin to the north. It thus represents an imported vessel. The fact that Khami-style pottery was found in the south and made in the south, indicates the movement of people and their ideas, rather than the movement of pottery.

The Mapungubwe-style samples were all found in the north (see Figure 3. 10b), yet one sample reflects the trace element composition more characteristic to the south. This shows the movement of pottery from the south to the north, either in trade or by other means, after the idea of the pottery style had been conveyed to the south.

The Eiland-style pottery was essentially southern in origin, and most of the samples show that they were made and were found in the south (see Figure 3.10c). However, one sample, found in the south was apparently made in the north, which shows a similar pattern of progress to that of the other in the Mapungubwe group, i.e., a transfer of pottery from the north to the south after the design idea had been "imported" into the north. The samples found in the north in the same style were manufactured in the north and thus reflect an importation of an idea.

All the Moloko-style pottery were found in the south (see Figure 3. 10d). Two of the analyzed samples had the trace element traits of the north. They were thus manufactured in the north after the transfer of the stylistic design to that region.

The influence of style

The above reasoning provides the means of synthesizing groupings based on style with those based on elemental analysis. The simplest model is that where two regions can

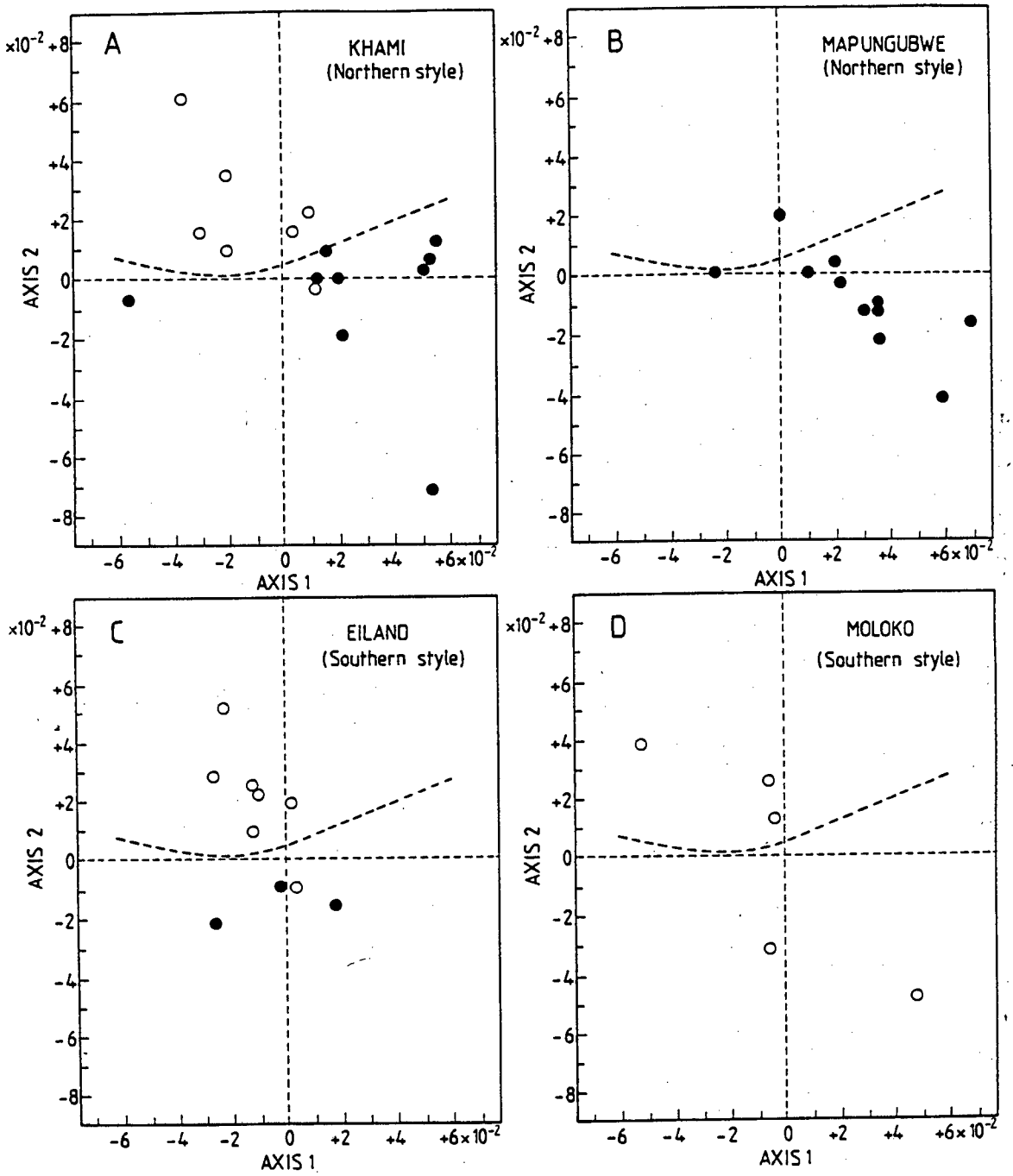

Figure 3.10: *Correspondence analysis plots of the first two axes for the separate stylistic groups of northern and southern styles: a - Khami; b - Mapungubwe; c - Eiland; d - Moloko. The symbols are the same as in Figure 3.9.*

Table 3.4: *Model for "trade" patterns.*

Case	Site of manufacture	Site of discovery	Regional style	
I	A	A	A	No inter-regional movement
II	A	B	A	Movement of artefact A → B
III	A	A	B	Movement of idea B → A
IV	A	B	B	Complex movement, Idea B → A then artefact A → B

be defined according to the elemental composition. The present work is an example of such a case, and the combinations with style are summarized in Table 3.4. In the present case, A refers to either north or south, and B to the other region. This model depends on identifiable styles and distinct regions defined by elemental composition. Its extension to a multiplicity of regions merely extends the number of cases, but the process of reasoning remains the same.

Although the monitored beam charge was the same for the irradiation of all samples, a degree of uncertainty in the value of the total absolute beam charge on each target makes it difficult to evaluate the absolute elemental concentrations, and hence a comparison of the count yields is justified. Mean values of the count yields for the elements considered for correspondence analysis are given in Table 3.5. The gross values included all the samples according to where they were found. After examination of the correspondence analysis results, it was found that some samples, though found in one region, had a trace element composition similar to that of the other region. These samples were excluded in the calculation of the "corrected" mean values. From Table 3.5 it is evident that the samples from the north are much richer in K, Ca and Zr, while those from the south have a higher content of Cr and Ni. This enabled the samples found in the two regions to be separated by correspondence analysis. When the stylistic characteristics were taken into account, details of trade, in its widest sense, became evident, as well as the likelihood that patterns were copied across the region boundary. A model describing the significance of combining elemental data with stylistic characteristics has been proposed [Pe 91].

Table 3.5: *Mean count yields.*

Element	All samples North	All samples South	Corrected values North	Corrected values South	Ratio N/S corrected values
K	2 578	2 507	2 771	2 111	1.31
Ca	22 121	14 853	23 741	12 381	1.92
Ti	13 338	14 604	13 287	14 995	0.89
V	1 819	2 042	1 825	2 072	0.88
Cr	532	2 205	448	2 501	0.18
Mn	6 465	6 849	6 718	5 990	1.12
Fe	408 802	448 592	395 731	454 494	0.87
Ni	1 149	1 674	1 121	1 797	0.62
Cu	421	526	427	514	0.83
Rb	87	112	87	102	0.85
Sr	333	359	232	334	0.97
Zr	187	169	195	98	1.99

3.2 Use of external standard

The ideal external standard is a reference material with the same matrix as the sample for analysis, containing the elements of interest at concentrations of the same order of magnitude. When such standards are available, there is no need to calculate either $K(Z)$ or $F(Z)$ values. The elemental concentration is then given by

$$C_z = \frac{Y(Z)}{Y(Z')} \cdot \frac{Q'}{Q} \cdot C_{Z'} \tag{3.2}$$

where $Z = Z'$.

If the standard does not contain an element of interest, the concentration can be calculated by equation 3.1, corrected by the ratio of the respective integrated charges. Since most samples of biological origin have very similar matrices [Cl 87], the use of standard reference materials as external standards has been applied extensively [Ma 80]. Thus, for example, the standard reference material, NBS orchard leaves, served adequately for the analysis of dried human blood [Kh 81]. In a similar fashion, the analysis of coins can be carried out by comparison with alloys of known composition, serving as external standards [Fe 81].

When samples have to be analysed in a matrix which cannot readily be approxi-

mated by available standard materials, because of the presence of some particular element at a relatively high concentration level, suitable standards for comparison may be prepared synthetically to have the same composition as the sample matrix. Thus, when trace and toxic elements had to be determined in bone [Hy 81] or teeth [Co 81],[Cu 87], hydroxyapatite was chosen as the carrier of known amounts of the elements under investigation, because its elemental composition was virtually the same as that of the samples.

An alternative semi-quantitative method is to use thick targets of pure elements or their compounds. From the X-ray yield of the element, equation 1.18 can be used to obtain the $K(Z)$-value for this particular element. When this element is then determined from the bombardment of the thick unknown material under the same experimental conditions, equation 1.18 can again be used to obtain the concentration of the element in the unknown sample [Bu 90],[Ca 84] and hence

$$C_z = [C_z]_{std} \left[\frac{Q}{Y(Z)F(Z)}\right]_{std} \left[\frac{Y(Z)F(Z)}{Q}\right]_{unknown} \tag{3.3}$$

This method has the disadvantage that it requires the evaluation of the MCF for every thick target standard as well as that for the unknown sample. However, this disadvantage need not be serious, since a database of MCF values as is shown in Table 1.5 can be constructed for all elemental standards, provided the conditions of analysis are kept constant.

3.2.1 Application in biology

Toxic effects of Al in vines

In certain wine-growing regions of the Western Cape it was known that the performance of the vines was below normal as regard growth vigour, grape yield and quality. These problem areas were all located on soils having a pH below 4 (KCl pH) and aluminium concentration of the order of 20 μg/g. To combat this condition, the standard practice is to apply lime in order to raise the pH level. The result of this treatment is that the top layers of the soil to a depth of not more than about 50-100 cm were depleted of assimilable aluminium, but below this depth the toxic effects of aluminium became evident. In an earlier investigation [Me 84] on plants grown in a

water culture medium with and without added aluminium, it was confirmed that the roots concentrated large amounts of aluminium and that consequently the uptake of the important nutrient elements magnesium and calcium was severely reduced.
Since, under normal growth conditions in Al-rich soils, the roots of the vines are exposed to favourable as well as unfavourable media, the effects of such varying media on the elemental content in the roots, of the main nutrient elements, using the split root technique was studied. Attention was directed to a variety which was badly affected by increased aluminium concentration, Sauvignon blanc (Vitis vinifera), and one which was more resistant, 2-1 (R99 x Jacquez). These varieties are referred to below as *Sauvignon* and *2-1*.

The split root technique

Soft wood cuttings of the selected varieties were rooted on a mist bed for about 3 weeks in a sand medium virtually free of nutrient material. Plants of about equal root vigour and top growth were then selected, removed from the root bed and their roots, after being rinsed free of supporting media, and divided in two roughly equal portions, by hand. Half the root system was placed in one compartment and the other half in a second compartment of a divided culture bath containing modified Hoagland solutions at pH 4. Separate tests were carried out on the two varieties. In order to verify that the divided root technique did not introduce spurious effects, some of the plants were grown in baths in which both compartments contained the same control solution without added aluminium. The remainder had half the roots growing in a control solution solution and the other half in a solution containing added aluminium at the 10mg/l level (see Figure 3.11). Groups 1, 2, 3 and 4 refer to 2-1 and groups 5, 6, 7 and 8 to Sauvignon. The root systems grown in the divided cell in which both compartments contained the control nutrient medium, are numbered groups 1 and 2 and groups 5 and 6. The remainder were from roots in the bath containing a control solution in one compartment, groups 3 and 7, and added aluminium in the other compartment, groups 4 and 8. After 90 days of growth the root systems were washed free of adhering solution and about 20% of the root system from each compartment was sampled for analysis.

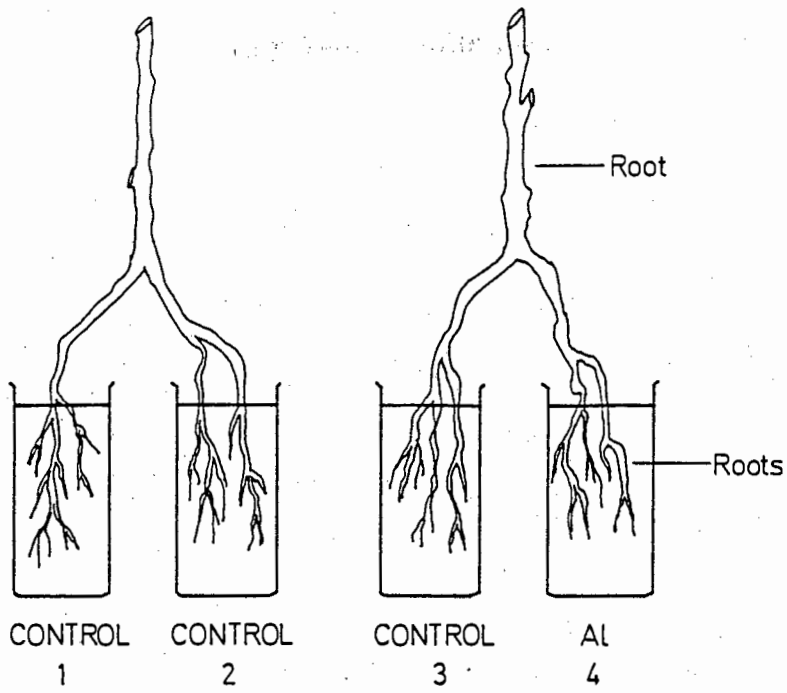

Figure 3.11: *Diagramatic representation of the split root technique showing the compartment numbers used for the 2-1 variety. A parallel system was used for Sauvignon with compartments 5 to 8.*

Since trace metals were not of interest in this application, it was permissible to use stainless steel equipment to cut and handle the root systems. The roots were separated from the stems and freeze-dried without heating. Dried powder material was prepared as stipulated in Chapter 2 in the form of compressed tablets. Similar targets were prepared from NIST SRM-1570 spinach leaves, SRM-1571 orchard leaves, SRM-1572 citrus leaves, SRM-1573 tomato leaves and SRM-1575 pine needles. The calibration sensitivity function was obtained from the data from the reference standard materials. It was assumed that the matrices of the standards and of the samples were similar and hence no corrections for matrix effects were applied.

Since the scattering chamber was made of aluminium, it was essential to prevent scattered protons from exciting Al K X-rays which may have found their way to the detector either directly or by scattering processes. This was achieved by surrounding the sample ladder with a sleeve of Perspex in which an entry hole allowed access to the beam, and an exit hole at 90° to allow generated X-rays from the sample to be viewed by the detector. Protons of 1 MeV were used to irradiate the samples with beam currents of about 2 nA. A thin absorber of Kapton protected the Si(Li)

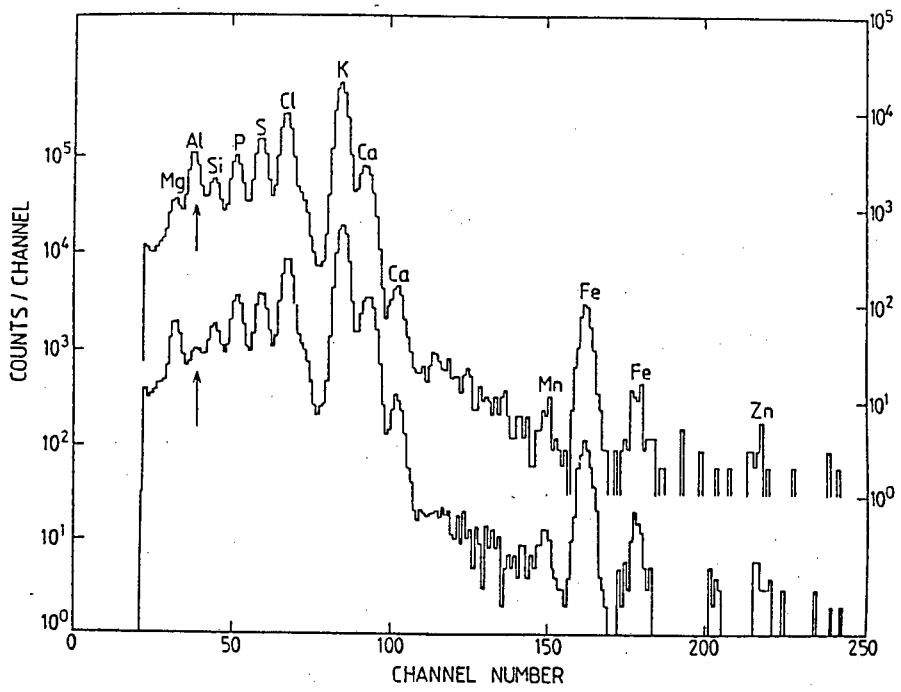

Figure 3.12: *Spectra obtained from samples of the grape variety 2-1 (R99 x Jacquez) showing the difference in aluminiun and magnesium concentrations of the test sample (upper curve) and control. The arrow identifies the Al-peak.*

detector from scattered protons.

Typical spectra obtained from the irradiation of thick targets of the the two varieties are shown in Figure 3.12. The main elements detected were Mg, Al, Si, P, S, Cl, K, Ca and metals such as Mn, Fe and Zn. However, since the main interest in this application was the effect of Al, the conditions chosen for spectrometry were those that optimised the yield of the light elements. No attempt was made to analyse for the trace metal composition. The analytical results are summarised in Table 3.6. Each value represents the mean of all root samples from the same compartment and the relative standard deviation is given under each value. The overall experimental error in the determination of elemental concentrations is composed of:

1. the error inherent in the technique. This error was given by the precision as determined from 8 duplicate analyses of Fe in SRM-1575 pine needles. The relative standard deviation was 0.49%;

2. the error due to the statistical nature of counting as given by $\sqrt{2B+S}$ where B and S are respectively the background and the nett sample counts;

Table 3.6: *Analysis of roots from grape vines of various groups grown under different conditions. Concentrations are given in μg/g.*

Element	2-1 (R99 x Jacquez)				Sauvignon blanc			
	1	2	3	4	5	6	7	8
Mg	6 478	4 105	5 717	2 962	6 780	5 467	6 085	2 613
	(4.3)	(2.8)	(5.5)	(8.9)	(28.1)	(12.0)	(16.9)	(44.5)
Al	1 198	1 017	482	6 590	4 375	1 931	7 339	6 592
	(27.9)	(42.1)	(17.2)	(3.8)	(25.7)	(20.3)	(9.3)	(19.7)
Si	1 977	2 578	1 437	1 230	9 338	5 072	22 893	3 580
	(28.5)	(26.8)	(25.2)	(16.9)	(38.8)	(28.2)	(18.8)	(30.6)
P	4 529	4 493	4 137	3 768	7 479	4 737	8 918	5 798
	(3.0)	(3.4)	(3.8)	(4.0)	(13.3)	(1.3)	(5.8)	(6.2)
S	4 488	3 743	4 189	5 567	4 551	6 038	4 288	5 062
	(8.6)	(9.0)	(7.9)	(6.6)	(12.8)	(11.4)	(9.5)	(11.7)
Cl	11 010	10 421	10 670	11 497	4 887	6 867	3 941	4 829
	(11.0)	(6.1)	(6.7)	(9.7)	(17.9)	(10.6)	(15.2)	(7.4)
K	56 624	48 923	49 127	46 896	41 523	46 216	24 937	29 271
	(7.6)	(11.8)	(6.1)	(11.8)	(7.4)	(10.1)	(19.0)	(11.8)
Ca	9 894	9 987	10 153	3 940	6 685	8 480	7 928	3 269
	(3.7)	(5.5)	(5.6)	(2.5)	(6.5)	(6.1)	(4.6)	(9.4)

- Groups 4 and 8 were grown on nutrients with added aluminium.
- Relative standard deviation in % is given under each value.

3. inaccuracies of correction for thick target yields, estimated at 1%.

4. errors due to differences in behaviour of biological specimens. These are the majors errors and are beyond the control of the experiment.

The mean values confirm the previous observation [Me 84] that the concentrations of Mg and Ca were reduced when the nutrient was enriched in Al. The increased absorption of Al in groups 4 and 8 was due to the increased concentration of this element in the feed. The concentrations of the other elements appear to be unaffected by changes in the Al concentration.

In order to visualise the correlation between group of samples, the data was submitted to correspondence analysis. A plot of the first two axes, calculated from all the measured concentrations is given in Figure 3.13 in which the samples are represented by the number of the compartment in which they were grown and the elements are identified by their chemical symbols. With few exceptions, the data points representing samples of the variety 2-1 were plotted to the right of the sloping broken line. This indicated that the concentrations of the determined elements differed from those of the variety Sauvignon. Since the points of groups 1,2 and 3 formed a tight cluster, the composition of the measured elements in these groups could be considered to be similar. This confirmed that the variety 2-1 was resistant to Al concentration changes. By contrast, while groups 5 and 6 formed an extended cluster, the smaller cluster of group 7 was situated at further negative values of axis 1. This proved that the roots in compartment 7 absorbed more Si and Al and confirmed that the variety, Sauvignon, was sensitive to the presence of Al even though part of the roots was grown in a control medium.

The horizontal dotted line in Figure 3.13 separates the points representing samples grown in feeds containing added aluminium. This confirmed the previous observation [Me 84] that roots grown in Al-rich media concentrate this element in the root system. The nutrient elements, Mg, P, S, Cl, K and Ca were all plotted in an extended cluster in the top right portion of Figure 3.13, while Si and Al were clearly not part of the cluster. The uptake of these elements was obviously different in the two varieties. The measured concentration of Al was then plotted as a function of the Si content

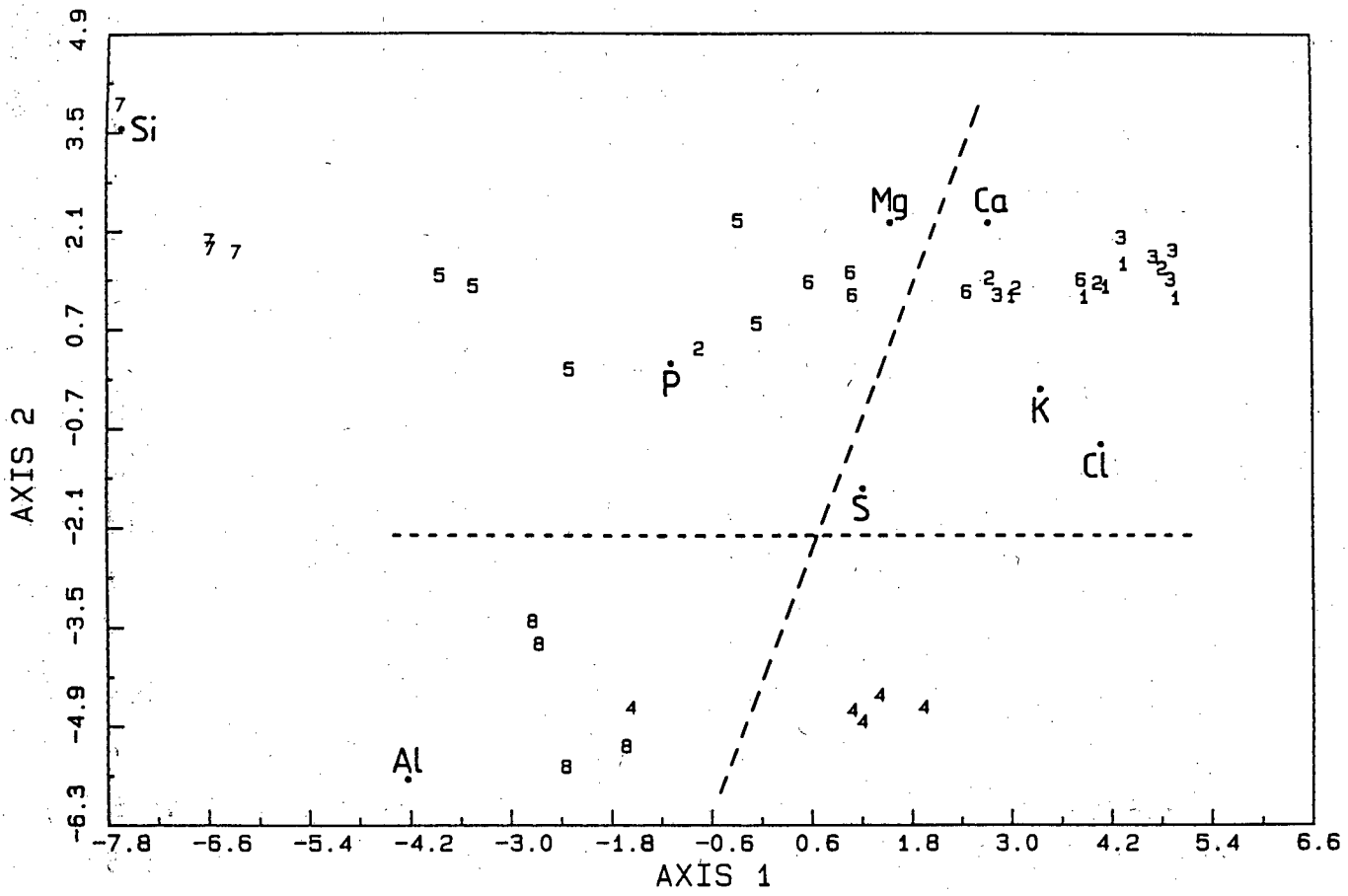

Figure 3.13: *Correspondence analysis plot of the first two axes of the data for 8 elements determined in the root specimens by PIXE. Each sample is represented by the group number to which it belongs. The sloping line indicates the separation between variety 2-1 on the right and Sauvignon on the left. The horizontal line separates controls from samples grown in feeds with added Al.*

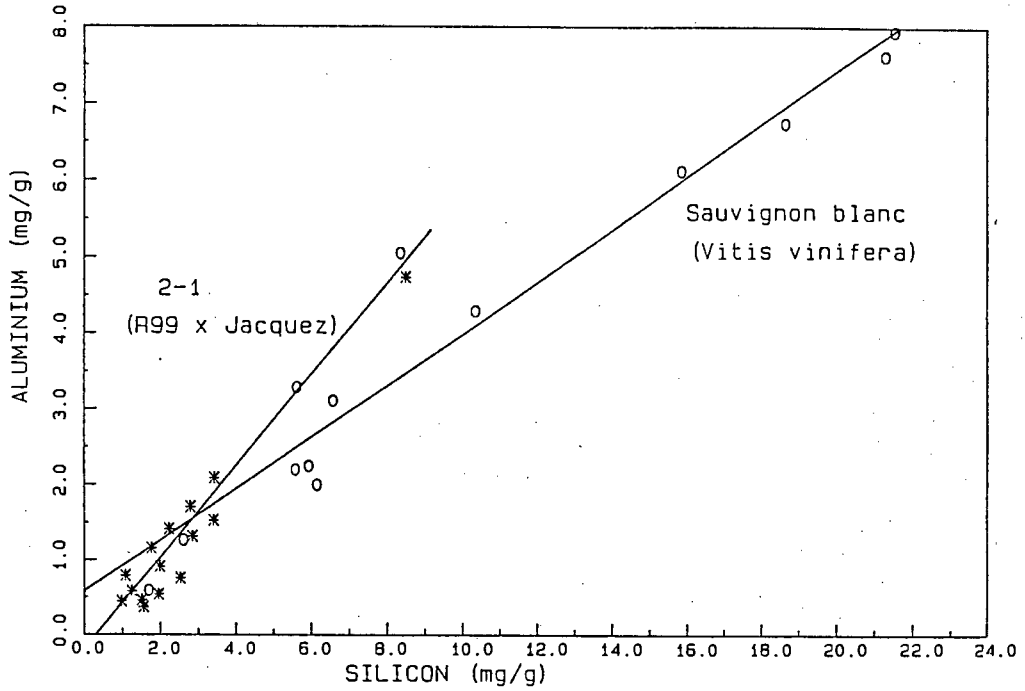

Figure 3.14: *The correlation between Al and Si content of the two grape vine varieties. Stars refer to (2-1) and circles to Sauvignon.*

for each of the two varieties. It was found that the Al content was proportional to the Si content, but that the proportionality constants for the two varieties differed, being 0. 580 for (2-1) and 0.343 for Sauvignon. In both cases the correlation factor was better than 0.96. The plots are shown in Figure 3.14, in which the values for variety (2-1) are plotted as stars and for Sauvignon as circles.

3.2.2 Application in archaeology

Cation-ratio differences in rock patinas

The determination of the age of archaeological artefacts from surface sites is often impossible using conventional methods such as radiocarbon dating, because they lack direct association with datable organic material. For about a century [Wa1891] interest has been directed to the coating observed on rocks and artefacts from arid regions. This coating has been referred to as "rock varnish" in the USA [Do 83], but the term "patina" seems more accurate and will be used here [Go 60]. Varnish or patina had long been considered by South African archaeologists as a means of

dating [Go 60] stone artefacts found in arid and semi-arid regions, but the mechanism of patina growth is not yet fully understood.

Rock patinas are relatively thin surface layers formed from dust particulates, silicate clays and small amounts of organic material. Their rate of formation depends on climatic factors and biological processes [Do 83]. Elemental analyses of the patina have shown that it is not necessarily derived from the matrix on which it was formed and usually consists of clay minerals containing, *inter alia*, Mn and Fe; the minor elements include Na, P, S, K, Ca and Ti [Du 86]. Because Ti deposited in the patina layers is less soluble and less mobile [Po 77],[Do 84], substitution of alkali metals by Ti can serve as a basis for dating. The ratio of alkali and alkali earth metals (K,Ca) to Ti, here called the cation ratio, gives an indication of how long the artefact has been exposed to the leaching process.

Previous analysis [Pi 88] of patina layers has established the presence of nitrogen and thus indicated that organic materials may play a role in patina formation. However, no correlation was established between the nitrogen content and the content of inorganic components. The presence of organic material in patinas has been indicated [Do 86], but the low carbon content required that large areas ($\approx 1\text{m}^2$) of patina be sampled for radiocarbon dating, thus making the technique unsuitable for dating relatively small archaeological artefacts.

An alternative method of dating patinas by cation-ratios has been demonstrated [Pi 88],[Do 86],[Do 83] in which the elemental concentrations of metals are determined in small areas of the patina and the cation-ratio of elutable to stationary elements is used to provide a time scale for dating purposes longer than that of radiocarbon dating.

The northern Cape area of South Africa and the central area of Namibia form part of the same geographic and climatic region. To establish whether the matrix composition of the rock substrate had any effect on the rate of growth of the patina, an investigation was undertaken, in which a leaching curve was established for samples of hornfels and compared to that on chalcedony.

A suite of samples from the northern Cape of South Africa and one from Damara-

land in central South West Africa/Namibia were selected for the study. The samples from the northern Cape were selected because they formed part of the only available typological sequence [Sa 88] from which a cation-ratio leaching curve could be determined. The Damaraland samples consisted of Middle Stone Age artefacts, apparently all dating from the same time period, and consisting mainly of chalcedony and basalt. Standard samples of SARM-18 and SARM-20 obtained from the South African Bureau of Standards were used to calculate elemental concentrations.

The study of patina composition on artefacts of interest to archaeologists rarely involves deposits of more than 1 mm. Accordingly, in order to ensure that the patina layer is analysed with as little interference as possible from the stone matrix, preference should be given to beams which have limited penetration. The disadvantage of using a beam with too little penetration is that the maximum age that can be determined is limited by the beam penetration. The best compromise was found to be alpha particles ($^4He^+$) of about 2 MeV. Under such bombardment, the range of elements that can readily be excited extends to beyond Fe, which is sufficient for the present investigation. Furthermore, the bremsstrahlung level is low in the energy region from 2.5 keV, which facilitates the evaluation of spectral peak areas for the elements K, Ca, Ti, Mn and Fe.

The major difference between the rock matrix of hornfels and of chalcedony is the higher levels of concentration of silicon in the latter. Backscatter spectra obtained from the two types of rock material are compared in Figure 3.15. The arrowed positions in the figure refer to backscatter energies corresponding to scatter from the surface. The curves have been normalised so that the steps corresponding to iron have equal heights. The known presence of a larger concentration of silicon in chalcedony is clearly shown. Comparative X-ray spectra obtained from patina layers on hornfels and on chalcedony are shown in Figure 3.16. The relative yield of Ti X-rays from the chalcedony sample is much greater than that from the hornfels, while the yields from K and Ca are appreciably less. The sensitivity calibration curve obtained from the standard materials using 2 MeV $^4He^+$ ions to excite the X-rays is given in Figure 3.17. From this curve, the concentrations of K, Ca, Ti, Mn and Fe in the patinas were deduced. These values are given in Table 3.8, together

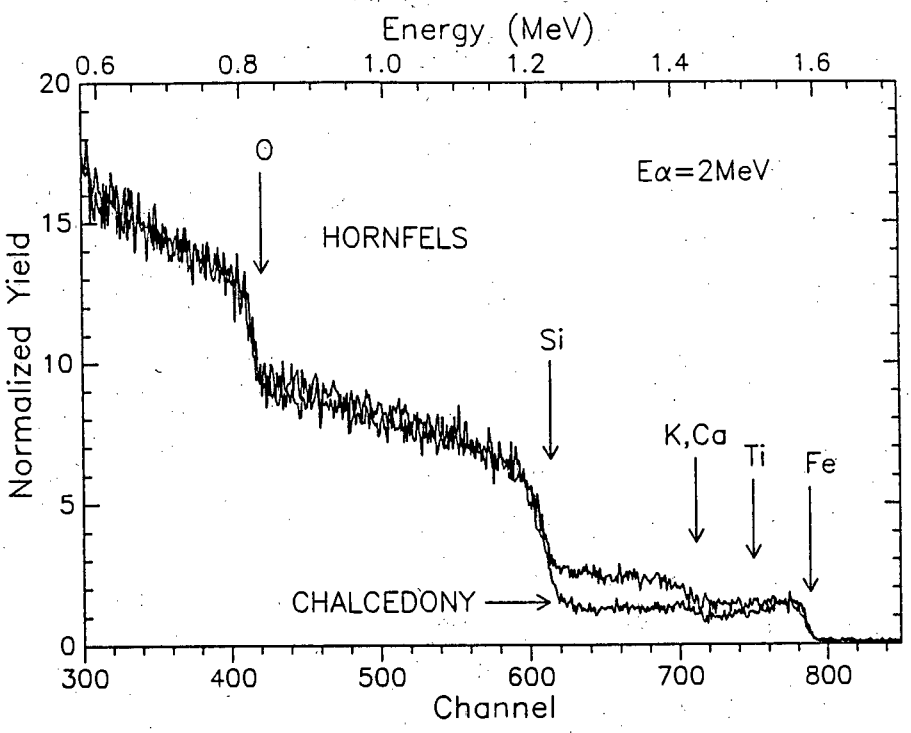

Figure 3.15: *Comparison of backscatter spectra obtained from hornfels and chalcedony. The spectra were normalised to iron. The increased silicon content in chalcedony may be noted.*

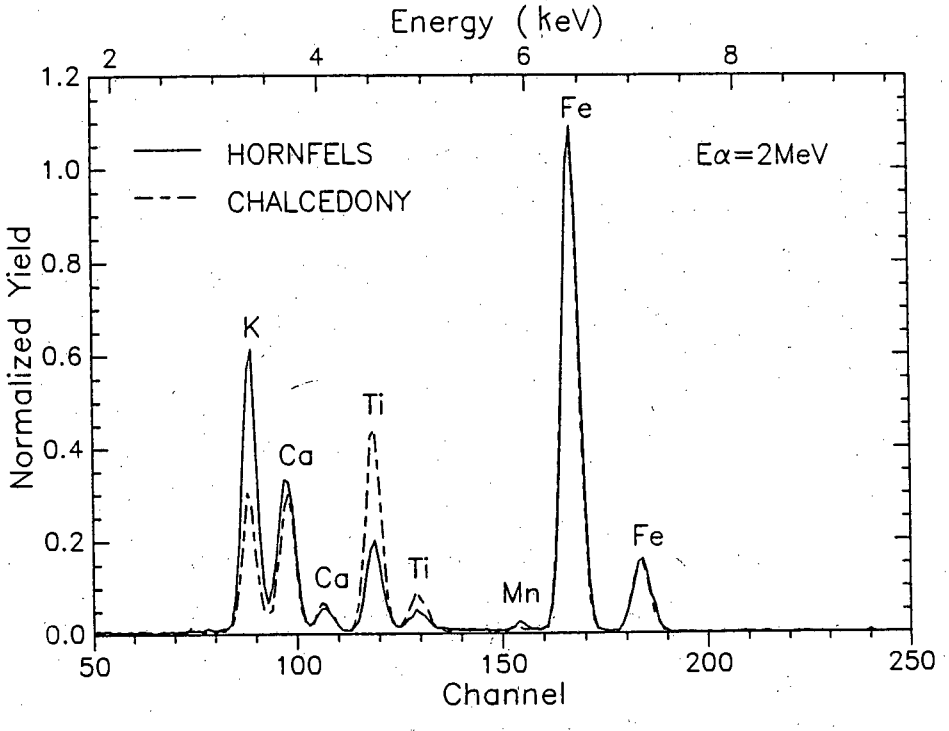

Figure 3.16: *X-ray energy spectra obtained from the bombardment of patina layers on hornfels (continuous line) and on chalcedony (dotted line) with 2 MeV alpha-particles and normalised to equal Fe peak heights. Note the difference in peak intensities of K, Ca, Ti and Mn.*

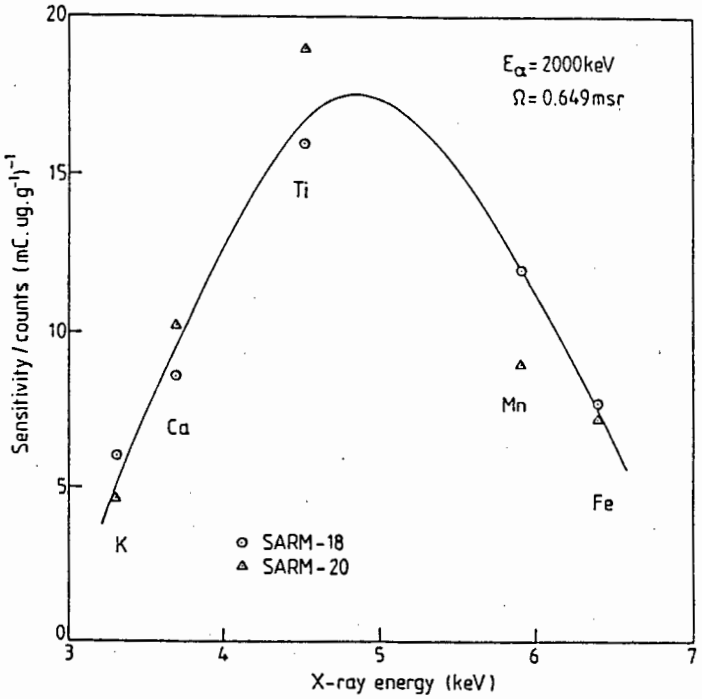

Figure 3.17: *Sensitivity calibration curve for the determination of elemental concentrations from X-ray generation by 2 MeV $^4He^+$ ions. The standards that were used were SARM-18 and SARM-20 and the solid angle of measurement was 0.649 msr.*

with typological (i.e. approximate) ages of the samples and their cation ratios of (K+Ca) relative to Ti. The linear correlation between typological age and cation ratios, shown in Figure 3.18, was calculated by the method of least squares in which every experimentally determined value was taken into account, except that for the single Lockshoek sample. The relationship represents the time-related leaching of the elements K and Ca, relative to the stationary Ti phase. This leaching curve confirms the previous findings [Pi 88]. It should be noted, however, that the previous values [Pi 88] were calculated as ratios of the X-ray count yields, whereas the present ratios are determined from the mass concentrations. The Lockshoek sample has a cation-ratio significantly at odds with the expected ratio for that time period. Replicate analyses of the patina from this sample agreed with a relative precision of about 8%, thus confirming that the sample was more akin to those attributed to the poorly understood Florisbad Industry. It therefore appears that this surface-derived sample may have been misattributed, possibly as a result of the assemblage being mixed. Another possible explanation is that the titanium concentration of the rock matrix may differ appreciably from one sample to another [Je 92] and that such variation

Table 3.7: *Results of elemental analyses of patinas.*

No.	Matrix	Age /k years	Period	Elemental concentration/%by mass					Cation Ratio (K+Ca):Ti by mass
				K	Ca	Ti	Mn	Fe	
1	H	0.5	Wilton	4.62	1.04	0.335	0.051	6.00	16.9
2	H	13	Lockshoek	4.32	1.04	0.479	0.052	6.27	11.2
3	H			2.39	0.848	0.277	0.0184	3.09	11.7
4	H	64	Florisbad	3.80	1.38	0.451	0.0051	12.10	11.5
5	H			3.97	1.41	0.490	0.0155	4.07	11.0
6	H			3.26	1.10	0.320	0.040	9.74	13.6
7	H			2.13	0.517	0.264	0.032	3.45	10.0
8	H			3.62	0.679	0.435	0.097	7.74	9.9
9	B			1.76	2.11	0.493	0.167	8.51	7.9
10	C	128	Orangian	1.20	0.560	0.600	0.019	3.56	2.9
11	C			1.44	0.422	0.458	nd	3.32	4.1
12	C			1.09	1.11	0.869	0.021	2.69	2.5
13	C			0.436	0.356	0.654	0.017	1.61	1.2

nd=not determined; H=Hornfels; B=Basalt; C=Chalcedony

may affect the titanium content in the patina. If this is the case, further work needs to be done on the distribution of titanium in the matrix material, and its effect on the titanium content of the patina. For these reasons the data from the Lockshoek sample were not included in the calculation of the leaching curve.

Since all the areas under discussion form part of the same climatic region, a single leaching curve should have been applicable for dating all the artefacts. The basalt sample, which is a coarser material than the chalcedony, is somewhat similar to the northern Cape hornfels samples and shows the expected cation ratio for its typological age. By contrast, the cation ratios of the four chalcedony samples differ markedly from those of the other Orangian artefacts by a factor of almost 4, even though all five South West African samples were collected at the same site. The implication therefore is that the nature of the matrix may play an important role in the formation and composition of the patina.

Chalcedony samples are fine-grained, highly siliceous materials with a smooth, al-

most porcelain-like surface. Examination of their surfaces showed that the patina layers were thinner than on samples of hornfels. If the smooth surfaces inhibited the rate of patina growth, the cation-ratio should have been relatively higher thus reflecting a younger age. However, the reverse was the case, indicating that the mobile elements were leached at a greater rate. In the absence of an established theory of patina growth, it seems suggestive that the mobile elements in a thin patina are not protected against leaching by the blanketing effect of an added fresher layer over it. The average rate could then appear to be more rapid than from thicker patina layers. It therefore appears that leaching curves should be determined for a uniform raw material and that such curves should be expected to yield reliable ages only for artefacts of the same raw material type.

3.2.3 Thin film thickness measurement via thick target yields

As an example of the practical uses of the tables in appendix C, the following application is presented.

When PIXE analysis is carried out on thin layers, the thickness of the target is usually measured by Rutherford Backscattering Spectrometry (RBS) analysis with alpha particles if the sample can withstand the radiation damage and the possible evaporation of certain elements. Various attempts have been made to measure the thickness of thin samples by PIXE. Some of them [Ol 87],[Ja 89],[Mi 89] made use of calculated yield curves from which the thickness and concentration profile can be obtained. Others used the variation of the K_α to K_β ratio [Ah 75],[Ca 89a] or of changes in the orientation of the sample, thereby altering the effective thickness.

The reported attempts were restricted to specific target types. What would be useful would be a method applicable in general to any matrix and for every element that would yield the sample thickness with a single irradiation and a single measurement of the PIXE yields. Such a method was tried as a parallel study in the methodology of TTPIXE, in which the X-ray yields from an unknown thin film and a thick target containing the same element under consideration were compared and were used to deduce the thickness of the thin film.

From equations 1.3 and 1.18 the sensitivity factor $K_t(Z)$ measured from the thin

film can be expressed as:

$$K_t(Z) = \frac{y_t(Z)}{t.q} \tag{3.4}$$

where here $y_t(Z)$ is the K X-ray yield measured on the thin film, t is the unknown thickness (in mass per unit area) and q the total integrated charge in Coulombs. Similarly, the sensitivity factor $K_T(Z)$, can be calculated from the K X-ray yield of the same element in the thick target, $Y_T(Z)$, by using the calculated values of the integral $I(Z)$. Then from equation 1.18 we deduce that:

$$K_T(Z) = \frac{Y_T(Z)}{C_z Q I(Z)} \tag{3.5}$$

Where C_z is the concentration of the element in the thick target given in parts per million. Since

$$K_t(Z) = K_T(Z) \tag{3.6}$$

combining equations 3.5 and 3.6;

$$t = \frac{y_t(Z)}{q} . \frac{1}{K_T(Z)} \tag{3.7}$$

This postulate should be true for any proton bombarding energy as far as the experimental conditions are kept the same for both $K_t(Z)$ and $K_T(Z)$ measurements. Accordingly, a set of thin film standards as described in Chapter 2 were irradiated with 2, 3 and 4 MeV protons in order to check their reported thicknesses. Table 3. 9 presents a resume of some of the results of these measurements. It must be stressed that the accuracy of the found thickness decreases as the bombarding energy increases. This is because the error on the evaluation of the $I(Z)$ factor increases with increasing proton energy. In spite of this fact, all the thin film thicknesses found at various energies compared well with the reported values. Given in the same table are the found values for the $K_T(Z)$. It is important to mention here that the experimental geometry, in terms of detector solid angle, plays a major role and must be defined as accurately as possible. The same applies to knowledge of the true thickness value for the absorber interposed between detector and target. If we assume that the error on the estimation of the solid angle is about 3%, and that for the absorber is 5%, then the total error for this technique is of the order of 7.6%.

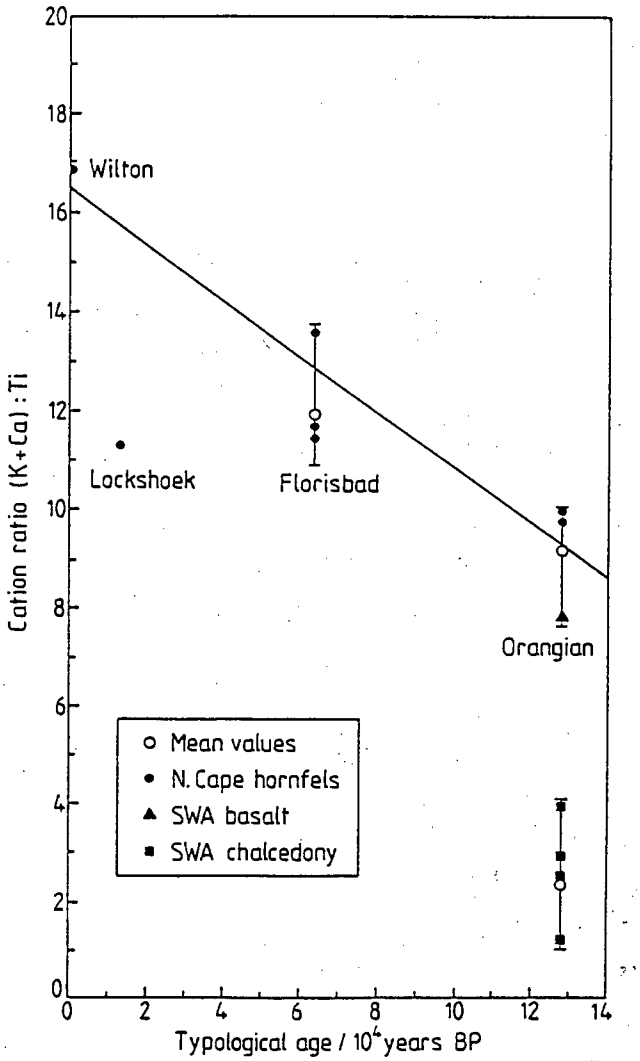

Figure 3.18: *Cation-ratio leaching curve for hornfels samples. The chalcedony samples differ significantly from those of hornfels from the same archaeological period. The time scale is given in years BP (Before Present).*

Table 3.8: *Thickness of thin film standards found via thick target yields using different proton energies.*

Thin Film	Thick Target	Element	Known	Found*			$K_T(Z)$**		
				2MeV	3MeV	4MeV	2MeV	3MeV	4MeV
GaP	$NaPO_3$	P	18.29	18.63	18.89	16.13	6.3	8.0	9.7
Ti	Ti	Ti	41.00	41.21	39.49	39.70	458.6	1422.0	1955.6
CuS	Cu	Cu	43.00	42.31	42.94	43.02	133.5	1093.4	1154.1
GaP	GaN	Ga	40.71	40.22	40.18	40.45	71.7	207.2	452.3
$RbNO_3$	Rb_2SO_4	Rb	24.36	28.56	23.67	26.7	11.1	98.5	171.4

* in $\mu g.cm^{-2}$
** in Counts/$\mu C/\mu g.cm^{-2}$

Table 3.9: *Sources for error in TTPIXE with 1-5 MeV protons.*

Parameter	Symbol	Relative Magnitude	Reference
Tabulations			
Ionisation cross sections	σ_I	~10%	[Co 88]
Fluorescent yields	ω_z	1-2%	[Ba 72]
Mass absorption coefficients	μ_z	2-5%	[Ma 84]
Stopping power	S(E)	~1%	[Zi 85]
Experimental			
Detector efficiency	ϵ_z	~3%[a]	[Ch 85]
Detector solid angle	Ω	~3%	[Ch 85]
Areal density of thin films	$M_a(Z)$	~5%	
Total charge	Q	~0.5%	
Dead time of measurement		~1%[b]	

(a) For X-rays with energies above 3.5 keV.
(b) For count rates ~1 kHz.

This error factor includes the variation range on the reported thickness values which is of the order of 5%.

3.3 Absolute method

Samples, of which the matrix is well known, may be analysed absolutely by the use of equation 1.18 only. When this procedure is followed, the experimental errors are those involved in the determination of the yield and the measurement of the bombarding charge. In the case of the former, the statistical error in the count must be increased by the errors involved in the spectrum analysis [Ca 86], while the error in the charge measurement can be separately determined by standard methods. For the calculation of the sensitivity factor, $K(Z)$, the more important sources of error are those from the calculation of the ECPSSR X-ray production cross sections [Co 88],[Pa 89], the fluorescent yield [Ba 72] and the measurements of the detector efficiency [Ma 84] and geometric factors. The two important parameters used in the calculation of $F(Z)$ values are the mass absorption coefficients [Ve 74],[Le 77]

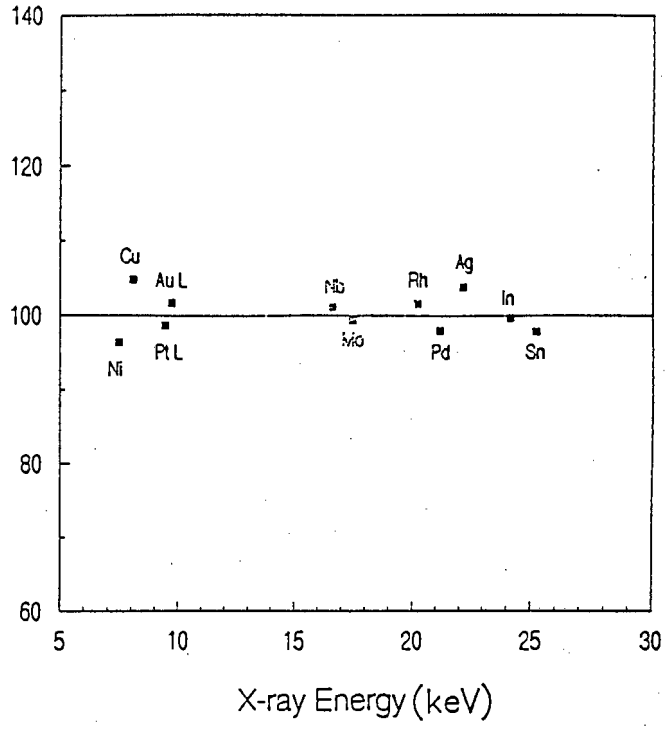

Figure 3.19: *Calibration curve obtained from the irradiation of pure metal standards with 2.4 MeV protons.*

and stopping powers [Zi 85]. A summary of the errors involved in the "absolute" method and their estimated magnitudes are given in Table 3.9. By appropriate choice of standardisation methodology, the transmission of analytical errors to the final calculated concentrations can be minimised.

3.3.1 Calibration of thick standards by Geo-PIXE

For the purpose of illustration the determination of minor and trace elements in steels is presented using the program Geo-PIXE [Ra 90], which calculates the sensitivity factor absolutely. Usually a set of pure thick standards is used to calibrate all the absolute parameters involved in the computation, including the MCF. A typical calibration curve generated by Geo-PIXE for elements between Ni and Sn was obtained and is shown in Figure 3.19. The estimated mean error for all determinations is of the order of 5%. This error does not include errors for solid angle of the geometry, efficiency of the Si(Li) detector or X-ray production cross sections [Ra 92]. If, as stipulated in Table 3.9, these errors are normally of the order of 3%, 3% and 10% respectively then the final total error could run close to 10%. The uncertainties in the

Table 3.10: *Determined elemental concentrations in steels by Geo-PIXE.*

Elem	Found (μg/g)	Error (μg/g)	Mean Error (%)	Mean Known (μg/g)	Mean MDL (μg/g)
NBS-1185					
Fe	733367	191400	26.1	n.r.(*)	3200
Ni	130633	22095	16.9	131800	741
As	75	11	14.6	n.r.	36
Nb	259	40	15.6	n.r.	-
Mo	20667	637	3.1	20100	48
NBS-1152					
Fe	733500	190967	26.0	n.r.	3000
Ni	97003	16373	16.9	102100	600
Cu	4470	632	14.1	4970	230
As	170	17	10.0	100	30
Zr	43	8	18.6	300	29
Nb	1405	42	3.0	2000	34
Mo	3641	117	3.2	3660	32
Sn	60	20	33.3	40	48

(*) not reported

tabulated attenuation coefficients are not a serious problem for the calculation of the absorption of generated X-rays in the filter interposed between detector and target, because these filters are calibrated beforehand and thus any possible filters thickness uncertainties are included in the effective thickness calculation. Two standard steels that were used as unknown samples for the determination of minor and trace elements were NBS-1185 and NBS-1152 steel alloys. A table of results is presented in table 3.10. The results which include the minimum detection limit (in μg/g) as calculated by the program are the mean values of three irradiations on each alloy. The smallest estimated errors were obtained for Nb and Mo in both alloys. The errors for elements such as Fe (the major component) and Ni are relatively high, although the concentrations agreed very well with the reported values. A similar situation existed for Cu in the NBS-1152 alloy.

Chapter 4

Unknown matrices

4.1 Previous work

4.1.1 The α-parameter method

Originally developed for targets of intermediate thickness, the α-parameter method was used to determine trace elements in samples of which the composition of the matrix was unknown [Al 86]. The parameter, α, is obtained as the ratio of the mass absorption coefficient and the stopping power of protons in the sample at the surface. Since the composition of the matrix is not known, the stopping power factor is modified from the yields obtained either by using two different irradiations with different proton energies, or by carrying out two measurements under changed geometrical conditions.

The α-parameter values have been tabulated [Al 89] for the elements $16 \leq Z \leq 30$, i.e. from S to Zn, for biological, environmental, geological and alloy materials. In this respect the approach is similar to that of common matrix types, discussed in the next section. However, values calculated for different matrix types, even among the same class of sample, vary by relatively large factors [Al 89], e.g. for Ca in the NBS standards 1673 and 1575, the respective α-values are 1.08 and 0.57.

The most serious disadvantage of this procedure is the need to perform double analyses under different experimental conditions. The obvious advantage is the fact that no assumptions are made about the matrix composition.

4.1.2 The Iteration Method

When every component of the matrix yields an X-ray which can be detected in the measured spectrum of the sample, an approximation may be made as to the elemental composition of the material from the X-ray counts, but care should be taken to correct for secondary X-ray excitation of higher components by the X-rays of heavier elements. Using this approximate composition, MCF-values are calculated for all the components, including the main matrix elements. These values are then used to calculate a better approximation to the concentration of the matrix elements. By continuing the iterative process, the determination of the matrix composition can be refined until the relative difference between successive iterations become acceptably small [Cl 81], [Pe 88], [Sm 84]. It is seldom necessary to continue for more than 4 or 5 iterations.

If some matrix components are not detected in the X-ray spectra, such as would be the case for hydrogen and other light elements with $Z \leq 11$, additional information on the matrix composition needs to be sought by other methods. Alternatively, if the sample can be compared with a common matrix type, one of the procedures discussed in section 4.2 could be applied.

An example to illustrate this approach is the study of semionic materials. The ternary chalcogenide semiconductors, of the type I-III-VI with ABX_2 stoichiometry adamantine structure and A=Cu or Ag, are known to have low but significant ionic conductivity, while retaining their semiconducting character. Several pieces of experimental evidence point to the monovalent species as the ones involved in ionic conductivity. Because these ions in interstitials, vacancies or antisite occupancy can serve as dopants as well, the materials have the interesting property that their semiconducting properties are, in principle, controllable by control of ion migration in them. Such materials are termed "semionics"[Pe 88].

By drifting Cu or Ag under an electric potential from electrodes of these metals into $AgInSe_2$ or $CuInSe_2$ respectively, components of the general form $Cu_xAg_{1-x}InSe_2$ may be formed. Different electrical potential differences were applied in a solid state electrochemical arrangement. The negative electrode was analysed for accumulation

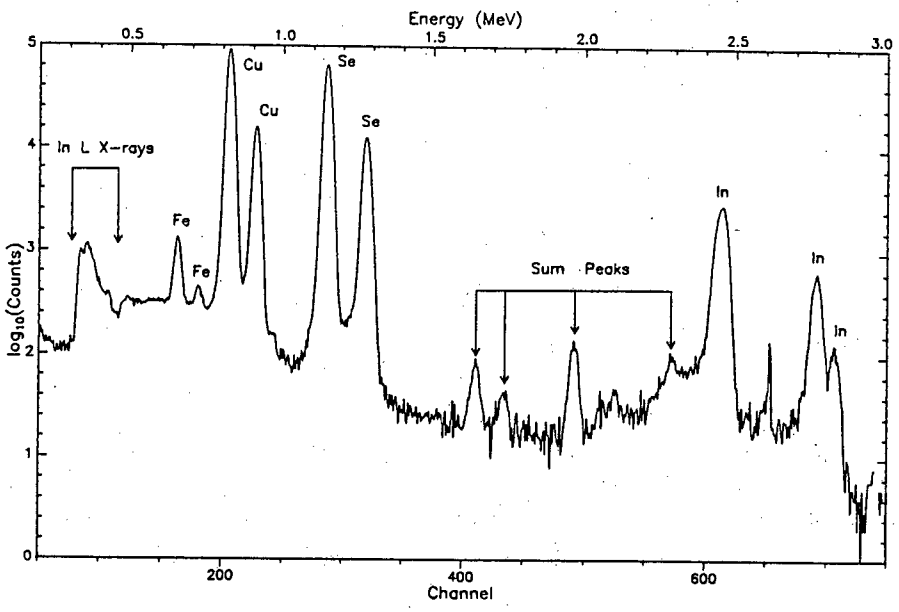

Figure 4.1: *PIXE spectrum of a $CuInSe_2$ compound irradiated with 4 MeV protons.*

of Ag or Cu.

Figure 4.1 shows a PIXE spectrum of a $CuInSe_2$ compound collected with 4.0 MeV protons. All major elements of its matrix are present on the energy spectrum. The analytical information obtained from RBS was not utilised because that technique cannot adequately resolve the steps for Ag and In.

The aim, from the point of view of analytical TTPIXE, was to find the "true" stoichiometry of the semionic compounds after treatment. In the case of Cu excess in $CuInSe_2$ the methodology was as follows:

1. From the PIXE spectrum the atomic ratios Cu:Se and Cu:In were deduced from the relative X-ray counts, Y(z) without taking into account the MCF:

$$\frac{C_{Cu}}{C_{Se}} = \frac{Y_{(Cu)}}{Y_{(Se)}} \frac{K_{(Se)}}{K_{(Cu)}}; \frac{C_{Cu}}{C_{In}} = \frac{Y_{(Cu)}}{Y_{(In)}} \frac{K_{(In)}}{K_{(Cu)}} \tag{4.1}$$

   where the values of $K_{(Se)}$, $K_{(Cu)}$ were obtained from the irradiation of thin standards.

2. From the atomic ratio an initial stoichiometry was deduced ($Cu_xIn_ySe_z$).

3. These initial concentration guesses by mass were used to calculate the $F(Z)$-values for each element in the compound $Cu_xIn_ySe_z$ using the program RD1 (see Appendix B).

4. Then a new set of atomic ratios was calculated but this time including the $F(Z)$-values previously calculated:

$$\frac{C_{Cu}}{C_{Se}} = \frac{K_{(Se)}}{K_{(Cu)}} \frac{F_{(Cu)}}{F_{(Se)}} \cdot \frac{Y_{(Cu)}}{Y_{(Se)}} \tag{4.2}$$

5. With a new set of atomic ratios the process of recalculating new $F(Z)$-values was extended until the change of atomic ratios between two consecutive iterations was less than 1%.

Table 4.1 shows a resume of the results for both the $CuInSe_2$ and $AgInSe_2$ cases. The atomic ratios were expressed relative to Se in both cases and the guesses were taken as the original i.e. before treatment. As seen in the table, the atomic ratios converge rapidly. It is noted that for the case of $AgInSe_2$ only two iterations were necessary. As an alternative, if there is no possibility to obtain the $K(Z)$ factors from thin film standards, the absolute method can be applied, when tabulated values of X-ray production cross sections σ and the efficiency of the detector ξ have to be used. Expressing this as in equation 4.2 for Cu and Se we have:

$$\frac{C_{Cu}}{C_{Se}} = \frac{\sigma_{Se}}{\sigma_{Cu}} \frac{\xi_{Se}}{\xi_{Cu}} \frac{F(Se)}{F(Cu)} = \frac{Y(Cu)}{Y(Se)} \tag{4.3}$$

Other values included in the $K(Z)$ factor such as the solid angle cancel out.

4.2 Common matrix type

Although the composition of the matrix may not be known in detail, samples may frequently be classified according to types in which the main components of the matrix do not vary appreciably in their concentrations. The calculation of elemental concentrations in TTPIXE can then be achieved if a generalisation of MCF-values can be applied in the form of universal values to a set of materials having similar types of matrix composition.

Table 4.1: *Iteration steps for calculation of atomic ratios in $AInSe_2$-based compounds with 4.0 MeV protons, where A=Cu or Ag.*

$Cu_xIn_ySe_1$

Element	Initial guesses	After 1st Iteration		After 2nd Iteration		After 3rd Iteration	
	At. Ratio	$F(Z)$	At. Ratio	$F(Z)$	At. Ratio	$F(Z)$	At. Ratio
Cu	0.5	14.84	0.4757	15.27	0.48	15.23	0.48
In	0.5	4.39	0.867	4.35	0.85	4.35	0.85
Se	1.0	9.10	1.000	9.20	1.00	9.20	1.00
		$Ag_xIn_ySe_1$					
Ag	0.5	4.56	0.71	4.71	0.71		
In	0.5	4.32	0.79	4.46	0.79		
Se	1.0	9.34	1.00	9.64	1.00		

4.2.1 Carbon-rich materials

Since the organic matrix composition of biological samples is often unknown, some empirical composition, usually that of cellulose, is assumed. To test the validity of this assumption $F(Z)$-values were calculated for the standard material NIES-CRM-3 Chlorella, the composition of which was first assumed to be that of cellulose $(C_6H_{10}O_5)_n$ and compared with those calculated from an empirical formula. From Rutherford backscattering analysis the carbon-to-oxygen ratio was found to be 4:1, which indicated an empirical formula of $(C_4H_xO)_n$. When the value of x was changed progressively from 1 to 6, the corresonding values of the range of 4 MeV protons were calculated to vary from 27.2 to 24.2 mg/cm^2 with a mean value of 25.7 mg/cm^2, corresponding to a value x=3. The same value for x was obtained for the mean value of the absorption and for the $F(Z)$-value of the K_α Ca X-ray. Accordingly, the empirical formula was accepted as $(C_4H_3O)_n$. Comparison of the variation of $F(Z)$-values with atomic number of the target material, calculated for 4 MeV protons, is given in Figure 4.2 where the composition of the organic material was assumed to be that of cellulose and that of $(C_4H_3O)_n$. The differences between $F(Z)$-values for corresponding elements decrease with increasing atomic number. The $F(Z)$-values

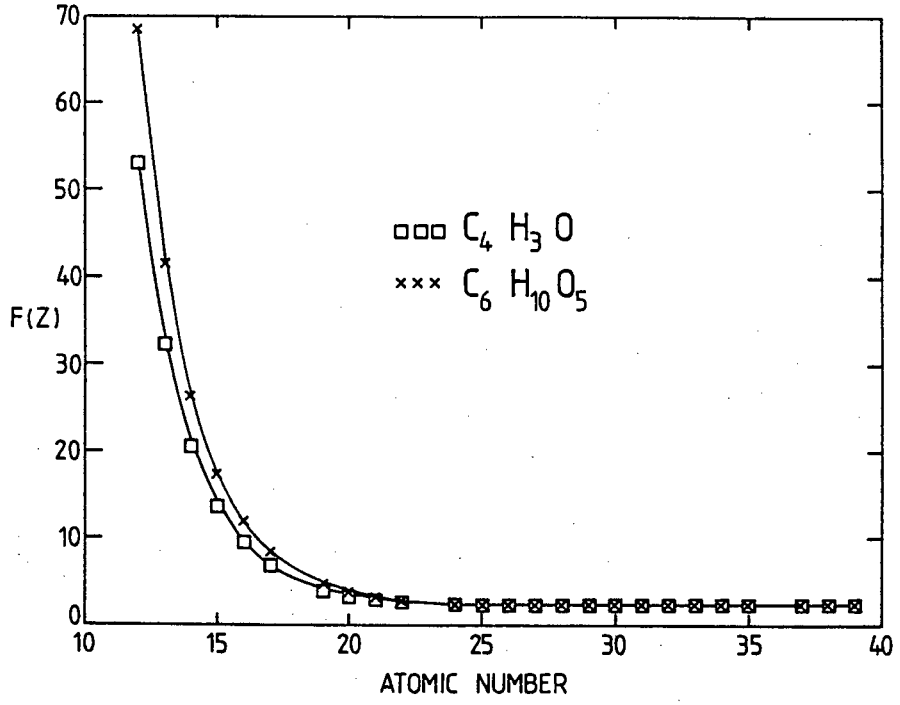

Figure 4.2: *The variation of the $F(Z)$-value with atomic number of the target material, calculated for 4 MeV protons on chlorella and K_α X-rays. The values are compared for the measured matrix composition $(C_4H_3O)_n$ and an assumed cellulose composition $(C_6H_{10}O_5)_n$.*

for cellulose exceeded those for the assumed chlorella matrix by more than 20% for target materials with $12 \leq Z \leq 17$, and between 10 and 20% for $19 \leq Z \leq 22$. When the atomic number of the target material was $23 \leq Z \leq 56$ the discrepancy was less than 10% and was acceptable for most analyses. For lighter elements the differences are large and increase with decreasing values of Z. Table 4.2 lists a comparison between data calculated for some elements on the assumption that the matrix is cellulose, and for the matrix composition calculated from analysis. While the precision of the two sets of data remained constant, the accuracy of the latter set is improved mainly for the light elements.

For the determination of light elements, accurate analysis required a knowledge of the true empirical formulation, either known or measured. However, when $Z \leq 23$, the exact empirical formulation of the organic matrix could not be replaced by that of cellulose. This conclusion is in agreement with similar suggestions [Cl 87], [Ah 77] made earlier, but for which no experimental proof was proffered. Measurements made on different matrix materials showed that the use of an assumed cellulose structure

Table 4.2: *Analysis of Chlorella*.*

Element	Known	Concentration ($mg.g^{-1}$)	
		Assumed Matrix** $(C_4H_{10}O_5)_n$	Analysed Matrix $(C_4H_3O)_n$
K	12400	12920	12380
Ca	4900	3374	4890
Mn	69	51.4	55.1
Fe	1850	1440	1550
Cu	3.5	2.6	2.6
Zn	20.5	19.3	19.6

*Japan Environmental Agency standard NIES-CRM-3
**Assumed composition of cellulose

was acceptable provided the results were compared to some selected standard.

Calculated $F(Z)$-values

$F(Z)$-values were calculated for each biological standard (listed in Table 4.3) according to equation 1.12 using the program RD1. In the calculation of $F(Z)$-values the inorganic composition was used as certified, but the residual organic component was assumed to have the composition of cellulose. The values in Table 4.4 are the mean values obtained from all the standard materials listed in Table 4.3. Values in parentheses refer to the relative standard deviation expressed as a percentage. The precision of $F(Z)$-values for elements from K to Cr, bombarded with the more energetic protons, is relatively poorer than for most of the other values. This implies that elemental concentrations of these elements analysed with 3 or 4 MeV proton beams and calculated by using the tabulated $F(Z)$-values may have a poor accuracy. For purposes of illustration the values of Table 4.4 are plotted in Figure 4.3. Clearly, the best energy for analysis would be somewhere between 1.0 and 2.0 MeV. But obviously there will be a limitation as regards the X-ray production cross section for the number of elements that could be excited. Plots of these MCF-values against proton energies showed a similar trend (see Figure 4.4). From the point of view of the TTPIXE analyst, these values have to be calculated for every proton

Table 4.3: *Identification of carbon-rich standard reference materials.*

Name of standard	Laboratory code	Supplier
Vegetable materials		
Wheat Flour	SRM-1567	NBS[a)]
Spinach	SRM-1570	NBS
Orchard leaves	SRM-1571	NBS
Citrus leaves	SRM-1572	NBS
Tomato leaves	SRM-1573	NBS
Pine needles	SRM-1575	NBS
Pepperbush	CRM-1	NIES[b)]
Chlorella	CRM-3	NIES
Tea leaves	CRM-7	NIES
Animal materials		
Oyster tissue	SRM-1566	NBS[a)]
Bovine liver	SRM-1577	NBS
Human hair	CRM-5	NIES[b)]
Animal muscle	H-4	IAEA[c)]
Horse kidney	H-8	IAEA

[a)] US National Bureau of Standards.
[b)] Japan National Institute for Environmental Studies.
[c)] International Atomic Energy Agency.

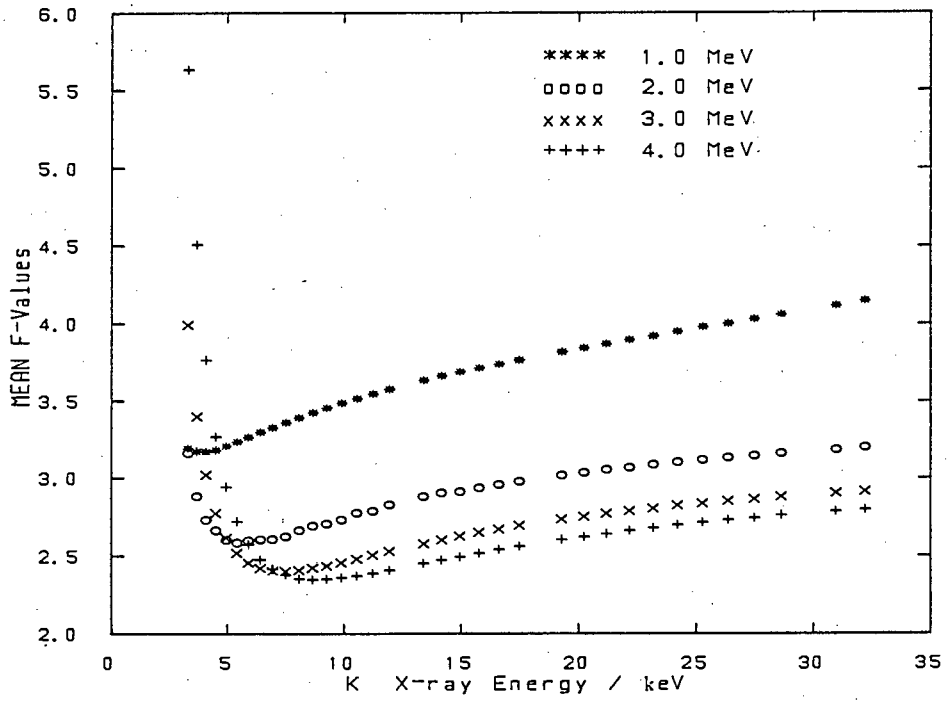

Figure 4.3: *The variation of $F(Z)$-values with the K_α X-ray energy for the bombardment of carbon-rich materials with protons between 1 and 4 MeV.*

Table 4.4: *Mean calculated $F(Z)$-values and relative standard deviations [%] for biological materials.*

Element	Incident proton energy [MeV]			
	1.0	2.0	3.0	4.0
K	3.19(1.7)	3.16(5.2)	3.99(8.8)	5.63(10.9)
Ca	3.17(1.4)	2.88(4.4)	3.40(7.8)	4.50(10.4)
Sc	3.17(1.1)	2.73(3.5)	3.02(6.7)	3.77 (9.2)
Ti	3.18(0.9)	2.66(3.2)	2.77(5.6)	3.27 (8.4)
V	3.21(0.7)	2.60(2.3)	2.62(4.6)	2.94 (7.2)
Cr	3.23(0.6)	2.59(1.9)	2.52(3.9)	2.72 (6.2)
Mn	3.27(0.5)	2.60(2.4)	2.46(3.2)	2.57 (5.2)
Fe	3.30(0.4)	2.62(2.3)	2.42(2.7)	2.48 (4.4)
Co	3.33(0.3)	2.62(1.1)	2.41(2.2)	2.42 (3.7)
Ni	3.36(0.3)	2.63(0.9)	2.40(1.0)	2.38 (3.1)
Cu	3.39(0.3)	2.67(2.1)	2.41(1.6)	2.36 (2.6)
Zn	3.43(0.3)	2.69(2.1)	2.42(1.3)	2.35 (2.2)
Ga	3.46(0.2)	2.70(0.5)	2.44(1.1)	2.35 (1.9)
Ge	3.49(0.2)	2.73(0.5)	2.46(0.9)	2.36 (1.6)
As	3.52(0.2)	2.77(2.1)	2.48(0.8)	2.27 (1.4)
Se	3.55(0.1)	2.79(0.4)	2.51(0.7)	2.39 (1.2)
Br	3.56(0.1)	2.83(2.1)	2.53(0.6)	2.41 (1.1)
Rb	3.63(0.1)	2.88(2.0)	2.58(0.5)	2.45 (0.8)
Sr	3.66(0.1)	2.90(2.0)	2.60(0.4)	2.47 (0.7)
Y	3.69(0.1)	2.91(0.2)	2.63(0.4)	2.47 (0.6)
Zr	3.71(0.1)	2.93(0.2)	2.65(0.3)	2.52 (0.6)
Nb	3.74(0.1)	2.96(0.2)	2.67(0.3)	2.54 (0.5)
Mo	3.77(0.1)	2.98(0.2)	2.59(0.3)	2.56 (0.5)
Ru	3.82(0.09)	3.02(0.1)	2.74(0.2)	2.61 (0.4)
Rh	3.84(0.09)	3.04(0.1)	2.75(0.2)	2.62 (0.4)
Pd	3.87(0.09)	3.05(0.1)	2.77(0.2)	2.64 (0.4)
Ag	3.90(0.09)	3.07(0.1)	2.79(0.2)	2.66 (0.3)
Cd	3.92(0.08)	3.09(0.1)	2.80(0.2)	2.68 (0.3)
In	3.95(0.09)	3.10(0.1)	2.82(0.1)	2.70 (0.3)
Sn	3.98(0.09)	3.12(0.1)	2.84(0.1)	2.71 (0.3)
Sb	4.00(0.1)	3.13(0.1)	2.85(0.1)	2.73 (0.3)
Te	4.03(0.09)	3.15(0.1)	2.85(0.1)	2.74 (0.3)
I	4.06(0.08)	3.16(0.1)	2.88(0.1)	2.76 (0.3)
Cs	4.12(0.07)	3.19(0.09)	2.90(0.1)	2.79 (0.3)
Ba	4.15(0.08)	3.20(0.09)	2.91(0.1)	2.80 (0.3)

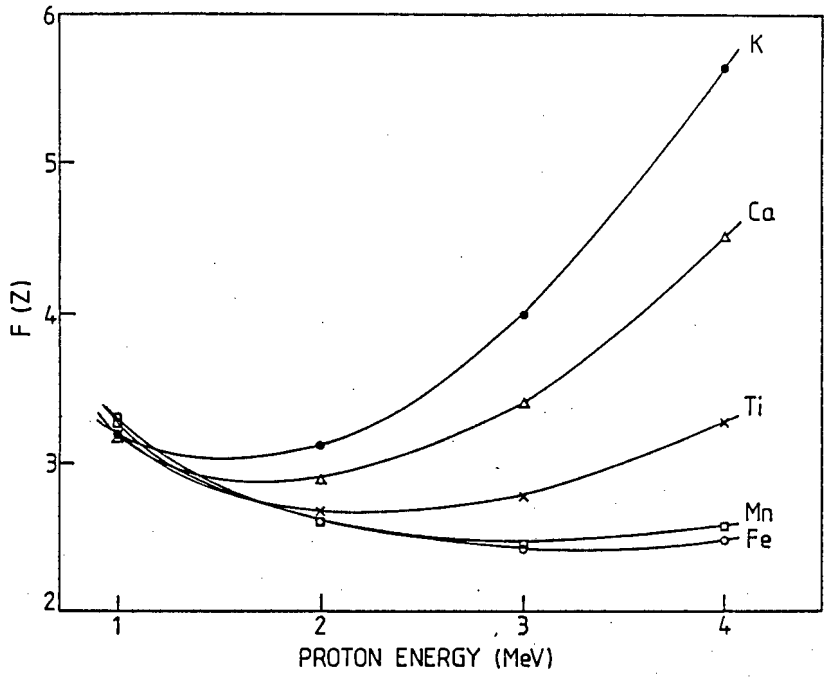

Figure 4.4: *Variation of $F(Z)$-values on carbon-rich materials with proton bombarding energy.*

energy selected for experimentation. Intermediate mean $F(Z)$-values showed that there were no irregularities or discontinuities. On the other hand the $F(Z)$-values are dependent on the ion bombarding energy and not on the geometrical factor $K(Z)$ or the experimental conditions. Hence fitted polynomials to these curves could be of some use, for interpolation at intermediate proton energies. Polynomial coefficients of mean $F(Z)$-values curves plotted for 1, 2, 3 and 4 MeV for carbon-rich materials are given in Table 4.5.

According to the methodology proposed here, the $F(Z)$-values alone could not give the analyst the complete information necessary for analytical work. Additional information about sensitivy factors $K(Z)$ as mentioned in Chapter 1, and the depth of analysis would be of value for the calculation of elemental concentrations. Table 4.6 presents values for these parameters for bombarding energy with 3 MeV protons, and the X-ray energy of the K_α line in keV. The values for the $K(Z)$ are very dependent on the experimental geometrical conditions. These values refer to the geometry which was used in Chapter 1 for the evaluation of the sensitivity factors.

Table 4.5: *Polynomial coefficients (order 3) of mean $F(Z)$-value curves for C-rich materials fitted for the proton energy range 0.5 to 4.5 MeV.*

Element	a(0)	a(1)	a(2)	a(3)
K	+4.13	-1.412	+0.480	-0.0083
Ca	+4.50	-1.927	+0.635	-0.038
Sc	+4.61	-2.030	+0.635	-0.045
Ti	+4.57	-1.905	+0.555	-0.040
V	+4.78	-2.160	+0.645	-0.055
Cr	+4.75	-1.978	+0.545	-0.046
Mn	+4.68	-1.803	+0.460	-0.047
Fe	+4.82	-1.973	+0.530	-0.460
Co	+4.88	-2.012	+0.540	-0.048
Ni	+4.82	-1.868	+0.480	-0.041
Cu	+4.91	-1.940	+0.505	-0.045
Zn	+5.05	-2.115	+0.580	-0.055
Ga	+5.05	-2.110	+0.580	-0.055
Ge	+5.06	-2.082	+0.565	-0.053
As	+5.11	-2.137	+0.610	-0.063
Se	+5.11	-2.067	+0.560	-0.053
Br	+4.97	-1.833	+0.465	-0.041
Rb	+5.11	-1.938	+0.505	-0.046
Sr	+5.17	-1.982	+0.520	-0.048
Y	+5.35	-2.226	+0.630	-0.063
Zr	+5.34	-2.172	+0.600	-0.058
Nb	+5.34	-2.120	+0.575	-0.055
Mo	+5.00	-1.463	+0.240	-0.007
Ru	+5.51	-2.258	+0.630	-0.061
Rh	+5.50	-2.207	+0.605	-0.058
Pd	+5.68	-2.388	+0.675	-0.066
Ag	+5.68	-2.388	+0.675	-0.066
Cd	+5.66	-2.318	+0.640	-0.061
Sn	+5.85	-2.518	+0.720	-0.071
Sb	+5.89	-2.543	+0.725	-0.071
Te	+5.88	-2.465	+0.680	-0.065
I	+6.04	-2.673	+0.770	-0.076
Cs	+6.15	-2.733	+0.780	-0.076
Ba	+6.24	-2.820	+0.810	-0.080

Table 4.6: *Information on relevant parameters for analysis with carbon-rich materials.*

Element	Z	K_α (keV)	$F(Z)$	$K(Z)^{(*)}$	p (mg/cm^2)	Mass$^{(**)}$ (μg)
K	19	3.313	3.99	108	10.75	338
Ca	20	3.691	3.40	216	11.33	356
Sc	21	4.090	3.02	364	11.45	360
Ti	22	4.510	2.77	519	11.83	372
V	23	4.952	2.62	672	12.02	378
Cr	24	5.414	2.52	784	11.98	376
Mn	25	5.898	2.46	792	11.98	376
Fe	26	6.403	2.42	716	11.98	376
Co	27	6.930	2.41	636	11.93	375
Ni	28	7.477	2.40	562	11.88	373
Cu	29	8.047	2.41	484	11.83	372
Zn	30	8.638	2.42	412	11.78	370
Ga	31	9.251	2.44	355	11.73	369
Ge	32	9.885	2.46	264	11.69	367
As	33	10.543	2.48	196	11.64	366
Se	34	11.221	2.51	132	11.59	364
Br	35	11.923	2.53	115	11.54	363
Rb	37	13.394	2.58	76	11.44	359
Sr	38	14.164	2.60	64	11.38	358
Y	39	14.957	2.63	58	11.33	356
Zr	40	15.774	2.65	53	11.33	356
Nb	41	16.614	2.67	48	11.28	354
Mo	42	17.478	2.59	48	11.23	353

$^{(*)}$ in Count/μC/μg/cm^2

$^{(**)}$ Mean value assuming a 2mm diameter beam spot on target. No beam spread was considered.

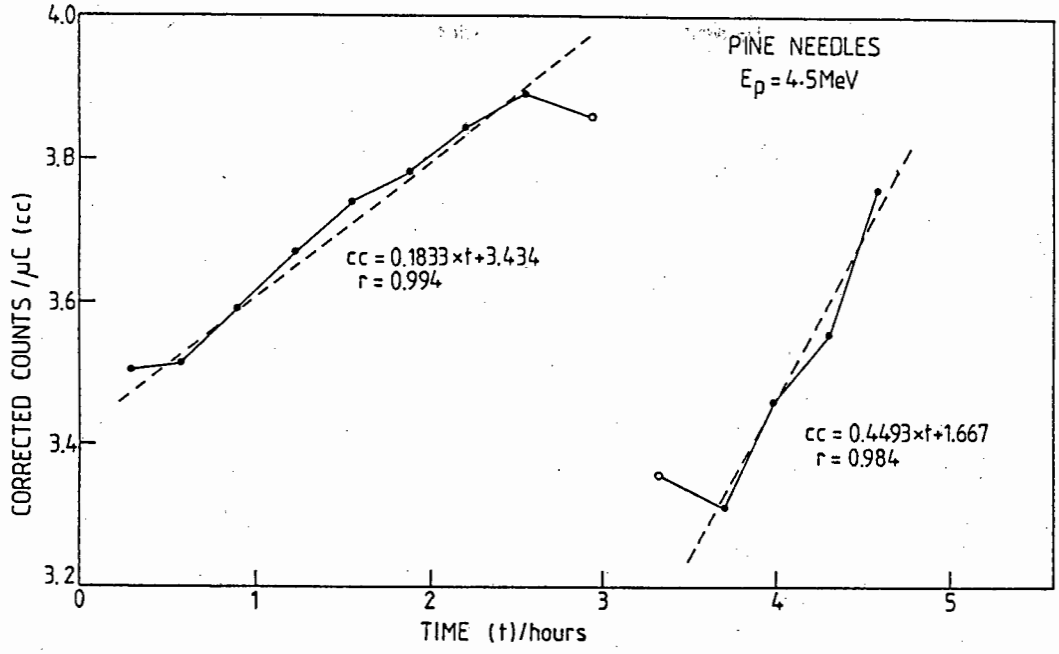

Figure 4.5: *Variation of the Fe X-ray yield with irradiation time in a pellet of pine needles irradiated with protons. The two stages of irradiation, before (left side) and after changing to a fresh pellet show linear trends.*

Experimental verification of $F(Z)$-values

Some results of analyses carried out with 4 MeV protons to test the validity of the calculated $F(Z)$-values are given in Table 4.7. The sensitivity factors $K(Z)$ were calculated experimentally from thin targets bombarded under the same experimental conditions as the biological thick targets. In most cases the agreement between the experimentally determined values and the known concentration, as certified, is acceptable. The values in parentheses are those reported as preliminary. As the RSD (relative standard deviation) decreases with decreasing proton energy it is expected that better results will be obtained with lower proton energy irradiations. Analysis of the organic pellets had to be performed either on fresh pellets or at a fresh site on a previously irradiated target [Wi 77]. Continued irradiation of a pellet on the same target site resulted in a steady increase of the signal intensity from one irradiation to the next by 2-3%, but the original yield was reproduced when a fresh target site was used. (see Figure 4.5). These results illustrate the absolute determination of elements with atomic number $23 \leq Z \leq 56$ in biological materials using a universal set of $F(Z)$-values for matrix correction, but without the use of comparative standards.

Table 4.7: *Determined elemental concentrations [μg/g].*

		Pine needles SRM-1575	Spinach SRM-1570	Tomato leaves SRM-1573	Orchard leaves SRM-1571	Chlorella CRM-3	Bovine liver SRM-1577
Mn	Known	675	165	238	91	69	10
	Found	754	170	175	64	52	9
Fe	Known	200	550	690	300	1850	268
	Found	245	546	397	215	1660	256
Cu	Known	3.0	12	11	12	3.5	193
	Found	3.5	14	14	12	2.6	183
Zn	Known	61[a)]	50	62	25	20.5	130
	Found	71	65	61	23	19.6	140
As	Known	0.21	0.15	0.27	10	-	0.055
	Found	0.5	ND	ND	7	2	ND
Rb	Known	11.7	12	16.5	12	-	18
	Found	23	14.6	18	12	2.8	13
Sr	Known	4.8	87	45	37	40	(0.14)
	Found	5.3	138	49	48	40.2	ND
Br	Known	(9)	(54)	(26)	(10)	-	-
	Found	11	81	29	9	4	17

[a)] See ref. [Gl 80]
ND = not detected.

Analysis of wood species

As a parallel study to the one presented for grape vines (see section 3.2.1), the analysis of chemical components of wood species was investigated as another application of the external standard methodology in TTPIXE analysis.

It has been shown [Fe 89] that chemical studies of wood can provide important information not only for its applicability but also for the economic feasibility of many processes involving wood. In particular, it has been found that the presence of intermediate and transition metal elements can affect the chemical and physical properties of various wood species [Gi 71],[Sc 73],[Hi 79]. It has been established that trace elements present in the production of paper could be responsible for the gradual discoloration of the paper and in some cases the slight odoriferous nature of certain types of paper. Thus there exist an obvious demand for the determination of the elemental components of wood. Previous work [El 65],[Ch 76],[Cu 80] on

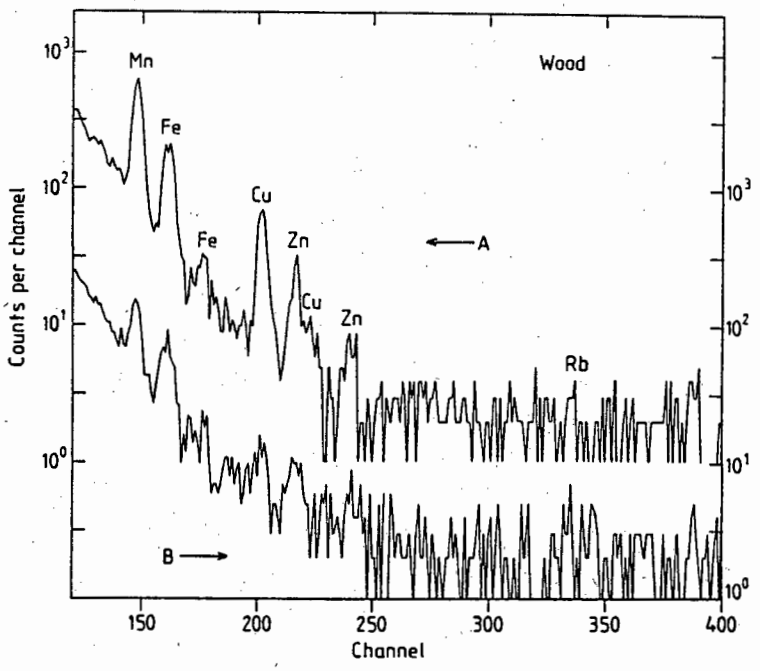

Figure 4.6: *Typical X-ray energy spectra from about 5 to about 17 keV obtained from the bombardment of wood samples with 3 MeV protons. A: Pinus Laxibaea from Zululand. B: Eucalyptus Grandus from Tzaneen, Transvaal.*

certain wood species has been carried out using neutron activation analysis and X-ray fluorescence. The present application involved the analysis of wood species from southern Africa by PIXE.

Finely ground wood samples from various locations in southern Africa were obtained from Messrs South African Pulp and Paper Industries, Transvaal. Details of the samples are listed in Table 4.9.

Standards that were used for quantification were Tomato Leaves, SRM 1573 and Pine Needles, SRM 1575 from the U.S. NIST, and Pepperbush CRM-1 from the National Institute for Environmental Studies, Japan. Typical spectra showing the most important trace metals in the wood types of *Pinus* and *Eucalyptus* trees are compared in Figure 4.6. The level of the concentration of most trace metals is higher in the former, except for rubidium, which is present in relatively low concentration in both wood types. Since the wood specimens are materials which are carbon-rich, the methodology devised in this chapter for thick target organic materials, in which universal matrix correction factors were calculated, was applied. The accuracy of this approach was checked from the data obtained from the standards listed above.

Table 4.8: *Elemental concentrations found in wood samples.*

Sample No.	Concentration (μg/g) K	Ca	Mn	Fe	Cu	Zn	Rb
1	2009.5	835.4	40.4	119.9	6.3	4.4	2.9
2	837.1	764.0	30.4	16.4	6.9	5.4	16.7
3	549.7	1184.7	191.6	289.6	2.7	9.1	7.2
4	728.7	637.7	26.0	12.9	3.4	6.5	9.4
5	675.3	662.9	16.6	14.7	0.9	n.d.	8.4
6	840.3	459.3	73.1	58.9	5.5	6.4	4.8
7	407.0	908.9	50.7	32.8	11.9	8.1	6.1
8	330.2	725.5	61.7	28.1	9.8	8.3	n.d.
9	1166.3	807.1	84.9	40.6	1.9	5.5	11.3
10	743.4	935.5	18.9	68.1	4.5	12.3	2.6
11	480.4	1177.6	84.7	38.5	9.7	9.9	10.0
12	532.2	915.2	109.3	27.4	17.1	11.0	6.5
13	971.2	594.2	59.8	20.1	1.0	3.8	2.6
14	837.7	1013.7	34.3	47.6	14.6	8.0	1.2
15	377.0	938.2	97.0	87.0	11.3	7.6	8.4
16	427.8	1144.9	122.0	54.3	13.2	11.4	7.9
17	686.6	499.6	70.3	16.6	0.8	2.0	4.5
Mean values							
Group A	846.6	632.1	51.6	25.7	2.9	4.2	8.2
Group B	425.8	968.4	87.6	44.7	12.2	9.4	6.5

n.d. - not detected

Results of the metal content of wood samples are given in Table 4.8. The sample numbers are those given in Table 4.9. The values included in the calculation of the means for the two groups are from those samples whose reference points formed separate groups in correspondence analysis. The analytical data obtained for the content of K, Ca, Mn, Fe, Cu, Zn and Rb were used for correspondence analysis. Since the first two axes had almost 93% of the information content, it was only necessary to plot the first two axes against each other. Such a plot is shown in Figure 4.7. The sample representative points are drawn towards the position of those elements present in relatively higher concentrations in the samples concerned. Thus Group A is situated near to the site of Ca because the mean calcium content

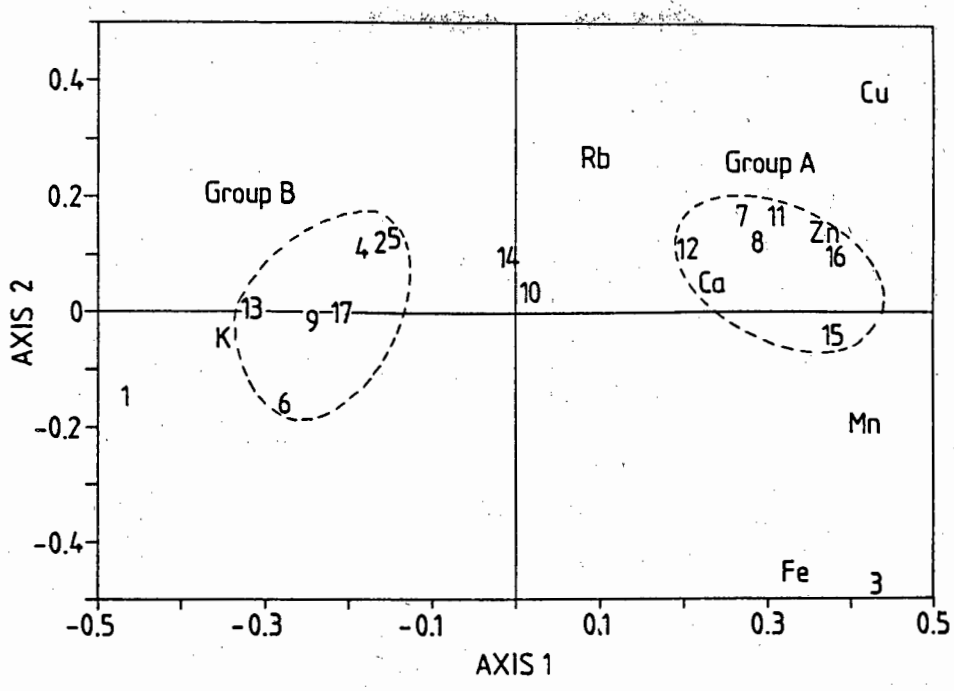

Figure 4.7: *Plot of the first two axes of the correspondence analysis of the data for 7 elements determined in wood specimens. The representative points of the samples are plotted as numbers (see Table 4.9) and those of the chemical elements by their symbols. Note the proximity of Ca to Group A and K to Group B.*

of the samples in this group is 53.2% higher than the corresponding mean value of Group B, whereas in the case of potassium, the mean value for Group B is 98.1% higher than that of Group A. It may be noted that the two intermediate samples, 10 and 14 have relatively high contents of both calcium and potassium. Of the two outliers, sample 1 has a high potassium content, and its representative point lies near that of K, while sample 3 has high content of manganese and iron, and its point lies near to both Mn and Fe. Most of the representative points separate into two groups, the contents of which are listed in Table 4.9 It is noted that Group A consists entirely from Pinus-type wood from Zululand, while Group B contains all Eucalyptus-type woods, as well as one Acacia-type. The intermediate samples are both Pinus-type while one outlier is Pinus and the other, Acacia. The strength of the correspondence analysis classification lies in the fact that, although only elemental contents were used in the calculation, the strong regional correlation is emphasized. Such correlation was not obvious from the analytical data shown in Table 4.8. If it is indeed the trace element composition in the wood which is responsible for the

Table 4.9: *Grouping of wood specimens from correspondence analysis.*

Sample	Wood type	Origin
Group A		
7	Pinus Idesiya	Zululand
8	Pinus Taeda	Zululand
11	Pinus Patula	Zululand
12	Pinus Laxibaea	Zululand
15	Pinus Elliottii	Zululand
16	Pinus Pseudostrobus	Zululand
Group B		
2	Eucalyptus Grandus 209/6	Tzaneen
4	Eucalyptus Grandus 11/3	Tzaneen
5	Eucalyptus Grandus 213/2	Tzaneen
6	Acacia Decurrens Wattle	Greytown
9	Eucalyptus Macarthuxia	Ixopo
13	Eucalyptus Grandus 37/7	Tzaneen
17	Eucalyptus Grandus 35/3	Tzaneen
Intermediates		
10	Pinus Elliottii	Dukuduku
14	Pinus Patula	Tecurmani
Outliers		
1	Acacia Dealbata Wattle	Greytown
3	Pinus Taeda	Renosterhoek

quality and the properties of the paper made from that wood, then the above results indicate that:

1. paper made from the wood from one variety of tree in a group, should have the same properties as paper made from any other variety of tree in the same group.

2. paper made from the wood from one variety of tree in a group should have different properties when compared to paper made from a variety of tree belonging to another group.

3. if one variety of wood is used to produce a paper with required properties, then another variety from the same group can be used as a substitute without affecting the properties of the paper.

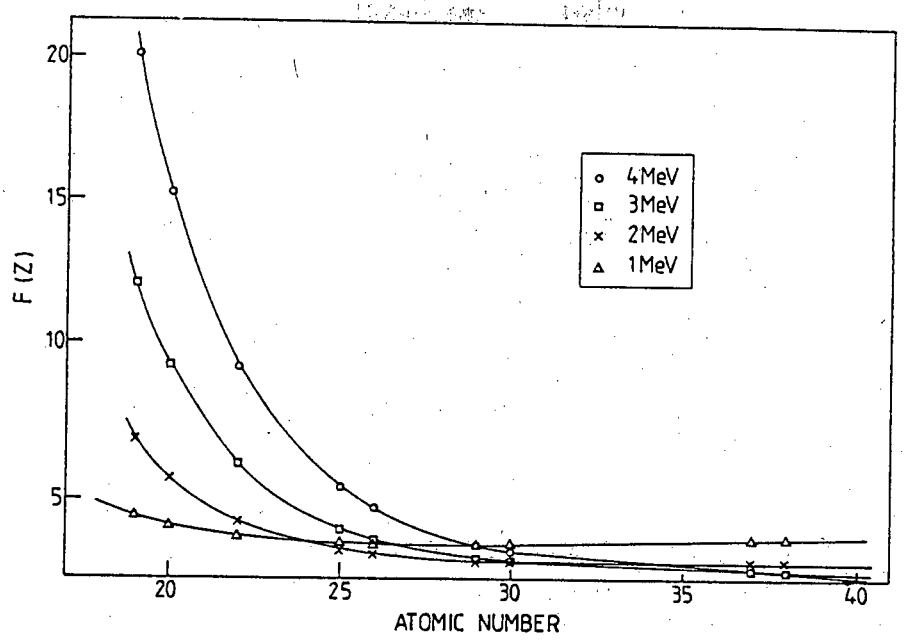

Figure 4.8: *Variation of the $F(Z)$-values with the K_α energy for the bombardment of silicon-rich materials with protons between 1 and 4 MeV.*

4.2.2 Silicon-rich materials

In a similar manner as for carbon-rich materials in section 4.2.1, the evaluation of MCF for silicon-rich materials (examples of which are most archaeological artefacts) can be applied. The $F(Z)$-values of silicon-rich materials with elements $Z \leq 19$ were found to be relatively constant over a wide range of samples of different origin and a wide range of proton beam bombarding energies (see Figure 4.8). Thus a universal set of $F(Z)$-values for matrix correction in silicon-rich materials could also be established. A set of environmental standards with known matrix composition listed in Table 4.10 was used as reference for the evaluation of these MCF. The computation used program RD1 (see Appendix B), and $F(Z)$-values are shown in Table 4.11.

It was found that the relative standard deviation of $F(Z)$-values (given in parentheses in Table 4.11), for a wide range of elements from K to Ba, was relatively small and decreased with increasing atomic number. The highest value ($\sim$ 10%) was that for the group of elements with $19 \leq Z \leq 32$ at the proton energy of 4 MeV. The lowest (0.1%) occurred for elements with $46 \leq Z \leq 56$ irradiated with 1 MeV protons.

Table 4.10: *Identification of silicon-rich standard reference materials.*

Name of standard	Laboratory code	Supplier
Feldspar	SRM-70a	NIST[a)]
Flint clay	SRM-97a	NIST
Basalt rock	SRM-688	NIST
River sediment	SRM-1645	NIST
Estuarine sediment	SRM-1646	NIST
Fly ash	SRM-1633a	NIST

[a)] US National Institute for Standards and Technology.

Plots of these MCF-values against proton energies showed a similar trend (see Figure 4.9). Since for analysis these values have to be calculated for the particular proton energy selected for measurement, the evaluation of intermediate mean $F(Z)$-values showed that there were no irregularities or discontinuities in these curves. It was thought that as in the case for carbon-rich materials, fitted polynomials to these curves could be of some use for interpolation at intermediate proton energies in the range of 1 to 4 MeV. Polynomial coefficients of mean $F(Z)$-values curves fitted for 1, 2, 3 and 4 MeV protons for silicon-rich materials are given in Table 4.12. According to the methodology described here, the $F(Z)$-values alone could not give the analyst the complete information necessary for analytical work. Additional information about the sensitivity factor $K(Z)$ evaluated for a particular experimental geometry as discussed in Chapter 1, and the depth of analysis would be of value for the calculation of elemental concentrations. Table 4.13 present values for 3 MeV protons for these parameters cited above.

Application in geochemistry

A common problem encountered in the simultaneous determination of adjacent elements by nuclear analytical methods is that of interference. Much of the research covered in this area has been by neutron activation analysis (NAA) [De 72]. The occurrence of primary interfering reactions in samples under neutron irradiation affects the accuracy of determining adjacent elements and hence this technique is not

Table 4.11: *Mean calculated $F(Z)$-values and relative standard deviation [%] for Si-rich geological materials.*

Element	Z	Incident proton energy [MeV]			
		1.0	2.0	3.0	4.0
K	19	4.46(1.6)	6.91(3.2)	11.84(3.7)	19.06(5.1)
Ca	20	4.15(1.7)	5.69(4.0)	9.27(4.9)	14.7(6.7)
Ti	22	3.80(1.8)	4.28(5.1)	6.14(7.4)	9.24(8.9)
Mn	25	3.63(1.5)	3.40(4.9)	4.06(8.4)	5.43(11.0)
Fe	26	3.61(1.3)	3.26(4.6)	3.71(8.2)	4.75(11.1)
Co	27	3.60(1.3)	3.16(4.2)	3.59(7.6)	3.34(10.5)
Ni	28	3.61(1.1)	3.09(3.8)	3.40(7.2)	3.12(10.2)
Cu	29	3.61(1.0)	3.05(3.5)	3.13(6.7)	3.58(9.9)
Zn	30	3.63(0.9)	3.02(3.2)	3.03(6.0)	3.37(9.3)
Ga	31	3.64(0.8)	3.00(2.9)	3.07(5.5)	2.77(9.0)
Ge	32	3.66(0.7)	2.99(2.6)	3.02(5.0)	2.71(8.8)
Rb	37	3.77(0.3)	3.02(1.5)	2.83(3.0)	2.80(4.5)
Sr	38	3.80(0.4)	3.03(1.4)	2.81(2.7)	2.78(4.1)
Y	39	3.82(0.3)	3.04(1.3)	2.92(2.5)	2.63(3.3)
Zr	40	3.84(0.3)	3.06(1.1)	2.93(2.2)	2.64(2.8)
Nb	41	3.87(0.2)	3.07(1.0)	2.93(2.0)	2.65(2.5)
Mo	42	3.89(0.2)	3.08(0.9)	2.94(1.9)	2.66(2.1)
Ru	44	3.94(0.2)	3.11(0.8)	2.97(1.5)	2.69(1.6)
Rh	45	3.97(0.2)	3.13(0.7)	2.97(1.4)	2.71(1.4)
Pd	46	3.99(0.1)	3.14(0.7)	2.98(1.3)	2.72(1.2)
Ag	47	4.02(0.2)	3.16(0.6)	3.00(1.2)	2.73(1.1)
Cd	48	4.04(0.1)	3.17(0.6)	3.01(1.1)	2.75(1.0)
In	49	4.07(0.1)	3.18(0.5)	3.02(1.0)	2.76(0.8)
Sn	50	4.10(0.1)	3.20(0.5)	3.03(0.9)	2.78(0.8)
Sb	51	4.12(0.1)	3.21(0.5)	3.04(0.8)	2.79(0.7)
Te	52	4.15(0.1)	3.22(0.4)	3.05(0.7)	2.80(0.6)
I	53	4.18(0.1)	3.24(0.4)	3.06(0.7)	2.81(0.5)
Cs	55	4.24(0.1)	3.26(0.4)	3.08(0.6)	2.84(0.4)
Ba	56	4.27(0.1)	3.27(0.3)	3.09(0.6)	2.85(0.4)

Table 4.12: *Polynomial coefficients (order 3) of mean $F(Z)$-values of Si-rich materials fitted for the proton energy region between 0.5 and 4.5 MeV.*

Element	a(0)	a(1)	a(2)	a(3)
K	+4.68	-1.618	+1.430	-0.033
Ca	+4.84	-1.868	+1.210	-0.031
Ti	+4.84	-1.847	+0.830	-0.023
Mn	+4.93	-1.895	+0.625	-0.030
Fe	+4.97	-1.935	+0.610	-0.035
Co	+5.55	-2.918	+1.075	-0.106
Ni	+5.68	-3.085	+1.135	-0.120
Cu	+5.08	-2.015	+0.590	-0.045
Zn	+5.15	-2.072	+0.600	-0.048
Ge	+5.64	-2.838	+0.960	-0.101
Rb	+5.48	-2.323	+0.680	-0.066
Sr	+5.48	-2.255	+0.635	-0.060
Y	+6.09	-3.292	+1.160	-0.138
Zr	+5.90	-2.910	+0.955	-0.105
Nb	+5.92	-2.872	+0.920	-0.098
Mo	+6.00	-2.970	+0.965	-0.105
Ru	+6.18	-3.185	+1.065	-0.120
Rh	+6.17	-3.106	+1.020	-0.113
Pd	+6.19	-3.095	+1.005	-0.110
Ag	+6.28	-3.193	+1.050	-0.116
Cd	+6.23	-3.053	+0.965	-0.101
In	+6.35	-3.195	+1.025	-0.110
Sn	+6.42	-3.260	+1.055	-0.115
Sb	+6.47	-3.303	+1.070	-0.116
Te	+6.49	-3.262	+1.030	-0.108
I	+6.54	-3.290	+1.040	-0.110
Cs	+6.74	-3.500	+1.120	-0.120
Ba	+6.72	-3.475	+1.115	-0.120

Table 4.13: *Relevant information of TTPIXE parameters for the analysis in silicon-rich materials.*

Element	Z	K_{α_1} (keV)	$F(Z)$	$K(Z)^{(*)}$	p (mg/cm^2)	Mass$^{(**)}$ (μg)
K	19	3.313	11.84	108	6.64	209
Ca	20	3.691	9.27	216	7.72	242
Sc	21	4.090	7.02	364	8.46	266
Ti	22	4.510	6.14	519	9.76	306
V	23	4.952	5.30	672	10.35	325
Cr	24	5.414	4.67	784	11.33	356
Mn	25	5.898	4.06	792	11.92	374
Fe	26	6.403	3.71	716	12.36	388
Co	27	6.930	3.59	636	12.87	404
Ni	28	7.477	3.40	562	13.06	410
Cu	29	8.047	3.13	484	13.26	417
Zn	30	8.638	3.03	412	13.40	421
Ga	31	9.251	3.07	355	13.52	425
Ge	32	9.885	3.02	264	13.66	429
As	33	10.543	2.99	196	13.70	430
Se	34	11.221	2.91	132	13.71	431
Br	35	11.923	2.87	115	13.72	431
Rb	37	13.394	2.83	76	13.73	431
Sr	38	14.164	2.81	64	13.73	431
Y	39	14.957	2.92	58	13.73	431
Zr	40	15.774	2.93	53	13.73	431
Nb	41	16.614	2.93	48	13.73	431
Mo	42	17.478	2.94	48	13.73	431

$^{(*)}$ in Count/μC/μg/cm^2.

$^{(**)}$ Mean value assuming a 2mm diameter beam spot on target. No beam spread was considered.

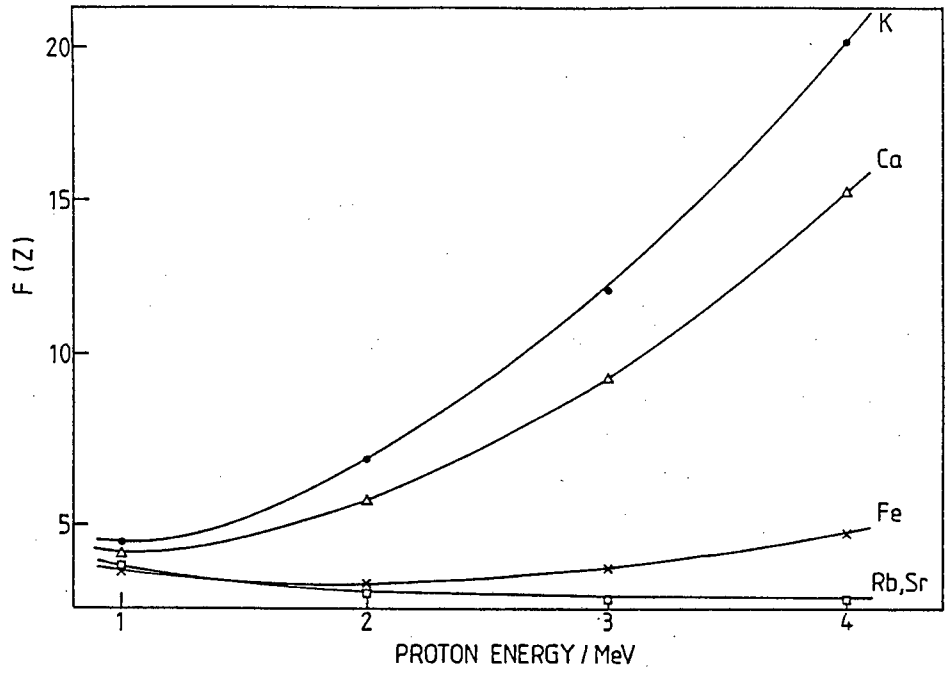

Figure 4.9: *Variation of $F(Z)$-values with proton energy for silicon-rich geological materials.*

well-suited for such analyses. The fact that an (n, p) reaction on element (Z+1) or an (n,α) reaction on element (Z+2) produces the same product as an (n,γ) reaction on element Z shows that the presence of elements (Z+1) and/or (Z+2) interferes with the determination of elements Z. This state of affairs is commonly encountered in the analysis of geological materials which frequently contain the range of elements Mg, Al, Si, P and S. Specifically, in the case of determining Al/Si ratios by NAA, where the yields of the nuclides ^{28}Al and ^{31}Si are measured, serious interference may be expected for the neutron-induced reactions ^{28}Si(n,p)^{28}Al, ^{31}P(n, α)^{28}Al, ^{31}P(n,p)^{31}Si and ^{35}S(n, αp)^{31}Si. For routine accurate analyses, therefore, a suitable alternative technique may be sought. In the cases of zeolites (a term which includes a host of crystalline ores all of which possess a framework of aluminosilicate structures from corner-sharing tetrahedra of SiO_4^{4-} and Al_4^{5-} [Hu 85]) the determination of Al/Si ratios becomes a matter of importance. It has been shown [Ja 77] that variation of this ratio has important consequences for the properties of zeolites. Thus, for example, the catalytic behaviour of zeolites in the isomerisation of hydrocarbons [Yo 82], is affected by the Al/Si ratio. In addition to zeolites, aluminium and silicon occur as major components in many geological materials as was shown previously in this

Table 4.14: *Some empirical formulae of zeolites and geological ores; atomic ratios are expressed relative to oxygen taken as 1000.*

Sample	C	(Al+Si)	S	(K+Ca)	Fe
Mobil zeolite	-	484	9.79	-	0.394
Union Carbide zeolite	-	561	483	-	-
Zululand zeolite	-	481	19.2	38.2	6.82
Quartzite	1670	384	36.4	-	2.13
Shale	-	308	-	-	149
Kaolinite	-	474	7.56	6.50	1.15
Granite	8620	465	186	33.2	34.3

Chapter. Thus the main thrust of the present application involved the development of a suitable analytical procedure, based on the common matrix type methodology presented in this work, for the rapid and accurate determination of Al/Si ratios in thick samples of zeolites and geological materials.

Samples submitted for analysis consisted of geological ores, roughly smoothed to provide a surface for ion beam analysis. Zeolite specimens were obtained from Zululand. Synthetic zeolites were obtained from Mobil and from Union Carbide. (See description in Table 4.14). In order to be able to deduce the approximate matrix composition for stopping power calculations [Gi 77], backscatter analysis was performed on the samples with approximately 50 nA of 2 MeV $^4He^+$ beams. PIXE was carried out with low currents (0.3 - 2.0 nA) of 1 MeV protons.

Experimental backscatter spectra were numerically differentiated [Pe 73] using a running interval of 15 keV across the spectrum. This interval was comparable with the resolution of the detector. A typical differential spectrum is shown in Figure 4.10. From the minima of the peaks, the exact energy of the inflexion points in the experimental spectra were obtained and the elements identified. Empirical formulae of the matrices were deduced [Gi 77] from the step heights in the measured spectra. Some examples of matrix formulae are presented in Table 4.14. Since Al and Si, as well as K and Ca, cannot be resolved by backscatter analysis, the values for these

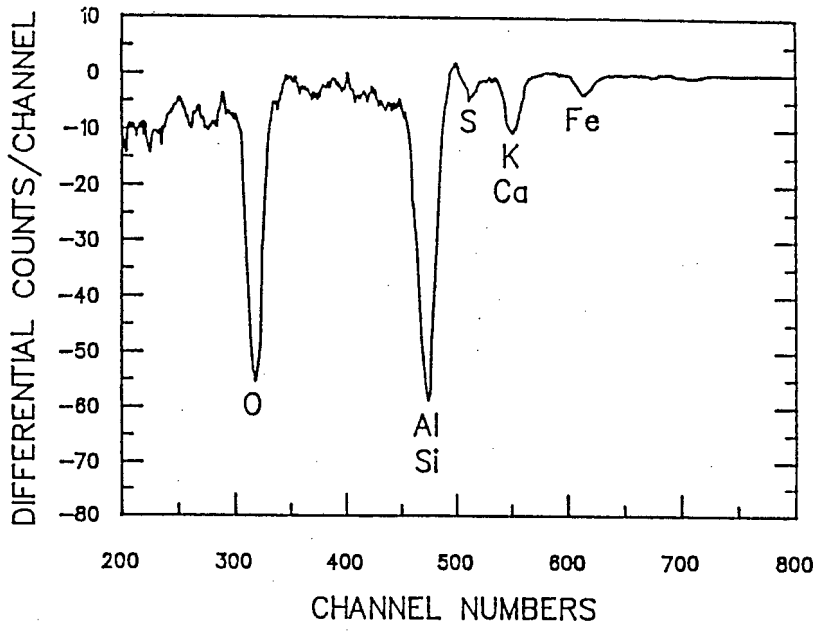

Figure 4.10: *Differentiated backscatter spectrum of Zululand zeolite to establish accurate identification of matrix component elements.*

pairs were considered as a unit. Such treatment is justified because of the small differences in atomic mass.

The relative value of the atom ratio Al:Si is given by

$$\frac{[Al]}{[Si]}_{atoms} = \frac{Y_{Al}}{Y_{Si}} \frac{\sigma_{Si}}{\sigma_{Al}} \frac{F_{Al}}{F_{Si}} f_{abs} \tag{4.4}$$

where f_{abs} is the ratio of absorption factors for Al and Si in absorbers interposed between the detector and the sample.

Range corrections

From empirical formulae, ranges of 1 MeV protons in the matrix were calculated according to the method of Ziegler et al. [Zi 85]. Some typical results are listed in column 4 of Table 4.15. The ranges in zeolites are relatively constant, despite the changes in the Al/Si ratio. Clay-type ores such as shale and kaolinite also show similar ranges, but slightly different values were obtained for granite and quartzite. The mean value for the proton range was 3.40±0.10 mg/cm^2 for the whole range of materials with a relative precision of 2.9%. Preliminary values for the $F(Z)$-values were obtained by using the matrix empirical formulae. Thereafter the calculation

Table 4.15: *PIXE analysis of zeolites and ores.*

Sample	Raw counts		Proton	$F(Z)$		$\frac{F(Al)}{F(Si)}$	Si/Al
	Si	Al	range [mg/cm^{-2}]	Si	Al		atoms
Alumina	414	175225	3.34	8.12	10.9	1.34	0.004
Mobil zeolite	135818	2452	3.32	8.80	11.7	1.33	95.4
Union Carbide zeolite	78369	24295	3.34	8.90	11.9	1.34	5.5
Zululand zeolite	79495	11548	3.38	8.90	11.7	1.31	11.6
Quartzite	56127	4209	3.10	6.50	8.50	1.31	22.3
Shale	24027	3113	3.56	9.00	11.50	1.28	12.6
Kaolinite	27662	9945	3.55	9.30	12.40	1.33	4.8
Granite	32475	12857	2.90	5.10	6.30	1.24	4.0

was reiterated using the results of the first approximation with a new calculated value for the oxygen content, and, by difference, a new value for carbon was obtained. In all cases a second iteration showed that the values had already converged to within an acceptably small margin and that, in essence, no second iteration was needed. While the matrix correction factors $F(Z)$ for both Al and Si differed appreciably from sample to sample, their ratio, which is used in equation 4.5, has a mean value of 1.31 ± 0.035 with a relative precision of 2.6%. The mean value of $F(Z)/F(Si)$ can thus be applied to all zeolites and siliceous materials with confidence for irradiations using 1 MeV protons.

Silicon/aluminium ratios

Examples of determined atomic ratios Si:Al are given in column 8 of Table 4.15. In the cases of zeolites, the values were confirmed by X-ray fluorescence analysis [Pe 92a] and are in agreement with the data available for synthetic samples. From the above discussions it can be concluded that:

1. TTPIXE offers an interference-free method for routinely determining Si/Al atomic ratios in thick targets rapidly and nondestructively.

2. Matrix correction factors calculated from empirical formulae deduced from backscatter data converged rapidly and hence required only one iteration.

Table 4.16: *Major components in NBS portland cements 633-639 (concentrations in %.*

	633	634	635	636	637	638	639
Oxygen	36.2	37.1	39.1	37.0	37.2	36.8	35.5
Silicon	10.1	9.6	8.6	10.8	10.7	9.9	10.0
Calcium	46.1	44.7	42.7	45.4	47.2	44.3	46.9

3. Absolute calculation of ratios is achieved without reference to standards.

4. A single calculation of $F(Z)$-values is sufficient to meet the needs for all siliceous sample materials.

4.2.3 Calcium-rich materials

There are numerous examples of calcium-rich materials in geology and biology such as cement and certain human kidney stones. Cements are Ca-rich materials with contents of silicon and calcium being in the region of 10% and 40-50% respectively. Compared to Si-rich materials like estuarine sediment and flint clay in which the Si,Al content is between 40-50%. Bone and certain types of kidney stones are organic materials comparable to chlorella, but with the concentrations of phosphorus and calcium around 10% and 20% respectively. A set of Portland cements standard reference materials NBS 633-639 were used to evaluate the MCF factors in Ca-rich materials over the proton energy range of between 1 and 4 MeV. Table 4.16 presents the concentration of the major components, oxygen, silicon and calcium in this set of cements. The percentage concentration of these components which account for about 92% of the whole matrix is very similar in all cements. The difference (~8%) is made up of Na, Mg, Al, P, S, K, Ti, Cr, Mn, Fe, Zn and Sr with concentration levels ranging from 0.0068% for Cr to 3.281% for Al. Although the Si content is still relatively high (~10%) the major component is calcium. The average content of oxygen (~36%) did not play a major role here due to the fact that the oxygen X-ray lines cannot excite other X-rays of heavier elements. Since the relative standard

Table 4.17: *Mean $F(Z)$-values and relative standard deviation (%) for calcium-rich materials.*

Element	Z	Incident proton energy [MeV]			
		1.0	2.0	3.0	4.0
K	19	5.11 (0.3)	8.85 (0.5)	15.85 (0.6)	24.78 (0.7)
Ca	20	4.67 (0.3)	7.25 (0.5)	12.56 (0.7)	19.39 (0.6)
Sc	21	4.36 (0.3)	6.11 (0.5)	10.16 (0.7)	15.41 (0.6)
Ti	22	4.15 (0.2)	5.29 (0.5)	8.39 (0.7)	12.44 (0.7)
V	23	4.00 (0.2)	4.70 (0.5)	7.07 (0.8)	10.21 (0.7)
Cr	24	3.90 (0.2)	4.26 (0.5)	6.09 (0.8)	8.52 (0.8)
Mn	25	3.83 (0.2)	3.95 (0.4)	5.35 (0.7)	7.24 (0.8)
Fe	26	3.78 (0.2)	3.72 (0.4)	4.80 (0.7)	6.25 (0.8)
Co	27	3.74 (0.2)	3.55 (0.3)	4.38 (0.7)	5.49 (0.8)
Ni	28	3.73 (0.1)	3.42 (0.3)	4.06 (0.6)	4.91 (0.8)
Cu	29	3.72 (0.1)	3.33 (0.3)	3.81 (0.6)	4.46 (0.7)
Zn	30	3.72 (0.1)	3.26 (0.3)	3.62 (0.5)	4.10 (0.7)
Ga	31	3.73 (0.1)	3.21 (0.3)	3.48 (0.5)	3.83 (0.6)
Ge	32	3.74 (0.1)	3.18 (0.2)	3.37 (0.4)	3.62 (0.6)
As	33	3.75 (0.1)	3.15 (0.2)	3.29 (0.4)	3.45 (0.5)
Se	34	3.77 (0.1)	3.13 (0.2)	3.22 (0.4)	3.32 (0.5)
Br	35	3.79 (0.1)	3.12 (0.2)	3.17 (0.3)	3.22 (0.5)
Rb	37	3.82 (0.05)	3.12 (0.1)	3.11 (0.3)	3.07 (0.4)
Sr	38	3.84 (0.05)	3.12 (0.2)	3.09 (0.3)	3.02 (0.3)
Y	39	3.86 (0.05)	3.13 (0.1)	3.08 (0.2)	2.98 (0.3)

deviation of the evaluation of $F(Z)$-values in cements resulted in very small values, as was the case for carbon and silicon-rich materials, a universal table of MCF for calcium-rich materials was calculated. Table 4.17 gives a list of the mean universal $F(Z)$-values. As observed in Table 4.17, although the standard deviation of analysis is very small, there is still a serious problem in analysing calcium-rich materials. That is, the high intensity Kα signal produces pile-up and sum peaks of first, second and third order in the energy spectrum. To overcome this problem a thick absorber of plastic or aluminium must be interposed between the detector window and the target surface to reduce the intensity of the calcium Kα signal as much as possible. In doing so, the X-rays of all elements with $19 \leq Z$ will also be absorbed. Another disadvantage is that elements below calcium will be impossible to analyse by PIXE. In a manner similar to the case for silicon-rich materials, a polynomial fitting of these $F(Z)$-values for Ca-rich materials is presented in Table 4.18. An application of the

Table 4.18: *Polynomial coefficients (order 3) of mean $F(Z)$-values for Ca-rich materials fitted for the proton energy region between 0.5 and 4.5 MeV.*

Element	a(0)	a(1)	a(2)	a(3)
K	+5.96	-3.588	+2.960	-0.221
Ca	+6.03	-3.733	+2.575	-0.201
Sc	+6.01	-3.717	+2.250	-0.183
Ti	+5.98	-3.652	+1.990	-0.168
V	+5.87	-3.455	+1.735	-0.150
Cr	+5.88	-3.440	+1.605	-0.145
Mn	+5.78	-3.248	+1.430	-0.131
Fe	+5.75	-3.182	+1.340	-0.134
Co	+5.69	-3.077	+1.250	-0.123
Ni	+5.73	-3.092	+1.215	-0.123
Cu	+5.68	-2.978	+1.135	-0.116
Ga	+5.75	-3.007	+1.105	-0.118
Ge	+5.74	-2.950	+1.065	-0.115
As	+5.81	-3.030	+1.090	-0.120
Se	+5.86	-3.055	+1.085	-0.120
Br	+5.90	-3.070	+1.080	-0.120
Rb	+5.93	-3.055	+1.065	-0.120
Sr	+5.98	-3.093	+1.075	-0.121
Y	+6.00	-3.088	+1.070	-0.122

methodology for Ca-rich materials will be described in Chapter 6 for the analysis of human kidney stones using the microprobe beam at NAC.

4.2.4 Iron-rich materials

For the case of iron-rich materials a similar methodology could be applied, but secondary effects due to X-ray fluorescence generated by the K lines of Fe on elements below its absorption edge become very important. This is the case of steel alloys. To determine more closely the variation of the physical parameters (proton range, depth of analysis, absorption of X-rays and $F(Z)$-values) involved in the calculation of matrix correction factors in this type of materials, the NBS-D837 steel reference material was taken as a case study. Its composition is given in Table 4.19.

Tables 4.20 and 4.21 show the results of the analysis at 4 and 1 MeV protons particularly when vanadium is determined. For the case of 4 MeV protons the depth of analysis ($\sim$25 mg/cm^2) was reached at the point when the proton energy inside the steel was 2.4 MeV, although the total range of the protons in the steel is 44.82

Table 4.19: *Calculation of $F(Z)$-values for the standard reference steel alloy NBS-D837.*

Matrix	Z	Amount (%)	K_α keV	$F(Z)$-values 1 MeV	4 MeV
C	6	0.70	0.28	–	–
Si	14	0.53	1.74	12.90	95.97
V	23	3.04	4.95	5.35	20.58
Cr	24	7.79	5.41	5.15	18.20
Mn	25	0.48	5.90	4.99	16.20
Fe	26	79.7	6.40	4.87	14.52
Co	27	2.9	6.93	4.76	13.10
Mo	42	1.5	17.48	4.38	5.14
W	74	2.8	59.31	–	3.42
Proton range (mg/cm^2)				5.37	44.82

mg/cm^2. Only 1/1000 of the X-ray yield excited at this particular energy is seen by the detector. This means that no contribution to the total X-ray yield is obtained after the proton energy have reached 2.4 MeV. The $I(Z)$ converged rapidly to the value 0.049145 and the absorption of X-rays by the matrix decreased rapidly, proportionally to $\exp^{-\mu x}$. When the proton energy reached 3.5 MeV the transmission was already down to ~2% for vanadium. This is a serious drawback of using PIXE in thick Fe-rich materials with 4 MeV protons. The evaluation of $F(Z)$-values presented in Table 4.19 for 1 MeV shows a much smaller value due to the fact that the range is only 5.37 mg/cm^2, i.e. 12% of that for 4 MeV irradiations. For elements like Co, Mo and W the secondary fluorescence effect does not play a role but the $F(Z)$-values are still high for both 1 and 4 MeV.

For the case of 1 MeV the depth of analysis (2.094 mg/cm^2) was reached at the point when the proton energy inside the steel sample was 705 keV. The $I(Z)$ converged rapidly to the value 0.18682. Contrary to the case of 4 MeV the transmission of X-rays did not converge rapidly. At the step when the proton energy was 450 keV there was still 20% transmission. Since the X-ray yield, at equal concentrations, is a smoothly varying function of the atomic number, the determination of vanadium and chromium in the steel D837 is aggravated by the overwhelming yield of iron X-rays from the predominently iron matrix (see Table 4.19). It has been shown [Gi

Table 4.20: *Calculated proton energy loss, MCF's, depth of analysis p, ionisation cross sections and transmission of X-rays in a thick target of steel reference material NBS-D837 irradiated with protons of 4 MeV. Case study for vanadium (Z=23).*

Proton energy (keV)	$I(Z)$ (x10^{-2})	Depth of analysis (mg/cm^2)	$\sigma_z(E)$ (barns)	X-ray transmission (%)
4000	0.3919	0.000	1614	100.00
3900	2.9311	1.819	1577	44.92
3800	4.0337	3.605	1539	20.46
3700	4.5185	5.361	1500	9.45
3600	4.7343	7.084	1459	4.43
3500	4.8315	8.775	1418	2.10
3400	4.8758	10.430	1375	1.01
3300	4.8963	12.060	1332	0.50
3200	4.9058	13.650	1287	0.25
3100	4.9103	15.210	1241	0.12
3000	4.9125	16.740	1194	0.06
2900	4.9135	18.230	1146	0.03
2800	4.9140	19.690	1096	0.02
2700	4.9143	21.120	1046	0.01
2600	4.9144	22.510	994	0.00
2500	4.9145	23.870	942	0.00
2400	4.9145	25.190	889	0.00
2300	4.9145	26.480	835	0.00
2200	4.9145	27.730	780	0.00
2100	4.9145	28.950	725	0.00
2000	4.9145	30.130	669	0.00

Table 4.21: *Same as for Table 4.20 but for 1 MeV protons.*

Proton energy (keV)	$I(Z)$ (x10^{-2})	Depth of analysis (mg/cm^2)	$\sigma_z(E)$ (barns)	X-ray transmission (%)
1000	0.10	0.00	160.20	100.00
950	6.30	0.38	141.40	84.51
900	10.70	0.75	122.50	71.76
850	13.90	1.12	105.00	61.24
800	16.10	1.46	89.43	52.53
750	17.70	1.80	74.78	45.29
700	18.80	2.12	61.44	39.26
650	19.50	2.44	50.14	34.22
600	20.00	2.74	38.88	29.99
550	20.30	3.02	30.38	26.45
500	20.50	3.30	21.90	23.46
450	20.60	3.55	15.50	20.94
400	20.79	3.79	10.35	18.82
350	20.80	4.03	6.48	17.02
300	20.81	4.24	3.65	15.50
250	20.81	4.44	1.81	14.21
200	20.81	4.62	0.71	13.10
150	20.81	4.80	0.20	12.13
100	20.81	4.97	0.02	11.25
50	20.81	5.15	0.01	10.37

80] that under such conditions the precision of the results for elements lying closely below iron, is appreciably worsened. Because the absorption edges of vanadium and chromium occur at energies below the absorption edge of Fe, it is expected that such uncertainty in the precision is due to secondary excitation of these elements by iron. Relatively high yields of chromium may be expected since the yield of fluorescent X-rays, increases with decreasing difference between the energies of the exciting Fe radiation and the absorption edge of excited elements as shown in Figure 4.11 for the K_α and K_β contributions. The shape of the curves is materially affected by the presence of the absorber in front of the detector which attenuated X-rays of lower energy to a larger extent. The low yield of manganese X-rays is due to the fact that the K-absorption edge of manganese is 6.537 keV. This energy lies above that of the high flux iron K_α X-rays of 6.403 and 6.390 keV, but below the K_β X-ray of 7.057 keV. Accordingly, excitation of manganese X-rays is caused only by the Fe K_β radiation, the intensity of which is only some 15% of that of the Fe K_α, and hence

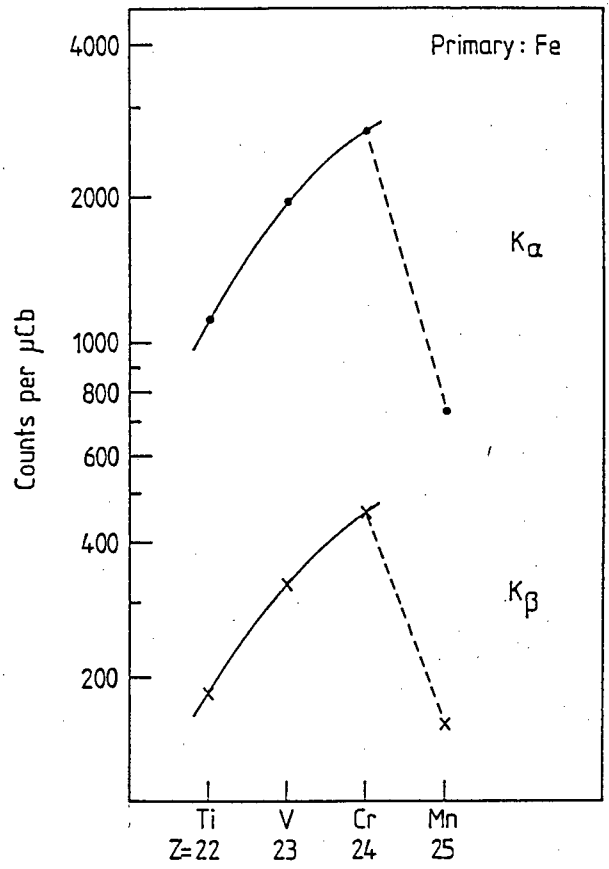

Figure 4.11: *The variation of the secondary X-ray yield with atomic number, of the elements excited by iron X-rays.*

the yield is proportionally lower. To overcome this problem it would be required to decrease or suppress the generation of iron X-rays.

To investigate the first alternative (decrease), PIXE analysis was carried out on the D837 steel alloy with irradiations at 1 and 4 MeV. Irradiations with 4 MeV showed a marked increase in the "true" X-ray yield for vanadium and chromium while the determination of Mo and W was more accurate. Analysis of Fe-rich materials such as steel alloys are more suitably performed with irradiation with low energy protons, although the sensitivity of analysis is not as good as with 4 MeV irradiations for heavier elements such as Mo and W. The sensitivity factor calculated for both 1 and 4 MeV showed a better accuracy for the case with 1 MeV protons. The second alternative (suppress), can be succesfully be achieved by PIXE-induced X-ray fluorescence analysis (XSQR) using an Fe primary target (see Figure 4.12). Although, this technique is a good choice for the determination of minor and trace metals in Fe-rich materials we have to be aware of the type of interferences that occur for adjacent elements such as V, Cr, Mn and Fe and the coherent Fe scatter, as well as the matrix corrections involved for this technique. It is not the purpose of this work

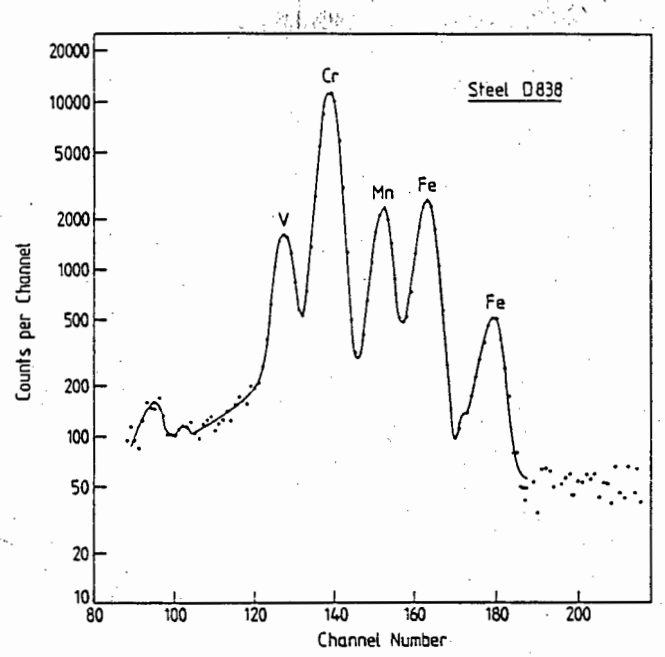

Figure 4.12: *PIXE-induced X-ray spectrum from the standard steel D838, using an iron primary target.*

to examine in detail the results of analysis obtained by XSQR. These details have been already reported elsewhere [Gi 82].

4.2.5 Gold-rich materials

Impurities may be introduced into fabricated gold objects either incidentally, as a result of the manufacturing process, or intentionally, in order to debase the gold content of the object or to produce alloys with properties to suit a particular purpose. Such objects are seldom available for destructive analysis, so that the choice of method for determining impurities is limited.

The analysis of Au-rich materials by PIXE has the disadvantage that the high intensity Au L X-rays blanketed the energy region from about 9 to 15 keV. In addition, the high count rate from Au made it difficult to measure X-rays in the lower energy range where the K X-rays of the metals of the first transition series are found. Furthermore, gold interfered with the determination of possible impurities of the rare noble metals Ru, Rh and Pd as well as with the common impurities such as Ag and Sn. Because these metals have lower cross sections for X-ray excitation it would be necessary to use bombarding proton beams of higher energy and higher currents.

Table 4.22: *Interference-free sensitivities of PIXE-induced X-ray fluorescence with a germanium primary target.*

Element	K_α X-ray energy (keV)	Sensitivity (μg/g)
Ti	4.510	5.02
V	4.952	2.65
Cr	5.414	1.76
Mn	5.898	1.14
Fe	6.403	0.73
Co	6.930	0.86
Ni	7.477	0.56
Cu	8.047	0.55
Zn	8.638	0.53
Ga	9.251	2.04

Under such conditions random coincident X-rays from gold would form sum peaks in the energy spectrum over the region of 20 to 30 keV, thereby making it impossible to measure the K X-rays of the heavy metals which lie in the same region. On the other hand the $F(Z)$-values, even for elements with high Z value, are extremely high, increasing the uncertainty of MCF evaluation.

Hence, as was the case with Fe-rich materials, the technique of choice was XSQR, where calculation of MCF is of a different nature. Interference-free sensitivities from measured XSQR yields from compounds of known composition and using a germanium primary target are given in Table 4.22. The expected deterioration of sensitivity was observed with the increase in the energy difference between the energy of the exciting X-rays and that of the absorption edge of the target material. The sudden deterioration in going from Zn(Z=30) to Ga(Z=31) is due to the fact that only the K_β X-rays of germanium have sufficient energy to excite Ga K X-rays. The energy spectra of fluorescence X-rays obtained from a sample of tooth alloy (upper curve) and of a standard gold disc are shown in Figure 4.13. The tooth alloy contained a high concentration of Cu, some Zn and traces of Fe, while the standard showed the presence of traces of Fe and Zn. The high intensity peaks were due to Ge K_α and K_β X-rays that were scattered into the detector from the primary target by elastic and inelastic scatter processes.

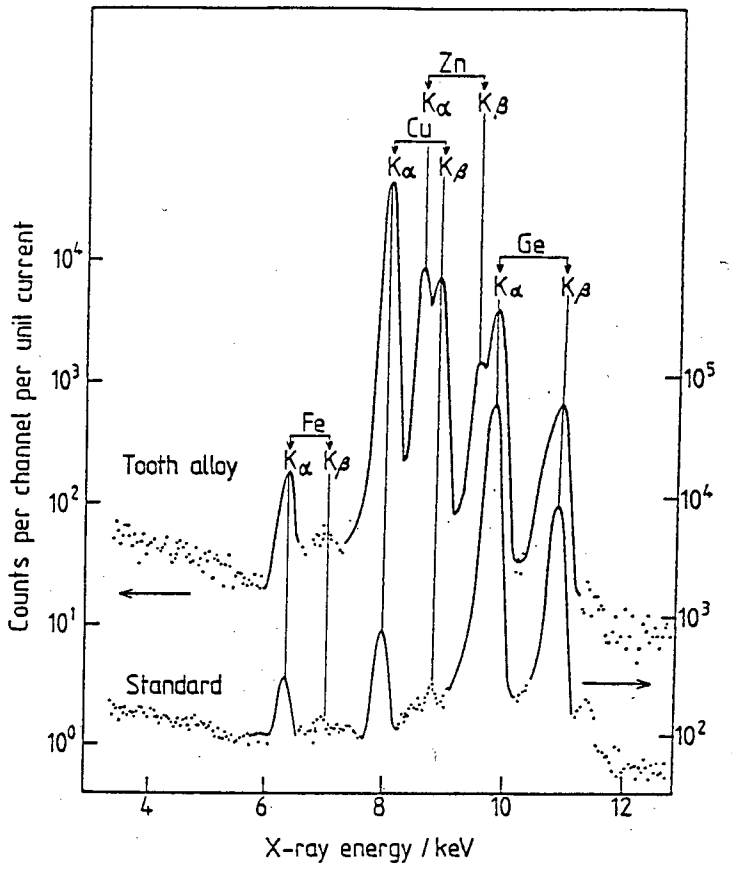

Figure 4.13: *PIXE-induced X-ray fluorescence spectra, of a standard gold disk, compared with a gold-based tooth alloy. A primary target of germanium was used.*

A Si escape peak should have been observed from the Ge K_α X-ray, corresponding to an energy of 8.145 keV. However, the Ge escape peak was not resolvable from that due to 8.047 keV Cu K_α, and accordingly should be considered as an added background to the peak, correction for which has to be made from the intensity of the Ge K_α X-ray yield.

From the analytical results obtained from the standards, it was found that the root mean square error, a good indicator of analytical sensitivity, for determining the elements Fe, Cu and Zn were respectively 0.73, 9.71 and 0.78 μg/g. The value for Fe was exactly the same as the calculated interference-free value in Table 4.20, and added support to the validity of the calculated values. The small decrease in the sensitivity for Zn was due to the fact that the background against which the Zn K_α X-rays had to be measured increased as a result of the tailing of the intense Ge K_α scattered X-rays. The very large decrease in sensitivity for determining Cu was due to the interference from the Ge K_α escape peak, which was not resolvable from the peak due to Cu. This cause of error could be eliminated by replacing the Si(Li) detector with one of Intrinsic Germanium.

In addition, as seen from Figure 1.6, the maximum of the sensitivity function decreases and moves to the left. For 1 MeV its value is one third of that at 4 MeV. This means that the absorption of X-rays in the matrix is much less than at 4 MeV. Thus, there exists a proton energy at which this maximum is very small, with the result that the sensitivity factor curve is approximately constant throughout the whole range of X-rays energies, i.e:

$$\frac{Y(Z)}{QC_z} = K(Z)I(Z) \sim constant \tag{4.5}$$

In other words, the $I(Z)$ factor is also constant at this particular energy and an average matrix correction factor may be calculated. A compromise must be achieved in the analysis of thick target by PIXE, to include low ranges and highest cross sections for X-ray production.

It is evident from the above investigations that the differences in the concentrations of the trace elements found in different types of materials by these methodologies are due to the inhomogeneity of the thick target through the range of the protons. Efforts have to be directed to improve protocols for sample surface preparation. This, in fact, is the case in micro-PIXE, which will be discussed in Chapter 6.

Chapter 5

High energy PIXE

5.1 Introduction

The determination of rare earth elements is becoming increasingly important for the characterisation of materials, and in general, rapid and sensitive analytical methods for these elements are limited. Over the past years, PIXE has been used to an increasing extent for elemental analysis. The most common procedure is to use proton beams of a few MeV and to measure the X-rays by Si(Li)-spectrometry. Under these conditions the determination of rare earths is aggravated by three factors. Firstly, the low cross section for the excitation of K X-rays results in yields that are too low for sensitive analysis. Secondly, the efficiency of the Si(Li) detector is so low for energies greater than about 20 keV, that the use of L X-rays is indicated. Thirdly, rare earths occur in natural ores as mixtures of elements. Since each element emits several L X-rays, the deconvolution of the resulting measured spectrum becomes complex due to the overlapping peaks, and hence requires a very high-level stripping program in order to obtain accurate results.

Because the energies of the K X-rays are sufficiently different to be separately resolved, it would be convenient to use K X-rays for rare earth determinations. This can be attained through increasing the cross section of K X-ray production by using higher energy protons, and improving the efficiency of the detection system by replacing the Si(Li) detector with the more efficient intrinsic germanium one. Few studies have been made with high energy particles. The earlier work is summarised in Table 5.1. Only one of the reported works used the efficient intrinsic germanium

detector [Du 88], but although rare earths were analysed, and an estimate was made of the attainable detection limits, no quantitative data were reported. Because there is a need to analyse rare earth concentration variation in minerals [Du 88], yield and cross section data for K X-ray excitation with energetic protons have to be measured to supply the necessary database. This is despite the opinion [Wi 77] that at higher energies Compton scattering could produce a high enough background to obscure the K X-rays completely. In fact, it was stated categorically "that cyclotrons can find only limited application in PIXE analysis and that there is no significant advantage in studying X-ray fluorescence at higher energies that a few MeV"[Ge 75].

5.2 The Cyclotron facility

For the measurements of the K-shell X-ray yields and detection limits of the rare earth and heavier metals, the 200 MeV Open Sector Cyclotron facility of the National Accelerator Center at Faure [Bo 84] was used. In the present investigation a scattering chamber similar to the one used for low energy PIXE (see figure 2.3) was mounted on one experimental line, behind two quadrupole focussing and two steering magnets. The charged particle beam was directed onto the target situated at the centre of the chamber, then exited from the chamber to a Faraday cup situated about 3 meters away. The beam was focussed to about 4 mm^2 while being viewed on a fluorescent plastic scintillator screen target by a closed-circuit television camera. The experiment required the quality of the incident proton beam to be as high as practicably obtainable and the beam had to be free of halo or other effects due to slit scattering of beam scanning devices in the beam transport system upstream of the target. The target ladder mounted at the centre of the chamber could accommodate 10 targets and was driven by remote control from the data room using a specially designed multi-dimensional goniometer.

Detection and counting system

Low energy gamma rays and K-shell X-rays of rare earth and heavier elements were detected with a Canberra dipstick planar germanium detector(for details see Chap-

Table 5.1: *Earlier high-energy PIXE studies.*

First Author	Reference	Particle Beam	Energy /MeV	Detector	Accelerator Site	Study
Bissinger	[Bi 70]	p	2-28	Proportional counter	(a)	Ca Ti Ni
Bissinger	[Bi 72]	p	2-30	Si(Li)	(a)	Ag
Watson	[Wa 71]	α	50	Si(Li)	(b)	Cu Sn Pb
Deconninck	[De 73]	α	40	Ge(Li)	(c)	Sn Ba W Au Hg Pb
		p	49			Sn Ba Ta W Au Pb
Randell	[Ra 76]	p	20-50	Ge(Li)	(d)	Ta
Wilk	[Wi 77]	p	20-50	Ge(Li)	(d)	In Ta Au Pb Satellite cross sections
Ramsay	[Ra 78]	p	22,31,44	Ge(Li)	(d)	Cu Rb Ag Eu Au
Durocher	[Du 88]	p	40	Int-Ge	(d)	Rare earths in ores

(a) Tandem Van de Graaff, Durham N.C., USA.
(b) Cyclotron, Texas A&M, College Sta. TX, USA.
(c) Isochronous cyclotron, Grenoble, France.
(d) Sector-focussed cyclotron, Winnipeg, Manitoba, Canada.

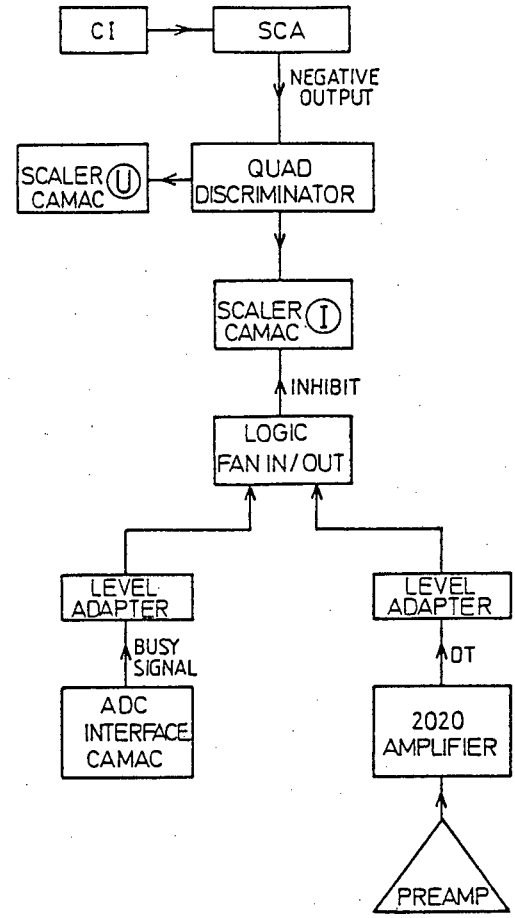

Figure 5.1: *Diagrammatic representation of the electronic circuit for High Energy PIXE.*

ter 2). The preamplification stage was similar to that of the Si(Li) detector used for low energy PIXE. The electronic circuit of the spectrometer system for high energy PIXE was designed specifically to record the accurate total dead time of the system. (see Figure 5.1). This included dead times arriving from pile-up and pulse processing. The digitised current signal was fed to a single channel analyser(SCA) and its negative pulse output was sent through a QUAD discriminator which fed the signal for the uninhibited and inhibited scalers. The dead time counting ratio was obtained by using the digitised current integrated pulse (unhibited scaler) in combination with the input of the logic FAN IN/OUT OR gate which decided whether or not the ADC interface (busy signal) or/and the amplifier were busy processing an event. If one of these were busy this unit inhibited the current pulse signal (inhibited scaler). The ratio of counts from the two scalers gave the total factor for dead time correction. The present setup did not take into consideration the background due to radioactive processes in the scattering chamber but generally speaking its contribution to the

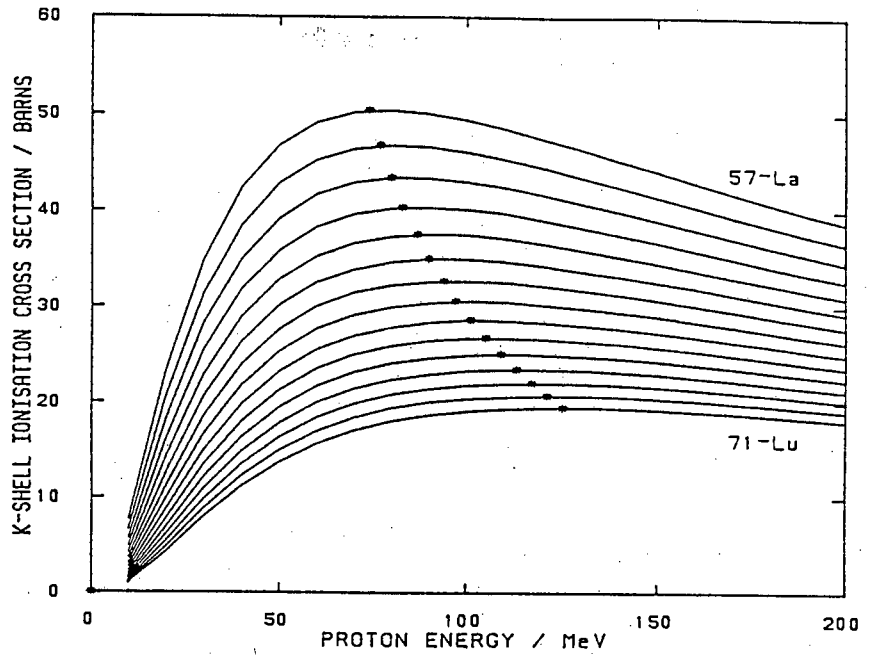

Figure 5.2: *PWBA calculation for K-shell ionization cross-sections for the rare earths, showing the energy (*) at which the maximum occurs for each element.*

total events was of less than 1%.

5.3 Theoretical considerations

Theoretical calculations of PWBA cross-sections were carried out for the K X-rays of each of the rare earth elements, in order to establish the most convenient energy for analysis. Corrections at high bombarding energies, for coulomb repulsion, polarisation and binding energy changes, relativistic effects and ion energy loss effects were negligible, so that ECPSSR corrections [Pi 90] were not incorporated in the calculation. The calculated curves are shown in Figure 5.2 in which the maximum value is indicated on each curve. These maxima occur at proton energies between 74 MeV, for La, and 125 MeV for Lu. However, for all the rare earths the rate of change of cross section with energy is relatively low in this energy region so that near-maximum yields can be obtained at bombarding energies less than those maxima.

The cross section for K X-ray production, σ_x, from thin targets is given by

$$\sigma_x = \sigma_I \omega_z \tag{5.1}$$

where σ_I is the ionisation cross section in barns

and ω_z is the fluorescence yield for the K shell of element Z, and

$$\sigma_I = \frac{kY_zA_z}{\Phi t\varepsilon\omega_z aN} \tag{5.2}$$

where Y is the measured K X-ray yield of element z (in counts)

A is the atomic mass of element z (in kg per mole)

Φ is the integrated flux of bombarding particles (in protons/sec)

t is the sample thickness (in mg/cm^2)

ε is the absolute counting efficiency for the particular X-ray, and

a is the corresponding absorption in the interposed absorbers

N is the Avogadro number (in atoms per Kg mole) and

k is the conversion factor for the units.

The experimental count yield was obtained by stripping the spectra with the program SAMPO [Ro 69].

5.4 Experimental cross sections

Thin deposits of the fluorides of each of the rare earth elements (excluding Pm), on 3 μm thick Mylar supports, obtained from Messrs. Micromatter Co., were irradiated with proton beams of 40, 66 and 85 MeV. The thickness of the deposits were given with an accuracy of $\pm 5\%$ in the range between 45 and 56 μg/cm^2, and were checked by backscatter analysis using 2 MeV $^4He^+$ ions (see Chapter 2).

From an experimental point of view the most critical step in the irradiation process is the focussing of energetic protons. Since the beam usually has a halo around it, this halo can generate an intense background if it is allowed to fall onto the aluminium of the sample frame. After the beam had been focussed to about 2mm diameter, further focussing was achieved on a blank sample frame until a minimum background was registered. It was also found useful to carry out periodic checks of the state of focus.

Beam currents were adjusted between 0.2 and 2.0 nA according to the count rate of the sample, to ensure that the dead-time of measurement did not exceed 20%. Irradiations usually lasted about 30 min but in some cases, the duration was extended

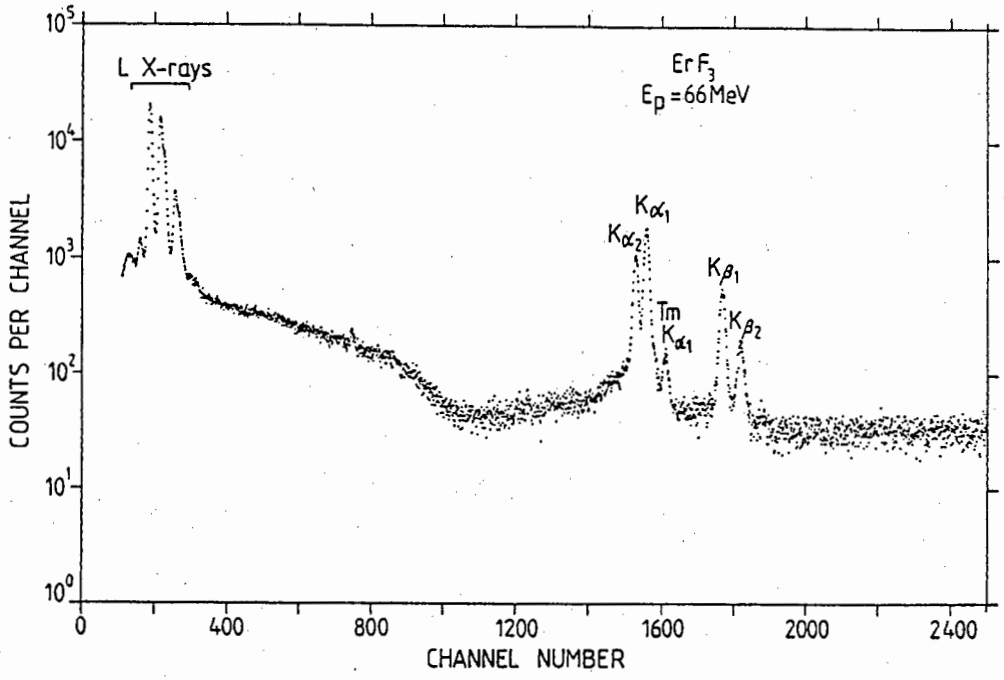

Figure 5.3: *X-ray energy spectrum from a thin target of erbium fluoride bombarded with 66 MeV protons, showing the relatively intense L X-rays and the low background over the energy region of the K X-rays.*

to obtain better sensitivity. A typical X-ray energy spectrum obtained from the bombardment of a thin target of erbium fluoride with 66 MeV protons is shown in Figure 5.3. It should be noted that the bremsstrahlung continuum falls at a much lower energy than that of the K X-rays. As a result, the background against which K X-ray yields have to be measured is relatively low, and can be assumed to be linear. The $K\alpha_1$ and $K\alpha_2$ X-rays have an energy difference of 894 eV, and are clearly resolved because the resolution of the detector is very much less than this energy difference. The precision with which K X-ray yields can be measured is therefore much improved. Peak-to-background ratios for thin films of some elements, given in Table 5.2, show the prominence of the peaks in the spectra and emphasize the ease with which they can be observed. At the higher proton energy the effect of the increased background is obvious. Experimental X-ray production cross sections at 66 MeV are listed in Table 5.3 for the $K\alpha_1$, $K\alpha_2$, $K\beta_1$ and $K\beta_2$ X-rays and include elements heavier than the rare earths. Data for the $K\alpha_1$ and $K\alpha_2$ X-rays from bombardments at 66 and 85 MeV are shown in Figures 5.4 and 5.5 respectively, where the plotted points refer to the experimental values and the lines are PWBA

Table 5.2: *Some $K\alpha_1$ peak-to-background ratios.*

Element	Peak-to-background ratios	
	66 MeV	85 MeV
Dy	33.0	5.5
Lu	33.7	3.7
W	24.9	3.4
Pt	24.2	2.8
Pb	14.3	1.7
U	6.3	2.0

calculations of the corresponding cross sections. The agreement between theory and experiment is satisfactory. The errors inherent in the above calculations were between 1.6 and 2.9% for the fluorescence yield, about 3% in the target thickness, about 10% in detection efficiency, about 2.5% in the measurement of the solid angle and counting errors which did not exceed 3%. When these errors were taken together, the overall experimental error in the determination of ionisation cross sections were taken as about ±12%.

5.5 X-rays from nuclear reactions

A complicating factor is the observation of 'nuclear' satellite K X-rays of element (Z+1) from targets of element Z as a result of nuclear reactions on the target material [Pe 90]. Furthermore, during long irradiations nuclear satellites of element (Z-1) became evident from targets of the fluorides of Tb, Dy, Ho, Er and Tm. As an example, the case of HoF_3 is shown in Figure 5.6. One possible explanation is that as a result of (p,xn) reactions, nuclei of the element (Z+1) were formed from element Z. These products decay mostly by electron capture, which results in vacancies in the atomic K subshell, the filling of which could generate the observed satellite X-rays. The relative intensities of the $K\alpha_1$ X-ray of the (Z+1) nuclear satellite to that of the target element Z under bombardment with 66 MeV is plotted in Figure 5.7 as a function of the atomic number of the target element. As is evident from the figure, the relative yield increases with atomic number, but the effect is negligible

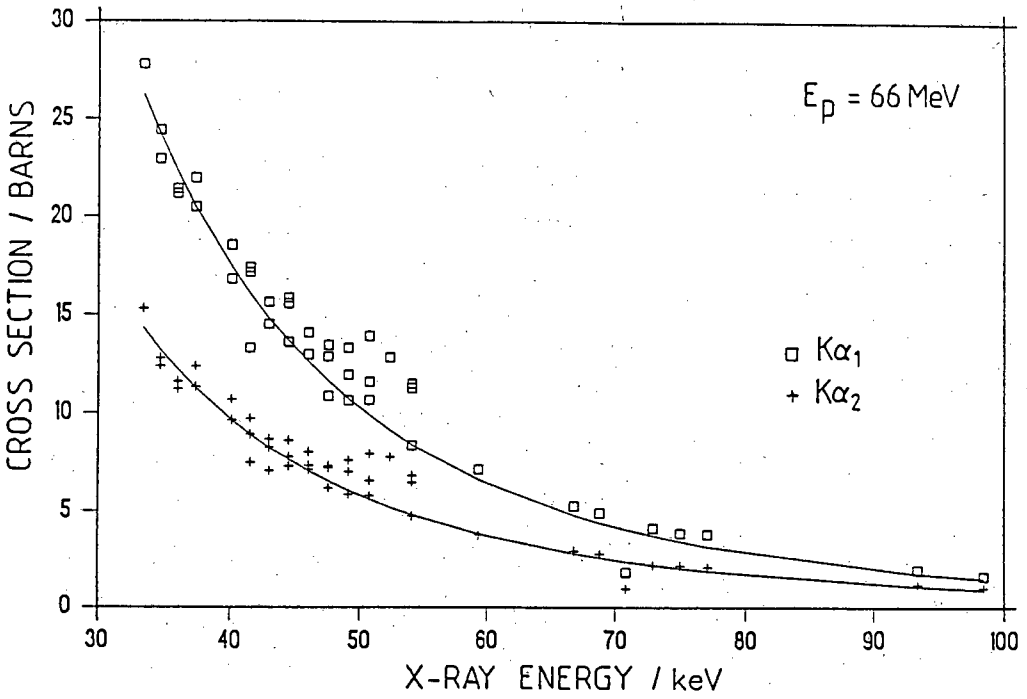

Figure 5.4: *Experimental values of K_{α_1} and K_{α_2} X-ray production cross sections obtained from bombardment with 66 MeV protons are compared with PWBA calculated values (shown as lines).*

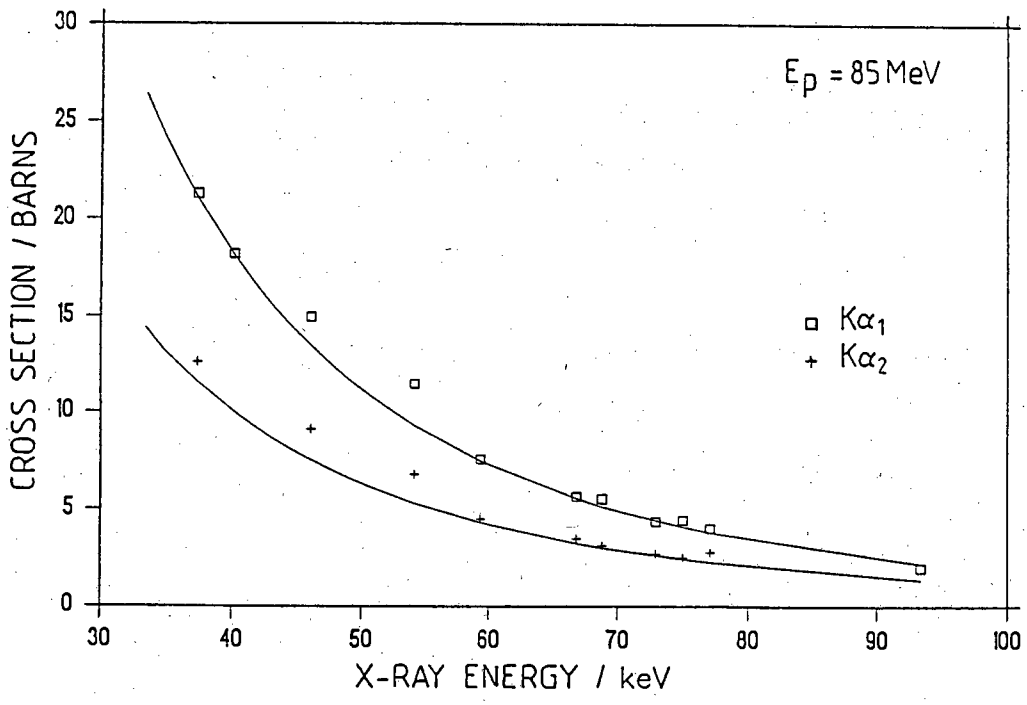

Figure 5.5: *As Figure 5.4, but for 85 MeV protons.*

Table 5.3: *Experimentally determined X-ray production cross section (mean values) for K X-rays of the rare earths excited by 66 MeV protons.*

Element	Cross section (barns)			
	$K\alpha_1$	$K\alpha_2$	$K\beta_1$	$K\beta_2$
La	27.8	15.3	8.02	1.91
Ce	23.7	12.6	6.49	1.67
Pr	21.3	11.4	6.25	1.53
Nd	22.0	12.3	6.20	1.59
Sm	18.5	10.7	5.68	1.58
Eu	17.3	9.3	5.25	1.38
Gd	15.6	7.9	4.36	1.17
Tb	15.7	7.9	4.92	1.28
Dy	13.5	7.6	4.40	1.15
Ho	13.2	7.2	4.34	1.43
Er	12.6	7.3	4.32	1.28
Tm	12.8	7.2	4.35	1.29
Yb	12.8	7.8	4.75	1.44
Lu	11.4	6.6	3.68	1.21

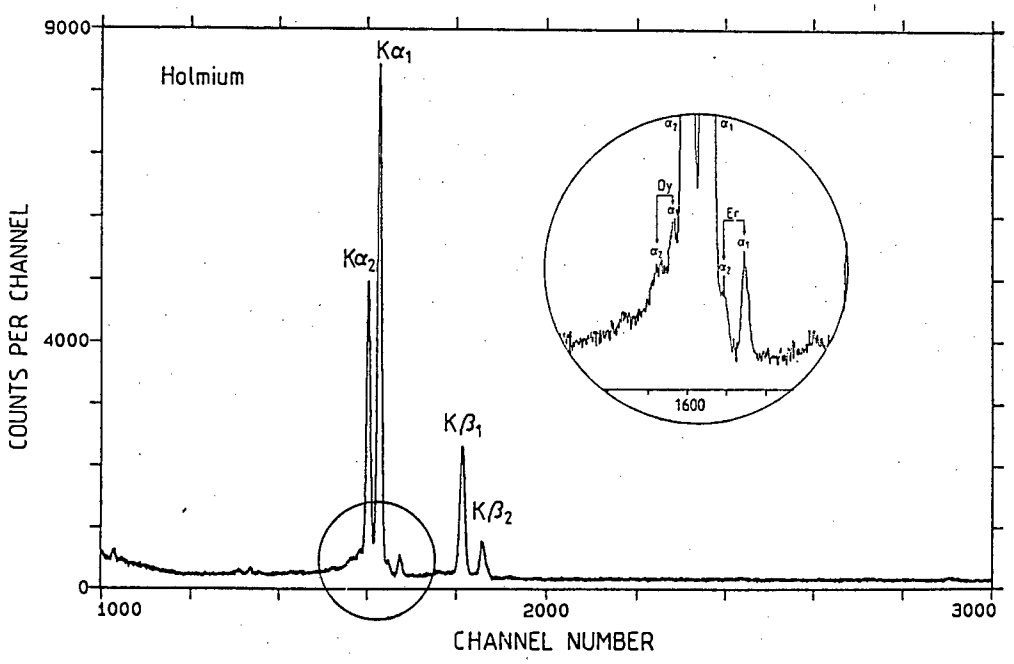

Figure 5.6: *X-ray spectrum from a thin target of holmium fluoride bombarded with 66 MeV protons. The inset shows the detection of nuclear satellites of both the (Z-1) and (Z+1) elements, Dy and Er respectively.*

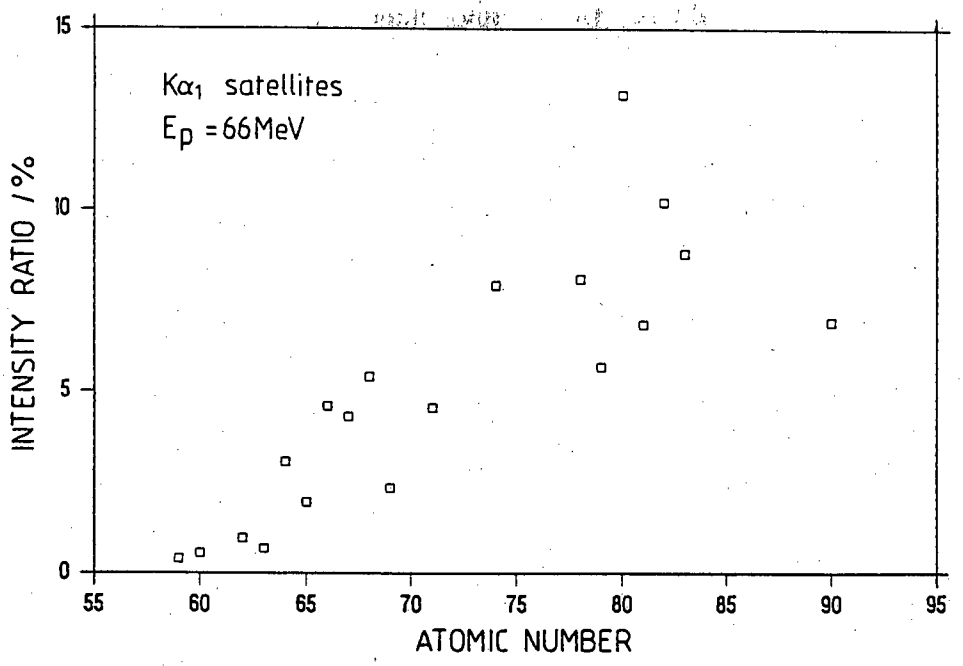

Figure 5.7: *The yield of the K_{α_1} X-rays at E_p=66 MeV from the (Z+1) nuclear satellite relative to that from the target Z, as a function of atomic number.*

for elements with Z≤60.

5.6 Sensitivity of analysis

From the data collected from thin target irradiation, interference-free sensitivities were calculated on the basis of the mass of element required to yield a count equivalent to three times the standard deviation of the background against which it has to be measured. Since the peak-to-background ratios obtained with 85 MeV protons is so much poorer than those obtained at 66 MeV, it is obvious that the higher energy is less suited for analytical purposes. Accordingly sensitivities were calculated only for 66 MeV protons. Since the sensitivity will obviously depend on the integrated bombarding flux, values given in Table 5.4 refer to an accumulated charge of 1μC and 1mC. Under suitable conditions, sub-microgram quantities of most heavy elements can be determined, but the background is materially affected by the composition of the target material, and hence will detrimentally affect sensitivity.

Table 5.4: *Interference-free sensitivities.* $E_p = 66MeV$.

Element	Sensitivity/ng	
	Charge = 1μC	Charge = 1mC
Nd	340	11
Sm	450	14
Eu	580	18
Gd	490	16
Tb	570	18
Dy	580	18
Ho	760	24
Er	830	26
Tm	860	27
Lu	860	27
W	1290	41
Pt	1430	45
Au	1700	54
Hg	3850	122
Tl	2140	68
Pb	2020	64
Bi	2240	71
Th	6000	190
U	6910	219

5.7 Analysis of standard ores

When 85 MeV protons are used, the drop in the background continuum occurs at a higher energy, as expected, but the K X-rays of the heavier elements are still measurable against a relative low background as before. Figure 5.8 shows part of the X-ray spectrum obtained from a target of carbonatite (an ore not previously analysed), about 6 mg/cm^2 in thickness, prepared by the technique mentioned in Chapter 2. The spectrum shows relatively well-defined peaks of Ba, La, Ce, Tm and Yb. Since there was the doubt about the uniformity of the prepared target, the concentration of La, Ce, Tm and Yb were calculated relative to that of Ba, and found to be 0.104, 0.212, 3.01 and 1.85 respectively. If we accept that the (non-certified) concentration of La is 121 μg/g then the concentrations found for Ba, Ce, Tm and Yb are 1163, 246, 3502 and 2152 μg/g respectively. The result for Ce is acceptably close

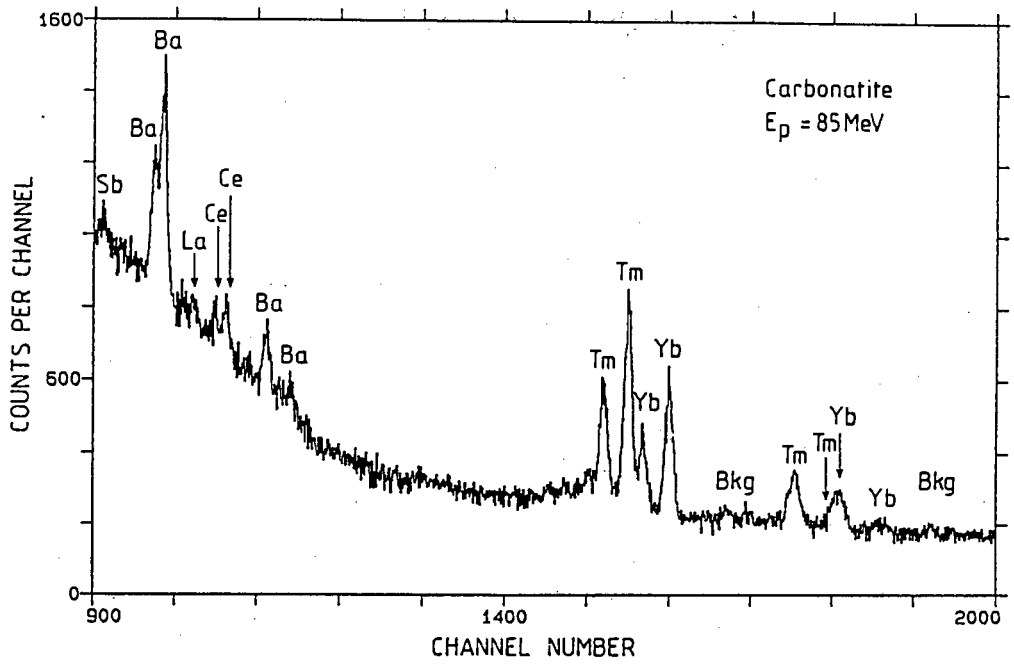

Figure 5.8: *X-ray spectrum from carbonatite with 85 MeV protons, showing the presence of Ba, La, Ce, Tm and Yb. The small peaks marked Bkg refer to low-energy gamma-rays in the background.*

to the (non-certified) value, 313 μg/g. Certified values for Ba, Tm and Yb are not available, so no comparison could be made for these elements. Targets made from the finely-ground portions of the standard reference materials SARM-1, SARM-3 and SY-3 were bombarded with 66 MeV and with 85 MeV protons for analysis. The relevant part of the energy spectrum obtained from SY-3 with 66 MeV protons is shown in Figure 5.9 The increase in the intensity of the background continuum, when compared with that in Figure 5.3, is due to the increased thickness of the material in the beam, detrimentally affecting the attainable sensitivity. Results of analyses are shown in Table 5.5, and are compared with the certified values and with values that were recommended, but not certified. The overall agreement is good, but relatively large discrepancies were noted for the uncertified concentrations of Pr and Nd in the case of SY-3. If the certified values are considered to be correct, the accuracy of the reported results is 6%, with the statistical error of counting being about 2.6%. Accordingly the accuracy of the method itself is of the order of 5.4%.

In order to obtain a measure of the uniformity of the prepared targets, one of the components of the standard ores was considered an internal standard, from which

Chapter 6

TTPIXE with microbeams

6.1 Introduction

The cross sections for X-ray excitation with proton beams of a few MeV are among the highest obtainable for ion beam reactions and hence, in microbeams, where the current intensities are relatively low, these reactions are the method of choice for most elemental analyses. Experience has shown that most materials requiring the use of microprobes are either geological or biological in origin. Thus, for example, the elucidation or isolation of grains of geological material in a complex matrix can readily be achieved, while a scan of a single hair across its width, typically 50μm, requires a microbeam of small dimensions. Similarly, the analysis of human kidney stones across a cut section can only be carried out with a microbeam when the rings of stone growth are of the order of a few microns apart.

The methodology of TTPIXE used in the macro-mode can equally be applied in the micro-mode. However, even though the principles of the technique are applicable in both environments, some effects, often neglected in ordinary TTPIXE, can determine the accuracy in the micro-mode.

In the case of thin, or intermediate thickness targets, any variation in target thickness during a mapping of a micro-region will show up as variations in elemental concentrations. This problem can be overcome by normalising the data by backscatter measurements that are recorded simultaneously [Th 86]. No such normalisation would be required if the material were available as a thick target.

The ideal conditions for good quantitative micro-PIXE spectrometry are that the

target material should be a perfectly flat surface with uniform areal density. Random variation of surface roughness, even of the order of some tens of microns, will cause changes in the extent of absorption, especially with low energy X-rays. The magnitude of this effect could be up to 100% or even more in some bad cases [Or 90]. Some attempt to correct for surface roughness has been reported [Co 83],[Ca 85a].

Due to the fact that the minimum detection limits in PIXE are proportional to the square root of the total charge, the detection limits of micro-PIXE are at least one order of magnitude inferior to that of macro-PIXE. Compared to the detection limits of EPMA, which are about 10^{-3} g/g, micro-PIXE is still better by two orders of magnitude. In spite of the poorer mass resolution of micro-PIXE compared to that of EPMA, micro-PIXE is the technique of choice, especially for some medical and biological applications where analysis required a small diameter spot beam and better detection limits. In this chapter the methodology used in Chapter 4 for the analysis of Ca-rich materials is applied for the study of human kidney stones in the micro-PIXE mode.

6.2 The Micro-PIXE facility at NAC

The component parts of the system, schematically presented in Figure 6.1, have been installed on a dedicated beam line. A 1 μm beam spot has been achieved with 100 pA of 3 MeV protons which is recognised to be a usable current. Larger beam spot sizes can be provided with correspondingly larger currents if the detection techniques can accomodate higher count rates. By scanning the focused beam spot across the target sample, a two-dimensional element map of the sample can be obtained using PIXE or secondary electron signals. With a 3 MeV proton beam PIXE produces very little bremsstrahlung and has an ultimate sensitivity of parts per million for elemental analysis. The precision focussing lenses in the system at NAC were manufactured by the Oxford group who has pioneered the development of sub-micron systems. The quadrupole lenses are cut from single pieces of high quality magnet iron to a dimensional precision of better than 2 μm. The resultant magnets have very high

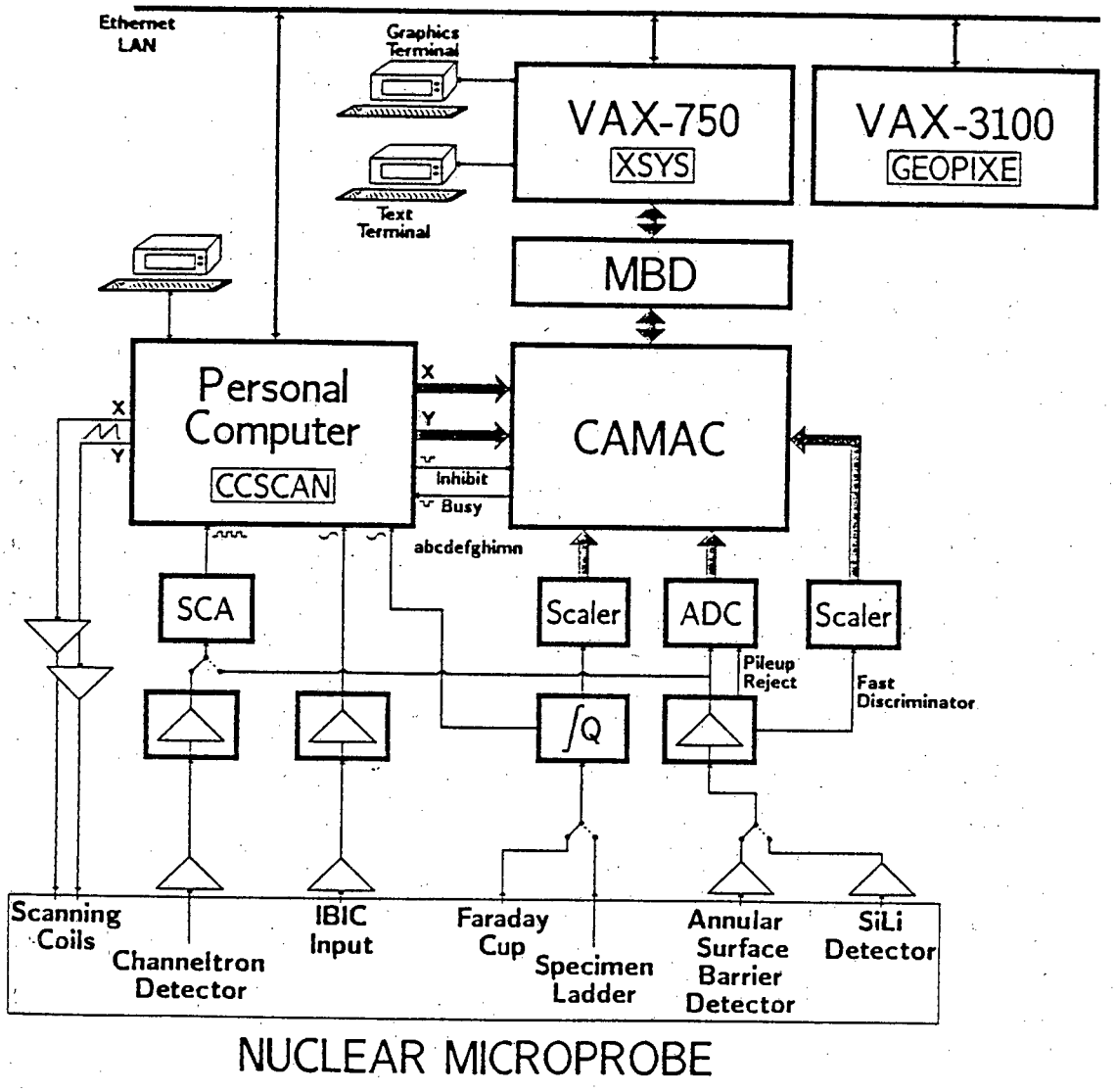

Figure 6.1: *Schematic diagram of the microprobe system [Ch 92].*

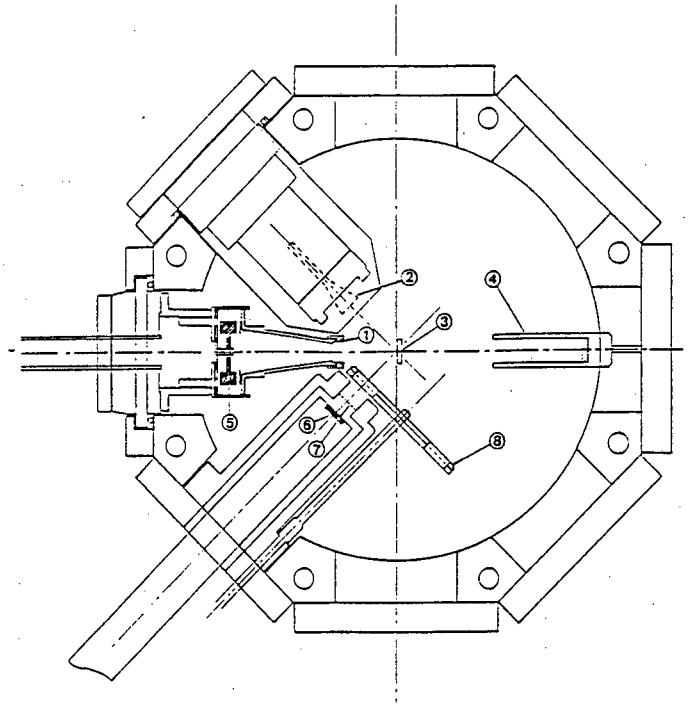

Figure 6.2: *Schematic diagram of the scattering chamber at the NAC nuclear microprobe. The beam enters the chamber from the left. 1 - Secondary electron suppressor; 2 - Channeltron detector (above microscope); 3 - Target; 4 - Faraday cup; 5 - Annular surface barrier detector; 6 - X-ray detector; 7 - Kevlar foil; 8 - X-ray filter wheel [Ta 92].*

quadrupole field purity which minimises aberrations and makes it possible to achieve sub-micron focusing of the object slits. As the NAC system consists of three lenses, it has asymmetrical focusing properties. The object slits are therefore set at about 100 x 40 μm. For 3 MeV protons, the demagnification factors already achieved at Faure are greater than 80 and 30 in horizontal and vertical directions respectively, using about 50 amps of current through the very low resistance magnet windings. The NAC microprobe system is supported on concrete blocks separated by damping material and is also isolated from the beam lines by a flexible bellows section of tubing. The beam travels through the xy deflection magnets and the three quadrupole lenses before entering the target chamber (see Figure 6.2). The target is supported on an xyz manipulator with micrometer position adjustments. The target is viewed by an optical microscope at 45° to set up the beam focus and target position. A Link Pentafet (model 6648) X-ray detector with 80 mm^2 active area and 8 μm beryllium window is supported at 135°, about 35 mm from the target. It is separated from the evacuated specimen chamber by means of an intervening 75 μm Kevlar window.

An annular surface barrier detector with a resolution of 30 keV, is positioned at 180° to provide backward Rutherford backscattering analysis for determination of major components in the target as a function of depth. A channeltron is used to detect secondary electrons. The beam current transmitted through or absorbed by the target is collected in a Faraday cup or extracted at the specimen ladder. For the accuracy of the current integration for TTPIXE work, a potential can be applied to an electron suppresor to ensure that the apparent current does not increase as a result of secondary electron emission. This is particularly important when currents of the order of pA are used.

A PC-based user-friendly interface was developed to drive the scan controller [Ch 92] to facilitate the focussing of the beam by means of the secondary electrons or X-ray input signals. Additionally, the microprobe has been interfaced to a CAMAC data acquisition and analysis computer systems in use at the Van der Graaff. The data analysis software package XSYS [Iu 84] is used in the multiparameter mode. The software Geo-PIXE package [Ra 90] has been installed to do on-line stripping of X-ray spectra with immediate report of elemental concentrations.

6.3 Analysis of human kidney stones

Stones are an ancient anguish of the human body and occur at several sites, in particular the kidney, bladder, gall-bladder, prostate gland, salivary gland and pancreas. Although not necessarily life-threatening, stones were and still are a source of considerable pain. Common features of the different types of stones have emerged. For example, basic physico-chemical principles dictate that the formation of a concretion is always associated with a highly concentrated fluid in a particular gland or secretory organ followed by precipitation of the stone salt. An organic matrix within the stone structure is another common feature.

Among the different stone sources, urinary calculus disease is one of the oldest known medical disorders of mankind. As early as the third century BC the Greek physician Ammonios used the technique of lithotrity to break up bladder stones mechanically so that they could be passed in the urine. The bladder stone was a typical urinary

concrement of history. Today, a fundamental change in the pattern of calculus disease reveals renal and ureteric stones to be the most common manifestations. Over the past 30 years, world-wide prevalence of renal calculi in particular has multiplied, paralleled by generally increasing prosperity. It is not surprising that a great deal of scientific effort has been directed at studying the prevention and dissolution of calculi [Br 81a], [Sm 81], [Sc 85]. However the hope that such studies would reveal the cause of urinary calculus formation has not yet been realized, the main reason being the multiplicity of factors contributing to the process of formation of stones. As a result, the specific combination of these factors has to be determined separately in each individual case.

Amongst these casual factors, pathological changes of the kidney and metabolic disorders (like hypercalciuria, cystinuria, etc [Pa 76]), in addition to geographical, environmental, ethnic and family related parameters have been shown to predispose certain people to stone formation [Va 79]. The prevalance of renal calculi is correlated directly with the net income of a population group, probably as a result of increased ingestion of animal protein. Changes in stone type and composition as countries become technologically developed have been observed [Su 71]. An increased incidence of renal stones with rise in atmospheric temperature has been observed and a high occurrence of stones in persons with occupations which entail exposure to high environmental temperatures [Bl 82]. Another factor is the physical activity associated with certain occupations (the more sedentary a job, the higher the frequency of stones). Regarding other personal parameters, a family history also seems to be correlated with multiple occurrences of calculi [Kl 80].

Since the stone is a kind of solid state crystal its analysis tends to be directed at the accurate characterization of the chemical composition. Moreover, careful analysis of the structure of a stone with respect to the sequential deposition of the various components provides data which reflect the changing chemical conditions during the stone's growth. In addition, nucleation and growth mechanisms may be deduced from structural studies. The analysis of calculi has shown that all stones formed within the urinary tract, irrespective of cause or composition, have, in addition to the crystalline inorganic substances a second basic component, namely an organic

matrix mixed with the crystal aggregates [Bo 59]. This knowledge, together with data obtained from crystallization experiments, has led to the development of two well-known theories of stone formation.

The present study concentrates mainly on concretions formed in the urinary tract and in particular the kidneys. The most common matrices observed in kidney stones are presented in table 6.1. The calcium oxalate appear in two forms: calcium oxalate monohydrate $CaC_2O_4.H_2O$ (COM) and dihydrate $CaC_2O_4.2H_2O$ (COD). In most cases kidney stone matrices are formed of a combination of all these compounds, but 100% pure phases are also encountered [Jo 87].

6.3.1 Theories of stone formation

Many theories have been proposed for the formation of human kidney stones [Oh 57], [Eu 67], [Me 77], [Le 78], [Jo 87], but the entire process has not yet been satisfactorily explained. In particular it has been pointed out that trace elements (TE) may play a role in stone formation [Jo 87]. If this is correct, it is expected that the trace elements concerned will be present in the stone itself. Most studies in kidney formation and growth refer to isolated stones from different patients, concentrating on the statistical characterisation of stones from a large number of cases [Le 78].

As far as the role of urinary elements in stone disease is concerned, attention has been focused on trace concentrations in calculi [He 77],[Le 78], [Ta 82],[Li 85],[Ce 86] and urine [An 73a],[Co 75],[Sc 82]. Two recent clinical studies have addressed the important question of whether any correlation exists between the trace element content of calculi and that of urine and serum of the patient from whom the stones were obtained [Jo 87], [Ho 89]. In both cases no correlation was found. Nevertheless it seems reasonable to pursue this line of research as studies have not, as yet, been able to identify major differences between stone formers and normals on the basis of urinary compounds.

The initiating factor in stone formation is not clear. On the one hand the stone matrix, which constitue about 2-10% of the total mass, plays an important role [Bo 56]. According to this theory, the condensation of specific organic colloids is thought to initiate the process of calculus formation. The deposition of inorganic

salts is then regarded as a secondary phenomenon. It is conceivable that these organic substances act as a trigger for heterogeneous nucleation of stone salts, which are then absorbed onto the matrix skeleton. Another hypothesis suggests that the stone matrix is not considered crucial but rather as being included in the stone by protein co-precipitation [Fi 61]. This theory emphasizes the physico-chemical and crystallographic elements of stone nucleation and growth [Ra 63]. According to this approach, urinary supersaturation is the driving force.

There are three mechanisms which are of importance in stone formation. These are nucleation, crystal growth and aggregation [Na 83a]. Nucleation refers to the *birth* of sub-microscopic molecular species of critical size within the supersaturated solution [Ve 66]. This initial event can be either homogeneous or hetergeneous, involving nucleation of more than one phase. As a consequence of recurrent supersaturation and other factors, aggregation of the formed crystal may occur, either by sintering or by interparticle bridging of polymeric material [Fi 77]. With the subsequent trapping of the resulting polycrystalline mass in the kidney, a stone is formed.

Today it is the role of macromolecules which is receiving most attention as far as stone formation. In contrast other urinary macromolecules are thought to have a protective (inhibitory) effect on the crystallization of stone salts [Gi 76a]. Among these are natural inhibitors like citrate, pyrophosphate and magnesium. Promoters and inhibitors of stone formation are thus thought to be another important factor in understanding urine crystallization parameters.

6.3.2 Dynamics of calcium oxalate stones and trace elements

The crystal growth of calcium oxalate kidney stones is governed by the general equation:

$$Ca^{2+} + C_2O_4^{2-} \longrightarrow CaC_2O_4 \tag{6.1}$$

This rate equation has been shown [Me 75] to be of second order and takes the form:

$$-\frac{dc}{dt} = kN^2 \tag{6.2}$$

where $-\frac{dc}{dt}$ is the instantaneous decrease in concentration of either calcium or oxalate.

k is the growth rate constant, and

N the degree of supersaturation

N is defined as $C - C_{oo}$, where C and C_{oo} are the concentration of calcium or oxalate at time t and at saturation, respectively. The relation of N and t after solution of equation 6.2 is:

$$t = k\frac{1}{N} \tag{6.3}$$

If a trace element inhibits the crystal growth of calcium oxalate, a decrease in the rate constant k is observed. In the context of calcium oxalate stones which this chapter addresses, particular interest has been paid recently to the effect of trace element aggregates as promoters or inhibitors in the three stages of stone formation. Accordingly, the aim of this research was to study the effect of TE on crystal growth of calcium oxalates and in particular to focus attention on the interrelationship of TE with time.

As mentioned earlier, stone formation is mainly governed by crystallization and supersaturation of urine in the most fundamental step of formation. From this, it is logical to conclude that any TE present in the urine are going to be concentrated in the supersaturation process. The role of those concentrated TE in the nucleation process is not clear yet, but the influence of TE in stone formation could be studied indirectly by the interrelationship between the TE.

Fe, Cu, Zn and Pb are adsorbed on the crystalline phases of calcium oxalate and calcium phosphate from urine [Me 77]. Although the TE distribution is similar in both, results suggest that the appatite phase tends to concentrate Zn to a greater extent than calcium oxalate phases. But in this respect some confusion still exists. The presence of the COD phase in the latter study did not alter the TE composition of calcium oxalate calculi, but this is in contradiction with other results [Le 78], which demonstrate how COD and COM have distinct distributions of TE.

Investigations of urinary kidney stones from a single patient, during a determined

period of time, have not yet been undertaken extensively. Thus the effects and variability of concentrations of trace elements present in the kidney stones with time presents a new alternative to study the formation of kidney concretions. Non-destructive sensitive techniques suitable for this type of study are available in proton micro-probe analysis.

A series of human kidney stones of different sizes, excreted by a single patient over a period of 11 years, at different intervals, was investigated in the present study. Major and trace metals were determined by RBS and PIXE respectively. A total of 8 kidney stones were excreted by the patient, but the first stone of the series was destroyed in its analysis and the second was lost. Therefore, this work is limited only to the study of the latest 6 kidney stones. For simplicity they are numbered 1, 2, 3, 4, 5 and 6 in chronological order. The mass of each stone varied from 5 to 50 mg and its size varied from about 0.5 mm to 3-4 mm in diameter.

Because the main aim of this experiment was to collect information on the bulk concentration of the kidney stones, no effort was made to analyse the samples with 1 μm size beam spots. Beams of the order of 10 μm were used. In this way, any surface effect due to the topography of the stones surface was minimised and allowed the beam current to be increased to tens of nano-amps, facilitating the determination of trace metals in the 1 to 100 μg/g range.

6.3.3 RBS spectrometry

Analysis by RBS spectrometry confirmed that the major components were calcium, oxygen and carbon, with possible empirical chemical formulae COM and COD (see Figure 6.3a). The first two and the last two stones in the series of 6, had the former structure while stones 3 and 4 had the latter one. Since in RBS spectrometry it is not possible to separate the steps due to Ca and P, it is likely that the amount of P is such that P is a major component, thereby indicating that the matrix composition was closer to that of calcium phosphate or a mixture of calcium phosphate and calcium oxalate phases. For comparison Figure 6.3b shows the differential RBS spectra of one of the stones. The presence of P in the spectra suggested that an admixture of apatite structure was present in combination with the calcium oxalate phases. No

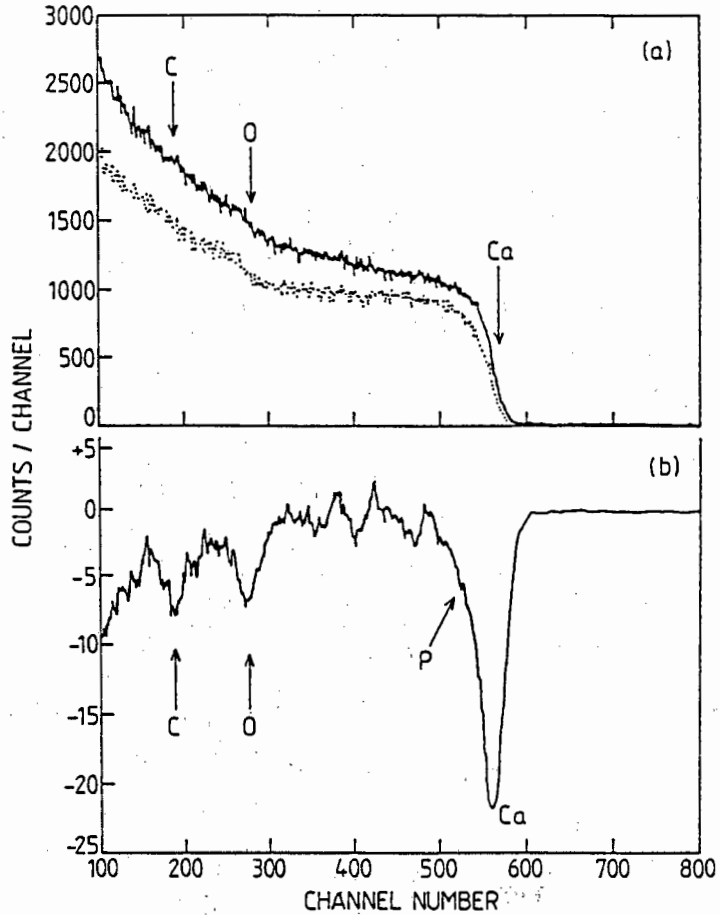

Figure 6.3: *(a) Comparison of RBS spectra for the two possible kidney stone matrix compositions and (b) differential RBS spectra for one of the structures, showing the presence of phosphorus.*

attempt was made to determine the exact crystallographic structures of the kidney stone series. The information obtained from this technique could serve to explain the type of stone matrix which is expected to be correlated to the trace metals present in the bulk of the stones. Several spots analysed in the stones showed similar compositions for major components, giving evidence of a homogeneity. There was no significant variation with time of the major components (C,Ca) of the kidney stone matrix . It may be noted in Figure 6.3b that the left of the calcium peak shows a tailing effect. This could be due to the presence of phosphorus as shown by the previous destructive analyses conducted on the first stone of the collection. The approximate total mass of this particular stone was 10 mg, of which 4 mg was Ca, 3 mg oxalate and 3 mg phosphate. Therefore 30% of the matrix component was phosphate. From the most common matrices which occur in kidney stones (see

Table 6.1: *Some common components of human kidney stones.*

Compound		Major inorganic elements
Calcium oxalate	$CaC_2O_4.H_2O$	27.43% Ca
Hydroxyapatite	$Ca_{10}(PO_4)_6.(OH)_2$	39.90% Ca, 18.50% P
Brushite	$CaHPO_4.2H_2O$	23.29% Ca, 18.0% P
Calcium carbonate	$CaCO_3$	40.04% Ca
Struvite	$MgNH_4PO_4.6H_2O$	9.91% Mg, 12.62% P
Uric acid	$C_5H_4N_4O_3$	
Cholesterol	$C_{27}H_{46}O$	
Cystine	$C_6H_{12}N_2O_4S_2$	
Mixture of calcium oxalate and hydroxyapatite		
Mixture of calcium oxalate and uric acid		
Mixture of uric acid and hydroxyapatite		

Table 6.1) it appears that hydroxyapatite corresponds to this level of phosphorus. It is therefore likely that the above stone belongs to a combination of several typical structures, such as hydroxyapatite, calcium oxalate, brushite or struvite [Kw 92].

6.3.4 X-ray spectrometry

Because of the possible role of TE in the formation and growth of urinary stones the series of stones were analysed by micro-PIXE. Trace elements detected were Mn, Fe, Ni, Cu, Zn, Br, Sr and Pb. Although, it has been suggested that Br may be an essential element [Cu 88],[Cr 78] very little data on the levels of this element in urine is available. Levels ranged from 2 to 18 $\mu g/cm^3$ [Ba 89]. Since kidney stones are insulators, the thin foil technique had to be used to prevent charge build-up and generation of bremsstrahlung and Compton background. Unfortunately, this is not possible in the micro-mode. To solve this problem without destroying the original state of the kidney stones it was decided to paint the surroundings of each stone with

aquadag (colloidal graphite). This treatment was sufficient to control the effect of charge buildup; because of the small size of the stones, the distance for the charge build-up to discharge is much shorter than in the macro-mode. The same technique was used to paint the CaF_2 and animal bone standards.

As demonstrated by [Kw 92] the heating up of samples analysed by proton beams causes a change of the matrix composition and is particularly critical for Sr. Therefore, care was taken to ensure that the current falling into the target did not exceed 1nA per 10 μm^2. Figure 6.4 shows that this was certainly controlled because the Sr signal is relatively constant in all 6 stones. Due to the high concentration of Ca in the calcium oxalate stones, the analysis was restricted to the determination of TE with X-ray energies greater than that of Ca. Since only L X-ray lines of Pb were detected, it was assumed that other heavy metals were not present.

The trace metal concentrations found in these analyses for all stones is presented in Table 6.2. The elements determined were Fe, Cu, Zn, Br and Sr. Due to the small count rate for those elements the typical analysis time was extended to two hours for each stone in order to obtain reasonably good statistics in the peak areas. Although Rb and Pb appeared in the spectra no attempt was made to quantify these elements.

For the calculation of elemental concentration two different approaches were used, according to the methodologies previously discussed in Chapter 4.

The first approach was based on the evaluaton of the sensitivity function using pure thick metal standards. By this approach the X-ray yield of element Z in the kidney stones $Y_{ks}(Z)$ is:

$$Y_{ks}(Z) = K_{ks}(Z) Q_{ks} C_{ks} I_{ks}(Z) \tag{6.4}$$

The sensitivity factor $K_p(Z)$ calculated as from the pure standard

$$K_p(Z) = \frac{Y_P(Z)}{Q_P I_P(Z) 10^6 (\mu g^{-1})}, \tag{6.5}$$

should be equal to the $K_{ks}(Z)$, then;

$$C_{ks} = \frac{Y_{ks}(Z)}{K_P(Z) Q_{ks} I_{ks}(Z)} \mu g g^{-1} \tag{6.6}$$

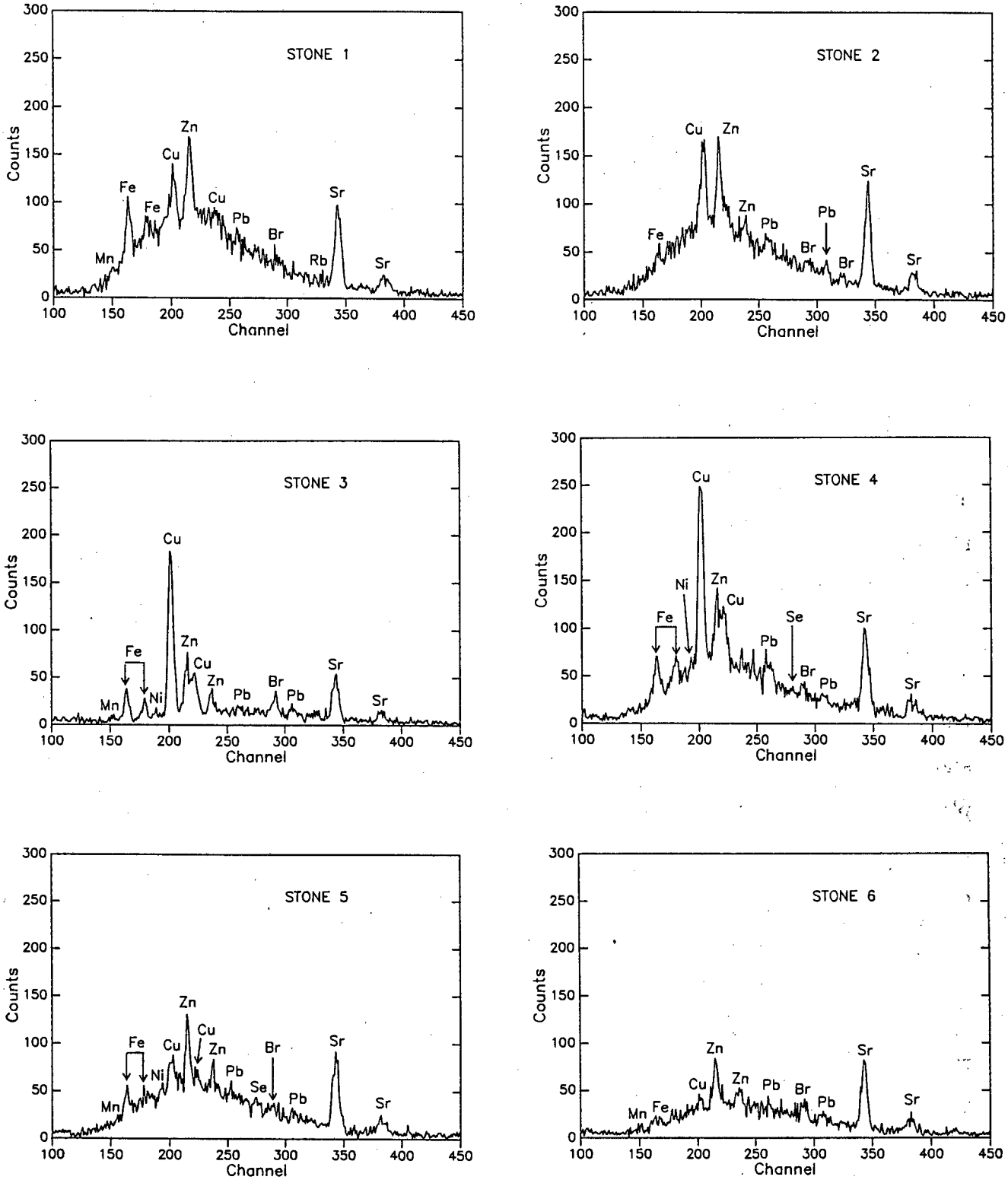

Figure 6.4: *X-ray energy spectra for the whole series of kidney stones.*

Table 6.2: *Elemental concentration in the kidney stone series($\mu g.g^{-1}$).*

Sample	Fe		Cu		Zn		Br		Sr	
Stone	a)*	b)**	a)	b)	a)	b)	a)	b)	a)	b)
1	58.4	57.2	9.1	9.4	14.7	13.6	0.9	0.8	19.1	20.1
2	9.3	9.2	13.9	14.1	11.8	11.2	2.5	2.3	18.7	19.7
3	24.9	25.2	28.1	27.0	8.6	8.0	8.7	8.9	10.9	10.2
4	32.6	32.8	29.0	29.2	9.6	8.5	1,6	1.7	16.6	15.5
5	17.9	18.1	5.4	5.3	10.0	10.7	2.9	2.6	17.6	18.7
6	4.3	4.2	2.0	2.2	7.7	7.9	4.5	4.6	13.7	13.3

*First method: using pure single metal standard.
**Second method: using animal bone IAEA-H-5 as external standard.

The values for $I_{ks}(Z)$ were taken from table 4.17 as mean values of calcium-rich materials.

For the second approach, the standard reference material IAEA-H-5 animal bone, being the standard with the closest matrix composition to that of calcium oxalate or calcium phosphate stones was used as an external standard. Because the sensitivity factors and the $I(Z)$-values are the same, when comparing the yields of the bone standard and the unknown stone, they cancel each other. The only parameters which play a role are the total integrated charge and the dead time correction. Because the count rate was very low, no correction for dead time was necessary. Thus, the concentration of element Z in the stone C_{ks} is;

$$C_{ks} = \frac{Y_{ks}(Z)}{Y_{AB}(Z)} \cdot \frac{Q_{AB}}{Q_{ks}} C_{AB} \tag{6.7}$$

Table 6.2 shows the results obtained with both methods. The variability on the current integration was of the order of 2% as calculated over all measurements. Because the two methods were applied to different experiments it can be considered that each one served as a standardisation method for the TE content in the kidney stone series. Accordingly, the accuracy of the determination is very good with an average for all elements of between 1 and 2%. With some exceptions these concentrations compare acceptably with previous reported data [Jo 87], for both COD and COM phases as well as apatite.

Table 6.3: *Elemental ratios in the Stones.*

Stone number	Cu/Zn	Cu/Sr	Zn/Sr
1	0.623	0.513	0.823
2	1.186	0.805	0.678
3	3.260	2.781	0/852
4	3.018	1.879	0.621
5	0.538	0.329	0.611
6	0.265	0.162	0.610
Mean	1.48±1.2	1.08±0.94	0.699±0.1

Figure 6.4 shows plots of the PIXE spectra for all 6 stones. From this it can be visualised that the content of Cu and Zn is variable and in particular their ratio and the Cu/Sr ratio follow a non-linear distribution as presented in Table 6.3. On the other hand the ratio of Zn/Sr seems more constant through the whole series i.e. with time. This indicates that Zn and Sr substitute each other in the calcium oxalate matrix in a similar manner. It has been reported that Zn is associated with crystallization of calcium oxalate-type structures. The fact that Zn and Cu concentrations change with time is of importance, since these two elements appear to be related to several pathological factors in the body. In general it has been demonstrated that at least, in patients with a history of kidney calculi, the correlation between Zn in the stones and urine is very high. By plotting the elemental concentrations for every stone against the atomic number certain features emerged. Firstly, there is a similarity between pairs of consecutive stones such as 1:2, 3:4 and 5:6 as shown in Figure 6.5. Because the times of excretion do not follow a linear scale, but rather a log scale, it is thought that the process of variation of TE profiles accelerate with time of recurrent kidney disease.

Another way of visualising the TE profile in the kidney stone series is shown in Figure 6.6 where the relative X-ray yield is plotted against the stone numbers for Fe, Cu, Zn and Sr. This graph demonstrates that the concentration of Fe remained relatively constant throughout the time of excretion, although it appears to decrease for the last two stones. A similar trend was found for Cu, Zn and Sr. It can

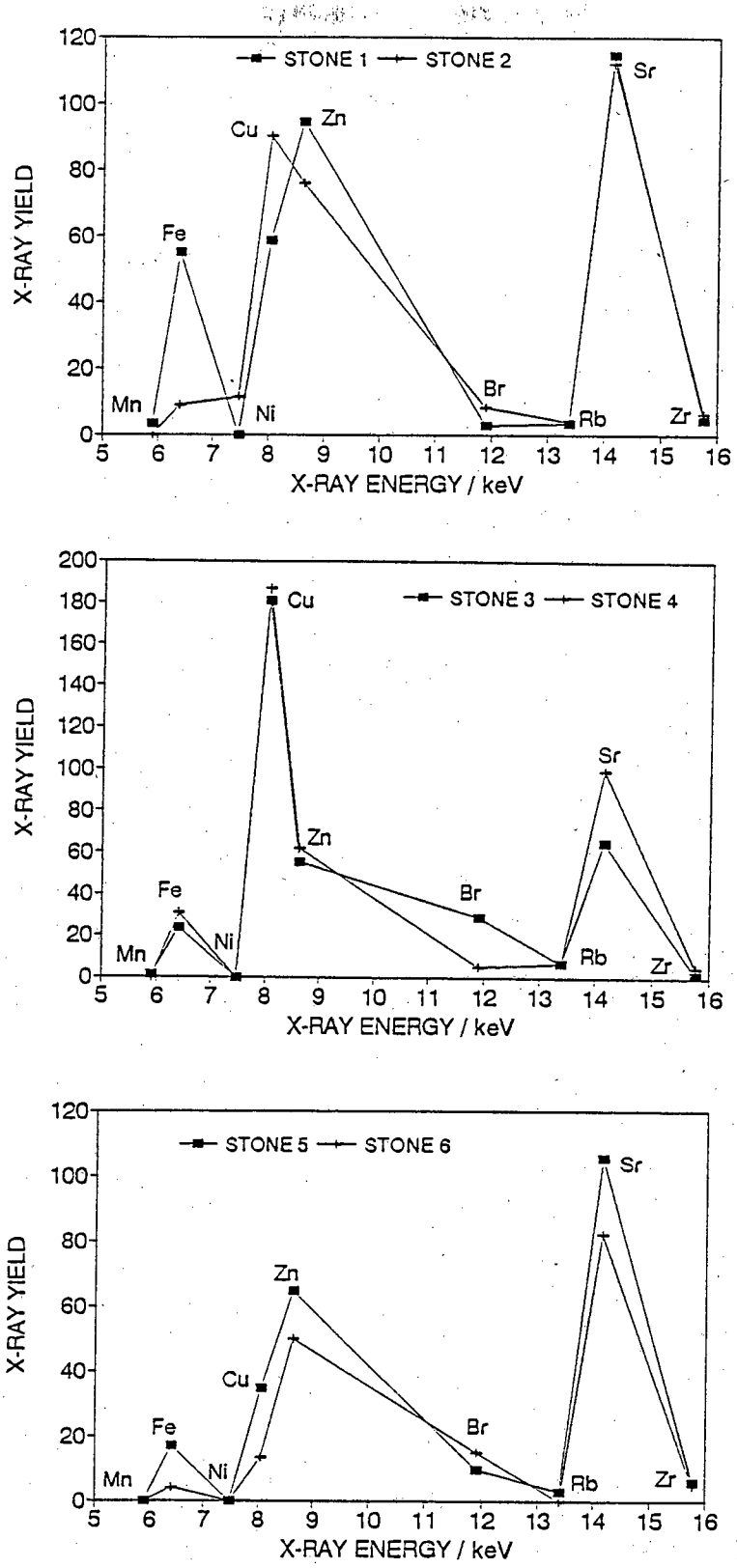

Figure 6.5: *X-ray yield profile similarity between pairs of consecutive stones 1:2 (top plot), 3:4 and 5:6 (lower plot).*

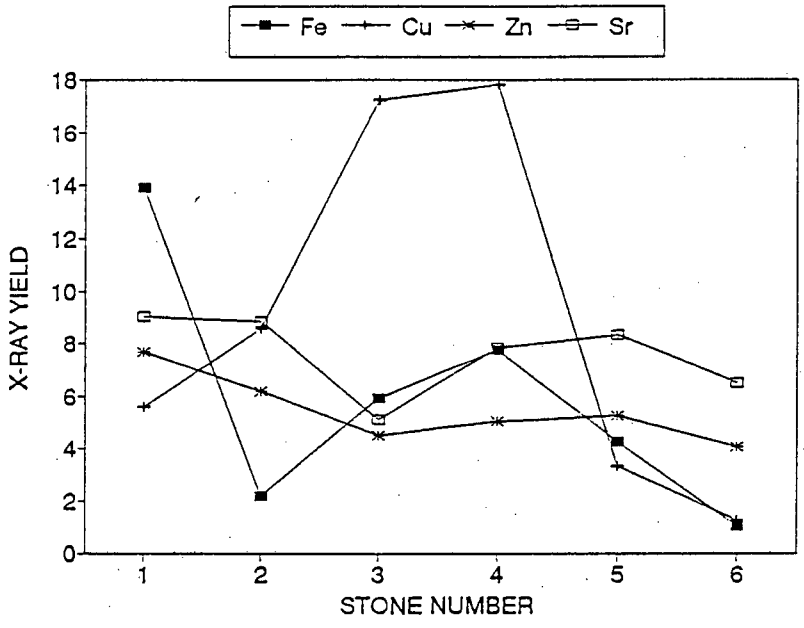

Figure 6.6: *Plot of the relative X-ray yield against stone number for Fe, Cu, Zn and Sr, showing a general trend of depletion of TE with time.*

be concluded that TE deposition in the stone matrix during the process of stone growth is being depleted. A possible explanation for this is a change in diet, which effectively occurred in this particular patient, or could be explained by physiological changes in the subject under investigation. Of interest is the fact that Cu was very high in stones 3 and 4 but decreased again in stones 5 and 6.

6.3.5 Discussion of the interrelationship of TE ratios

Since more subtle interrelationships in biological systems could be obtained by considering ratios of elements, an attempt was made to correlate ratios to elements and ratios to ratios as an exploratory way to visualize more clearly the analytical data obtained in this study.

The types of correlation found can be divided into two groups:

1. Linear correlation: It was found that the Cu/Sr and Cu/Zn ratios correlated linearly with the content of Cu. Figure 6.7 shows this relationship for the case of the Cu/Zn ratio. Similarly the Cu/Fe ratio correlated linearly with Cu but, although the number of points is relatively low in this case it appears to exist two different types of linear correlation associated to the Cu/Fe ratios

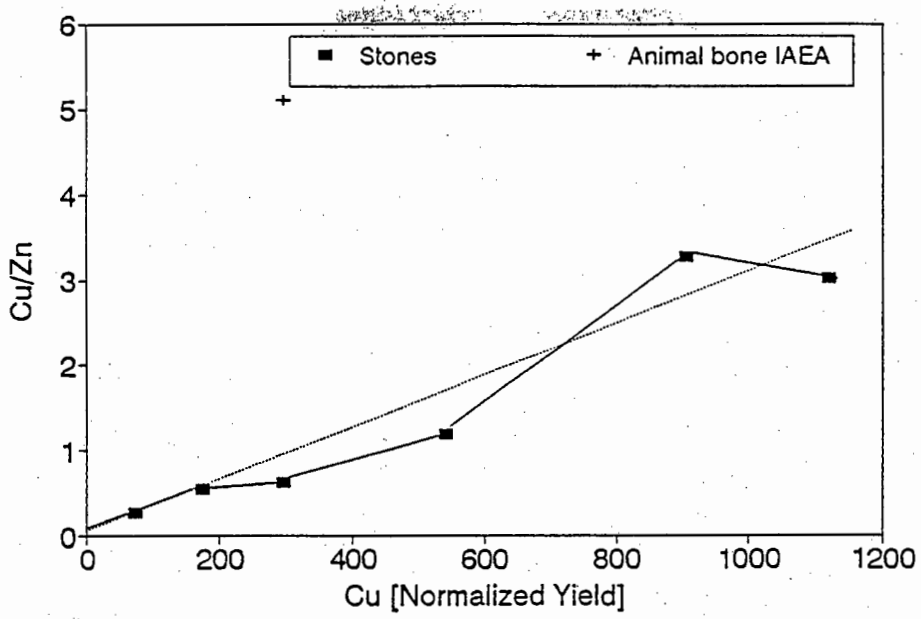

Figure 6.7: *Relationship between the Cu/Zn ratio and the Cu content (normalized to counts per unit charge) in the series of stones. A linear regression line is fitted (r=0.95) to demonstrate the linearity between variables. The value for the animal bone standard is plotted for comparison.*

and indicated in Figure 6.8 by fitted lines. This could be explained by the two different calcium oxalate types of phases discussed earlier.

2. Non-linear correlation: The more typical of these were found to be the Fe/Br ratio plotted against Br and the Br/Sr plotted against Sr (see Figure 6.9).

Since the point numbers in these plots are not associated with the chronological number of stones it can be concluded that these type of interrelationship are not related with a particular type of orientation with time.

6.3.6 Conclusions

The factors upon which kidney stone formation depends remain unclear. Nevertheless, it is apparent that this disease must be generated by fundamental physico-chemical laws. As such, the presence of any substance in a kidney stone is likely to have some significance. Elemental analysis, such as those described in this chapter are extremely useful in determining the structure and ultrastructure of a particular stone. It is clear from the present study that trace element trends and correlations

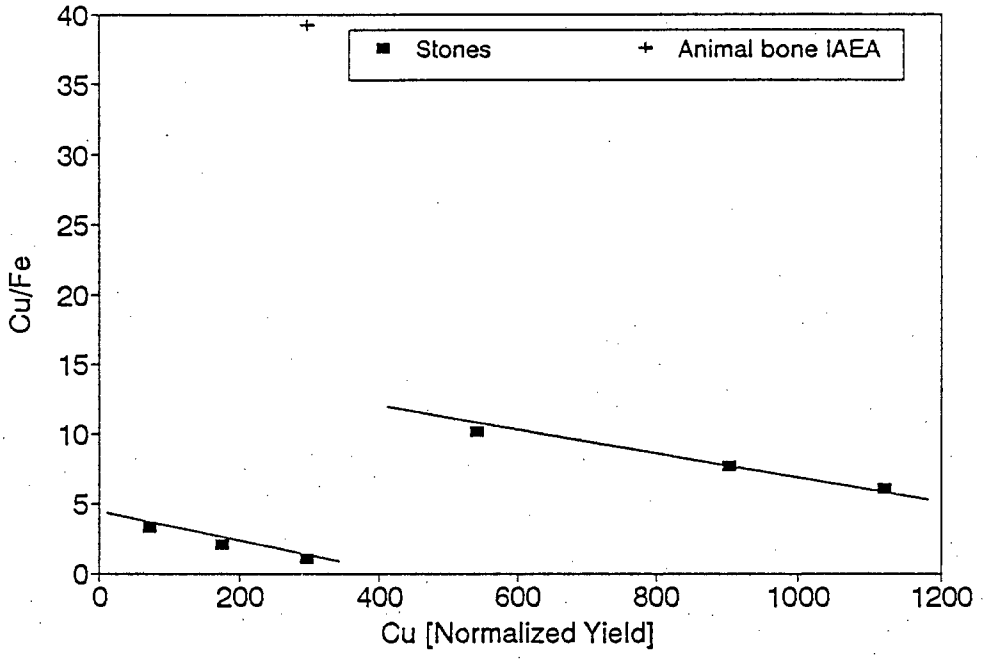

Figure 6.8: *As for Figure 6.7, but for Cu/Fe ratio.*

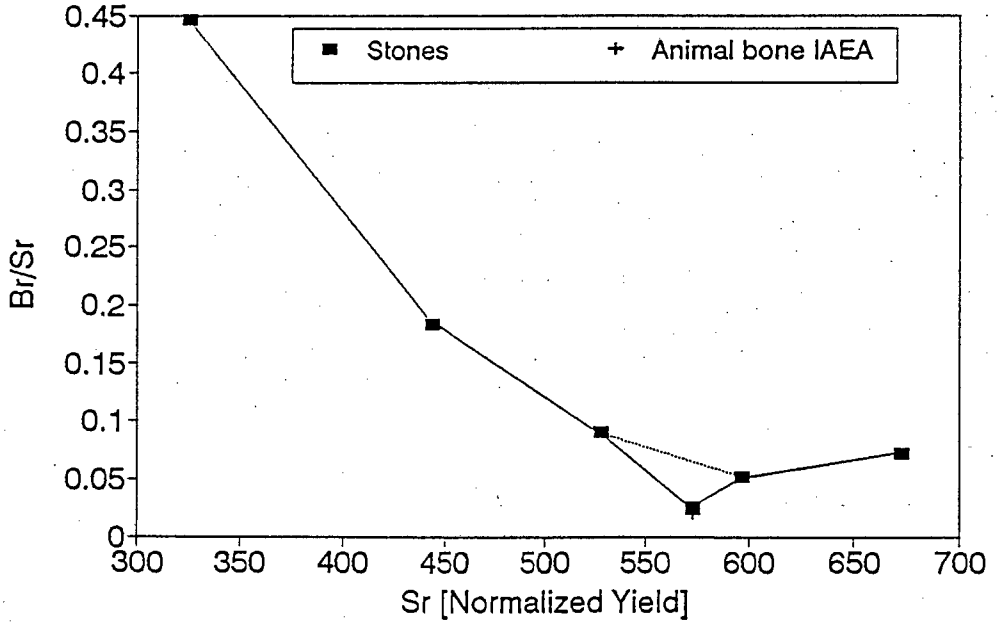

Figure 6.9: *Relationship between the Br/Sr ratio and the Sr content (normalized to counts per unit charge) in the series of stones. Apart from point number 4 all the others appear to follow the pattern of a non-linear relation. The value for the animal bone standard coincides with that of point 4 in the plot.*

can be identified and these might very well give rise to new insights into stone formation and ultimately might provide clues as to how clinicians may either retard the formation of stones or, indeed, how their formation might be totally prevented.
The fact that the stones have been analysed in their natural forms is more meaningful, because their structure is preserved from the time of excretion from the urinary system. The information obtained is more representative of the role of trace elements in kidney stone formation and growth, contrary to other work where the stones were destroyed for sample preparation. The use of a proton microprobe for the systematic PIXE scans of stone sections will minimize the risk of missing important constituents [Po 88]. This study shows that the technique has useful applications in kidney stone research and particularly when stones are small with low levels of TE concentrations.

Appendix A

Numerical integration of $I(Z)$

The definition of $I(Z)$ as stipulated in equation 1.10 is written as:

$$I(Z) = \int_{E_o}^{0} \frac{\sigma_R(E,Z)T(E)}{S(E)} dE \tag{A.1}$$

where all the parameters have already been defined in Chapter 1. From the definition of stopping power this integral can be written as:

$$I(Z) = \int_{0}^{R} \sigma_R(E,Z)T(x)dx \tag{A.2}$$

if the target is sliced into n layers of equal amounts of proton energy loss, then the contribution of the layer (x_i, x_{i+1}) is given by

$$\int_{x_i}^{x_{i+1}} \sigma_R(E,Z)T(x)dx. \tag{A.3}$$

The total contribution from all n layers will be:

$$\Sigma_{l=0}^{n-1} \int_{x_i}^{x_{i+1}} \sigma_R(E,Z)T(x)dx. \tag{A.4}$$

Assuming, that the thickness of each layer is thin enough, then $\sigma_R(E,Z)$ will be almost constant in the interval x_i, x_{i+1} and it would be correct to take a mean value of the cross section for each interval. Let this value be $\sigma_R(E_l,Z)$, which can be taken out of the integral, then:

$$I(Z) = \Sigma_{l=0}^{n-1} \sigma_R(E_l,Z) \int_{x_i}^{x_{i+1}} T(x)dx. \tag{A.5}$$

From the definition of absorption of X-rays we know that,

$$T(x) = \exp(-\mu f(\theta)x) \tag{A.6}$$

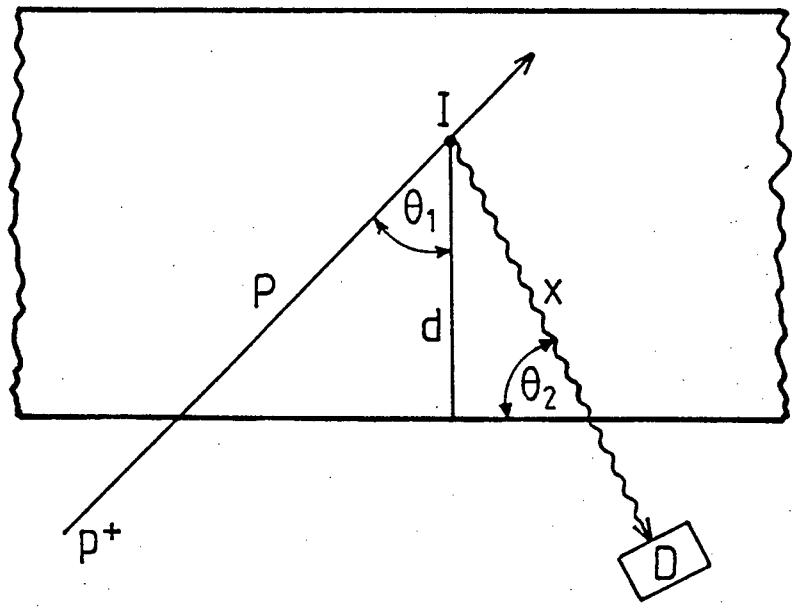

Figure A.1: *General geometry for thick target PIXE analysis. Where x is the total path of X-ray measured from the point of X-ray generation to the surface of the target; p is the total path of the protons measured from the target surface up to the point of interaction; d is the depth of analysis at the point of interaction taken perpendicular to the target surface; θ_1 is the proton incidence angle; θ_2 is the X-ray take-off angle.*

where μ and x have already been defined in Chapter 1, and $f(\theta)$ is a geometrical factor related to the angles of proton incidence into the target surface and the X-ray take-off direction from the point of interaction in the X-ray detector as shown in Figure A.1. From the figure we can deduce that;

$$f(\theta) = \frac{\sin\theta_2}{\cos\theta_1}. \tag{A.7}$$

Then the absorption factor $T(x)$ becomes,

$$T(x) = \exp(-\mu\frac{\sin\theta_2}{\cos\theta_1}x) = \exp(-\mu f(\theta)x) \tag{A.8}$$

For an experimental geometry where $\theta_1 = \theta_2 = 45°$ then the factor $f(\theta) = 1$.

Solving the integral in equation A.4 we have;

$$I(Z) = \Sigma_{l=0}^{n-1}\sigma_R(E_l, Z)\frac{\exp(-\mu x)}{-\mu}\Big]_{x=x_i}^{x=x_{i+1}} \tag{A.9}$$

and

$$I(Z) = \Sigma_{l=0}^{n-1}\frac{\sigma_R(E_l, Z)}{\mu}(\exp(-\mu x_i) - \exp(-\mu x_{i+1})) \tag{A.10}$$

Because x_i and x_{i+1} are ranges, the exponentials inside the parentheses can be further simplified by using the definition of range for each one of these, that is,

$$x_i = \int_{E_i}^{E_o} \frac{dE}{S(E)} \tag{A.11}$$

and

$$x_{i+1} = x_i + \int_{E_{i+1}}^{E_i} \frac{dE}{S(E)}. \tag{A.12}$$

Introducing these values in equation A.6, the integral $I(Z)$ becomes;

$$I(Z) = \Sigma_{i=0}^{n} \frac{\sigma_R(E_i, Z)}{\mu_z} \exp(-\mu x_i)(1 - \exp(-\mu_z \int_{E_{i+1}}^{E_i} \frac{dE}{S(E)})) \tag{A.13}$$

For the sake of simplicity we call $x_i = x_1$ and

$$x_2 = \int_{E_{i+1}}^{E_i} \frac{dE}{S(E)}. \tag{A.14}$$

For every layer n we have to evaluate the term x_2. To do that the method of stepwise initial value by Runge-Kutta [Ko 61] was used.

Two assumptions were made:

a) To evaluate x_1 we define;

$$x_1 = \int_{E_i}^{E_o} \frac{dE}{S(E)} \tag{A.15}$$

b) similarly,

$$x_2^r = \int_{E_{r+1}}^{E_r} \frac{dE}{S(E)} \tag{A.16}$$

then

$$x_1 = \Sigma_{r=0}^{i-1} x_2^r \tag{A.17}$$

where $E_r = E_o - r\delta E$.

Normally, after 50 iterations the value of $I(Z)$ did not change by more than 0.1%. The following appendix describes more in detail the mechanics of the program RD1.FOR used for the computation of MCF.

Appendix B

Program RD1.FOR

B.1 Description

The main block of the program calls the following subroutines:

- INPT: input block with associated read only file, RD5.DAT, which sets up initial values for proton bombarding energy, matrix composition, absorption coefficients (A and B) and K or L energy lines. In addition specific Ziegler coefficients [Zi 85] for proton stopping powers calculations are selected through subroutine SPCOEF and stored in array A(20,12). Then, it computes the number of iterations required and the total X-ray absorption for each iteration based on interpolation of non-linear square fits of McMaster data values [Mc 69] by the program AXABSP [Va 81].

- OUTPT: output block of program, which sets up formats and opens appropriate files according to the type of information required from the program, i.e., total range or $F(Z)$-values. The output in file XDKK.DAT, also includes information on rounding errors, Y-STEP, depth of analysis, p, exit proton energy, E-Exit (see definition on Chapter 1) and ionisation cross section if required .

- SGMA: the more sensitive part of the program, i.e., the evaluation of the X-ray cross-sections at each iteration, is performed by this subroutine, which depends heavily on only-read ionisation cross-section files, SIGMAK. DAT, SIGMAL3.DAT and SIGMAL2.DAT [Co 88]. The values for these cross-sections are found by linear interpolation.

- DISST: this subroutine computes the R-K integration [Ko 61](see Appendix 1), for the evaluation of the terms x_1 and x_2 in expression A.13.

B.2 Methodology to use the program

- Construct an RD5.DAT file for the material under investigation:
  - select X-ray shell;
  - select print option;
  - select proton energy and geometry angles;
  - input matrix composition (in %);
  - give an estimated value for absorption coefficients A and B;
  - set value for ΔE for each iteration;
  - put the X-ray energy value for only one element to be analysed;
  - give an estimated value for the thickness (e.g. 100 mg/cm^2);
  - An example of input file RD5.DAT is given in Table B.1 for the case of CsCl.
- Run RD1.FOR with options screen=00 and data option 1=01.
  - Remark: if the Y-STEP (rounding error) is too large then ΔE must be decreased. One must be aware of the fact that there is not a rule as far the step size is concerned. You must try several times until the Y-STEP is acceptably small. Note as ΔE decreases the computer CPU time increases.
- Collect output results on file XDKK.DAT and check what is the p (Range) at Ep=0, the final energy.
- The obtained range value is then used to calculate the absorption coefficients A and B, using the AXABSP program.
- Once A and B are found return to the RD5.DAT file and correct the values for the thickness (the range just found) and the attenuation coefficients A and B.
- Once decided on the size of ΔE, run RD1.FOR, with options screen=03 and data option 1=03 (data option 2 is always set to 08).
- A final output with the values of $I(Z)$ and $F(Z)$ will be stored in file XDKK.DAT.

Table B.1: *Example of input file RD5.DAT for the case of CsCl irradiated with 3 MeV protons.*

```
SIGMAK=0,SIGMAL1=1,SIGMAL2=2,SIGMAL3=3          00
DO YOU WANT THE RANGE  YES=00,NO=01             01
THE SKIP OF PRINT DATA                          10
THE FIRST ENERGY NUMBER TO BE PRINTED           01
PRINT DATA OPTION SCREEN (0,1,3)                03
PRINT DATA OPTION 1      (1,2,3,4)              03
PRINT DATA OPTION 2      (1,8)                  08
THE NUMBER OF NUCLEONS                           1
THE PROTON BEAM ENTRANCE ENERGY IN keV     3000.0000
THE PROTON BEAM EXIT ENERGY IN keV            0.0000
THE BEAM ANGLE IN DEGREES                     0.0000
THE DETECTOR ANGLE IN DEGREES                45.0000
THE NUMBER OF ELEMENTS IN THE MATRIX             2
*                                      (CL)  17  21.05
*                                      (CS)  55  78.94
ABSORPTION PARAMETERS FROM AXABSP:      (A) +0.62099E+03
*                                       (B) -0.22054E+01
MATERIAL THICKNESS IN MGRAMS/CM2 FOR AXABSP  35.65
MATERIAL THICKNESS IN MGRAMS/CM2 ACTUAL      35.65
THE ENERGY STEP INTERVAL IN KEV               5.0
THE NUMBER OF TRACE ELEMENTS                  6
*                                      KA1   55  30.970
*                                      KA2   55  30.623
*                                      KB1   55  34.984
*                                      KB2   55  35.819
*                                      KA1   17   2.622
*                                      KB1   17   2.815
```

B.3 Listing

```
C
C
C                    **********************
C                    *     PROGRAM RD1    *
C                    **********************
C
C       A PROGRAM TO CALCULATE MATRIX CORRECTIONS IN THICK TARGETS
C         ANALISED BY PROTON INDUCED X RAY EMISSION SPECTROMETRY
C
C                 Written and Compiled by C.A. PINEDA
C                           March 1987
C                     Updated: September 1988
C
C
C
C
      REAL EKEV0,COMP(20),A(20,12),AW(20),DELTA,ABS(20),EB,ET,DIST
      REAL SUM,EN,SIGMA0,SIGMA,ELH,DIS1,SMM,FACT,RHO,NSA,RHO1
      INTEGER NELEM,NZ(20),LAYERS,I,J,K,NOIT,NNUC,FLAG1,I9,ELNO(20),PRT
      INTEGER OTP,PDAT,PRS,STSKP,SKP,NSP,NLM,DISP,NTRACE,LS,STFL,CUT,CROSS

      COMMON/ONE/NNUC,NELEM,A,NZ,AW,COMP
      COMMON/TWO/ELNO,EKEV0,RHO,ABS,PRS,PRT,RHO1,NTRACE

C       INPUT THE INITIAL VALUES

      CALL INPT(DELTA,LAYERS,PDAT,SKP,STSKP,CUT,CROSS)
      STFL=1
      IF(CUT.EQ.0)NTRACE=1
      DO 600 LS=1,NTRACE
        DISP=0
        SUM=0
        DIS1=0
        EN=EKEV0
        CALL OUTPT(STFL,EN,SUM,SMM,DIS1,SIGMA,SMM2,DISP,LS)
        STFL=0
        CALL SGMA (EKEV0,SIGMA0,ELNO(LS),1,I9,PDAT,CROSS)
        FACT=RHO*SIGMA0*ABS(LS)
        L=1

500       IF(L.LE.LAYERS.AND.DIS1.LE.RHO)THEN

C           CALCULATION OF CROSS SECTION

          ELH=EN-DELTA/2
          CALL SGMA(ELH,SIGMA,ELNO,0,I9,PDAT,CROSS)
          NOIT=50
          EB=EN-DELTA
          ET=EN
          CALL DISST(EB,ET,NOIT,DIST)
          SM1=ABS(LS)*DIST-(ABS(LS)*DIST)**2/2
          SMM2=EXP(-ABS(LS)*DIS1)
```

```
        SMM1=SMM2*(SM1)
        SMM=SMM1*SIGMA
        SUM=SUM+SMM/FACT
        IF(CUT.EQ.1)THEN
         IF(SMM/FACT.LT.SUM/1000.)GOTO 599
        END IF
        IF(L.GE.STSKP)THEN
        NSA=(L+SKP-STSKP)*1.0
        NSP=INT(NSA/SKP)*SKP
      IF(NSP.EQ.NSA)CALL OUTPT(2,EN,SUM,SMM,DIS1,SIGMA,SMM2,DISP,LS)
        END IF
        EN=EN-DELTA
        DIS1=DIS1+DIST
        L=L+1
        GOTO 500
      ELSE IF(DIS1.GT.RHO.AND.L.LT.LAYERS)THEN
        DISP=1
599     END IF
      CALL OUTPT(3,EN,SUM,SMM,DIS1,SIGMA,SM1,DISP,LS)
600    CONTINUE
     CALL OUTPT(4,EN,SUM,SMM,DIS1,SIGMA,SM1,DISP,LS)
     STOP
     END

C       ***************************************************
C       *************   SUBROUTINE INPT    ****************
C       ***********  Input block of program   *************
C       ***************************************************


     SUBROUTINE INPT(DELTA,LAYERS,PDAT,SKP,STSKP,CUT,CROSS)


C       READS THE DATA FROM FILE RD5.DAT , SORTS THE DATA THEN FINDS THE
C       ZIEGLER COEFFICIENTS AND ATOMIC WEIGHTS FROM FILES:
C                ZIEGLER.DAT      ATWT.DAT
C       OUTPUTS DATA FOR THE MAIN PROGRAM

     REAL EKEVO,THETA,AP,BP,RHO,XKEV(20),DELTA,ABS(20),A(20,12),AW(20)
     REAL COMP(20),ALPHA,RHO1,EKEVF
     INTEGER ELMNO(20),LAYERS,PRT,PDAT,NZ(20),NNUC,NELEM,PRS,STSKP,SKP
     INTEGER NTRACE,CUT,CROSS
     COMMON/ONE/NNUC,NELEM,A,NZ,AW,COMP
     COMMON/TWO/ELMNO,EKEVO,RHO,ABS,PRS,PRT,RHO1,NTRACE

15   FORMAT(43X,I4)
35   FORMAT(43X,F9.4)
45   FORMAT(43X,2PE15.7)
55   FORMAT(43X,I4,1X,F7.3)

C       INPUT OF BOMBARDING CONDITTIONS

     OPEN(10,FILE='RD5.DAT',STATUS='OLD')
```

```
      READ(10,15) CROSS
      READ(10,15) CUT
      READ(10,15) SKP
      READ(10,15) STSKP
      READ(10,15) PRS
      READ(10,15) PRT
      READ(10,15) PDAT

      READ(10,15) NNUC
      READ(10,35) EKEVO
      READ(10,35) EKEVF
      READ(10,35) ALPHA
      READ(10,35) THETA
      READ(10,15) NELEM
      DO 10 I=1,NELEM
      READ(10,55) NZ(I),COMP(I)
10    CONTINUE

C        SORT ELEMENTS IN INCREASING ATOMIC NUMBER

      CALL SORT (NELEM,NZ,COMP)

C        STORE ZIEGLER COEF(S) IN FILE

      CALL SPCOEF(NELEM,NZ,COMP,A,AW)

      READ(10,45) AP
      READ(10,45) BP
      READ(10,35) RHO1
      READ(10,35) RHO
      READ(10,35) DELTA
      READ(10,15) NTRACE
      DO 60 I=1,NTRACE
       READ(10,55) ELMNO(I),XKEV(I)

C      CALCULATE ABSORPTION COEFFICIENTS

       ABS(I)=(AP*XKEV(I)**BP)/(RHO1*1E-3)*COSD(ALPHA)/COSD(THETA)
60    CONTINUE

C      CONVERT TO GRAMS FROM MILLIGRAMS

       RHO=RHO*1E-3
       LAYERS=NINT((EKEVO-EKEVF)/DELTA)
       CLOSE(10,STATUS='KEEP')
       RETURN
       END


       SUBROUTINE SORT(N,NZ,AZ)


C      FOR ARRANGING IN INCREASING ORDER OF ATOMIC NUMBER
```

```
      REAL AZ(20)
      INTEGER NZ(20)
      K=N-1
      DO 20 I=1,K
      M=I+1
      DO 10 J=M,N
      IF(NZ(J).GT.NZ(I)) GO TO 10
      NZZ=NZ(J)
      AA=AZ(J)
      NZ(J)=NZ(I)
      AZ(J)=AZ(I)
      NZ(I)=NZZ
      AZ(I)=AA
10    CONTINUE
20    CONTINUE
      RETURN
      END

      SUBROUTINE SPCOEF(N,NZ,C,A,AW)


C     STORES ZIEGLER COEFFICIENTS FOR CALCULATING STOPPING
C     POWERS OF HYDROGEN IONS


C     NZ=ATOMIC NUMBERS OF COMPONENT ELEMENTS
C     C =CONTENT OF EACH ELEMENT
C     A =THE 12 COEFFICIENTS FOR EACH ELEMENT
C     N =NUMBER OF ELEMENTS


      DIMENSION Z(12)
      CHARACTER  ANAME*2
      REAL C(20),AW(20),A(20,12)
      INTEGER NZ(20)
      INTEGER    ATN

      OPEN(20,FILE='ZIEGLER.DAT',STATUS='OLD')
      OPEN(30,FILE='ATWT.DAT',STATUS='OLD')

      DO 20 I=1,N
 5    READ(20,50)MZ,CHEM,(Z(J),J=1,12)
      READ(30,60)ATN,ANAME,AW(I)
      IF (MZ.NE.NZ(I)) GO TO 5
      DO 10 K=1,12
      A(I,K)=Z(K)
10    CONTINUE
20    CONTINUE

      CLOSE(20,STATUS='KEEP')
      CLOSE(30,STATUS='KEEP')
50    FORMAT(I2,1X,A2,2(1X,F5.3),2(1X,F6.1),2(1X,F8.6),2(1X,F6.3),
     +1X,F5.3,1X,F7.4,/,F7.5,1X,F10.7)
60    FORMAT(I3,1X,A2,F12.6)
```

```
      RETURN
      END

C       ******************************************************
C       **************   SUBROUTINE OUTPT   ******************
C       ************  Output block of program  ***************
C       ******************************************************

        SUBROUTINE  OUTPT(I,KEVO,INT,SUM,XSTEP,CRSSN,ABS1,DISP,LS)

        INTEGER PRT,I,NE(20),PRS,DISP,LS,NTRACE
        REAL KEVO,INT,XSTEP,CRSSN,ABS1,ABS(20),EKEVO,RHO1
        COMMON/TWO/NE,EKEVO,RHO,ABS,PRS,PRT,RHO1,NTRACE

15      FORMAT(2X,'ENERGY',5X,'INTEGRAL',6X,'Y-STEP',6X,'X-DIST',6X,
     \&  'CRSSCN',6X,'ABSORPTN')
25      FORMAT(2X,'ENERGY',8X,'INTEGRAL',9X,'Y-STEP')
35      FORMAT(2X,'ENERGY',5X,'INTEGRAL',6X,'Y-STEP',6X,'X-DIST',7X,
     \&  'CRSSCN',4X,'ABSORPTION')
45      FORMAT(2X,'ENERGY',8X,'INTEGRAL',9X,'Y-STEP')
55      FORMAT(1X,F7.2,3X,1PE11.4,3X,0PF9.3,3X,1PE9.3,3X,
     \&  0PF10.3,3X,F8.4)
65      FORMAT(1X,F7.2,3X,1PE11.4,3X,0PF9.3,3X,1PE9.3,3X,
     \&  0PF10.3,3X,F8.4)
75      FORMAT(1X,F7.2,6X,1PE11.4,6X,0PF9.3)
85      FORMAT(1X,F7.2,6X,1PE11.4,6X,0PF9.3)
95      FORMAT(2(/)1X,'TRACE ELEMENT ATOMIC NUMBER:',1X,I3)
99      FORMAT(1X,'               X-RAY ENERGY:',1X,F6.3,' KeV')
105     FORMAT(1X,'         ENERGY OF BEAM WAS:',1X,F8.3,' KeV')
115     FORMAT(1X,'     ABSORPTION COEFFICIENT:',1X,1PE10.4,' CM2/GM')
125     FORMAT((/),1X,'TRACE ELEMENT ATOMIC NUMBER:',1X,I3)
135     FORMAT(1X,'         ENERGY OF BEAM WAS:',1X,F8.3,' KeV')
145     FORMAT(1X,'     ABSORPTIOM COEFFICIENT:',1X,1PE10.4,' CM2/GM')
155     FORMAT(1X,'          TOTAL INTEGRAL IS:',1X,1PE11.5)
165     FORMAT(1X,'          TOTAL INTEGRAL IS:',1X,1PE11.5)
175     FORMAT(1X,'              THICKNESS WAS:',1X,1PE11.5,' mGM/CM2')
185     FORMAT(1X,'              THICKNESS WAS:',1X,1PE11.5,' mGM/CM2')
195     FORMAT(1X,'        BEAM EXIT ENERGY IS:',1X,F8.3,' KeV')
205     FORMAT(1X,'        BEAM EXIT ENERGY IS:',1X,F8.3,' KeV')
215     FORMAT(2X,'EL',4X,'X-DIST',7X,'INTEGRAL',7X,'F(Z)',7X,'ABSORPTION',
     \&  5X,'E-EXIT')
225     FORMAT(1X,I3,2X,1PE9.3,3X,1PE11.4,3X,1PE11.4,3X,1PE11.5,4X,0PF8.3)
235     FORMAT(1X,I3,1PE11.4)
245     FORMAT(30(/))

        IF(I.EQ.1)THEN
          WRITE(6,245)
          IF(PRT.EQ.1)THEN
            OPEN(40,FILE='XDKK.DAT',STATUS='NEW')
            WRITE(40,15)
          ELSE IF(PRT.EQ.2)THEN
            OPEN(40,FILE='XDKK.DAT',STATUS='NEW')
            WRITE(40,25)
```

```
      ELSE IF(PRT.EQ.3)THEN
        OPEN(40,FILE='XDKK.DAT',STATUS='NEW')
        WRITE(40,215)
      ELSE IF (PRT.EQ.4)THEN
        OPEN(40,FILE='P10.DAT',STATUS='NEW')
        WRITE(40,235) NTRACE
      END IF
      IF(PRS.EQ.0)THEN
        WRITE(6,35)
      ELSE IF(PRS.EQ.1)THEN
        WRITE(6,45)
      ELSE IF(PRS.EQ.3)THEN
        WRITE(6,215)
      END IF
    ELSE IF(I.EQ.2)THEN
      IF(PRT.EQ.1)THEN
        WRITE(40,55) KEV0,INT,SUM,XSTEP*1E3,CRSSN,ABS1
      END IF
      IF(PRS.EQ.0)THEN
        WRITE(6,65) KEV0,INT,SUM,XSTEP*1E3,CRSSN,ABS1
      ELSE IF(PRS.EQ.1)THEN
        WRITE(6,85) KEV0,INT,SUM
      END IF
      IF(PRT.EQ.2)THEN
        WRITE(40,75) KEV0,INT,SUM
      END IF
    ELSE IF(I.EQ.3)THEN
      IF (PRT.EQ.1.OR.PRT.EQ.2)THEN
        WRITE(40,95) NE(LS)
        WRITE(40,105) EKEV0
        WRITE(40,115) ABS(LS)
        WRITE(40,165) INT
        WRITE(40,185) RHO*1E3
        IF(DISP.EQ.1)WRITE(40,205) KEV0
      ELSE IF(PRT.EQ.3)THEN
        WRITE(40,225) NE(LS),XSTEP*1E3,INT,1/INT,ABS(LS),KEV0
      ELSE IF(PRT.EQ.4)THEN
        WRITE(40,235) NE(LS),1/INT
      END IF
      IF (PRS.EQ.3)THEN
        WRITE(6,225) NE(LS),XSTEP*1E3,INT,1/INT,ABS(LS),KEV0
      ELSE IF(PRS.NE.3)THEN
        WRITE(6,125) NE(LS)
        WRITE(6,135) EKEV0
        WRITE(6,145) ABS(LS)
        WRITE(6,155) INT
        WRITE(6,175) RHO*1E3
        IF(DISP.EQ.1)WRITE(6,195) KEV0
      END IF
    ELSE IF (I.EQ.4)THEN
      IF(PRT.EQ.3)THEN
        WRITE(40,*)
        WRITE(40,105) EKEV0
        WRITE(40,185) RHO*1E3
```

```
        END IF
        IF (PRS.EQ.3)THEN
          WRITE(6,*)
          WRITE(6,105) EKEV0
          WRITE(6,185) RHO*1E3
        END IF
        CLOSE(40,STATUS='KEEP')
      END IF
      RETURN
      END

C     ************************************************************
C     ******************  SUBROUTINE DISST  **********************
C     **********  Depth computation block of program  **********
C     ************************************************************

      SUBROUTINE DISST(EB,ET,NO,DIST)

      REAL EB,ET,DIST,ZIG(20,12),AW(20),COMP(20)
      INTEGER I,NZ(20),NELEM,NO,NNUC
      REAL ESTEP,STP,STPP,K1,K2,K4,E1,E2,E4
      COMMONM/ONE/NNUC,NELEM,ZIG,NZ,AW,COMP
      STP=0
      ESTEP=(ET-EB)/NO
      EN=EB
      DO 10 I=1,NO
        E1=EN
        CALL STPPWR(E1,K1)
        K1=1/K1
        E2=E1+ESTEP/2
        CALL STPPWR(E2,K2)
        E4=E1+ESTEP
        K2=1/K2
        CALL STPPWR(E4,K4)
        K4=1/K4
        STP=STP+(K1+4*K2+K4)/6
        EN=EN+ESTEP
10    CONTINUE
      DIST=STP*ESTEP
      RETURN
      END


    SUBROUTINE STPPWR(E,SPCOMP)


C     CALCULATION OF PROTON STOPPING POWERS IN UNITS OF
C     keV / GRAMS / CM**2

C     E=ENERGY
C     M=HYDROGEN ION MASS
C     N=NO.OF ELEMENTS IN TARGET
```

```
      REAL E,SPCOMP,A(20,12),AW(20),COMP(20)
      INTEGER NZ(20),N,M
      REAL*8 BB
      COMMON/ONE/M,N,A,NZ,AW,COMP

      SPCOMP=0.
      SUM=0.
      IF(E.GT.999)  CALL BETASQR(M,E,BB)
      DO 2 I=1,N
        IF(E.GT.999)THEN
          SPCOMP=SPCOMP+SP(BB,A,E,I)*COMP(I)/AW(I)
        ELSE
          SPCOMP=SPCOMP+SP1(E,A,I)*COMP(I)/AW(I)
        END IF
2     CONTINUE
      SPCOMP=SPCOMP*6.023E+03
      RETURN
      END


      SUBROUTINE BETASQR(M,E,BB)


C     CALCULATION OF BETA-SQUARED VALUES AT ENERGY E

C     M =MASS OF HYDROGEN ION
C     E =ENERGY IN KEV
C     BB=CALCULATED VALUE OF BETA-SQUARED


      REAL*8 EMOCC(3),BB
      DATA EMOCC/1.50330744D-10,3.00512283D-10,4.500477058D-10/

      EMCSQR=EMOCC(M)
      EJOULE=E*1.6022E-16
      BB=1.0-(EMCSQR/(EJOULE+EMCSQR))**2
      RETURN
      END


        REAL FUNCTION SP(BB,A,E,I)

        REAL*8 BB
        REAL A(20,12),E
        INTEGER I
        SUM=0.
        DO 1 J=1,4
          SUM=SUM+A(I,J+8)*(ALOG(E)**J)
        CONTINUE
        SP=(A(I,6)/BB)*(DLOG(A(I,7)*BB/(1.0-BB))-BB-A(I,8)-SUM)
        RETURN
        END
```

```
      REAL FUNCTION SP1(E,A,I)

      REAL E,SH,SL,A(20,12)
      INTEGER I
      IF (E.GT.10)THEN
        SL=A(I,2)*E**.45
        SH=A(I,3)/E*ALOG(1+A(I,4)/E+A(I,5)*E)
        SP1=1/(1/SL+1/SH)
      ELSE
        IF (E.EQ.0)THEN
          SP1=.1
        ELSE
          SP1=A(I,1)*E**.5
        END IF
      END IF
      RETURN
      END

C     ************************************************************
C     ******************  SUBROUTINE SGMA  ***********************
C     ********  Cross-section computation block of program  ******
C     ************************************************************

      SUBROUTINE SGMA ( E , CRSS , EL , FLAG1,I9,PRNT,CROSS)


      REAL E,CRSS,X(100),Y(100)
      INTEGER I,I1,FLAG1,NFL,EL,PRNT,I9,NO,CROSS
      IF(FLAG1.EQ.1)THEN
        IF(PRNT.EQ.1) OPEN(20,FILE='TEST.DAT',STATUS='NEW')
        CALL DATX2(X,Y,NO,EL,CROSS)
      END IF
      I=1
10    IF(E.GT.X(I))THEN
        I=I+1
        IF(I.GT.NO)THEN
        PRINT *,'ENERGY TO LARGE READ ERROR...!'
        PRINT *,'RUN STOPPED'
        PRINT *,'ERROR DEBUG...  E=',E
        PRINT *,'       MAX ENERGY=',X(NO)
        STOP
        END IF
        GOTO 10
      ELSE IF(E.EQ.X(I)) THEN
        CRSS=Y(I)
      ELSE
        I1=I
        IF(I.EQ.1)I1=2
        CRSS=(Y(I)-Y(I-1))/(X(I)-X(I-1))*(E-X(I-1))+Y(I-1)
      END IF
      IF(PRNT.EQ.0)THEN
       NFL=6
       WRITE(NFL,*)E,CRSS
      ELSE IF(PRNT.EQ.1)THEN
```

```
        NFL=20
        WRITE(NFL,*)E,CRSS
      END IF

      IF(PRNT.EQ.1.AND.I9.EQ.NO)CLOSE(20)
      RETURN
      END

      SUBROUTINE DATX2(X,Y,NO,EL,CROSS)

      REAL A(7)
      REAL X(100) , Y(100)
      INTEGER I,J,K,NO,ATN,EL,CROSS
15    FORMAT(I2)
25    FORMAT(I2,1X,7(2X,1PE9.3))
35    FORMAT(7(/))
45    FORMAT(10(3X,7(2X,1PE9.3)/))

      IF(CROSS.EQ.0)THEN
        OPEN(UNIT=10,FILE='SIGMAK.DAT',STATUS='OLD')
      ELSE IF(CROSS.EQ.1)THEN
        OPEN(UNIT=10,FILE='SIGMAL1.DAT',STATUS='OLD')
      ELSE IF(CROSS.EQ.2)THEN
        OPEN(UNIT=10,FILE='SIGMAL2.DAT',STATUS='OLD')
      ELSE IF(CROSS.EQ.3)THEN
        OPEN(UNIT=10,FILE='SIGMAL3.DAT',STATUS='OLD')
      END IF

C     READ CROSS SECTION DATA POINTS FROM FILE SIGMA(?).DAT
C     ====================================================

      READ(10,15) NO
10    READ(10,25) ATN,(A(I),I=1,7)
      IF(ATN.NE.EL)THEN
        READ(10,35)
        GOTO 10
      ELSE
        DO 20 I=1,7
          Y(I)=A(I)
20      CONTINUE
        READ(10,45)(Y(I),I=8,NO)
      END IF
C     ******************************
C     CREATE X VALUES

      X(1)=100
      DO 30 I=2,NO
        IF(I.LE.21)X(I)=X(I-1)+20
        IF(I.GT.21.AND.I.LE.23)X(I)=X(I-1)+100
        IF(I.GT.23.AND.I.LT.26)X(I)=X(I-1)+50
        IF(I.GE.26.AND.I.LT.58)X(I)=X(I-1)+100
        IF(I.GE.58)X(I)=X(I-1)+200
30    CONTINUE
C     ******************************
```

```
      CLOSE(10,STATUS='KEEP')
      RETURN
      END
```

Appendix C

MCF for pure elements and compounds: K-shell

Table C.1: K_α, E_p=1.0 MeV.

Target	Element Z	p mg/cm^2	$I(Z)$	$F(Z)$	ABS	E-Exit keV	Range mg/cm^2
$Ce_2(SO_4)_3$	16	1.02	0.07	14.40	2647	847	4.71
$Ce(SO_4)_2$	16	1.04	0.08	12.92	2440	836	4.50
CsCl	17	1.07	0.05	21.66	2940	885	6.68
$BaCl_2$	17	1.06	0.05	19.06	2842	875	6.01
KI	19	1.58	0.09	11.06	1484	824	6.02
Mn	25	2.16	0.21	4.82	305	687	5.28
Fe	26	2.17	0.20	4.90	306	690	5.33
Co	27	2.30	0.20	4.91	264	687	5.72
Ni	28	2.26	0.20	5.00	262	686	5.69
GaN	31	2.26	0.23	4.30	144	669	5.17
Ge	32	2.57	0.21	4.67	150	675	6.24
$As2O_3$	33	2.26	0.24	4.22	118	669	5.13
Se	34	2.56	0.22	4.64	131	674	6.20
$RbNO_3$	37	1.97	0.25	4.00	59	665	4.35
$SrCO_3$	38	1.98	0.25	4.00	52	665	4.36
Y_2O_3	39	2.30	0.24	4.14	60	669	5.17
Zr	40	2.78	0.23	4.30	64	673	6.39
NbO	41	2.44	0.24	4.13	46	670	5.47
Nb_2O_3	41	2.45	0.28	3.56	38	668	4.76
Mo	42	2.89	0.24	4.25	44	672	6.61
Ru	44	2.97	0.24	4.25	29	672	6.82
Ag	47	3.05	0.21	4.79	42	680	7.76
Cd	48	3.25	0.22	4.63	27	677	8.02
In	49	3.21	0.21	4.66	34	681	7.94
Sn	50	3.27	0.22	4.64	29	681	8.04
Sb	51	3.21	0.22	4.63	24	683	7.92
Te	52	3.36	0.23	4.43	22	684	7.92
KI	53	2.71	0.24	4.16	22	685	6.02
CsCl	55	2.75	0.22	4.54	13	687	6.68
$CsNO_3$	55	2.20	0.23	4.44	10	688	5.28
$BaCl_2$	56	2.49	0.22	4.50	11	689	6.01
La_2O_3	57	2.65	0.22	4.59	12	691	6.49
$Ce(SO_4)_2$	58	1.85	0.22	4.51	7	693	4.50
$Ce_2(SO_4)_3$	58	1.93	0.22	4.53	8	693	4.71
CeO_2	58	2.54	0.22	4.63	12	693	6.26
Pr_2O_3	59	2.66	0.21	4.79	13	695	6.77
Pr_6O_{11}	59	2.57	0.21	4.76	12	695	6.52
$Nd(NO_3)_3.6H_2O$	60	1.47	0.23	4.43	4	698	3.51
Nd_2O_3	60	2.70	0.21	4.75	12	697	6.80
Gd_2O_3	64	2.81	0.20	4.94	11	705	7.29
Dy_2O_3	66	2.92	0.20	5.12	10	708	7.81
Lu_2O_3	71	3.03	0.18	5.44	10	718	8.46
Ta	73	3.90	0.17	5.94	11	722	11.68
W	74	3.93	0.16	6.07	11	725	11.98
Pt	78	4.02	0.16	6.43	14	736	12.76
Au	79	3.83	0.16	6.42	13	739	12.12
Pb	82	3.65	0.15	6.80	38	754	11.94
ThF_4	90	2.30	0.15	6.75	7	771	7.44
UO_2	92	2.66	0.14	6.97	8	777	8.78

Table C.2: K_α, E_p=2.0 MeV.

Target	Element Z	p mg/cm^2	$I(Z)$	$F(Z)$	ABS	E-Exit keV	Range mg/cm^2
$Ce_2(SO_4)_3$	16	7.66	0.23	43.70	2440	1140	13.67
$Ce(SO_4)_2$	16	1.84	0.03	37.08	2647	1825	13.14
CsCl	17	1.79	0.02	57.03	2940	1875	18.95
$BaCl_2$	17	1.85	0.02	50.24	2842	1860	17.27
KI	19	3.02	0.04	28.15	1484	1785	18.23
Mn	25	6.90	0.16	6.41	305	1330	14.93
Fe	26	6.81	0.15	6.50	306	1335	14.92
Co	27	7.31	0.16	6.19	264	1310	15.70
Ni	28	7.23	0.16	6.18	262	1305	15.49
GaN	31	4.66	0.18	5.45	144	1560	14.66
Ge	32	5.16	0.17	6.00	150	1578	17.23
$As2O_3$	33	4.85	0.19	5.16	118	1549	14.78
Se	34	5.21	0.17	5.78	131	1568	17.07
$RbNO_3$	37	4.60	0.23	4.37	59	1511	12.82
$SrCO_3$	38	4.66	0.23	4.32	52	1508	12.89
Y_2O_3	39	8.94	0.27	3.76	60	1115	15.03
Zr	40	10.47	0.25	4.05	64	1140	18.24
NbO	41	9.64	0.27	3.67	46	1105	16.01
Nb_2O_3	41	9.73	0.32	3.14	38	1095	14.11
Mo	42	11.22	0.26	3.83	44	1115	19.01
Ru	44	11.64	0.27	3.66	29	1100	19.50
Ag	47	11.89	0.25	4.07	42	1130	21.10
Cd	48	12.41	0.26	3.87	27	1110	21.67
In	49	12.33	0.25	3.99	34	1125	21.70
Sn	50	12.65	0.26	3.92	29	1120	22.09
Sb	51	12.93	0.26	3.81	24	1115	22.21
Te	52	13.30	0.27	3.70	22	1115	22.21
KI	53	11.11	0.28	3.58	22	1110	18.23
CsCL	55	11.22	0.28	3.60	13	1105	18.95
$CsNO_3$	55	9.27	0.29	3.48	10	1100	15.35
$BaCl_2$	56	10.31	0.28	3.54	11	1105	17.27
La_2O_3	57	10.91	0.28	3.61	12	1110	18.46
$Ce(SO_4)_2$	58	7.99	0.30	3.39	1	1095	13.14
$Ce_2(SO_4)_3$	58	8.21	0.29	3.47	8	1105	13.67
CeO_2	58	10.47	0.28	3.61	12	1110	17.76
Pr_2O_3	59	10.89	0.27	3.73	13	1115	18.97
Pr_6O_{11}	59	10.63	0.27	3.70	12	1110	18.36
$Nd(NO_3)_3.6H_2O$	60	6.49	0.30	3.37	4	1110	10.62
Nd_2O_3	60	11.09	0.27	3.68	12	1115	19.03
Gd_2O_3	64	11.65	0.27	3.74	11	1120	20.21
Dy_2O_3	66	12.01	0.26	3.82	10	1125	21.20
Lu_2O_3	71	12.69	0.25	3.92	10	1135	22.76
Ta	73	15.57	0.24	4.22	11	1145	29.46
W	74	15.75	0.23	4.26	11	1145	29.97
Pt	78	16.17	0.23	4.44	14	1165	31.61
Au	79	16.06	0.23	4.36	13	1170	30.95
Pb	82	15.20	0.20	5.02	38	1235	31.07
ThF_4	90	11.15	0.24	4.15	7	1210	20.98
UO_2	92	12.87	0.24	4.24	8	1220	24.26

Table C.3: K_α, E_p=3.0 MeV.

Target	Element Z	p mg/cm^2	$I(Z)$	$F(Z)$	ABS	E-Exit keV	Range mg/cm^2
$Ce_2(SO_4)_3$	16	1.88	0.01	75.23	2440	2165	26.23
$Ce(SO_4)_2$	16	1.96	0.01	70.45	2647	2860	25.28
CSCL	17	1.95	0.01	106.86	2940	2895	35.65
$BaCl_2$	17	1.89	0.01	94.78	2842	2890	32.75
KI	19	3.28	0.02	52.66	1484	2820	34.81
Mn	25	9.06	0.10	10.07	305	2350	28.25
Fe	26	8.91	0.10	10.14	306	2355	28.12
Co	27	9.83	0.11	9.36	264	2310	29.40
Ni	28	9.69	0.11	9.06	262	2305	28.29
GaN	31	6.51	0.13	7.46	144	2538	27.82
Ge	32	7.03	0.12	8.36	150	2562	32.22
$As2O_3$	33	6.94	0.15	6.86	118	2516	28.20
Se	34	7.19	0.13	7.84	131	2545	31.85
$RbNO_3$	37	7.05	0.19	5.24	59	2441	24.72
$SrCO_3$	38	7.19	0.20	5.11	52	2433	24.86
Y_2O_3	39	17.64	0.24	4.09	60	1640	28.66
Zr	40	20.06	0.22	4.57	64	1700	34.28
NbO	41	19.19	0.26	3.88	46	1600	30.48
Nb_2O_3	41	19.62	0.31	3.27	38	1560	27.11
Mo	42	21.84	0.24	4.11	44	1630	35.72
Ru	44	23.23	0.27	3.75	30	1560	36.57
Ag	47	19.52	0.22	4.48	42	1890	38.92
Cd	48	20.92	0.25	4.05	27	1830	39.92
In	49	20.48	0.23	4.30	34	1870	40.11
Sn	50	21.22	0.24	4.16	29	1850	40.88
Sb	51	21.87	0.25	3.99	24	1830	41.30
Te	52	22.60	0.26	3.85	22	1825	41.30
KI	53	19.19	0.27	3.74	22	1815	34.81
CsCL	55	19.87	0.28	3.57	13	1775	35.65
$CsNO_3$	55	16.75	0.29	3.39	10	1765	29.36
$BaCl_2$	56	18.46	0.29	3.47	11	1770	32.75
La_2O_3	57	19.45	0.28	3.57	12	1780	34.88
$Ce(SO_4)_2$	58	14.80	0.31	3.18	1	1735	25.28
$Ce_2(SO_4)_3$	58	15.05	0.30	3.33	8	1760	26.23
CeO_2	58	18.73	0.28	3.55	12	1780	33.57
Pr_2O_3	59	19.40	0.27	3.66	13	1785	35.61
Pr_6O_{11}	59	18.89	0.28	3.63	12	1785	34.57
$Nd(NO_3)_3.6H_2O$	60	12.20	0.31	3.21	4	1755	20.78
Nd_2O_3	60	19.73	0.28	3.61	12	1785	35.73
Gd_2O_3	64	20.68	0.27	3.65	11	1790	37.77
Dy_2O_3	66	21.25	0.27	3.70	10	1795	39.30
Lu_2O_3	71	22.38	0.27	3.77	10	1800	41.87
Ta	73	26.76	0.25	4.05	11	1815	52.51
W	74	27.07	0.25	4.08	11	1815	53.29
Pt	78	27.82	0.23	4.26	14	1840	56.01
Au	79	27.74	0.24	4.20	13	1840	55.28
Pb	82	24.86	0.18	5.41	38	1995	55.82
ThF_4	90	21.11	0.27	3.71	7	1830	39.42
UO_2	92	24.05	0.26	3.85	8	1845	45.83

Table C.4: K_α, E_p=4.0 MeV.

Target	Element Z	p mg/cm^2	$I(Z)$	$F(Z)$	ABS	E-Exit keV	Range mg/cm^2
$Ce_2(SO_4)_3$	16	2.23	0.01	116.17	2647	3870	42.05
$Ce(SO_4)_2$	16	2.25	0.01	103.70	2440	3070	40.62
CSCL	17	2.23	0.01	181.17	2940	3900	56.29
$BaCl_2$	17	2.29	0.01	158.95	2842	3890	52.00
KI	19	3.96	0.01	84.21	1484	3820	55.31
Mn	25	12.55	0.07	14.48	331	3340	44.93
Fe	26	12.05	0.07	14.72	306	3290	44.63
Co	27	13.45	0.07	13.42	264	3230	46.49
Ni	28	13.31	0.08	13.19	262	3220	45.63
GaN	31	7.89	0.10	10.12	144	3546	44.32
Ge	32	8.38	0.09	11.43	150	3573	50.83
$As2O_3$	33	8.53	0.11	9.12	118	3518	45.04
Se	34	8.66	0.09	10.53	131	3551	50.19
$RbNO_3$	37	9.18	0.16	6.41	59	3413	39.74
$SrCO_3$	38	9.41	0.16	6.18	52	3401	39.97
Y_2O_3	39	24.98	0.21	4.79	60	2450	45.70
Zr	40	27.36	0.18	5.52	64	2560	54.10
NbO	41	27.55	0.23	4.42	46	2370	48.48
Nb_2O_3	41	28.52	0.27	3.65	38	2300	43.41
Mo	42	30.76	0.21	4.73	44	2420	56.29
Ru	44	33.53	0.25	4.08	29	2290	57.56
Ag	47	32.13	0.20	4.94	42	2450	60.73
Cd	48	35.40	0.24	4.23	27	2310	62.27
In	49	34.11	0.22	4.65	34	2400	62.65
Sn	50	35.71	0.23	4.42	29	2350	63.87
Sb	51	37.16	0.24	4.16	24	2300	64.63
Te	52	38.43	0.25	4.00	22	2290	64.63
KI	53	33.16	0.26	3.84	22	2260	55.31
CsCL	55	34.80	0.29	3.50	13	2170	56.29
$CsNO_3$	55	29.81	0.31	3.27	10	2140	46.90
$BaCl_2$	56	32.66	0.30	3.37	11	2150	52.00
La_2O_3	57	34.13	0.29	3.50	12	2180	55.24
$Ce(SO_4)_2$	58	26.85	0.34	2.93	1	2060	40.62
$Ce_2(SO_4)_3$	58	27.05	0.32	3.16	8	2120	42.05
CeO_2	58	33.06	0.29	3.46	12	2170	53.22
Pr_2O_3	59	26.60	0.28	3.57	13	2175	46.77
Pr_6O_{11}	59	33.28	0.28	3.54	12	2180	54.68
$Nd(NO_3)_3.6H_2O$	60	22.23	0.33	3.00	4	2100	33.74
Nd_2O_3	60	34.68	0.28	3.52	12	2180	56.41
Gd_2O_3	64	36.26	0.28	3.56	11	2190	59.47
Dy_2O_3	66	37.31	0.28	3.60	10	2190	61.60
Lu_2O_3	71	39.06	0.27	3.66	10	2200	65.28
Ta	73	45.98	0.25	3.96	11	2230	80.30
W	74	49.74	0.30	3.33	1	2080	81.39
Pt	78	47.20	0.24	4.25	14	2290	85.35
Au	79	47.28	0.24	4.18	13	2280	84.53
Pb	82	39.99	0.16	6.07	38	2610	85.54
ThF_4	90	37.91	0.29	3.48	7	2200	62.21
UO_2	92	42.76	0.27	3.65	8	2230	71.80

Appendix D

MCF for pure elements and compounds: L-shell

Table D.1: L_α, E_p=1.0 MeV.

Target	Element Z	p mg/cm^2	$I(Z)$	$F(Z)$	ABS	E-Exit keV	Range mg/cm^2
CsCl	55	1.94	0.11	9.04	994	786	6.68
$BaCl_2$	56	1.93	0.13	7.68	870	765	6.01
La_2O_3	57	2.11	0.13	7.48	765	759	6.49
CeO_2	58	1.96	0.14	7.14	745	737	6.26
$Ce_2(SO_4)_3$	58	1.88	0.19	5.21	534	702	4.71
$Ce(SO_4)_2$	58	1.85	0.20	4.93	494	693	4.50
Pr_6O_{11}	59	2.09	0.13	7.52	745	757	6.52
Nd_2O_3	60	2.20	0.13	7.48	710	758	6.80
$Nd(NO_3)_3.6H_2O$	60	1.64	0.25	3.93	317	659	3.51
Sm_2O_3	62	2.35	0.14	7.15	622	750	7.08
SmF_3	62	2.25	0.16	6.37	557	731	6.39
Gd_2O_3	64	2.48	0.15	6.80	544	742	7.29
Dy_2O_3	66	2.60	0.14	6.97	512	743	7.81
HfF_4	72	2.62	0.18	5.41	302	704	6.92
Ta	73	3.39	0.12	8.34	406	761	11.68
W	74	3.51	0.12	8.19	396	756	11.98
Pt	78	3.98	0.14	7.31	284	739	12.76
Au	79	3.94	0.15	6.87	261	731	12.12
Pb	82	4.28	0.17	5.72	156	707	11.94

Table D.2: L_α, E_p=2.0 MeV.

Target	Element Z	p mg/cm^2	$I(Z)$	$F(Z)$	ABS	E-Exit keV	Range mg/cm^2
CsCl	55	5.48	0.08	13.23	628	1600	18.95
$BaCl_2$	56	4.34	0.06	16.33	870	1660	17.27
La_2O_3	57	4.80	0.06	15.47	765	1645	18.46
$Ce_2(SO_4)_3$	58	5.27	0.11	8.75	534	1465	13.67
$Ce(SO_4)_2$	58	5.39	0.13	7.96	494	1430	13.14
CeO_2	58	4.87	0.07	14.25	725	1625	17.76
Pr_6O_{11}	59	4.80	0.07	15.12	745	1635	18.36
$Nd(NO_3)_3.6H_2O$	60	5.74	0.20	5.02	317	1235	10.62
Nd_2O_3	60	5.02	0.07	14.96	710	1635	19.03
Sm_2O_3	62	5.51	0.07	13.78	622	1610	19.72
SmF_3	62	5.70	0.09	11.48	557	1550	17.84
Gd_2O_3	64	6.03	0.08	12.57	544	1580	20.21
Dy_2O_3	66	6.31	0.08	12.51	512	1575	21.20
HfF_4	72	7.87	0.13	7.61	302	1395	18.99
Ta	73	7.97	0.07	13.98	406	1590	29.46
W	74	8.25	0.07	13.78	396	1580	29.97
Pt	78	10.09	0.09	11.06	284	1505	31.61
Au	79	10.54	0.10	10.17	261	1480	30.95
Pb	82	13.23	0.14	7.10	156	1345	31.07

Table D.3: L_α, E_p=3.0 MeV.

Target	Element Z	p mg/cm^2	$I(Z)$	$F(Z)$	ABS	E-Exit keV	Range mg/cm^2
CsCl	55	4.47	0.03	36.68	998	2755	35.65
$BaCl_2$	56	4.81	0.03	29.63	870	2715	32.75
La_2O_3	57	5.35	0.04	27.87	765	2700	34.88
$Ce_2(SO_4)_3$	58	6.39	0.07	15.21	532	2525	26.33
$Ce(SO_4)_2$	58	6.61	0.07	13.70	494	2490	25.28
CeO_2	58	5.51	0.04	25.52	725	2680	33.57
Pr_6O_{11}	59	5.39	0.04	27.02	745	2690	34.57
Nd_2O_3	60	5.71	0.04	26.60	710	2685	35.73
$Nd(NO_3)_3.6H_2O$	60	7.89	0.13	7.92	317	2250	20.78
Sm_2O_3SM2O3	62	11.33	0.04	22.94	376	3490	58.18
SmF_3	62	6.59	0.05	20.01	558	2610	33.49
Gd_2O_3	64	6.91	0.05	21.91	544	2635	37.77
Dy_2O_3	66	7.30	0.05	21.55	512	2625	39.30
HfF_4	72	10.93	0.09	10.54	252	2365	35.45
Ta	73	9.10	0.04	23.05	406	2630	52.51
W	74	9.33	0.04	22.71	396	2625	53.29
Pt	78	11.87	0.06	17.68	284	2540	56.01
Au	79	12.44	0.06	16.23	261	2515	55.28
Pb	82	16.93	0.09	10.62	156	2340	55.82

Table D.4: L_α, E_p=4.0 MeV.

Target	Element Z	p mg/cm^2	$I(Z)$	$F(Z)$	ABS	E-Exit keV	Range mg/cm^2
CsCl	55	5.30	0.02	57.21	994	3760	56.29
$BaCl_2$	56	5.96	0.02	46.26	870	3710	52.00
La_2O_3	57	6.51	0.02	43.30	765	3700	55.24
$Ce_2(SO_4)_3$	58	8.15	0.04	25.00	534	3510	45.05
CeO_2	58	6.71	0.03	39.57	725	3680	53.22
$Ce(SO_4)_2$	58	8.51	0.05	20.95	494	3470	40.62
Pr_6O_{11}	59	6.76	0.02	41.79	745	3680	54.68
$Nd(NO_3)_3.6H_2O$	60	10.94	0.09	11.65	317	3170	33.74
Nd_2O_3	60	7.03	0.02	41.09	710	3680	56.41
Sm_2O_3	62	7.89	0.03	37.24	622	3650	58.18
SmF_3	62	8.26	0.03	30.56	557	3600	53.02
Gd_2O_3	64	8.72	0.03	33.43	544	3620	59.47
Dy_2O_3	66	9.18	0.03	32.68	512	3610	61.60
HfF_4	72	13.10	.06	18.06	302	3380	55.85
Ta	73	11.37	0.03	33.99	406	3610	80.30
W	74	11.79	0.03	33.54	396	3600	81.39
Pt	78	14.96	0.04	25.66	284	3510	85.35
Au	79	16.08	0.04	23.50	262	3470	84.53
Pb	82	22.74	0.07	14.85	156	3250	85.54

References

[Ah 75] M.S. Ahlberg, G. Johansson and K. Malmqvist, *Nucl. Instrum. Methods*, **131** (1975) 377.

[Ah 77] M.S. Ahlberg, *Nucl. Instrum. Methods*, **142** (1977) 61.

[Al 86] P. Aloupogiannis, G. Robaye, I. Roelandts, G. Weber, J.M. Delbrouck-Habaru and J.P. Quisefit, *Nucl. Instrum. Methods,* **B14** (1986) 297.

[Al 87] M.S. Al-Armaghanr, D. Crumpton and P.N. Cooper, *Nucl. Instrum. Methods*, **B18** (1987) 297.

[Al 89] P. Aloupogiannis, G. Weber, J.P. Quisefit, J.M. Delbrouck, I. Roelandts, M.C. Rouelle and G. Robaye, *Nucl. Instrum. Methods*, **B42** (1989) 359.

[Am 86] G. Amsel, Ch. Heitz and M. Menu, *Nucl. Instrum. Methods*, **B14** (1986) 30.

[An 73] M.R. Anderberg, *Cluster analysis for applications*, Academic Press, New York, 1973.

[An 73a] M. Anke and H.J. Schneider, III Jenaer Harnsteinsymposium, (1973) 116.

[Ba 72] W. Bambynek, B. Crasemann, R.W. Fink, H.U. Freund, H. Mark, C.D. Swift, R.E. Price and R.P. Venugopala, *Rev. Mod. Phys.,* **44** (1972) 716.

[Ba 78] K.G. Bauer, Q. Fazly, T. Mayer-Kuckuk, H. Mommsen and P. Schürker, *Nucl. Instrum. Methods*, **148** (1978) 407.

[Ba 89] L.J. Barbour, M.A.B. Pougnet and M. Peisach, *J. Radioanal. Chem. Letters*, **137** (1989) 327.

[Be 69] J-P. Benzecri, "Statistical analysis as a tool to make patterns emerge from data." In *Methodologies of Pattern Recognition*, edited by S. Watanabe, pp. 35-74. New York: Academic Press, 1969.

[Bi 70] G.A. Bissinger, J.M. Joyce, E.J. Ludwig, W.S. McEver and S.M. Shafroth, *Phys. Rev.,* **A1** (1970) 841.

[Bi 72] G.A. Bissinger and S.M. Shafroth, *Phys. Rev.*, **A5** (1972) 2046.

[Bl 82] N.J. Blacklock, In *Scientific foundations of urology Vol I*, D.A. Williams and G.D. Chisholm (Eds), William Heinemann Medical Books, London, (1982) 235.

[Bo 56] W.H. Boyoe and F.K. Garvey, *J. Urol.*, **76** (1956) 213.

[Bo 59] W.H. Boyoe and J.S. King, *J. Urol.*, **81** (1959) 351.

[Bo 79] G.J. Boulle and M. Peisach, *J. Radioanal. Chem.*, **50** (1979) 205.

[Bo 84] A.H. Botha and H.N. Jungwirth, *Proc. Tenth Intern. Conf. on Cyclotrons and their applications,* Michigan (1984) 263.

[Br 81] W. Brandt and G. Lapicki, *Phys. Rev.*, **A23** (1981) 1717.

[Br 81a] J.G. Brockis and B. Finlayson (Eds) Proceedings Int. Urinary Stone Conf. Perth, Australia, 1979 PSG Publishing Corp. Littleton, Mass., USA, 1981.

[Bu 90] M. Budnar, A. Smit and P. Kump, *Nucl. Instrum. Methods*, **B49** (1990) 138.

[Ca 75] J.L. Campbell, H.O. Orr, A.W. Hermann, L.A. McNelles, J.A. Thomson and W.B. Cook, *Anal. Chem.*, **47** (1975) 1542.

[Ca 80] T.A. Cahill, *Ann. Rev. Nucl. Part. Sci.*, **30** (1980) 211.

[Ca 81] L.E. Carlsson, K.G. Malmqvist, G.I. Johansson and K.R. Akselsson, *Nucl. Instrum. Methods*, **181** (1981) 179.

[Ca 83] J.L. Campbell and J.A. Cookson, *Nucl. Instrum. Methods,* **212** (1983) 427.

[Ca 84] J.L. Campbell, *Nucl. Instrum. Methods,* **B3** (1984) 185.

[Ca 85] J.L. Campbell, W.J. Teesdale and R.G. Leigh, *Nucl. Instrum. Methods,* **B6** (1985) 551.

[Ca 85a] J.L. Campbell, R.D. Lamb, R.G. Leigh, B.G. Nickel and J.A. Cookson, *Nucl. Instrum. Methods*, **B12** (1985) 402.

[Ca 86] J.L. Campbell, W. Maenhaut, E. Bombelka, E. Clayton, K. Malmqvist, J.A. Maxwell, J. Pallon and J. Vandehaute, *Nucl. Instrum. Methods*, **B14** (1986) 204.

[Ca 88] J.L. Campbell, *Nucl. Instrum. Methods*, **B31** (1988) 518.

[Ca 89] J.L. Campbell, J.-X. Wang, J.A. Maxwell and W.J. Teesdale, *Nucl. Instrum. Methods*, **B43** (1989) 539.

[Ca 89a] J.L. Campbell, W.J. Teesdale and J.A. Maxwell, *Nucl. Instrum. Methods*, **B43** (1989) 197.

[Ce 86] R. Cesareo, V. Bisceglie and L.J. Pedraza, *Br. J. Urol.*, **58** (1986) 253.

[Ch 76] E.T. Choong, G. Abdullah and J. Kowalczuk, *LSU Wood Utiliz. Notes*, No 29, 1976.

[Ch 81] M.H. Chen, B. Crasemann and H. Mark, *Phys. Rev.,* **A24** (1981) 177.

[Ch 81a] M.A. Chaudhri and A. Crawford, *Nucl. Instrum. Methods,* **181** (1981) 31.

[Ch 85] M.H. Chen and B. Crasemann, *At. Data Nucl. Data Tables*, **A24** (1985) 217.

[Ch 92] C.L. Churms, J.V. Pilcher, K.A. Springhorn and U.A.S. Tapper, *Nucl. Instrum. Methods,* in press (1992).

[Cl 81] E. Clayton, *Nucl. Instrum. Methods*, **141** (1981) 567.

[Cl 87] E. Clayton, *Nucl. Instrum. Methods*, **B22** (1987) 145.

[Co 75] M. Cohanim and E.R. Yendt, *Johns Hopkins Med. J.*, **136** (1975) 137.

[Co 81] D.D. Cohen, E. Clayton and T. Ainsworth, *Nucl. Instrum. Methods*, **188** (1981) 203.

[Co 83] J.A. Cookson, J.L. Campbell, *Nucl. Instrum. Methods*, **216** (1983) 489.

[Co 87] D.D. Cohen, *Nucl. Instrum. Methods*, **B22** (1987) 55.

[Co 88] D.D. Cohen and M. Harrigan, *At. Data & Nucl. Data Tables*, **33** (1988) 255.

[Cr 78] J.D. Cross and H. Smith, *Forensic Science*, **11** (1978) 147.

[Cu 80] B.E. Cutter, E.A. McGinnes and D.H. McKowan, *Wood Fibre*, **12** (1980) 72.

[Cu 87] F.T. Cua and G.S. Hall, *Biol. Trace Element Res.*, **12** (1987) 133.

[Cu 88] R.E. Cuenca, W.J. Pories and J. Bray, *Biol. Trace Elem. Res.*, **16** (1988) 151.

[De 72] D. De Soete, R. Gijbels and J. Hoste, "Neutron Activation Analysis", Wiley Interscience, 1972.

[De 73] G. Deconninck and N. Longequeue, *Phys. Rev. Lett.*, **30** (1973) 863.

[Do 83] R. I. Dorn, *Quaternary Res.*, **20** (1983) 49.

[Do 84] R. I. Dorn and D.S. Whitley *Ann. Assoc. Am. Geogr.*, **74** (1984) 308.

[Du 86] P. Duerden, D.D. Cohen, D. Dragovich and E. Clayton, *Nucl. Instrum. Meth.*, **B15** (1986) 643.

[Du 88] J.J.G. Durocher, N.M. Halden, F.C. Hawthorne and J.S.E. McKee, *Nucl. Instrum. Methods*, **B30** (1988) 470.

[El 65] E.L. Ellis, *Inorganic elements in wood*, Syracuse University Press, Syracuse, N.Y. 1965)

[Eu 67] E. Eusebio and J.S. Elliot, *Invest. Urol.*, 4 (1967) 431.

[Fe 81] G.P. Ferreira and F.B. Gil, *Archaeometry*, **23** (1981) 189.

[Fe 89] D. Fengel and G. Wegener, *Wood Chemistry, Ultrastructure, Reactions*, Walter de Gruyter, New York, 1989.

[Fi 61] B. Finlayson, C.W. Vermeulen and E.J. Stewart, *J. Urol.*, **86** (1961) 355.

[Fi 77] B. Finlayson, In *Calcium metabolism in renal failure and nephrolithiasis*, D.S. David (Ed), J. Wiley & Sons, New York, (1977) 337.

[Ga 81] R.P.H. Garten, K.-O. Groeneveld and K.-H. König, *Nucl. Instrum. Methods*, **B17** (1986) 156.

[Ge 75] A. Gervè and G. Schatz, *7th Int. Conf.on Cyclotrons and their applications, Experentia Suppl*, **24** (1975) 496.

[Ge 89] I. Gertner, O. Heber, J. Zajfman, D. Zajfman and B. Rosner, *Nucl. Instrum. Methods*, **B36** (1989) 74.

[Gi 71] W. Ginzel, *Papier*, **25** (1971) 305.

[Gi 76] I.S. Giles and M. Peisach., *J. Radioanal. Chem.*, **32** (1976) 105.

[Gi 76a] W.B. Gill and J.W. Karesh, *Urolithiasis Res. Proc. Int. Symp., 3rd*, (1976) 277.

[Gi 77] I.S. Giles and M. Peisach, *J. Radioanal. Lett.* (1977) 135.

[Gi 80] D. Gihwala and M. Peisach, *S. Afr. J. Chem.*, **33** (1980) 4.

[Gi 82] D. Gihwala, C. Olivier, M. Peisach and C.A. Pineda, *J. Trace Microprobe Tech.*, **1** (1982) 199.

[Gi 84] D. Gihwala, L. Jacobson, M. Peisach and C.A. Pineda, *Nucl. Instrum. Methods*, **B3** (1984) 408.

[Gi 85] D. Gihwala, L. Jacobson, M. Peisach, C.A. Pineda and H.N. Vos, *S. Afr. Archaeol. Bull.*, **40** (1985) 96.

[Gl 80] A.S. Gladney, *Anal. Chim. Acta*, **118** (1980) 385.

[Go 60] A.J.H. Goodwin, *S. Afr. Archaeol. Bull.*, **15** (1960) 67.

[Go 82] M.H.N. Golden, "Trace elements in human nutrition." *Human Nutrition: Clinical Nutrition* **36C** (1982) 185.

[Go 83] M. Goclowski, M. Jaskóla and L. Zemlo, *Nucl. Instrum. Methods*, **204** (1983) 553.

[Gr 82] M.J. Greenance and L.G. Underhill. "Scaling a data matrix in a low-dimensional Euclidean space." In *Topics in Applied Multivariate Analysis*, edited by D.M. Hawkins, pp. 183-268. Cambridge: University Press, 1982.

[Gr 84] M.J. Greenacre, "Theory and applications of correspondence analysis," Academic Press, London 1984.

[Gr 88] G.W. Grime and F. Watt, (Eds), "Nuclear Microprobe Technology and Applications," North-Holland, Amsterdam, 1988. Also in *Nucl. Instrum. Methods*, **B30** (1988) 227.

[Gr 90] M.J. Greenacre, "SIMCA version 2; PC software for correspondence analysis", 1990.

[Ha 72] K.M. Hambidge, C. Hambidge, M. Jacobs, and J.D. Baum., *Pediatric Research*, **6** (1972) 868.

[He 77] A. Hesse, H.J. Dietze, W. Berg and E. Heinzsch, *Eur. Urol.*, **3** (1977) 359.

[Hi 79] W.E. Hillis and D. de Silva, *Holzforschung*, **33** (1979) 47.

[Ho 71] D. Hodgkiss, "Woodstock glass", Grafix, Cape Town, 1971.

[Ho 89] J. Hofbauer and I. Steffan, In *Urolithiasis*, ed. V.R. Walker, R.A. Sutton, E.C. Cameron, C.Y. Pak and W.G. Robertson, New York: Plenum (1989) 229.

[Hu 81] L.S. Hurley, *Philosophical Transactions of Royal Society of London* **B.294**, (1981) 141.

[Hu 85] G.L. Hutchings and R.G. Copperthwaite, *S. Afr. J. Sci.*, **81** (1985) 537.

[Hy 81] M. Hyvönen-Dabek, J. Räisänen and J.T. Dabek, *J. Radioanal. Chem.*, **63** (1981) 163.

[Iu 84] Indiana University Cyclotron Facility Scientific and Technical Report, (1985) 165.

[Iy 76] G.V. Iyengar, *Radiochem. Radioanal. Letters*, **24** (1976) 35.

[Iy 77] G.V. Iyengar and K. Krasperek, *J. Radioanal. Chem.*, **39** (1977) 301.

[Ja 77] P.A. Jacobs, "Carboniogenic activity of zeolites", Elsevier, Amsterdam, 1977.

[Ja 89] M. Jakšić, M. Vajić, S. Fazinić, D. Rendić, T. Tadić and V. Valković, *Nucl. Instrum. Methods*, **B40/41** (1989) 643.

[Ja 91] L. Jacobson, J.H.N. Loubser, M. Peisach, C.A. Pineda and W. Van der Westhuizen, *S. Afr. Archaeol. Bull.*, **46** (1991) 19.

[Je 92] H. Jervis, (unpublished data) private communication (1992).

[Jo 62] R.C. Jopson, H. Mark and C.D. Swift, *Phys. Rev.*, **127** (1962) 1612.

[Jo 70] T.B. Johansson, R. Akselsson and S.A.E. Johansson, *Nucl. Instrum. Methods*, **84** (1970) 141.

[Jo 87] J. Joost and R. Tessadri, *Eur. Urol.*, **13** (1987) 264.

[Jo 88] S.A.E. Johansson and J.L. Campbell, "PIXE, a novel technique for elemental analysis", John Wiley & Sons, Great Britain,1988.

[Jo 92] S.A.E. Johansson, *Int. J. PIXE*, **2** (1992) 33.

[Kh 81] M. Khaliquzzaman, M.B. Zaman and A.H. Khan, *Nucl. Instrum. Methods*, **181** (1981) 209.

[Kl 80] C.R. Kleeman, J.W. Coburn, A.S. Brickman, D.B.N. Lee, R.G. Narins and R.M. Ehrlich, *West J. Med.*, **132** (1980) 313.

[Ko 61] G.A. Korn and T.M. Korn, "Mathematical handbook for scientists and engineers", McGraw-Hill, New York, 1961.

[Kr 79] M.O. Krause, *J. Phys. Chem. Ref. Data,* **8** (1979) 307.

[Kw 92] W.M. Kwiatek, J. Lekki, C. Paluskiewicz and N. Preikschas *Nucl. Instrum. Methods*, **B64** (1992) 512.

[Le 77] J. Leroux and T.P. Thinh, "Revised tables of X-ray mass attenuation coefficients," Report Corporation Scientifique Claisse Inc., Quebec (1977).

[Le 78] A.A. Levinson, M. Nosal, M. Davidman, E.L. Prien, Sr., E.L. Prien, Jr. and R.G. Stevenson, *Invest. Urol.*, **15** (1978) 270.

[Li 85] S.M. Lin, C.H. Chiang, C.H. Huang, C.L. Tseng and M.H. Yang, *J. Radioanal. Chem. Letters*, **96** (1985) 153.

[Lo 88] J.H.N. Loubser, *Archaeological contributions to Venda ethnohistory*, Thesis University of the Witwatersrand, 1988.

[Ma 63] D.W. Marquardt, *J. Soc. Ind. Appl. Math.*, **11** (1963) 431.

[Ma 80] W. Maenhaut, L. De Reu, H.A. Van Rinsvelt, J. Cafmeyer and P. Van Espen, *Nucl. Instrum. Methods*, **168** (1980) 557.

[Ma 84] W. Maenhaut and H. Raemdonck, *Nucl. Instrum. Methods*, **B1** (1984) 123.

[Ma 89] J.A. Maxwell, J.L. Campbell and W.J. Teesdale, *Nucl. Instrum. Methods*, **B43** (1989) 218.

[Mc 69] W.H. McMaster, N.K. del Grande, J.H. Mallet and J.H. Hubbell, University of California Technical Report, UCRL-50174 (1969) 1970.

[Me 75] J.L. Meyer and L.H. Smith, *Invest. Urol.*, **13** (1975) 30.

[Me 77] J.L. Meyer and E.E. Angino, *Investigative Urology*,**14** (1977) 347.

[Me 84] B.R. Meyer, E. Le Roux, M.J. Renan and M. Peisach, *Nucl. Instrum. Methods*, **B3** (1984) 557.

[Mi 89] J. Miranda, A. Olivier and E.C. Montenegro, *Nucl. Instrum. Methods*, **B43** (1989) 203.

[Mo 74] E.J. Moynahan, "Acrodermatits enteropathica., *Lancet*, **2** (1974) 399.

[Na 83] NAG FORTRAN Library manual, Mark 10, Numerical Algorithms group, Oxford,1983.

[Na 83a] G.H. Nancollas, *Proc. Eur. Dial. Transplant. Assoc.*,**20** (1983) 386.

[Ne 70] G.C. Nelson, B.G. Saunders and S.I. Salem, *Atom. Data,* **1** (1970) 377.

[Ne 79] H.L. Needleman, C. Gunnoe, A. Leviton, et al. *New England J. Med.*, **300** (1979) 689.

[Oh 57] N.Ohta, *Bull. Chem. Soc. Jpn.*, **30** (1957) 833.

[Ol 87] A. Olivier and J. Miranda, *Nucl. Instrum. Methods*, **B29** (1987) 521.

[Or 90] I. Orlić, F. Van Langevelde and R.D. Vis, *Nucl. Instrum. Methods*, **B49** (1990) 74.

[Pa 72] A. Pape and J.C. Sens, *Nucl. Instrum. Methods*, **105** (1972) 161.

[Pa 76] C.Y.C. Pak, In *The Kidney Vol II*, B.M. Brenner and F.C. Rector Jr. (Eds), W.B. Saunders, Philadelphia, Pa USA, (1976) 1326.

[Pa 78] C.S. Papper, M.A. Chaudhri and J.L. Rouse, *Nucl. Instrum. Methods*, **154** (1978) 219.

[Pa 89] H. Paul and J. Sacher, *At. Data & Nucl. Data tables,* **42** (1989) 105.

[Pe 73] M. Peisach, *Thin Solid Films*, **19** (1973) 297.

[Pe 85] M. Peisach, C.A. Pineda, D. Gihwala and H.N. Vos, *J. Trace Microprobe Tech.*, **3** (1985) 129.

[Pe 88] M. Peisach, C.A. Rabe, C.A. Pineda, D. Mahalu and R. Tenne, *J. Vac. Sci. Technol.,* **B6** (1988) 1506.

[Pe 90] M. Peisach and C.A. Pineda, *Nucl. Instrum. Methods*, **B49**(1990) 10.

[Pe 91] M. Peisach, C.A. Pineda, L. Jacobson and J.H.N. Loubser *J. Radioanal. Nucl. Chem.*, **151**(1991) 229.

[Pe 92] M. Peisach, A.E. Pillay and C.A. Pineda, *Nucl. Instrum. Methods*, (in press).

[Pe 92a] M. Peisach, A.E. Pillay and C.A. Pineda and T. Themistocleous, *Nucl. Instrum. Methods, J. Radioanal. Nucl. Chem.*, **159**(1992) 71.

[Pi 88] C.A. Pineda and M. Peisach, *Nucl. Instrum. Methods*, **B35** (1988) 344.

[Pi 88a] C.A. Pineda and M. Peisach, Annual Report, NAC/AR/88-01, National Accelerator Centre, June 1988, p. 202.

[Pi 90] C.A. Pineda and M. Peisach, *Nucl. Instrum. Methods*, **299** (1990) 618.

[Po 77] R.M. Potter and G.R. Rossman, *Science.*, **196** (1977) 1446.

[Po 88] M.A.B. Pougnet, M. Peisach and A.L. Rodgers, *Nucl. Instrum. Methods*, **B35** (1988) 472.

[Rä 86] J. Räisänen, *X-ray Spect.*, **15** (1986) 159.

[Ra 63] J. Raaflaub, *Helv. Med. Acta*, **30** (1963) 724.

[Ra 76] C.P. Randell, J.S.C. McKee and S.F.J. Wilk, *J. Phys. G: Nucl. Phys.*, **2** (1976) L69.

[Ra 78] W.D. Ramsay M.S.A.L. Al-Ghazi, J. Birchall and J.S.E. McKee, *Phys. Lett.*, **A69** (1978) 258.

[Ra 90] C.G. Rayn, D.R. Cousens, S.H. Sie, W.L. Griffin, G.F. Suter and E. Clayton, *Nucl.Instrum. Methods*, **47** (1990) 55.

[Ra 92] C.G. Rayn, Private communication, 1992.

[Re 75] W. Reuter, A. Lurio, F. Cardone and J.F. Ziegler, *J. Appl. Phys.*, **46** (1975) 3194.

[Ro 69] J.T. Routti and S.G. Prussin, *Nucl. Instrum. Methods*, **72** (1969) 125.

[Sa 74] S.I. Salem, S.L. Panossian and R.A. Krause, *At. Data & Nucl. Data Tables,* **14** (1974) 91.

[Sa 88] C.G. Sampson, *Memoirs Natl. Museum Bloemfontein*, **20** (1988) 1.

[Sc 73] G. Scurfield, A.J. Mitchell and S.R. Silva, *Bot. J. Linnean Soc.*, **66** (1973) 277.

[Sc 74] J.H. Scofield, *At. Data & Nucl. Data Tables*, **14** (1974) 121.

[Sc 74a] J.H. Scofield, *Phys. Rev.*, **A9** (1974) 1041.

[Sc 74b] J.H. Scofield, *Phys. Rev.*, **A10** (1974) 1507.

[Sc 82] R. Scott, C. Cunningham, A. McLelland, G.S. Fell, O.P. Fitzgerald-Finch, and N. McKellar, *Br. J. Urol.*, **54** (1982) 584.

[Sc 85] P.O. Schwille, L.H. Smith, W.G. Robertson and W. Vahlensiek (Eds), *Urolithiasis and related clinical research*, Plenum Press, New York, 1985.

[Sh 72] L. Shabason, B.L. Cohen, G.H. Wedberg and K.C. Chan, *J. Appl. Phys.*, **44** (1972) 4749.

[Sl 72] V.W. Slivinsky and P.J. Ebest, *Phys. Rev.*, **A5** (1972) 1581.

[Sm 76] B.T. Smith, EISPACK II Manual, Springer-Verlag, New York, 1976.

[Sm 81] L.H. Smith, W.G. Robertson and B. Finlayson (Eds), *Urolithiasis, Clinical and basic research*, Proceedings 4th Int. Sym. Urolithiasis Res., Williamsburg, Virginia, U.S.A., 1980. Plenum Press, New York, 1981.

[Sm 84] Z. Smit, M. Budnar, V. Cindro, V. Ramsak and M. Ravnikar, *Nucl. Instrum. Methods*, **B4** (1984) 114.

[Sm 86] Z. Smit, *Nucl. Instrum. Methods*, **B17** (1986) 156.

[Sn 81] P.G.W. Snyman, *Bull. S. Afr. Cul. Hist. Mus.*, **2** (1981) 14.

[Su 71] D.J. Sutor, *Biochem. J.*, **122** (1971) 6P.

[Sz 81] S.Szymczyk, J. Kajfosz and A. Hrynkiewicz, *Nucleonika*, **26** (1981) 561.

[Ta 82] B.R. Taylor and A. Saied, *Br. J. Urol.*, **54** (1982) 346.

[Ta 92] U.A.S. Tapper, *Nucl. Instrum. Methods*, in press (1992).

[Th 86] K. Themer and K.G. Malmqvist, *Nucl. Instrum. Methods*, **B15** (1986) 404.

[Ts 79] L. Tsang-Lang, L. Chein-Shu and Ch. Jen-Chang, *Nucl. Instrum. Methods*, **159** (1979) 387.

[Un 85] L.G. Underhill and M. Peisach, *J. Trace Microprobe Tech.*, **3** (1985) 41.

[Va 79] W. Vahlensieck, In *Urolithiasis 1*, W. Vahlensieck (Ed), Springer, Berlin, 1979.

[Va 81] P. Van Espen, H. Nullens and F. Adams, "Proc. A.N.S. Topical Conference", Mayaguez, Puerto Rico, U.S. Dept. of Energy, 1978, p. 96. (Copyright, Canberra Industries Inc., Meriden, CT, 1981).

[Ve 66] C.W. Vermeulen, J.E. Ellis and H. Te-Chin, *J. Urol*, **95** (1966) 681.

[Ve 74] W.J. Veigele, "Mass attenuation and absorption cross section for 94 elements; 0.1 keV to 1 MeV", Handbook of Spectroscopy, CRC Press, Vol 1, Baton Rouge, 1974.

[Ve 85] J. Versiek, "Trace elements in human body fluids and tissues", CRC Critical Reviews in Clinical Laboratory Vol 22, 1985, p. 97.

[Vi 85] R.D. Vis, "The Proton Microprobe: Applications in the Biomedical Field," CRC Press, Boca Raton, Florida, 1985.

[Wa1891] J. Walther, *Akad. Wissensch. Math.-Phys. Klasse, Abhand.*, **16** (1891) 431.

[Wa 71] R.L. Watson, J.R. Sjurseth and R.W. Howard, *Nucl. Instrum. Methods*, **93** (1971) 69.

[Wa 80] P.A. Walravens, *Clinical Chemistry*, **26/2** (1980) 185.

[Wa 87] F. Watt and G.W. Grime, "Principle and Applications of High-Energy Ion Microbeams", Adam Hilger, Bristol, England, 1987.

[Wi 77] S.F.J. Wilk, J.S.C. McKee and C.P. Randell, *Nucl. Instrum. Methods*, **142** (1977) 33.

[Wi 81] E.T. Williams and H.L. Finston, *Nucl. Instrum. Methods*, **181** (1981) 195.

[Wo 73] World Health Organization. "Trace elements in human nutrition.", *Technical Report Series*, No. 532 Geneva, 1973.

[Wr 64] C. Wrays, Lightings emporium oil and fittings, Catalogue **6**, London, 1964.

[Yo 82] L.B. Young, S.A. Butter, and W.W. Kaeding, *J. Catal.*, **76** (1982) 418.

[Zi 85] J.F. Ziegler, J.P. Biersack and U. Littmark, "The stopping and range of ions in solids," Vol 1, Pergamon Press, New York, 1985.